# Volcanology and Secondary Alteration of the 1.6 Ma Ngaroma Ignimbrite, Upper Waipari Valley

A thesis

submitted in partial fulfilment

of the requirements for the degree

of

***Master of Science (Research)*** in **Earth Science**

at

**The University of Waikato**

by

**ChrisAnne Tyler Ross**


THE UNIVERSITY OF
WAIKATO
*Te Whare Wānanga o Waikato*

2020

This achievement is dedicated to Shawn P. Ross

March 21st 1978 - July 26th 2019

# Abstract

The 1.6 Ma Ngaroma eruption from the Mangakino Volcanic Centre (MVC) is the first known rhyolitic event of the Taupo Volcanic Zone (TVZ), and variations of primary components recorded throughout the Ngaroma Ignimbrite provide insight(s) into pre-eruptive processes and post-emplacement mechanisms.

A field study of the Ngaroma Ignimbrite was undertaken proximal to the source caldera (~25 km) around the township of Ngaroma. Two primary facies (a lithic-rich and lithic-poor facies) and four subfacies have been identified and are presented in four stratigraphic logs, which vary both vertically and laterally throughout the field area. The facies reflect syn- and post-deposition process that are identifiable from one another based on macroscopic observations including changes in primary componentry, the degree of welding and nature of secondary alteration. Variations in depositional structures and textures highlight the intense welding, limited incorporation of vent-derived lithics, and the absence of a pumice/ash fall deposit underlying the ignimbrite, which suggest that the parent pyroclastic flow formed from the immediate collapse of a highly explosive, caldera-forming eruption column.

Petrographic observations and mineralogic analyses involving optical microscopy, scanning electron microscopy (SEM), and X-ray diffraction (XRD) record high concentrations of sanidine and cristobalite, followed by clay minerals (kaolinite), which suggest the deposit endured significant post-emplacement processes such as vapour-phase alteration and devitrification. The ignimbrite matrix varies from a eutaxitic texture comprising (a) visible, well-formed, but devitrified, glass shards typically 300 to 800 μm, to (b) a fine-grained, homogenous, optically unresolvable medium; the latter can be resolved under SEM and comprises intergrown <3 μm-sized K-feldspar (sanidine), amorphous/nano-crystalline silica (cristobalite ± tridymite), and pore cavities.

Geochemical analyses of major and trace elements on bulk ignimbrite and pumice were determined using x-ray fluorescence (XRF) spectrometry and laser ablation inductively coupled plasma mass spectrometry (LA-ICP-MS), and on individual minerals by electron microprobe analysis (EPMA). Samples used in these

geochemical analyses have been pervasively altered, and that due to the lack or absence of primary material (fresh glass and pumice), some of the patterns observed here are presumed to in part reflect post alteration processes (vapour-phase alteration and devitrification) and therefore, are of limited use for understanding primary magmatic processes. The major and selective trace elements of bulk rock ignimbrite and pumice confirm a rhyolitic composition and are consistent with the effect of syn- and post-emplacement alteration processes. Geochemical signatures of rare earth elements (REE) observed on multielement diagrams are associated with subduction related magmas and indicative of crustal contamination. Major element compositions of both feldspar and pyroxene phenocrysts range from $An_{15}$- $An_{28}$ and $Or_5$-$Or_{12}$ and from $En_{32}$ to $En_{41}$, respectively, and are typical composition of rhyolitic magmas.

# Acknowledgements

First and foremost I thank my supervisor Dr. Adrian Pittari for giving me the opportunity to learn and grow as a young, aspiring volcanologist. Adrian - your time, patience, and willingness to leave your door open every day does not go unnoticed and nor should it to those reading this thesis, as completion of this project would not have been possible with a closed door – your advice, input, and knowledge is truly appreciated. New Zealand has been filled with many, although challenging, exciting learning opportunities that were also accompanied with great difficulties. I am eternally grateful for the understanding and encouragement in which I have received so much of during these past two years.

I am also grateful for the additional guidance received from Dr. David Lowe and professor Roger Briggs during this research. Your input and advice, and willingness of time is truly appreciated.

Many thanks to the laboratory technicians in the Department of Earth and Ocean Sciences at the University of Waikato (UoW) for the assistance I received during laboratory work, especially to Renat Radosinsky, Helen Turner, and Annette Rodgers. Special thanks to Kirsty Vincent for the many laughs and endless help during what seemed like never ending days of preparing samples - your time and assistance is greatly appreciated. I'd like to also extend this appreciation to Dr. Ian Schipper (Victoria University of Wellington) for the assistance I received during EPMA analyses in Wellington. Finally, a tremendous thank you to Cheryl Ward (Academic Liaison Librarian) for the time, patience, and willingness to assist in formatting this thesis.

I would like to also acknowledge the Department of Earth and Ocean Sciences at the University of Waikato (UoW) for the Broad Memorial Fund scholarship which helped cover living expenses while being in New Zealand. This appreciation also applies to the Western Australian Skeptics for a grant which provided funding for EPMA analyses.

To the families of Ngaroma Township who have kindly welcomed me to explore their wonderful ignimbrite-filled paddocks – thank you for allowing me to carry out this research and expand my knowledge in these volcanic deposits.

I would also like thank my fellow colleagues, who have also become wonderful friends during these past two years; Krystal Geraghty, Jackson White, Kristyn Numa, Oliver McLeod, and Marlena Prentice to name a few – thank you for being always so kind to me here in the land down unda. To my friends and colleagues Matthew House, Maddie Hansen, and Doney Kuman - thank you also for assisting me during field days.

I am very lucky and grateful for the consistent love and support from my family and friends back home in New York and would like to thank especially my Dad (Chris Ross), Mom (Hope DellaStua), and Nana and Poppy (Lucille and Bob Ross). To those at home who have also provided words of comfort and encouragement during these past two years – you being there for me is reflected in this work and I am forever thankful.

Finally, from the bottom of my heart, and with all of my heart, I am eternally grateful for my New Zealand family (Bruno, Robyn, André, and Krystal Geraghty, and Nana n' Pop) for the unconditional love, strength, and encouragement which I have been given so much of – I truly would not be who I am, or where I am today without you.

# Table of Contents

# List of Figures

# List of Tables

# Chapter One

# Literature Review

## 1.1 Introduction

The Taupo Volcanic Zone (TVZ) in the North Island of New Zealand represents an active volcanic arc basin comprised of eight caldera-forming complexes including the Mangakino Volcanic Centre (MVC) (McCormack et al., 2009). Occurrence of explosive volcanic activity within the TVZ reflects a major rifting sequence associated with the currently active Pacific and Australian plate boundary system. These volcanic processes have produced, in total, approximately 16,000 $km^3$ of magma since 1.6 Ma through ~34 caldera-forming events, including that of the 1.6 Ma Ngaroma eruption (Cooper et al., 2012).

Amongst the preserved deposits of explosive volcanic eruptions, the Ngaroma Ignimbrite is unique in that it represents the first-known rhyolitic (caldera-forming) event to have occurred at the MVC and of the TVZ as a whole (Wilson, 1986). The eruption deposits are well preserved with respect to their age, and they record emplacement mechanisms through variations in facies and primary components. Previous studies involving stratigraphic observations and field mapping were first conducted by Martin (1961) who named the Ngaroma Ignimbrite and described the exposure at a quarry three-quarters of a mile west-northwest of Ngaroma School (N84/055 853). Likewise, Martin (1961) classified and related the overlying ignimbrite deposits to each of the associated episodic events at the MVC. This research describes and interprets the textural and lithological characteristics of primary products produced at the MVC during the 1.6 Ma Ngaroma eruption.

## 1.2 Reason for Thesis and Primary Purpose

This work aims to understand the transport, emplacement and post-emplacement processes of the 1.6 Ma Ngaroma eruption sourced from the Mangakino Volcanic Centre (MVC). Understanding large ignimbrite-forming eruptions provide outstanding

insights regarding the behaviours and volcanic processes of both recent and future eruption events. Contributions from this research will provide new perspectives associated with the behaviour of early rhyolitic eruptions associated with the MVC and of the TVZ as a whole. Using the 1.6 Ma Ngaroma eruption as a case study, this research will be approached through field observations and petrographic and geochemical analyses, and will provide detailed understanding of how these volcanic products were transported and deposited during the time of this eruption. Mangakino-derived ignimbrites and their respective stratigraphic units have previously been recorded and defined by Martin (1961).

## 1.3 Objectives

The primary research objectives are as follows:

1. Understand stratigraphy and facies variation by constructing stratigraphic logs and a locality map.

2. Describe and quantify bulk ignimbrite textures and composition; and the texture and composition of its components, through petrographic (optical and SEM) and XRD techniques.

3. Determine bulk rock ignimbrite and pumice geochemical composition and mineral chemistry.

## 1.4 Thesis Structure

The primary objectives of this research project will be addressed in six interrelated chapters. Each chapter will correspond to a specific component of this research project and provide a systematic framework for understanding the primary volcanic processes associated with early rhyolitic eruptions of the MVC. For the purpose of clarification, please note that each consecutive chapter will be based off the findings from its previous chapter.

Chapter One: The remainder of chapter one reviews the general tectonic setting and geological history of the Taupo Volcanic Zone (TVZ) followed by a detailed literature review from previous case studies that focused on the Mangakino Volcanic Centre (MVC). Detailed descriptions of Mangakino eruptives, including the major ignimbrite successions, will also be discussed in this chapter.

Chapter Two: Chapter two will provide a general overview of the field area, as well as describe in detail, lithological characteristics of the exposed geological units recorded throughout the area of Ngaroma and in this study. A locality map and stratigraphic logs will also be presented in this chapter to show the vertical variations that occur within these recognised geological units throughout the area of Ngaroma.

Chapter Three: The textural variations and mineralogy in the Ngaroma Ignimbrite were observed and analysed using the scanning electron microscope (SEM), energy-dispersive spectra (EDS), x-ray diffraction (XRD) analyses, and optical microscopy. Detailed descriptions of these petrographic analyses will therefore be presented in this chapter.

Chapter Four: This chapter will describe the bulk rock and mineral geochemical compositions of the Ngaroma Ignimbrite. The geochemical data was obtained from x-ray fluorescence (XRF) spectrometry, laser ablation inductively coupled plasma mass spectrometry (LA-ICP-MS), and electron probe microanalysis (EPMA) analyses. The data will be presented on a series of geochemical diagrams to show the compositional changes related to post-alteration processes and also to explain the composition of crystalline phases.

Chapter Five: Chapter five will provide detailed explanations related to the physical eruption and emplacement mechanisms, and post- emplacement geochemical alteration processes of the 1.6 Ma Ngaroma Ignimbrite.

Chapter Six: This chapter will integrate the overall significance and primary findings obtained from this research, as well as address any new or ongoing findings that have potential for future research.

## 1.5 Tectonic Setting

The North Island of New Zealand straddles a boundary zone located tectonically between the converging Pacific and Australian plates (Figure 1.1; Wallace, 2004). In particular, subduction of the Pacific Plate occurs obliquely along the dextral fault belt, east of the North Island and west of the oceanic Hikurangi Plateau along the Hikurangi Trough, which has established a volcanic front represented by back-arc extension, high heat flow, prolific volcanism, geothermal activity, and active doming and exhumation at the continental surface (Deering et al., 2011; Stern et al., 2006). This volcanic front constitutes a wedge-shaped area, currently recognised as the Taupo Volcanic Zone (TVZ) and denotes the most frequently active and productive siliceous magmatic system on Earth today (Wilson, 1984).

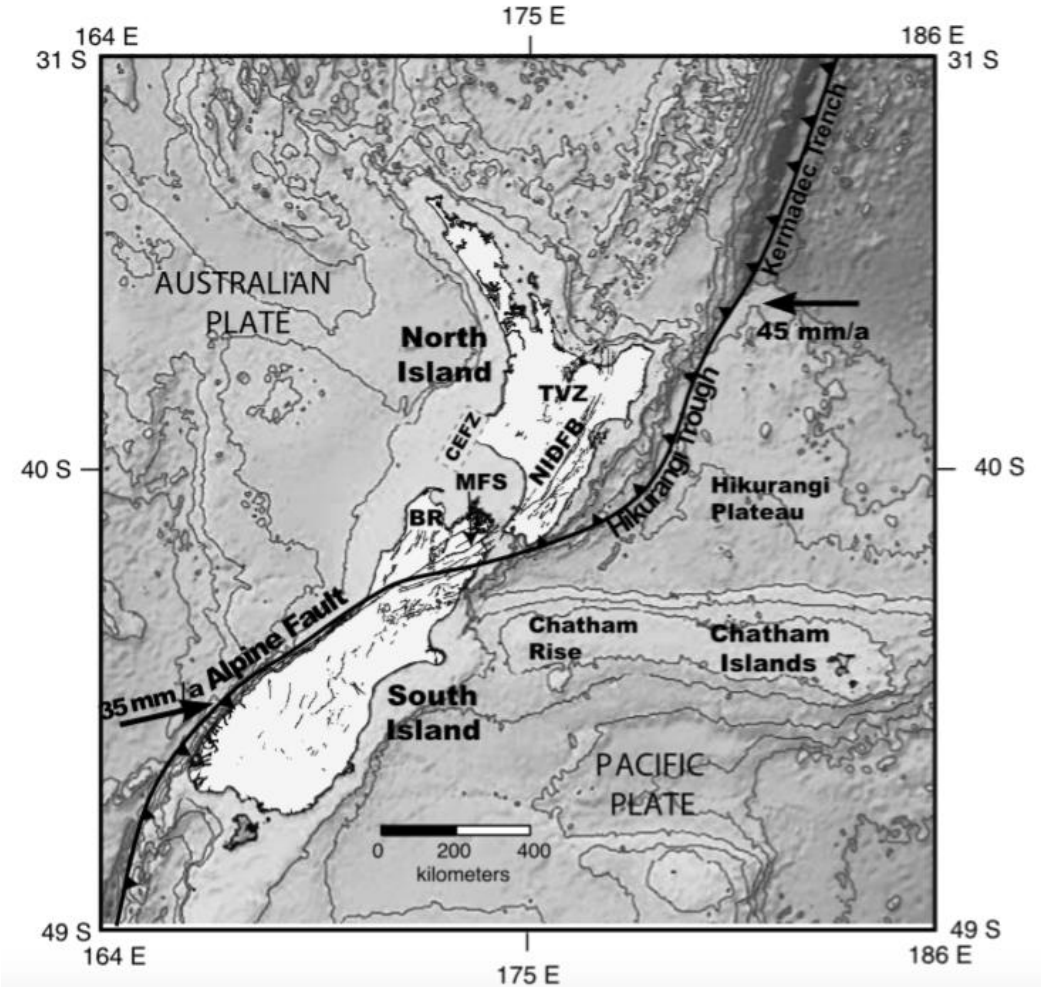


**Figure 1.1:** Geological map representing the North Island of New Zealand and its tectonic relationship between the Pacific and Australian plates. Notice the Hikurangi Plateau and Hikurangi Trough to the west of the Pacific Plate and east of the North Island (Wallace, 2004).

## 1.6 Geological History of the TVZ

The TVZ is a NNE-SSW trending volcanic arc basin that extends from Mt. Ruapehu to White Island in the central North Island of New Zealand (Figure 1.2; Wilson et al., 1995; Cooper et al., 2012; Cooper and Wilson, 2014). The zone is 300 km long and 60 km wide, and coexists with active extension (at a rate of ~8-10 mm/year) and westward subduction of the Pacific Plate beneath the Indo-Australian plate (Deering et al., 2011; McCormack et al., 2009; Price et al., 2005). Early volcanic activity of the TVZ which was chiefly andesitic in composition, commenced at c. 2 Ma, and erupted approximately 10,000 km$^3$ of magma. This was later joined by large and volumetrically intense rhyolitic eruptions (producing >16,000 km$^3$ of magma in total) from c. 1.6 Ma, including approximately 34 caldera-forming events (Cooper et al., 2012; McCormack et al., 2009).

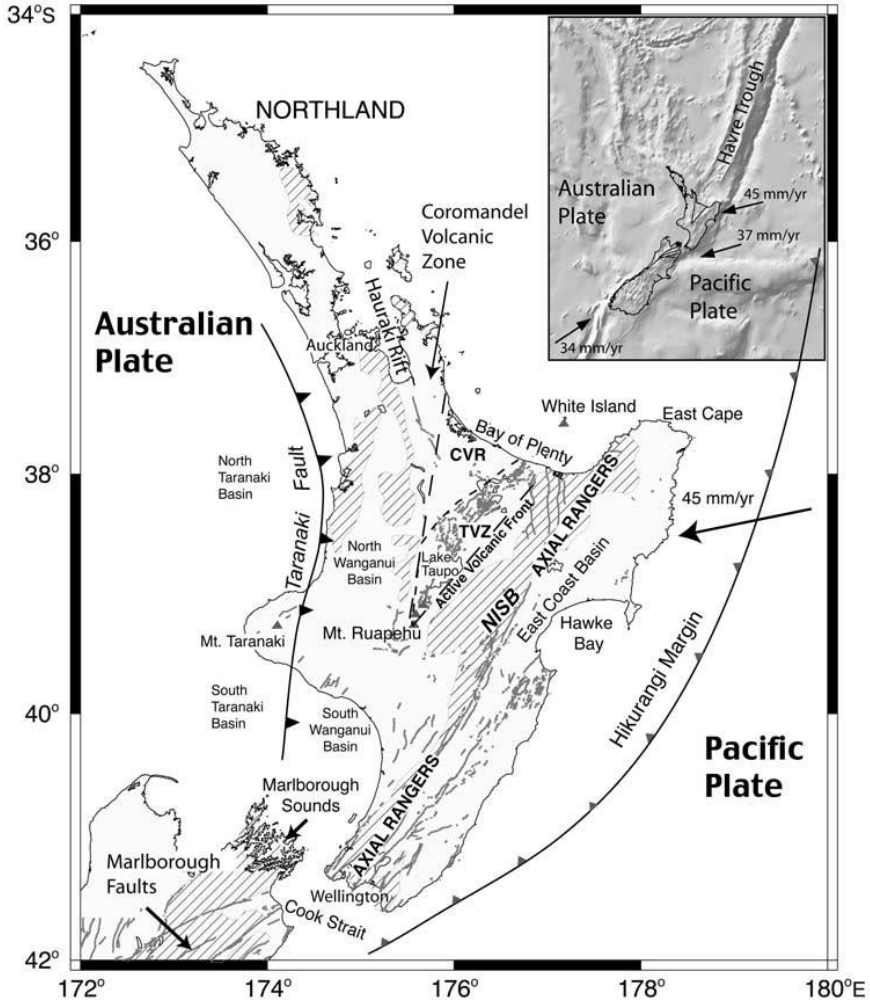


**Figure 1.2**: Geological setting of the NNE-SSW trending TVZ in the central North Island of New Zealand (Stern et al., 2006).

Early volcanic centres of the TVZ and their associated deposits have been buried due to subsequent volcanism, destroyed by caldera collapse and regional subsidence, or concealed by erosion; therefore detailed understanding of the history of the TVZ decreases with age (Wilson et al., 1995).

The TVZ encompasses a total of eight volcanic centres that together form three identifiable boundaries currently termed the old, young, and modern TVZ (Figure 3; McCormack et al., 2009; Wilson et al., 1995). These boundaries are defined by the structural margins of caldera complexes and their respective vent positions, and exemplify changes in both eruption composition and style.

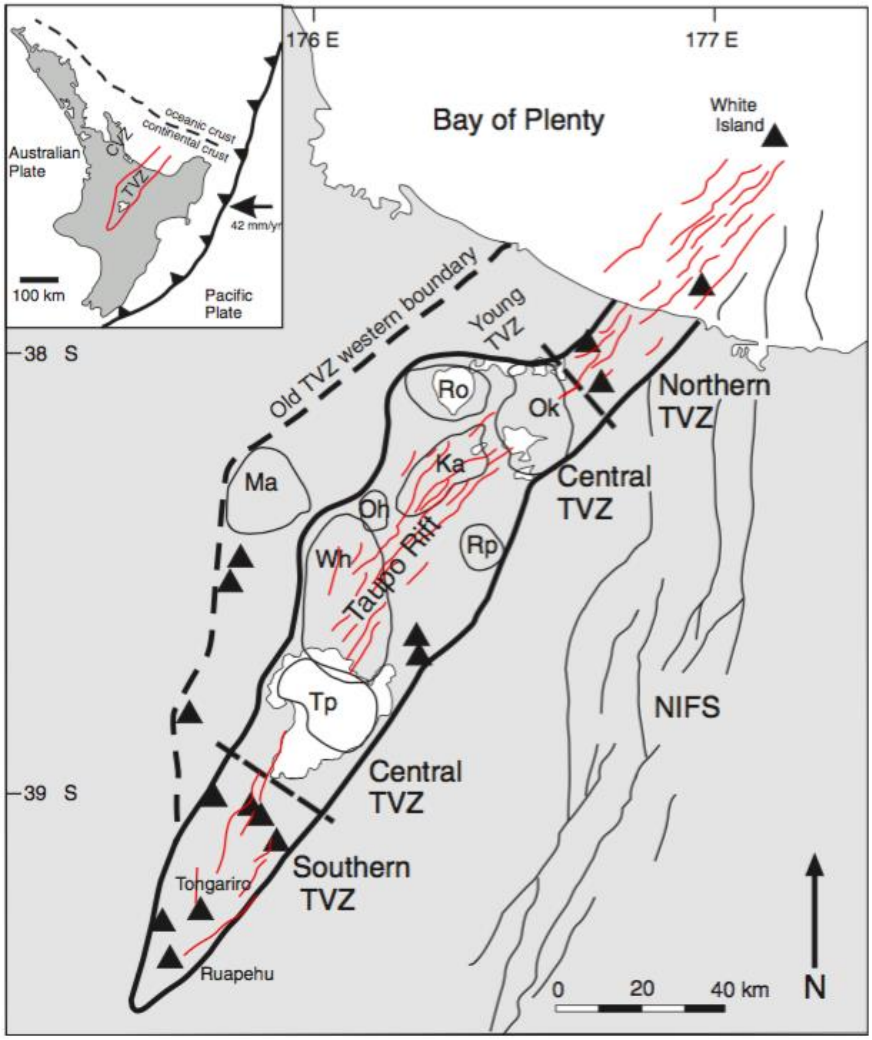


**Figure 1.3**: Regional map depicting the whole Taupo Volcanic Zone (TVZ) in the central North Island of New Zealand. The old, young, and modern TVZ are defined by the eight caldera complexes and volcanic structures. Rhyolitic calderas are outlined in black while andesitic composite cone volcanoes are represented by black triangles. NIFS, North Island Fault System (Deering et al., 2011).

### 1.6.1 Old TVZ

The old TVZ occupies the western-most boundary of the whole TVZ (Figure 1.3; Martin, 1961; Wilson et al., 1995). The area is defined by a thin westward sloping apron of stratified ignimbrite deposits which rest directly above Mesozoic and Tertiary sediments, forming the northwest-trending tilted greywacke blocks, known as the Hauhungaroa and Rangitoto Ranges. Martin (1961) describes this apron as a stable fringe that denotes the western sector of a high plateau which has since collapsed to form one of many complex graben structures within the whole TVZ.

Volcanic products of the old TVZ outcrop in restricted areas in the west of King Country. These products include a succession of ignimbrites, and smaller pyroclastic units and lavas, that are presumed to represent volcanic activity from c. 2 Ma up until the onset of the 0.34 Ma Whakamaru group eruptions. The voluminous and widely distributed ignimbrites include, in stratigraphic order, the *Ngaroma, Ongatiti, Ahuroa, Rocky Hill, Kidnappers, and Marshall ignimbrites* (Wilson et al., 1995). Smaller, locally distributed eruption units were also distributed from the Mangakino caldera and collectively are termed the Pakaumanu Group (Table 1.1; Leonard et al., 2010).

## 1.7 The King Country Basin

The King Country basin (formerly termed the North Wanganui basin) occurs immediately east of the northern-most sector of the Taranaki basin and north of the Wanganui basin, where it sits within a southward dipping monocline (the Wanganui monocline) (Kamp et al., 2002). It is defined by the Herangi structural high to the west, and by the northwest-tilted Rangitoto and Hauhungaroa Ranges to the east, and forms the western-most boundary of the TVZ. The basin is currently ~200-300 m above sea level, however at the eastern volcanic uplands, it is approximately 1,100 m above sea level (Brink, 2012).

Major stratigraphic formations exposed within the Wanganui monocline, or King Country basin reveal evidence regarding the tectonic evolution of the King Country basin, and hence the geological development of the old TVZ (Kamp et al., 2004). A

thick succession of early Miocene - late Pleistocene marine sediments and Quaternary volcanic products that display significant fault displacement (along the Ohuroa and Taranaki faults) reflect emplacement of the subducting Pacific plate beneath the central northwest region of New Zealand's North Island.

During the early Miocene (Otain Stage), the Australia-Pacific plate boundary system shifted from extension to oblique shortening along with crustal shortening across the central North Island of New Zealand (Kamp et al., 2002; Kamp et al., 2004) particularly along the eastern margin of the Taranaki fold-thrust belt.

The King Country basin is a long-lived marine depocentre that represents an intense period of crustal shortening followed by rapid subsidence and, in turn, over-thrusting of Mesozoic basement rock onto the Taranaki Fault (Evans, 2003; Kamp et al., 2004). In particular, concurrent uplift, tilting, and erosion of the over-thrusted basement rock is presumed to have occurred simultaneously as the through-going plate boundary (system) continued to migrate south, thereby establishing a 'piggy-back' basin and, thus, the development of a regional high to the west of the King Country basin, along the eastern Taranaki basin. This regional high, termed the Herangi high, serves as a structural boundary which separates the King Country basin from the Wanganui basin and is, in part, responsible for influencing the migration path(s) of the subsequently pyroclastic flows derived from the Mangakino Volcanic Centre (MVC).

## 1.8 Mangakino Volcanic Centre

The Mangakino Volcanic Centre (MVC) defines the western-most boundary of the TVZ, and lies directly east of the King Country basin (Figure 1.3; Wilson, 1986). The centre is defined by a major (oval-shaped) gravity anomaly that extends approximately 30 km in length and 15 km in width, with a depth to basement rock of ~4 km. The current topographic expression of this centre denotes a volcanic basin resting 200-400 m beneath an ignimbrite plateau that is partially infilled by subsequent volcanic products derived from the east, particularly the 0.37 Ma and >200 m thick Whakamaru-group ignimbrites (Krippner et al., 1998). Blank (1965) was the first to infer the possible presence of Mangakino volcano, however the gravity low was first

documented by Stern (1979) and Rogan (1982), as a non-volcanic (tectonic) basin due to the unrecognizable presence of a caldera structure and absence of a significant magnetic signature(s). Geophysical evidence, however, pertaining to the age and volume of these eruptive products was later used by Wilson (1984) to confirm Mangakino as a major caldera volcano.

Volcanic deposits derived from the MVC are poorly preserved due to erosion and burial by later eruptions therefore the eruptive history of this centre is poorly constrained (Wilson, 1986). Most of the well-preserved deposits occur to the west of the centre, and evidence based on textural variations, dispersal, and relative complexity, indicate that these were derived from a volcano resting directly beneath the current Mangakino basin, and represent the earliest pyroclastic deposits attributable to a TVZ source.

Explosive volcanic activity at the MVC produced more than 10,000 $km^3$ of magma from 1.62 Ma to 0.91 Ma through approximately six caldera-forming events (Briggs et al., 1993, Wilson, 1986). The caldera serves as a major source for several members of an ignimbrite succession that correspond to intense periods of caldera-forming eruptions from 1.62 to 1.51 Ma and 1.23 to 0.91 Ma (Briggs, 2005; Brown and Smith, 2004). These explosive volcanic eruptions in particular, produced multiple major welded and non-welded ignimbrites, two voluminous phreatomagmatic eruption units, and multiple smaller pyroclastic units and lava domes (Briggs et al., 1993, McCormack et al., 2009).

At least five ignimbrites (Ngaroma, Ongatiti, Ahuroa, Rocky Hill, and Kidnappers ignimbrites) are preserved in areas exceeding 50 km from the probable source (Figure 1.4). Wilson (1986) suggested that these deposits amount to approximately $\geq$ 700 $km^3$ in volume, and because of their confined areas of deposition (being particularly to the west of the MVC) are presumed to represent at least that volume of magma.

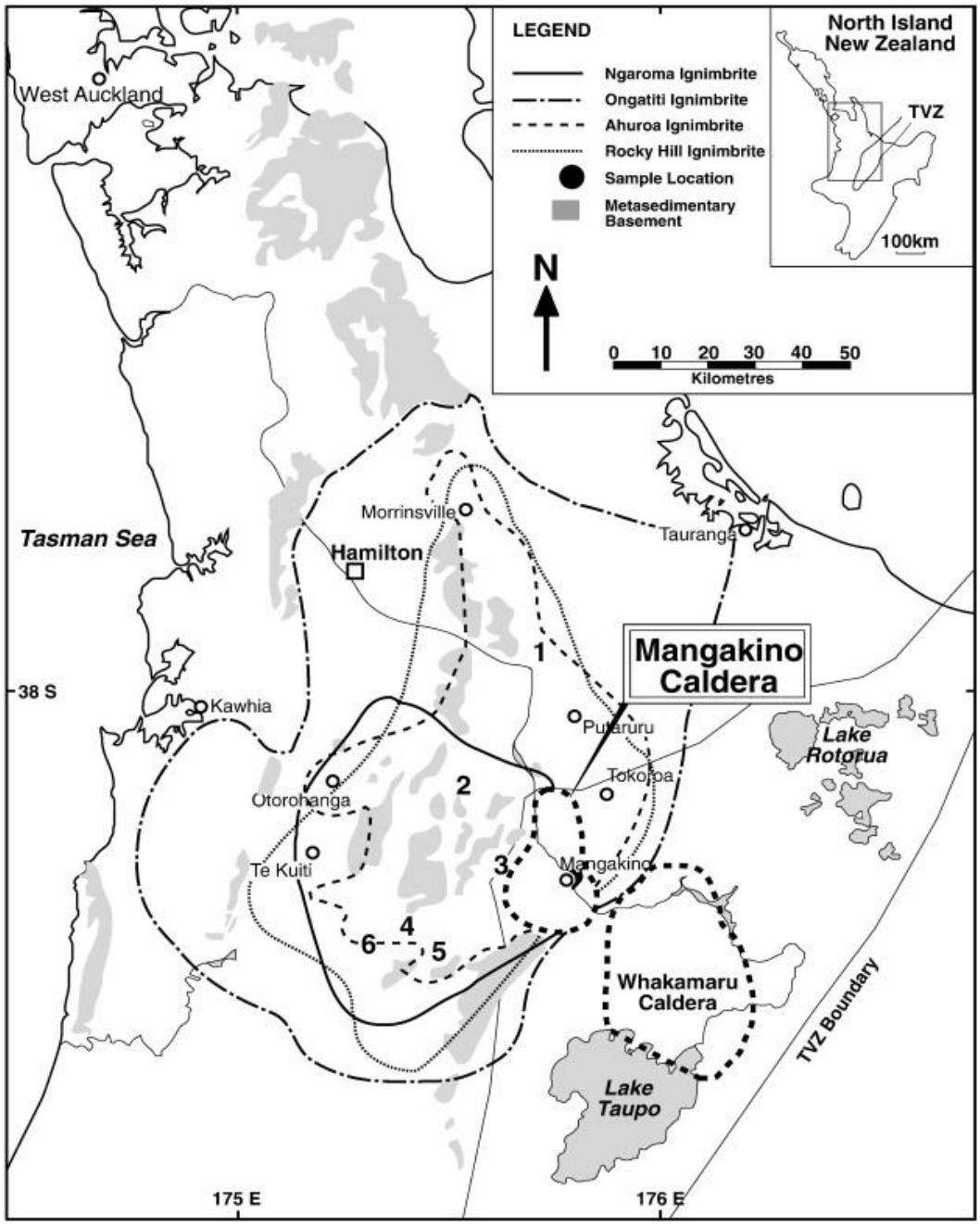


**Figure 1.4:** Mapped out distribution of the four major ignimbrite successions within the old TVZ. Notice the deposits are mostly restricted to areas west of the caldera. The elongated and irregular enclosed grey areas represent outcrops of uplifted basement greywacke rock while the boundary zone separating the old TVZ from both the young and modern TVZ is marked by a solid black line (McCormack et al., 2009).

### 1.8.1 Precursor Activity

The King Country ignimbrites are preserved primarily as large-scale welded and non-welded ignimbrites that represent the first TVZ caldera-forming eruptions documented

today (Wilson, 1986). Andesitic volcanoes southwest of the MVC, however, are most likely associated with a pre-existing phase of volcanism within this area. In particular, Pureora and Titiraupenga, are two composite cone volcanoes perched on the greywacke ridge of the northern-most Hauhungaroa Range, with ages of 1.6 and 1.9 Ma (Graham et al., 1995; Wilson, 1986).

### 1.8.2 Mangakino Volcanic Centre Ignimbrite Characteristics and Implications

Mangakino-derived ignimbrites are characterised as non-welded to densely welded, crystal-rich, and pumice-rich ignimbrites (Briggs et al., 1993; Krippner et al., 1998). Pumice clasts throughout these deposits vary from dense to highly vesicular and fibrous in texture, range in size from 30-200 mm, and comprise 2-35% of the bulk rock. Likewise, crystals throughout these deposits consist primarily of plagioclase, quartz, orthopyroxene, and hornblende, followed by lesser amounts of ilmenite, zircon, and apatite, and form 10-30% of the bulk rock. Lithics throughout these deposits show a wide range in composition and in lithological characteristics, and form 1-10 % of the bulk rock.

Three types of lithics have been recorded and identified throughout these ignimbrites and include plutonic, metamorphic, sedimentary, and volcanic (Krippner et al., 1998). Plutonic lithics of which are comprised of biotite, granite and granodiorite porphyry, while metamorphic types consist of metagreywacke, metaconglomerate, biotite schist, and hornblende-biotite schist.

Likewise, sedimentary lithic types are rich in greywacke, sandstone, and siltstone, while volcanic lithic types are comprised entirely of lavas and include rhyolite, dacite, andesite, basaltic andesite, welded ignimbrite, tuff, and volcanic breccia. The highest concentrations of lithic fragments recorded throughout ignimbrites produced at the MVC occur throughout the transitional regime which extends 10-50 km away from the source, while the lowest concentrations are recorded throughout the distal regime extending greater than 50 km from the vent (Krippner et al., 1998).

The overall abundance of these lithic clasts, however, are not accounted for in proximal localities (less than 5 km from the source), due to caldera collapse and subsequent volcanism. Of these MVC ignimbrite deposits, the Ngaroma Ignimbrite is recognised by high concentrations of lithic fragments that are dominated by andesitic lavas (Krippner et al., 1998). Younger deposits associated with subsequent volcanism however, including the Ahoroa, Rocky Hill, Kidnappers, and Marshall ignimbrites (Table 1.1), are dominated by volcanic lithic types that are rhyolitic in composition. Lastly, both metamorphic and plutonic lithic types are recorded only within the Ongatiti Ignimbrite.

*Volcanic Implications*

The immense volume of welded ignimbrites produced from rhyolitic eruptions at the MVC display compositional variations between fragmented pumice clasts that reflect different degrees of fractional crystallisation of a parent magma, in addition to minor inheritance of their partial melt composition (Krippner et al., 1998). These variations are further evidenced by small-scale variations in source mineralogy and composition throughout these deposits. For example, the dacitic to rhyolitic pumice clasts which occur together at the same time and within the same ignimbrite reflect compositions which likely co-existed together, however derived from either different magmatic sources or from adjacent bodies of magma (Figure 1.5). These interpretations further suggest that magmas associated with the MVC reflect a partially-derived crustal melt which likely seeped into the magma reservoir and remained poorly mixed with pre-existing magma, until eruption (Briggs et al., 1993). From these observations, Briggs et al (1993) suggest that these magmas derived from numerous probable sources which include: (1) a crustal source upholding a similar composition to a greywacke having derived from a provenance that was andesitic in composition (2) a plagioclase-rich plutonic source which would result in an anorthosite, and (3) a more mafic component derived from the upper mantle (Figure 1.5).

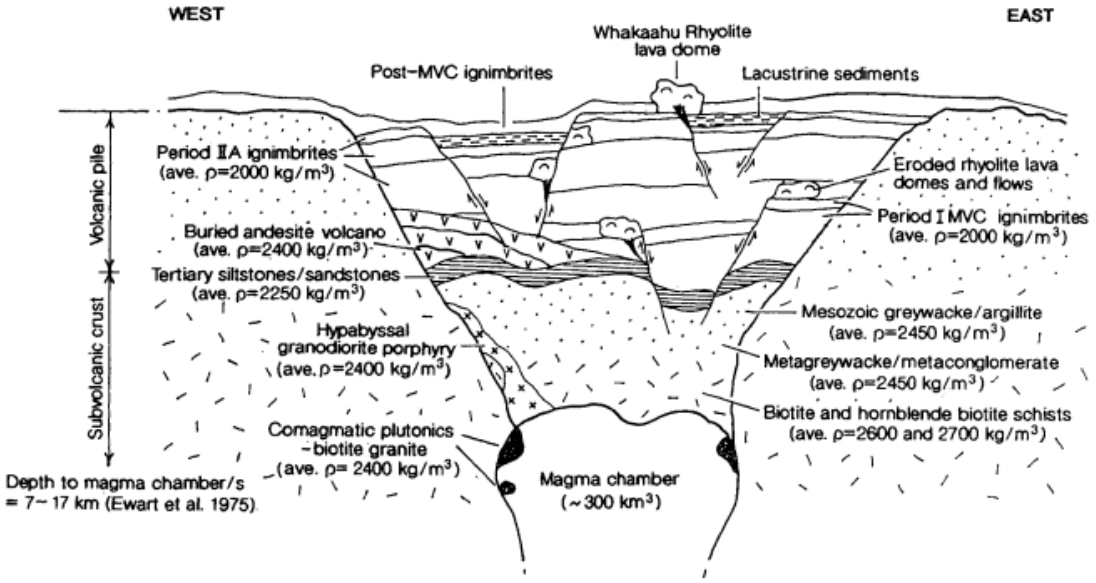


**Figure 1.5:** Schematic diagram showing the sub-volcanic crust and volcanic pile at the MVC. Notice the plutonic origin(s) of various lithic compositions (Krippner et al., 1998).

## 1.9 Major Ignimbrites of the MVC

### 1.9.1 Link formation

The Link Formation, also recognised as Ignimbrite F of Wilson (1986) is a poorly exposed, highly welded ignimbrite that can be recognised by its fine-grained, crystal-rich, however comparably pumice-lithic poor matrix (Leonard et al., 2010). The deposit is poorly exposed and outcrops in restricted areas along Link Road, southeast of Pureora. It is presumed to represent the earliest silicic ignimbrite sourced from Pureora and Titiraupenga, as it records an age of 1.60 Ma (Soengkono et al., 1992), and rests stratigraphically below the Ngaroma Ignimbrite. The source of this deposit is unknown, however based on studies conducted by Leonard et al., (2010), it is unlikely to be of Mangakino origin and therefore is not presented in Table 1.1.

### 1.9.2 Ngaroma Ignimbrite

The Ngaroma Ignimbrite (Table 1.1) was first defined by Martin (1961), who described the exposed deposit as a lenticulate sheet in a quarry three-quarters of a mile west-northwest of Ngaroma School (N84/055853). Martin (1961) recognised and defined two ignimbrites, namely the Ngaroma and Ranganui Ignimbrites. However, Blank (1965) suggested, based on mineralogy, lithology, and componentry, that these

ignimbrites are indistinguishable from one another, and have since been renamed to represent the currently-termed Ngaroma Ignimbrite. At the type locality, the Ngaroma Ignimbrite is underlined by basement greywacke and, while this observation has been recorded over a rather extensive area of Ngaroma town, it is most noticeable at Titiraupenga. In other areas, the deposit rests directly above Tertiary sedimentary rocks.

The Ngaroma Ignimbrite is 1.55 $\pm$ 0.03 Ma (Briggs et al., 1993) and represents the earliest stage of ignimbrite-producing eruptions sourced from the MVC and of the TVZ as a whole (Cooper at el., 2014). This deposit outcrops in restricted areas to the west of Mangakino, and due to subsequent volcanism, downfaulting, and erosion, is poorly exposed and rarely exceeds a thickness of 30 m.

The Ngaroma Ignimbrite (also recognised as Ignimbrite A of Wilson, 1986) is a partially welded, purple-brown, vapour phase altered ignimbrite (Table 1.1) that is most recognised for its uniform fine-grained texture and felsitic matrix of pastel-like colours that vary from light blue to pink, to brown (Briggs et al., 1993; McCormack et al., 2009). Perhaps the most distinct and noticeable component of this deposit, aside from its colour, is the high concentration of fiamme described by Martin (1961) as thin, wispy, and fibrous in texture, and scattered throughout a fine-grained (felsitic) matrix. This highly eutaxitic texture suggests the deposit is extremely welded. Intensive weathering, devitrification, and vapour phase alteration both during and after deposition, and the abundance of recrystallised secondary minerals gives the ignimbrite a unique chalky texture (Brink, 2012; Wilson, 1986). Phenocrysts throughout this deposit are sparse and fragmented, and consist mostly of plagioclase followed by minor amounts of pyroxene, and in rare occasions, preserve traces of opaque oxides and altered amphiboles. The Ngaroma Ignimbrite is the focus of this study and is discussed further in Chapter Two.

### 1.9.3 Tolley Formation

The Tolley Formation (Table 1.1; Leonard et al., 2010), also recognised as Ignimbrite B of Wilson (1986) or the Pumice lapilli ignimbrite of Blank (1965) can be observed overlying the Ngaroma Ignimbrite in areas west of the Mangakino basin, nearby the town of Ngaroma (Leonard et al., 2010; Wilson, 1986). The deposit is characterised as

a partly- welded, extensively vapour phase altered and recrystallised ignimbrite (Briggs et al., 1993). It is comprised almost entirely of white (altered) pumice lapilli clasts and displays phenocrysts only on rare occasions. Aside from its stratigraphic position, resting directly between the Ngaroma Ignimbrite (Ignimbrite A of Wilson, 1986) and the Pouakani Formation (Ignimbrite C of Wilson, 1986), the Tolley Formation (Ignimbrite B of Wilson, 1986) is unique for its relatively high concentration of vent-derived lithic clasts which are comprised strictly of andesite and greywacke.

### 1.9.4 Pouakani Formation

The Pouakani Formation of Leonard et al., (2010) represents a non-welded to highly welded ignimbrite that may be characterised by its conspicuous abundance of andesite lithics (up to 40%) which vary from non-welded to highly welded, and comprise an abundance of lapilli-sized pumice (Table 1.1). The deposit has also been recognised by Blank (1965) as a crystal lithic-lapilli ignimbrite and by Wilson (1986) as Ignimbrite C. It is commonly observed overlying the Tolley Formation (Ignimbrite B of Wilson, 1986) and is presumed to underlie the Ongatiti Ignimbrite. It is unique for it light grey to yellow colour and abundance of sparse, fragmented phenocrysts comprised mostly of quartz, plagioclase, and pyroxenes.

There is a notable contact change directly above Ignimbrite B of Wilson (1986) and at the base of Ignimbrite C of Wilson, (1986). It is described by Blank (1965) as a basal unit (50-100 ft thick) and can be recognised for its relatively high abundance of sub-rounded felsite cobbles that are dark blue-grey in colour, and scattered throughout a densely welded matrix. There is no distinct contact change between the basal unit of Ignimbrite C and the overlying Ongatiti Ignimbrite, and lithological similarities between the two ignimbrites suggest that these two deposits represent a compound cooling unit.

### 1.9.5 Ongatiti Ignimbrite

The Ongatiti Ignimbrite (Table 1.1) was first recognised by Martin (1961) above the Ongatiti Stream, near to the southern slope of Rocky Hill, Pakaumanu Survey District (N83/282474). Martin (1961) described this deposit as a relatively thick (46 m) welded

crystal tuff which typically rests above the Ngaroma Ignimbrite and, at the type locality, forms a simple cooling unit. It is distinct from the underlying Ngaroma Ignimbrite due to its yellow colour, high abundance of elongated feldspar crystals, and small traces of opaque oxides (Martin, 1961). Additional minerals preserved in the Ongatiti Ignimbrite include pyroxene and hornblende, followed by a minor abundance of quartz. Lithics are abundant at the base of the deposit, and appear compositionally similar to the host rock while the upper-most portion of the deposit is dominated by recrystallised pumice inclusions of white powdered lapilli (Blank, 1965). Lithics in particular, include sparse fragments of greywacke that are angular in shape or, in rare occurrences, of dark-coloured felsite.

Recent studies conducted by Leonard et al., (2010) suggest however, that the deposit reaches a maximum thickness of 100 m and is also observed resting above either the Ngaroma Ignimbrite, Poukakani Formation, or Waipapa (composite) terrain rocks. Moreover, the deposit is presumed to represent a poorly to highly welded ignimbrite that is characterised as a vitrophyric, pumice-rich, crystal-rich compound ignimbrite which comprises a moderate abundance of vent-derived lithics of andesite, rhyolite, highly welded ignimbrites, finely crystalline mafic material, and basement greywacke (Leonard et al., 2010). This somewhat complex deposit has been divided into zones by Blank, (1965) which have also been recognised and described by Briggs et al., (1993) in the Waipari Gorge (~ 25 km from source) and in the Hinuera Quarry (~ 55 km from source).

At the Waipari Gorge, Briggs et al., (1993) recognised and described two units, namely the lower and upper units. The lower unit represents a pumice-rich and crystal-rich flow unit that is partially welded while the upper unit is recognised as a weakly welded and vapour phase altered deposit. Moreover, Briggs et al., (1993) suggest that additional flow boundaries are likely to be present within these units however cannot be characterised based on the percentage abundance and clast size of both pumice and lithics.

When observed in the Hineura Quarry, the ignimbrite consists of a lower unit, which is described by Briggs et al., (1993) as a pumice-poor lithic-poor however comparably

crystal-rich densely welded flow unit. The upper unit however, represents a pumice-rich and partially welded flow unit. A middle unit, described as moderately pumice-rich crystal-rich densely welded flow unit was also recognised at this locality, and is presumed to in part form a coarsening upwards sequence (Briggs et al., 1993).

### 1.9.6 Unit D

Unit D represents one of two phreatomagmatic fall deposits which is observed resting between the Ongatiti and Ahuroa ignimbrites (Table 1.1; Briggs et al., 1993; Wilson, 1986). The deposit was first interpreted by Blank (1965) as lacustrine sediment however, was later recognised and described by Wilson (1986) as a single (0.5 to 1.5 m thick), thinly bedded, fine-grained, non-welded flow unit. The deposit extends ~ 75 km away from the source, is poorly exposed, and is presumed to result from a phreatomagmatic ash fall. It consists of a lower bedded air-fall ash and an upper non-welded ignimbrite. The layers of which are poorly sorted, fine-grained and consist of accretionary lapilli, although in some occurrences, are interbedded with fines-poor and are presumed to result from a plinian style eruption (Wilson, 1986).

## 1.9.7 Ahuroa Ignimbrite

The Ahuroa Ignimbrite (Table 1.1) represents a relatively thin ($\leq$ 20 m) veneer deposit that is inversely thermally zoned (Wilson, 1986). In particular, the deposit comprises a non-welded base (typically $\leq$ 15 m thick) which gradually transitions into a zone (<10 m thick) of partially-densely welded lenticulate ignimbrite. The Ahuroa Ignimbrite was first defined by Martin (1961) as two lenticulate sheets (the upper and lower Ahuroa Ignimbrite) overlying the Ongatiti Ignimbrite and underlying the Rocky Hill Ignimbrite on Ahuroa Road, at the southern slopes of Rocky Hill, Pakaumanu Survey District (N92/964592). A third member of this deposit was later recognised by Blank (1965) near-by the Maraeroa Plains (N83/921662). It represents a gradational zone of black sintered material resting directly between the two ignimbrite sheets.

Blank (1965) suggests that this deposit is restricted to areas in the northern half of the Central King Country, however is also preserved and recorded in areas nearby Arapuni

Dam, where it extends into the Maraeroa Plains and forms a partially dissected surface encompassing the Rangitoto Range.

Recent studies conducted by Leonard et al., (2010) suggest this deposit extends in areas north of Tirau and west of Titiraupenga. Moreover, it is described that the Ahuroa Ignimbrite serves not only as a horizontal cap above the Ongatiti Ignimbrite but is also, in some occurrences, observed overlying Waipapa (composite) terrane rocks, and in extremely rare occurrences, rests above Mesazoic Basement rocks (Brink, 2012; Leonard et al., 2010). The deposit records an age of $1.18 \pm 0.02$ Ma, and is uniquely distinct when compared to underlying deposits due to the extensive variations of pumice clasts (Cooper et al., 2014; Houghton et al., 1995; Wilson, 1986).

Similar to the previous observations made by Martin (1961), Blank (1965), Wilson (1986), and Briggs et al., (1993), this deposit when described by Leonard et al., (2010), comprises a non-welded base which grades upwards into a highly welded top. The upper and lower ignimbrite sheets can be recognised by their conspicuous abundance of plagioclase and pyroxene, and absence of quartz (Blank, 1965; Leonard et al., 2010; Martin, 1961). Likewise, small fragments of opaque oxides are persistent throughout, and traces of amphibole occur rarely. These ignimbrite sheets are therefore identifiable from one another based on variations in colour, degree of welding, and the development of flattened pumice clasts.

The lower Ahuroa Ignimbrite was first described by Blank (1965) as a highly welded lenticulate vitric ignimbrite that varies in colour from cream to dark blue, to grey. However, studies conducted by Briggs et al., (1993) describe the lower Ahuroa Ignimbrite as a non- to weakly welded pumice-rich, moderately crystal-rich and comparably lithic-poor flow unit, which comprises a black fine-grained matrix (Briggs et al., 1993). While Martin (1961) described the pumice as being lenticular, and dark grey in colour, Briggs et al., (1993) suggest that these clasts are rather unique and comprised either of orange, high-silica rhyolite or dark grey dacite.

The upper Ahuroa Ignimbrite is a densely and reversely welded lenticulate flow which is unique for its conspicuous abundance of lenticulates and additional flattened fiamme

(Briggs et al., 1993). The deposit is <10 m thick, and rests directly above the transition zone of black, sintered material (Wilson, 1986). Pumice clasts throughout this ignimbrite are yellow to dark grey in colour, strongly eutaxitic and fibrous in texture, and appear scattered throughout a grey coloured matrix of highly welded vitric tuff (Martin, 1961).

### 1.9.8 Unit E:

Unit E is the second phreatomagmatic air-fall ash deposit which commonly rests between the Ahuroa and Rocky Hill ignimbrites (Table 1.1; Wilson, 1986). The deposit is poorly exposed and relatively thin (1.6 to 3.5 m), and similar to unit D, is overlain by a non-welded ignimbrite (Briggs et al., 1993, Wilson, 1986). Unit E however, is relatively coarse-grained and consists of fine-grained ash beds which are presumed to be of plinian style ash, in addition to accretionary-lapilli bearing layers which are characteristic of phreatoplinian ash (Wilson et al., 1986).

### 1.9.10 Rocky Hill Ignimbrite

The youngest widespread Mangakino-derived ignimbrite was first recognised by Martin (1961), who named this deposit the Rocky Hill Ignimbrite at Rocky Hill, 8 miles southeast of Te Kuiti in the Pakaumanu Survey District (Cooper et al., 2014). The deposit is highly eroded and described as a stratified pumice-breccia that unconformably overlies the Ahuroa Ignimbrite (Table 1.1) and forms the caprock at Rocky Hill. Similar to the Ahuroa Ignimbrite, the Rocky Hill Ignimbrite displays a non- to poorly welded base and ~25 m thick densely welded top and is, therefore, inversely thermally zoned (Wilson, 1986). The two sheets (termed the upper and lower sheets) which comprise this deposit have previously been described by Blank (1965) as two distinct lithological units that grade into one another to form a simple compound cooling unit.

The 1.00 $\pm$ 0.05 Ma Rocky Hill Ignimbrite forms the cap rock of widely dispersed isolated hills, and overlies either Ongatiti Ignimbrite, uplifted basement greywacke, or Tertiary sedimentary rocks (Brink, 2012). The lower sheet in particular outcrops in

areas both near the Arapuni Dam and alongside the northern fringes of the Rangitoto Range, in the Waipa graben, where it rests directly above Ongatiti Ignimbrite or on uplifted basement greywacke (Blank, 1965). The upper sheet however, is perhaps the most widespread, as it outcrops in the Waipa graben, forming the highest ignimbrite surface on the Pahi greywacke block just west of the Maraeroa plains and east of the Waimiha depression.

Juvenile clasts throughout the Rocky Hill Ignimbrite vary in both density and phenocryst content (Table 1.1; Wilson, 1986). Grey pumice clasts for example, are typical while mafic scoria fragments are rather unique and sparse. Lithic clasts are predominantly andesitic to rhyolitic in composition, and are vent-derived. Additional lithics, which are fragmented, are similar to those described in the Ongatiti Ignimbrite and comprise a re-vesiculated and glassy texture (Wilson, 1986).

The lower pumice breccia sheet is characterised as a non-welded crystal vitric-lithic ignimbrite (Blank, 1965). Crystals of which are comprised mostly of plagioclase followed by quartz, pyroxene, and amphibole. Opaque oxides are persistent and include traces mostly of biotite and rarely of sanidine. Cognate inclusions are sparse and include non-vesicular to vesicular autoliths that are sub-angular in shape and light grey in colour, followed by highly flattened pumice clasts that vary in colour from dark grey to black.

The upper sheet represents a $\leq$ 25 m thick densely welded top that is most recognised for its fine scale microstructure pattern and hackly fracture appearance, similar to that of the Ahuroa Ignimbrite (Blank, 1965; Wilson, 1986). The crystal content here mirrors that of the lower sheet, however traces of opaque oxides, including biotite and pyroxene, are persistent and uniform throughout. Pumice clasts are less abundant and conspicuously more flattened, and are described by Blank (1965) as blue lithoidal streaks that are scattered throughout a buff grey to pink-coloured matrix.

### 1.9.11 Kidnappers Ignimbrite

The 1.0 Ma Kidnappers super eruption sourced from the MVC is preserved as a widespread, non-welded, lithic-rich, crystal-rich ignimbrite (Table 1.1; Cooper et al.,

2017; Wilson et al., 1995). The ignimbrite records an average thickness of 10 m, is typically overlain by an exceptionally widespread, non-welded ignimbrite (i.e., the Rocky Hill Ignimbrite), and is presumed to have exceeded a deposition of ~45,000 $km^2$ from the source. Wilson et al., (1995) suggest that the ignimbrite comprises at least two flow units that are separated by air-fall ash material which, because of their poorly sorted, multiple bedded, ash-rich nature, and presence of accretionary lapilli, are presumed to result from a large phreatomagmatic eruption.

The Kidnappers Ignimbrite and its associated phreatomagmatic air-fall deposits (i.e., the Raepahu Formation of Leonard et al., 2010) have also been recognised and described as fine-grained, exceptionally widespread (~1200 $km^3$ DRE), and frequently underlain by wide-spread, non-welded ignimbrite (i.e., the Rocky Hill Ignimbrite) (Cooper et al., 2017). Moreover, these deposits are biotite-bearing and include both air-fall ash beds (up to 4 m) and crystal-rich non-welded ignimbrites (up to 30 m) (Leonard et al., 2010).

### 1.9.12 Marshall Ignimbrites

The Marshall Ignimbrites were first recognised by Martin (1961) and later described by Wilson (1986) and Briggs et al., (1993) as a sequence of ignimbrites which comprise a lower, upper, and middle unit(s) that together rest (stratigraphically) beneath the Whakamaru Ignimbrites (Table 1.1; Wilson, 1986). The three ignimbrite units have been recently described by Leonard et al., (2010), and coincide with those previously described by Wilson (1986) as Ignimbrites G, H, and I.

The lower unit (Ignimbrite G of Wilson, 1986) represents a dark, non-welded to partially welded deposit that is recognised by its sintered and glassy matrix, conspicuous abundance of pale-orange-brown pumice clasts, and rare occurrence of lithic clasts which consist of rhyolite (Leonard et al, 2010; Wilson, 1986). It is presumed to comprise at least two flow units, of which the lower is capped by a concentration zone of pumice (Wilson, 1986).

The lower unit gradually transitions into the middle unit (Ignimbrite H of Wilson, 1986) and is described as a non-welded to sintered deposit that is recognised for its light grey

colour (Leonard et al., 2010). This unit comprises relatively large (lapilli-block sized) pumice clasts and a ubiquitous abundance of lithics which vary in composition from rhyolite, welded ignimbrite, and hydrothermally altered material (Wilson, 1986).

The upper unit (Ignimbrite I of Wilson, 1986) can be observed succeeding the middle unit (Ignimbrite H of Wilson, 1986). It is described as a poorly welded and glassy to densely welded vapour phase altered ignimbrite that comprises a crystal-rich, pale-brown, pumiceous matrix (Briggs et al., 1993; Leonard et al., 2010). Lithic clasts throughout this unit are compositionally similar to those in the middle unit (Ignimbrite G of Wilson, 1986) however are noticeably smaller ($\leq$ 5 cm) in size.

**Table 1.1:** Table summarizing the six major stratigraphic formations produced from the MVC. The formations are listed in stratigraphic order and are followed by their corresponding units, age, and lithological descriptions. These descriptions have been modified from those of Briggs et al., (1993), Leonard et al., (2010), and Wilson (1986). Ignimbrites A-C of Wilson (1986) are listed here as the formations described by Leonard et al., (2010). The remaining formations however, are listed here as ignimbrite names.

| Formation | Units within Formation | Age | Lithology |
|---|---|---|---|
| Marshall Ignimbrite(s) | Upper Unit (Ignimbrite I)<br>Middle Unit (Ignimbrite H)<br>Lower Unit (Ignimbrite G) | 0.91 ± 0.02 Ma | -Non-welded to densely welded ignimbrite (s)<br>-Black to brown to orange pumice<br>-Crystal-poor to crystal-rich<br>-Brown to black matrix<br>-Vapour-phase altered |
| Kidnappers Ignimbrite | Multiple flow units | 1.0 Ma | -Non-welded ignimbrite<br>-Lithic-rich and crystal-rich |
| Rocky Hill Ignimbrite | Upper Ignimbrite<br>Lower Ignimbrite | 0.97 ± 0.02 Ma | -Non-welded to densely welded ignimbrite<br>-Pumice-rich and crystal-rich |
| Unit E | Fine-grained ash beds | 1.01 ± 0.06 Ma | -Phreatomagmatic ash fall deposit<br>-Poorly exposed, with overlying non-welded ignimbrite |
| Ahuroa Ignimbrite | Upper Ignimbrite<br>Lower Ignimbrite | 1.19 ± 0.03 Ma | -Non-welded to densely welded ignimbrite<br>-Inverse thermal zonation<br>-Lenticular pumice and fiamme in upper unit<br>-Lower, crystal-rich unit comprised of orange, platy rhyolite pumice and black dacitic pumice |
| Unit D | | 1.18 ± 0.02 Ma | -Phreatomagmatic ash fall deposit<br>-Poorly exposed, with overlying non-welded ignimbrite |
| Ongatiti Ignimbrite | Upper Unit<br>Lower Unit | 1.23 ± 0.02 Ma | -Non-welded to partially welded ignimbrite<br>-Pumice-rich and crystal-rich |
| Pouakani Formation (Ignimbrite C) | | 1.62 ± 0.11 Ma | -Non-welded to highly welded ignimbrite<br>-Poorly exposed |
| Tolley Formation (Ignimbrite B) | | 1.51 ± 0.02 Ma | -Non-welded to partially welded, vapour-phase altered ignimbrite<br>-Poorly exposed |
| Ngaroma Ignimbrite (Ignimbrite A) | | 1.60 ± 0.03 Ma | -Partially to densely welded ignimbrite<br>-Purple to brown, vapour-phase altered |

# Chapter Two

# Stratigraphy

## 2.1 Introduction

This chapter provides a broad overview of the field area as well as addresses, in detail, the macroscopic observations and lithological characteristics of the well preserved and frequently exposed geological units in the area around the town of Ngaroma, with a focus on the Ngaroma Ignimbrite. Stratigraphic logs are used to show the vertical variations occurring both within the geological units, and throughout the Ngaroma Ignimbrite.

## 2.2 Methods

The area of study was chosen due to its proximal distance to Mangakino caldera and frequent occurrence of the Ngaroma Ignimbrite. Field localities were selected based on outcrop appearance and accessibility, and are presented in Figure 2.1. Geological coordinates (Appendix I) of these localities were obtained using a geological map and GPS and digitised into ArcGIS. The major lithologies in the field area were described and classified into geological units.

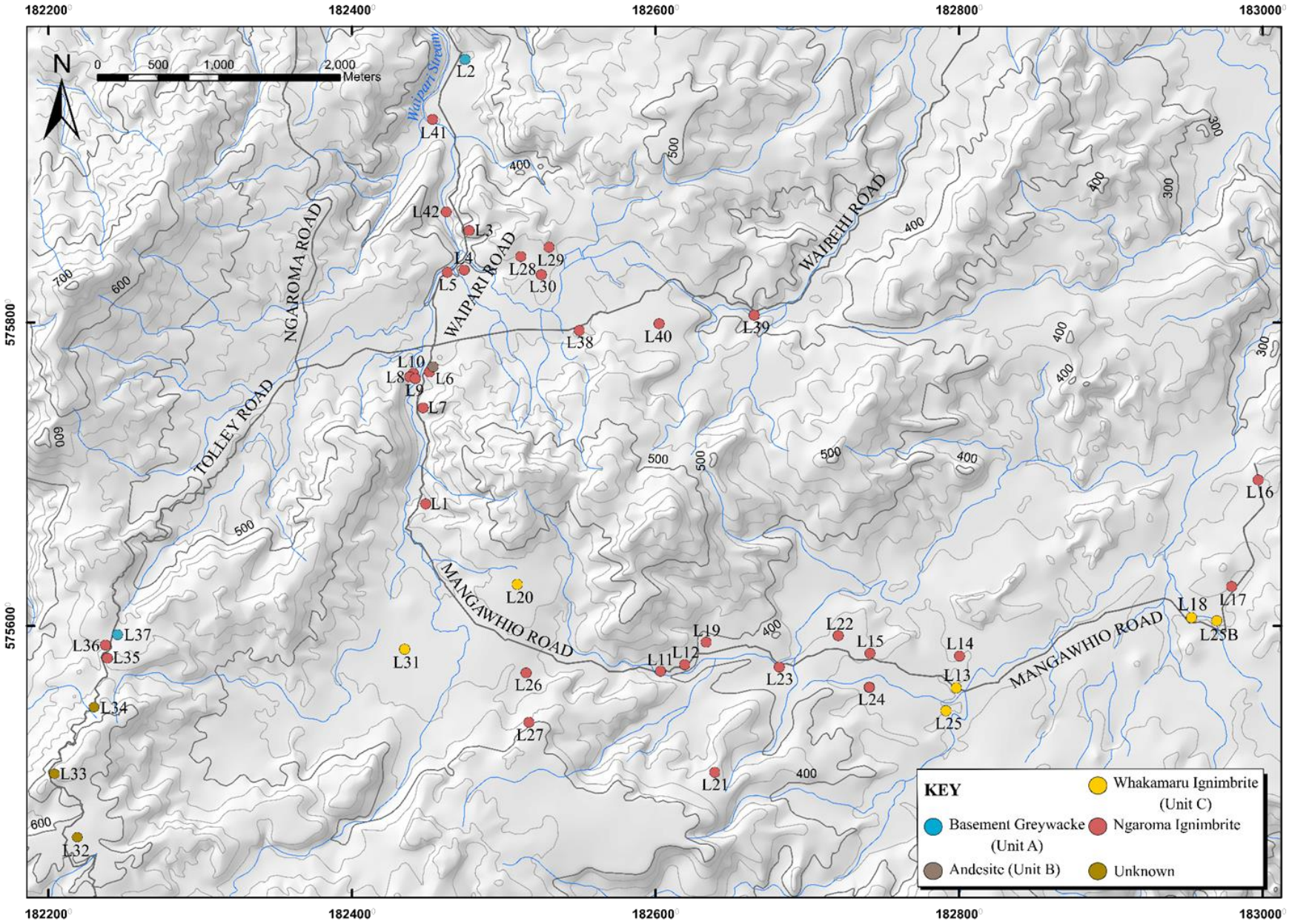


**Figure 2.1:** Locality Map showing the lateral distribution of the Ngaroma Ignimbrite and of exposed geological units recognised throughout the field area.

### 2.2.1 Stratigraphic Logging

Five stratigraphic logs were drawn to record the vertical variations of ignimbrite units identified in the Ngaroma area. Vertical variations in texture and primary componentry are recorded in four stratigraphic logs of the Ngaroma Ignimbrite and are presented in Figures 2.9-2.12. The average pumice size and pumice aspect ratios, were acquired by measuring five pumice clasts per sample. The five stratigraphic logs presented in this chapter were produced using Inkscape.

### 2.2.2 Sample Collecting

Samples of accessible rock were collected from 42 field localities (Appendix II). The samples were used to examine macroscopic characteristics such as changes in colour and the degree of welding. In particular, the samples record various changes in primary components, including the average size, shape, and percentage abundance of crystals, pumice, and lithic clasts.

## 2.3 Physiography

The town of Ngaroma encompasses four main roads: Waipari, Mangawhio, Tolley, and Wairehi Roads (Figure 2.1). The Waipari stream and its stream tributaries can be seen meandering alongside these roads, and occur across a majority of the field area. The stream is narrow and observed most frequently along Mangawhio Road. It is interrupted by a waterfall (of 10 m in height) at the southern-end of Waipari Road, however north of Waipari Road, at the base of the waterfall, the stream widens and comprises increased stream sediment. North of the waterfall, at the northern-end of Waipari Road, is a quarry of uplifted basement rock (Figure 2.3).

The field area encompasses a low lying valley comprised of gently- sloping hills that make for a rather hummocky, or undulating topographic surface (Figure 2.2). These gently- sloping hills in particular, form shallow bench-like steps which comprise outcropping boulder fields that are presumed to represent underlying ignimbrite (Figure 2.2). Slump scarps (observed along these hillsides) are prominent, and comprise either weathered ignimbrite or densely compact soil, which is typically underlain by tephra of TVZ origin.

The town of Ngaroma and its low lying valley are almost completely surrounded by high hills (up to 942 m above sea level). These mountains have steep slopes, and display relatively narrow and flattened peaks and ridgelines. Due to the absence of outcropping boulder fields, and minimal occurrence of slump scarps, it is assumed that these mountains are of uplifted basement greywacke rock that form part of the northwest-southwest trending Rangitoto Range.

The distribution of gently-sloping hills, with outcropping ignimbrite, and uplifted basement rock vary throughout the field area. The gently-sloping hills for example, occur most frequently in areas north-northwest and south-southwest of the field area (Figure 2.2) and become more abundant, and steepened in areas south-southeast. Likewise, boulder fields comprising the gently-sloping hills become noticeably less abundant as slump scarps become increasingly pronounced from north to south. Moreover, the steep greywacke ranges, which surround areas to the west of this low-lying valley, diminish exponentially towards the northeast.

Scattered and isolated hills with rounded tops are observed in areas west and south-southeast of the field area (Figure 2.2). These dome-like features, appear to be erosional remnants which consist mostly of outcropping ignimbrite.


**Figure 2.2:** Photos showing the general landscape in the area around Ngaroma Township. (A) Photo taken from Mangawhio Road looking east at the undulating topography. Notice the gently-sloping hills with slump scarps and the ignimbrite-forming plateau. (B) Gently-sloping hills and stream tributaries observed north of Wairehi Road. (C) Waterfall observed alongside Waipari Road. Photo taken from the base of the waterfall. (D) Dome-like features observed in areas northwest and southeast of Mangawhio Road. Notice the Waipari stream, flood plain, and uplifted basement rock. Photo taken from east side of Mangawhio Road.

## 2.4 Stratigraphy

The geology of this field area is mantled by a succession of weathered composite tephra and paleosols (particularly the Hamilton Ash ± Kauroa Ash beds) which are generally not recognised here as geological units. Likewise, the recent alluvium recorded throughout the field area is confined and observed only along the flood plains of the Waipari stream and its tributaries. For this reason, the stream alluvium is not recognised as a geological unit here and therefore further descriptions are not provided.

The Ongatiti Ignimbrite is a well-known and frequently exposed ignimbrite formation recognised throughout the King Country region and in the town of

Ngaroma (Leonard et al., 2010). However, this ignimbrite was not recognised in this area during this study, therefore it is not discussed in this chapter.

Four distinct geological units have been identified throughout the Ngaroma area here labelled A to D (Figure 2.1). The units vary both vertically and laterally and are identifiable from one another based on outcrop appearance, and macroscopic observations such as colour, texture, and variations in primary componentry.

Two ignimbrites are recognised in this field area (Ngaroma and Whakamaru ignimbrites) and both are described in this chapter, however, additional petrographic descriptions of the Whakamaru Ignimbrite have been provided to confirm the existence of this deposit while petrographic observations of the Ngaroma Ignimbrite will be presented in chapter three.

Lastly, the four units identified (Figure 2.1) are, in order from oldest to youngest: uplifted basement greywacke and argillite (unit A), andesite (unit B), the Whakamaru Ignimbrite (unit C), and the Ngaroma Ignimbrite.

### 2.4.1 Basement Greywacke and Argillite (Unit A)

Unit A represents a relatively thick (~12 m) sheet of uplifted basement greywacke (Figure 2.3). The unit is restricted to areas north and west of the field area, particularly at the northern-end of Waipari Road, and along the eastern side of Tolley Road (Figures 2.1 and 2.3). Outcrops are poorly vegetated, significantly weathered, and measure an average thickness of ~ 12 m. Perpendicular and vertical joint sets are discrete at the exposed outcrop in a quarry along Waipari Road. Greywacke (sandstone) is interbedded with argillite (mudstone). There is a NNE-SSW trending fault observed at the exposed greywacke unit that occurs east of Tolley Road (Figure 2.3). Here, the greywacke is severely weathered and deformed.

The uplifted basement rock, or unit A, is a crystal-rich lithic-rich greywacke that is fine-grained and homogenous and varies in colour from dark brown to grey to black (Figure 2.3). Vertical joint sets observed here are highly fractured. The interbedded, fine-grained argillite appears light brown to orange in colour.

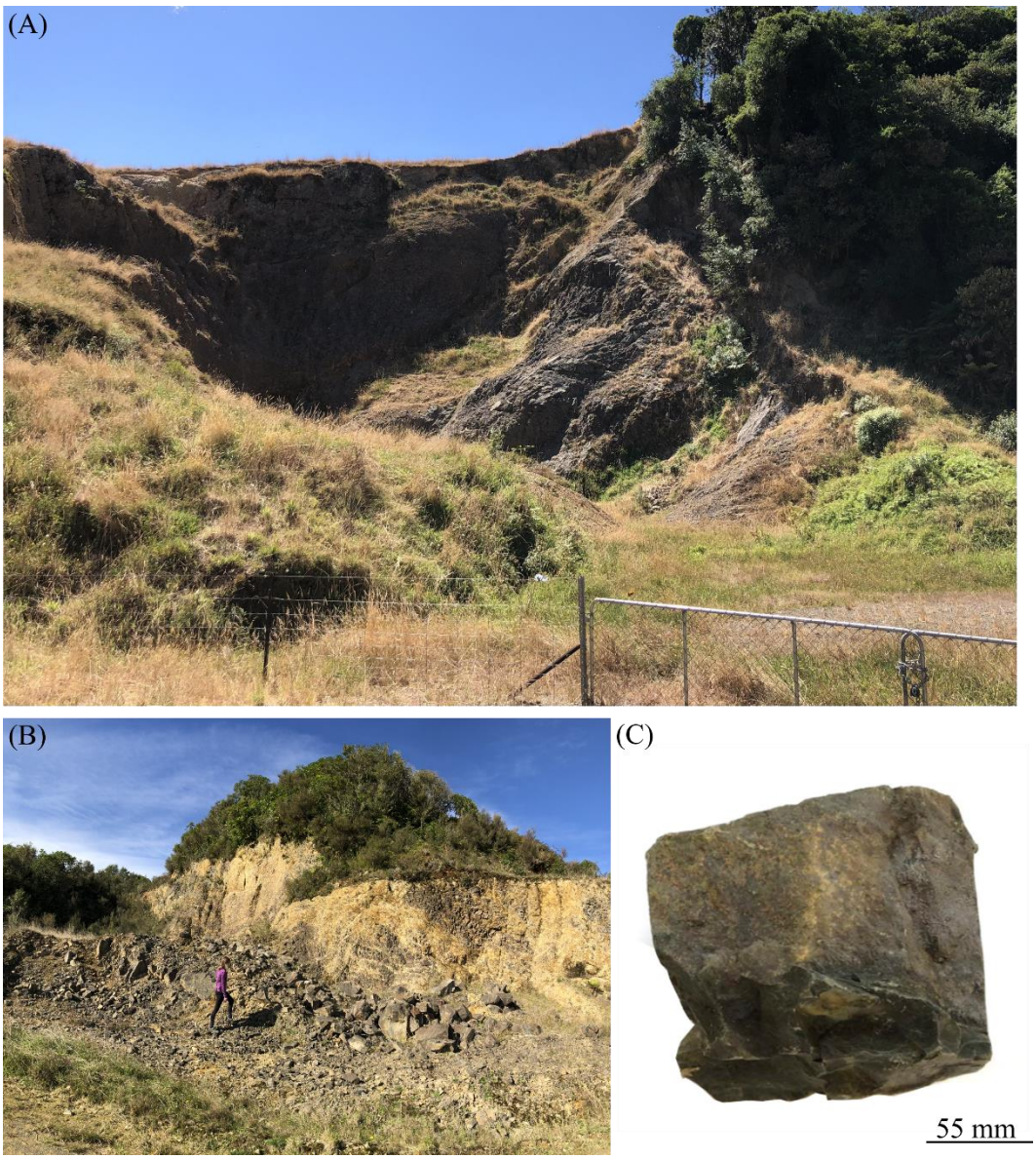


**Figure 2.3:** Uplifted basement rock observed within the town of Ngaroma: (A) quarry of uplifted greywacke rock observed at the northern-end of Waipari Road; (B) severely weathered basement rock observed to the east of Tolley Road, notice the local fault extending from NNE-SSW; (C) hand sample of basement greywacke, notice the dark brown to back colour and fine- grained matrix.

### 2.4.2 Andesite (Unit B)

Unit B is a thin, layer of crystal-rich andesite that is preserved in the north and north-central region of the field area (Figures 2.1 and 2.4). The exposed outcrop is well –vegetated. It is extremely confined and observed particularly at the northern end of Mangawhio Road where it measures a relative thickness of 0.2 m. The underlying deposit of this unit is unknown, however, at this locality unit B is directly overlain by the Ngaroma Ignimbrite (Figure 2.9).

Unit B represents a porphyritic andesite that is characterised by its dark grey colour and conspicuous abundance of feldspar phenocrysts (Figure 2.4), which are large (up to 9 mm) in size, are typically white to light pink in colour and sub-angular in shape. They are dispersed and fragmented throughout a fine-grained groundmass, and comprise 7-10% of the bulk rock.


**Figure 2.4:** Thin layer of andesite observed at the northern end of Mangawhio Road. Notice the conspicuous abundance of feldspar.

### 2.4.3 Whakamaru Ignimbrite (Unit C)

The Whakamaru Ignimbrite(s), referred to here as unit C, represent a voluminous succession of poorly defined ash-flow sheets, or massive tuffs (Barker et al., 2014; Martin, 1961). The ignimbrite(s) may be recognised by their conspicuous occurrence of large (up to 10 mm) crystals of quartz, plagioclase, orthopyroxene, and minor abundance of hornblende and biotite. These clasts, in addition to lithic and pumice fragments comprise 15-25 % of the bulk rock (by volume) and are typically overprinted by a coarse-grained, vitric tuff which appears light grey to pink in colour, and soft, or porous in texture (Barker et al., 2014).

When observed in the field area of this study, unit C is relatively wide-spread occurring north and south (southeast and southwest) of the field area, particularly along Mangawhio Road (Figure 2.1). Preserved outcrops at the northeastern end of

this road occur as boulders which are either scattered across, or weathering through the slump scarps of the gently-sloping hills (Figure 2.6). At the southern-end of the field area, the deposit is presumed to form the underlying surface of Mangawhio Road. The deposit varies in thickness from .8 to 7 m (Figure 2.5). It is poorly-welded and can be recognised by its light brown to yellow colour and conspicuous abundance of relatively large (up to 5 mm) quartz crystals. A stratigraphic log of the Whakamaru Ignimbrite is presented in Figure 2.5, and a detailed petrographic description is also included here.

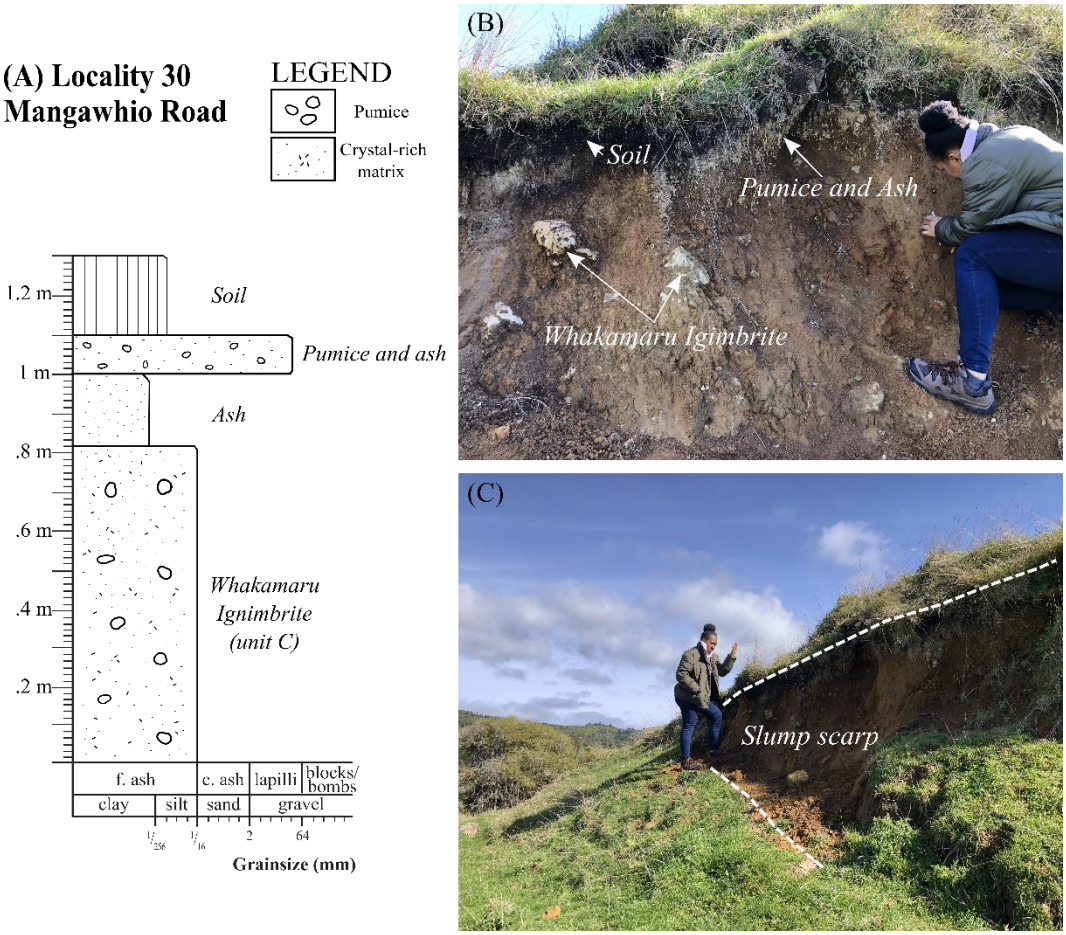


**Figure 2.5:** Whakamaru Ignimbrite observed at the northern end of Mangawhio Road: (A) stratigraphic log of Whakamaru Ignimbrite and its overlying deposits commonly observed within the field area; (B) slump scarp with weathered ignimbrite (Whakamaru), notice the overlying layer of pumice and ash; (C) slump scarp comprised of weathered ignimbrite.

Unit C is typically overlain by a succession of composite weathered tephra (namely the Hamilton ± Kauroa ash beds). There is an abrupt contact change observed at Mangawhio Road (Figure 2.5). At this locality, the unit extends from 0 to .8 m, measuring a maximum (representative) thickness of .8 m (Figure 2.5). It is overlain by a thin (<1 m) layer of ash from .8 to 1 m, which in turn is succeeded by a layer

of pumice and ash, occurring from 1 to 1.1 m (Figure 2.5). The exposure is mantled by top-soil which occurs from 1.1 to 1.3 m (Figure 2.5).

Unit C is a poorly welded ignimbrite that is distinct for its pale cream colours, porous texture, and conspicuous abundance of crystals (Figure 2.6). Crystals observed here record an average size of 4 mm and comprise 15-20 % of the bulk rock. They are comprised mostly of quartz, feldspar, opaque minerals, and to a lesser extent, of hornblende and biotite. Pumice throughout the deposit comprise 34% of the bulk rock. These clasts are typically 7 mm in size (with a maximum of 24 mm), porphyritic in texture, round to sub-round in shape, and light brown in colour (Figure 2.6). Lithic clasts are extremely rare and comprise $\leq$ 2% of the bulk rock. When visible, these clasts are typically 2 mm in size and sub-angular in shape. They appear light grey in colour, and because of their fine-grained texture are presumed to be of rhyolite or greywacke.

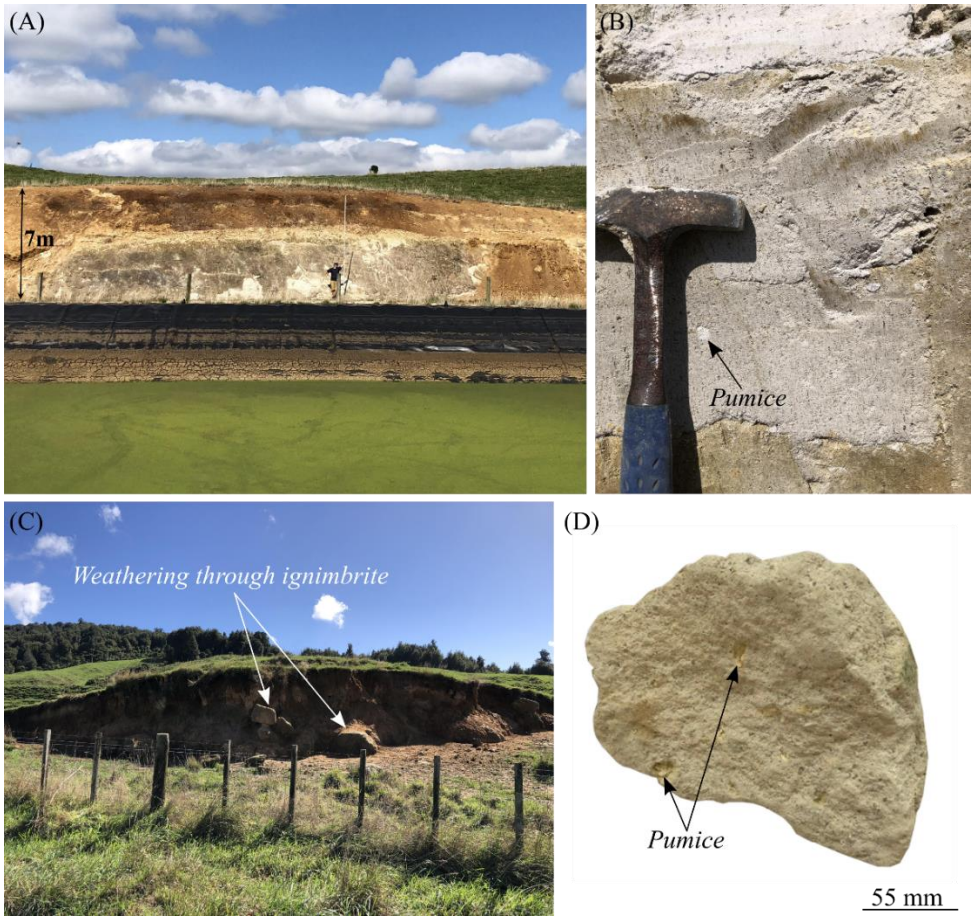


**Figure 2.6:** Whakamaru Ignimbrite lithology and outcrop appearance: (A) maximum observed thickness recorded at the northern end of Mangawhio Road; (B) outcrop appearance showing the soft, porous texture and light cream, or brown colour of the ignimbrite, notice the white, round to sub-round pumice; (C) typical outcrop of Whakamaru Ignimbrite exposed in slump scarp(s), photo taken standing east of Mangawhio Road; (D) hand specimen of Whakamaru Ignimbrite, notice the pale cream colour(s) and round to sub-round pumice.

Petrographically, the Whakamaru Ignimbrite exhibits a crystal-rich, vitriclastic matrix of glass shards which account for 90% of the bulk rock (Figure 2.7). Crystals throughout this deposit are abundant, and comprise 15-20% of the bulk rock. They are dominated by quartz (10%), feldspar (5%), and pyroxene (3%) (Figure 2.7). Opaque minerals are unique, and comprise 2% of bulk rock. Likewise crystals of hornblende, biotite and augite are rare, and comprise <1 % of bulk rock (Figure 2.7). Lithics throughout the deposit are comprised mostly of argillite. These clasts appear anhedral in shape and form <1 % of the bulk rock.

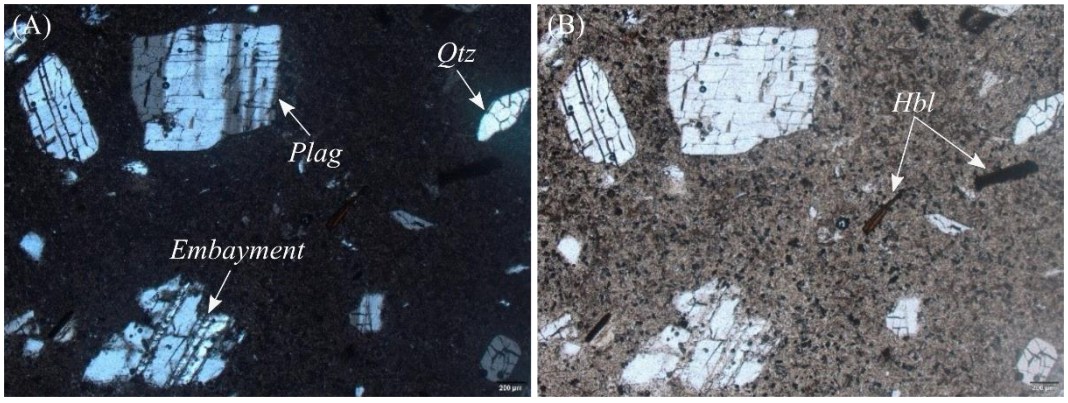


**Figure 2.7:** Photomicrographs of Whakamaru Ignimbrite showing phenocrysts scattered throughout a vitriclastic matrix; (A) observed under XPL, notice the embayed feldspar, and presence of quartz; (B) under PPL, notice the fine-grained, vitriclastic matrix and presence of hornblende (Hbl).

## 2.5 The Ngaroma Ignimbrite

The Ngaroma Ignimbrite, as previously discussed, is a moderate to densely welded, vapour-phase altered deposit that is unique for its pastel-like colours and high concentration of consolidated fiamme (Briggs et al., 1993; McCormack et al., 2009). The deposit in particular, can be recognised by its light pink to blue colours, and fine-grained, homogenous matrix (Martin, 1961). This section describes in detail the internal stratigraphy, facies and distribution of the Ngaroma Ignimbrite.

### 2.5.1 Distribution within field area and outcrop appearance

The Ngaroma Ignimbrite is relatively widespread (Figure 2.1), and forms either the underlying surface of the gently-sloping hills, or is exposed as boulder fields (Figure 2.8). The contact with overlying and underlying units is rarely exposed except in rare occurrences where it is observed resting directly above a thin layer of andesite, or unit B (Figure 2.9).

Outcrops of Ngaroma Ignimbrite occur frequently, and vary both laterally and vertically throughout the field area (Figure 2.1). Detailed field measurements, including stratigraphic logging, records an average thickness of 20 meters with a maximum thickness of 40 meters (Figures 2.12 and 2.19).


**Figure 2.8:** Photographs showing the general outcrop appearance of Ngaroma Ignimbrite: (A) weathered boulder field observed at the northwest end of Mangawhio Road; (B) outcrop appearance in an exposed boulder, notice the relatively large lithics, occurrence of fiamme, and grey to purple colour; (C) outcrop at Mangawhio Road; (D) outcrop at Waipari Road recording a thickness of 8m.

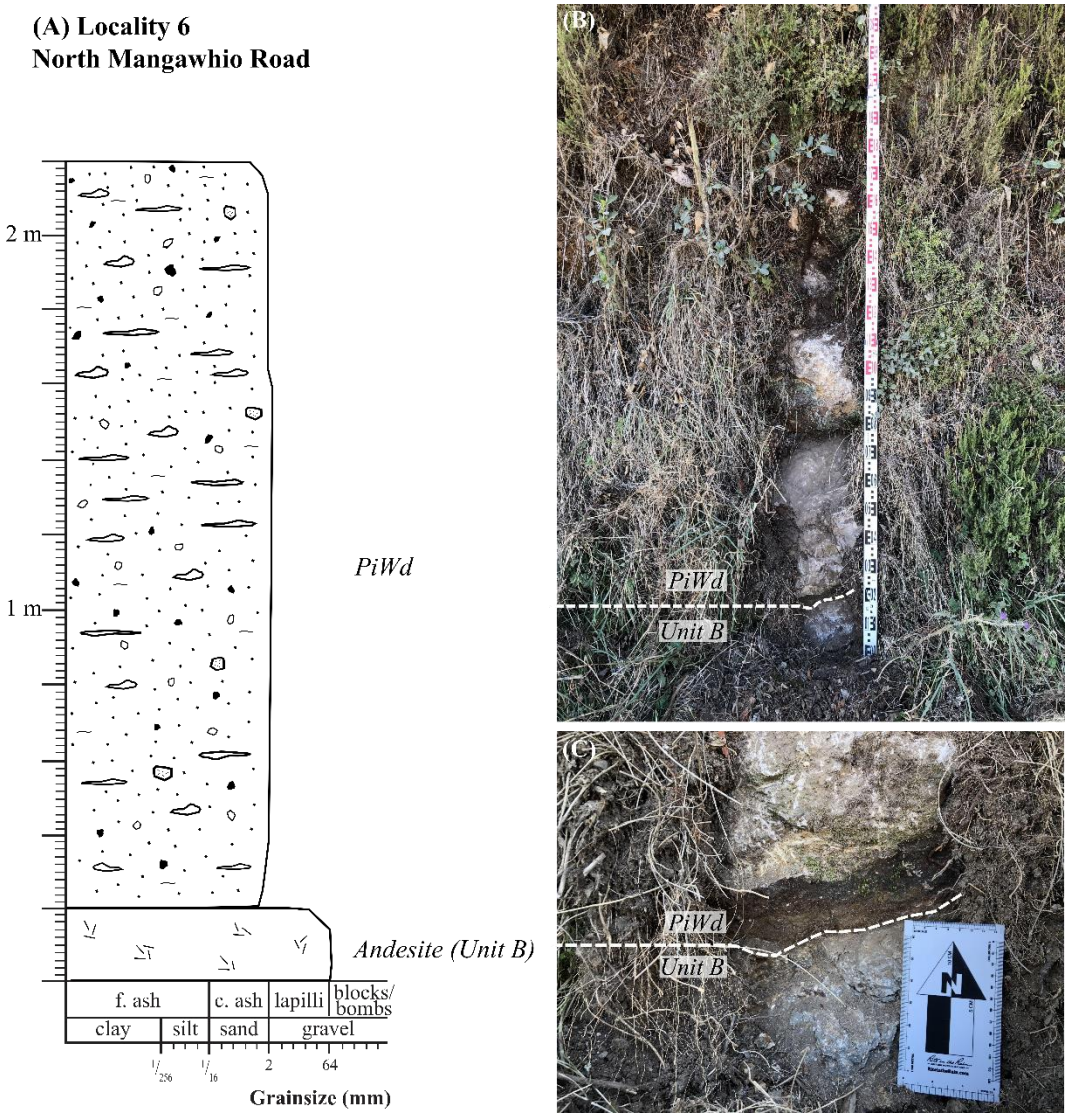


**Figure 2.9:** Outcrop occurrence and stratigraphy of Ngaroma Ignimbrite and unit B observed east of Mangawhio Road: (A) stratigraphic log showing subfacies PiWd directly overlying unit B; (B) exposed outcrop showing the abrupt contact occurring between subfacies PiWd and unit B from afar; (C) abrupt contact between subfacies PiWd and unit B.

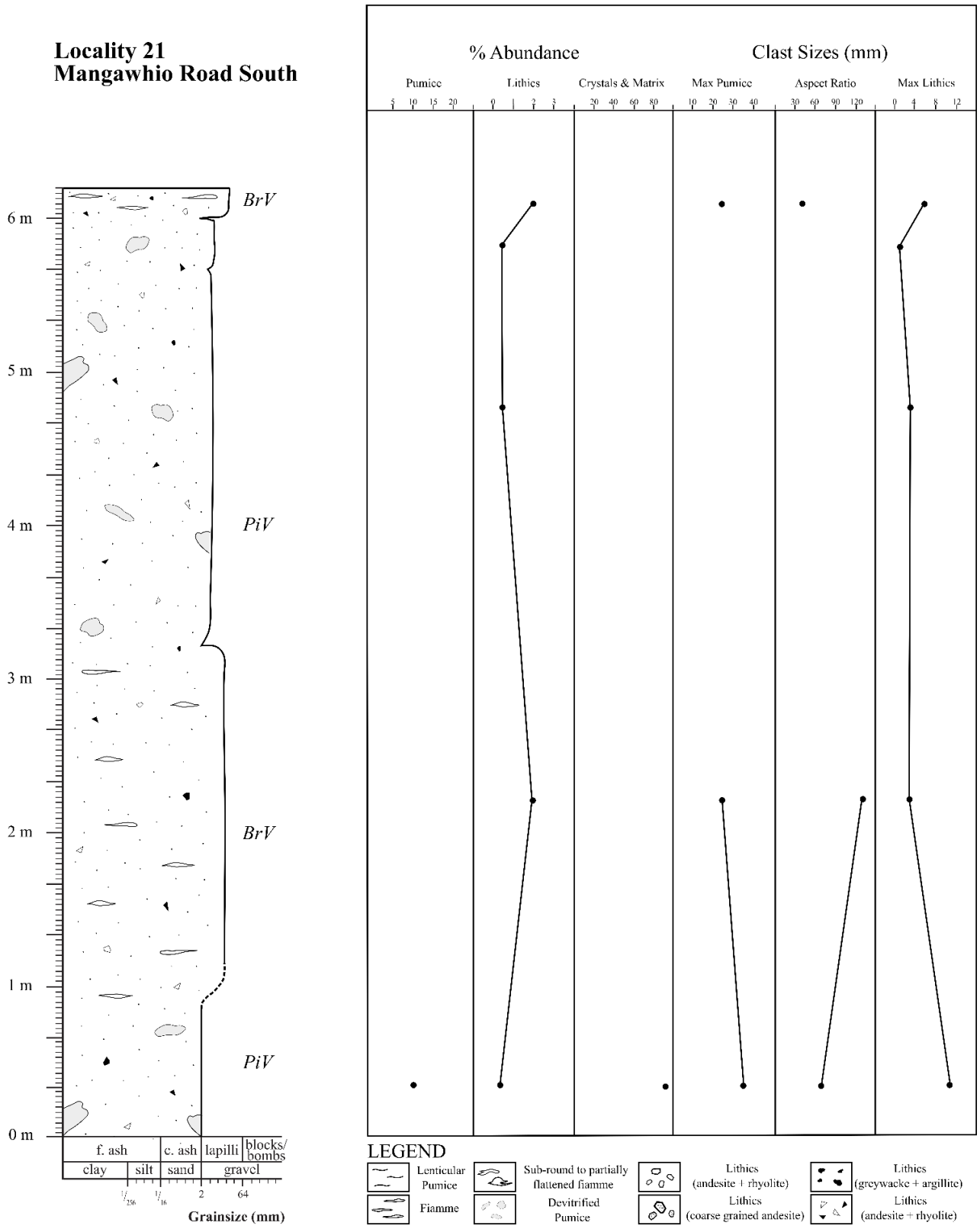


**Figure 2.10:** Stratigraphic log showing subtle vertical variations occurring between subfacies PiV and BrV to the west of Mangawhio Road. Notice the change in the percentage abundance of lithics and corresponding changes in clast size. Note the percentage abundance of pumice, crystals and matrix, and the size and aspect ratios of pumice are not recorded due to their indistinguishable appearance or soft, devitrified material.

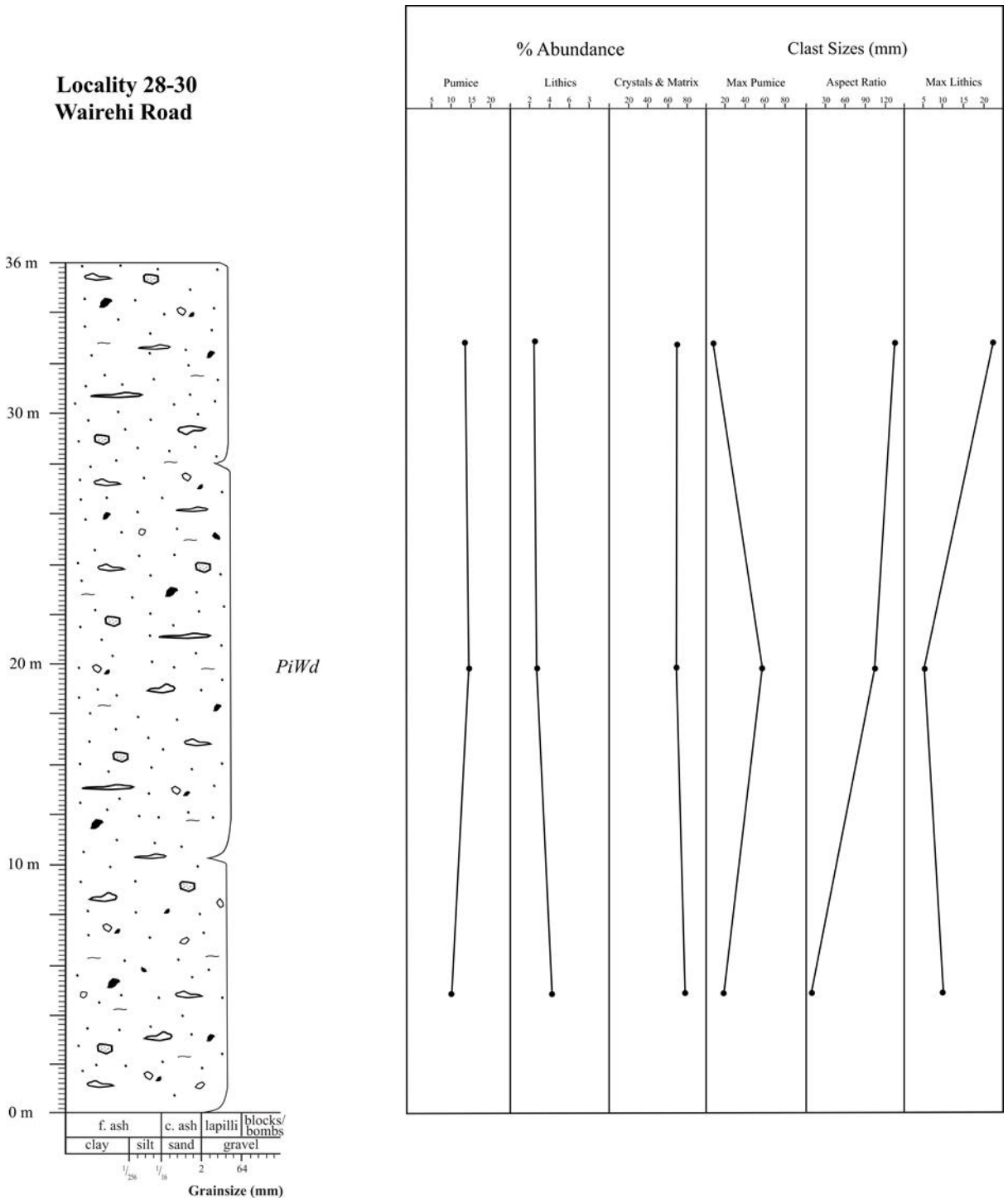


**Figure 2.11:** Stratigraphic log representing the underlying surface of the gently-sloping (ignimbrite) hills recorded north of Wairehi Road. Variations occurring within subfacies PiWd are subtle and most noticeable at 2 0m. Notice the maximum thickness recorded here is 36 m.

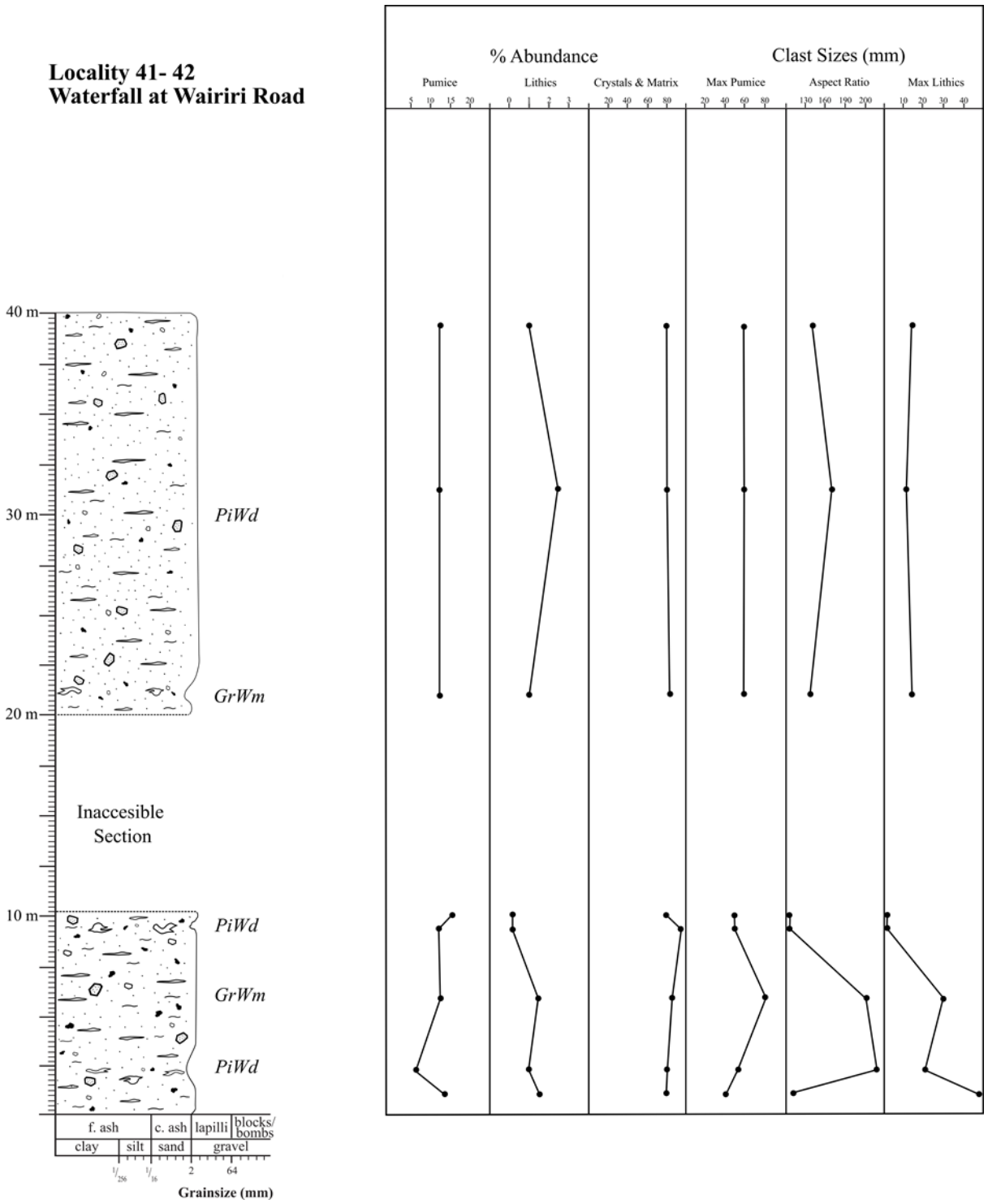


**Figure 2.12:** Stratigraphic log representing the maximum thickness of Ngaroma Ignimbrite recorded from the base to the top of the waterfall alongside Waipari Road. Sample collecting and field analyses were not obtained from 10 to 20 m. Notice the discrete changes occurring at the base of the waterfall at 3 and 9 m.

In the field area the Ngaroma Ignimbrite is a moderate to densely welded ignimbrite that varies in colour from light pink to purple to grey. This deposit, may be recognised by its high concentration of wispy lenticular pumice or fiamme, conspicuous abundance of lithics and somewhat chalky, or devitrified appearance. Here, lithic clasts vary in composition from andesite and rhyolite to greywacke and argillite while crystals are comprised almost entirely of feldspar. Pumice occurs either as thin, wispy lenticular forms (Figure 2.13), or as partially flattened fiamme (Figures 2.14 and 2.15). Fiamme, appear either porous or chalky in texture, and yellow in colour, or are extremely devitrified in texture and light grey in colour.

Perhaps the most notable component of this ignimbrite, is the conspicuous abundance of coarse-grained, crystal-rich andesite lithics (Figure 2.13). These lithics are porphyritic in texture, and comprise large (up to 8 mm) crystals of feldspar.

### 2.5.2 Facies

Two primary facies (a lithic-rich and lithic-poor facies) and four subfacies have been identified and described, and are presented in four stratigraphic logs (Figures 2.9-2.12) which vary both vertically and laterally throughout the field area (Figure 2.1). The facies and subfacies reflect syn- and post-deposition and alteration processes, and can be recognised by changes in primary componentry, and in the degree of welding.

#### 2.5.2.1 Lithic-rich ignimbrite facies

The lithic-rich facies is a moderate to densely welded ignimbrite that varies in colour from light grey to purple (Figures 2.13 and 2.14). This facies may be recognised by its relatively high lithic content and high concentration of thin, wispy lenticular pumice (Figure 2.13), and frequent occurrence of fiamme (Figure 2.14). While lithic clasts here are abundant, and typically comprised either of andesite and rhyolite, or of greywacke and argillite; this facies is unique for its frequent occurrence of relatively large (up to 25 mm), coarse-grained, and crystal-rich fragments of andesite (Figure 2.13).

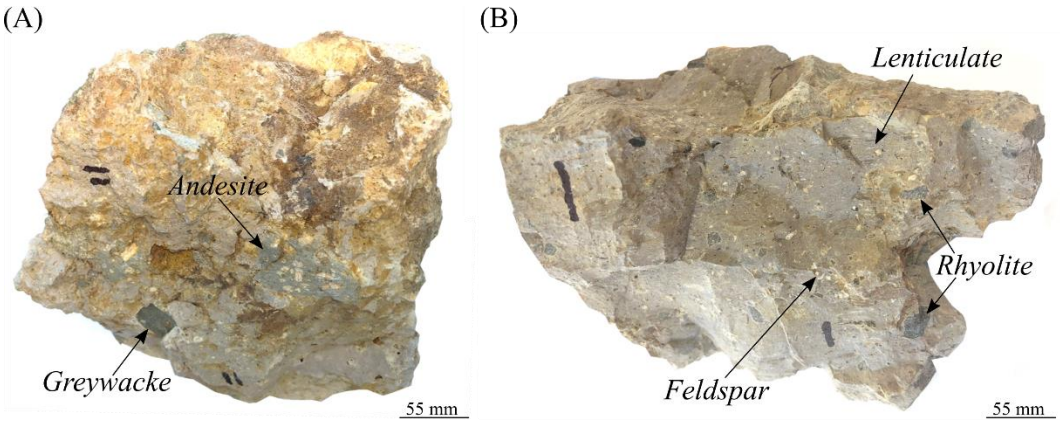


**Figure 2.13:** Lithic-rich facies identified within the Ngaroma Ignimbrite, with varying colours of light grey to purple: (A) notice the coarse-grained, crystal rich andesite lithic comprised of feldspar, and fine-grained lithic of greywacke; (B) notice the conspicuous abundance of extremely compact lenticular pumice preserved throughout a fine-grained, light purple matrix. Notice the crystal-poor matrix, and the relatively large greywacke lithic.

*Light-medium grey and moderately-densely welded subfacies (GrWm)*

The GrWm subfacies represents a moderate to densely welded ignimbrite that is recognised by its light to medium grey colour, conspicuous abundance of fiamme, and frequent occurrence of coarse-grained, crystal-rich lithics of andesite (Figure 2.14). Crystals throughout this deposit, chiefly of plagioclase, are typically 1 mm in size, angular to sub-angular in shape and white in colour, and account for 3% of the bulk rock. Opaque crystals however, are rare, and comprise <1 % of bulk rock. Lithic fragments vary in composition from greywacke and argillite to andesite and rhyolite. These clasts are typically 6 mm in size, sub-round to sub-angular in shape, and comprise 5-7% of the overall rock. Large (up to 19 mm) fragments of coarse-grained, crystal-rich andesite are abundant throughout this subfacies (Figure 2.13). They are discrete for their large ($\leq$ 4 mm on average, or up to 8 mm) crystals of feldspar that, similar to those observed throughout the matrix, are angular to sub-angular in shape and light pink in colour.

Unique to subfacies GrWm, as previously mentioned, is the conspicuous concentration of fiamme which comprise 40% of the overall rock (Figure 2.14). These clasts record an average size of 20 mm (with a maximum of 60 mm and a minimum of 3 mm), and aspect ratio of 2.8 mm. They are characterised by their somewhat porous, or chalky texture, pale cream to yellow colour, and darkened rims which vary in colour from brown to black (Figure 2.14).

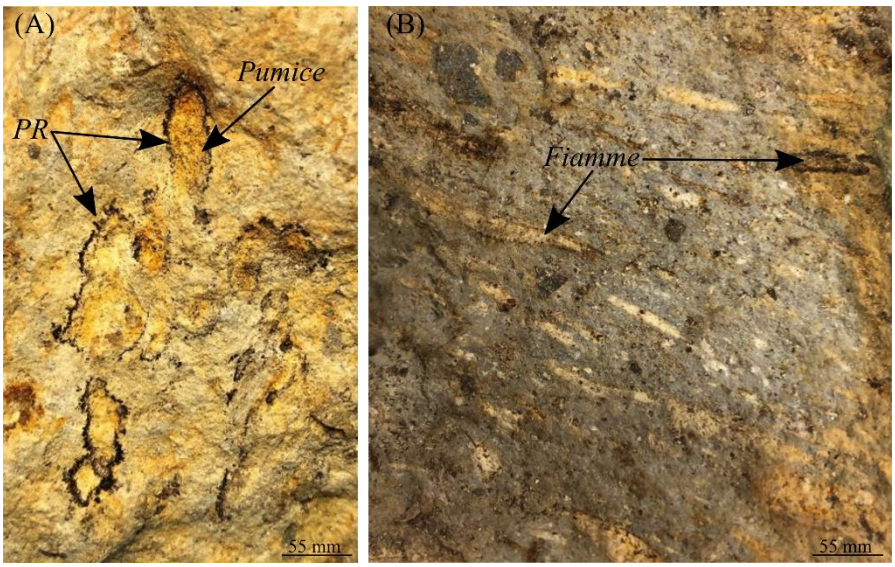


**Figure 2.14:** Photographs showing the conspicuous abundance of partially flattened pumice and fiamme observed within subfacies GrWm: (A) sub-round to partially flattened pumice with discrete black rims; (B) frequently occurring fiamme with notable pumice rims (PR) of brown to dark brown in colour.

*Pink-purple densely welded subfacies (PiWd)*

The PiWd subfacies represents a moderate to densely welded, lithic-rich ignimbrite that is perhaps most recognised by its pastel-like colours of light pink and purple (Figure 2.15). Crystals throughout this deposit comprise 3-7% of the bulk rock and consist mostly of large ($\leq$ 5mm) feldspar, followed by scattered fragments of opaques. Lithics vary in composition from greywacke and argillite to andesite and rhyolite, presumably (Figure 2.15). These clasts record an average size of 8 mm (with a maximum of 26 mm), are angular to sub-angular in shape, and account for 3-5% of the bulk rock. Similar to subfacies GrWm, lithics observed throughout the PiWd subfacies, are dominated by coarse-grained, crystal-rich andesite.

Pumice throughout subfacies PiWd are mostly thin, wispy, and lenticular, and vary in colour from light purple to white, and comprise 40 % of the overall rock. Additional pumice observed here, and unique to this deposit, is the conspicuous abundance of partially flattened fiamme (Figure 2.15). These clasts record an average size of 13 mm (with a maximum of 35 mm), and aspect ratio of 2.7 mm. They are commonly recognised by their yellow to grey colour, and somewhat chalky texture.

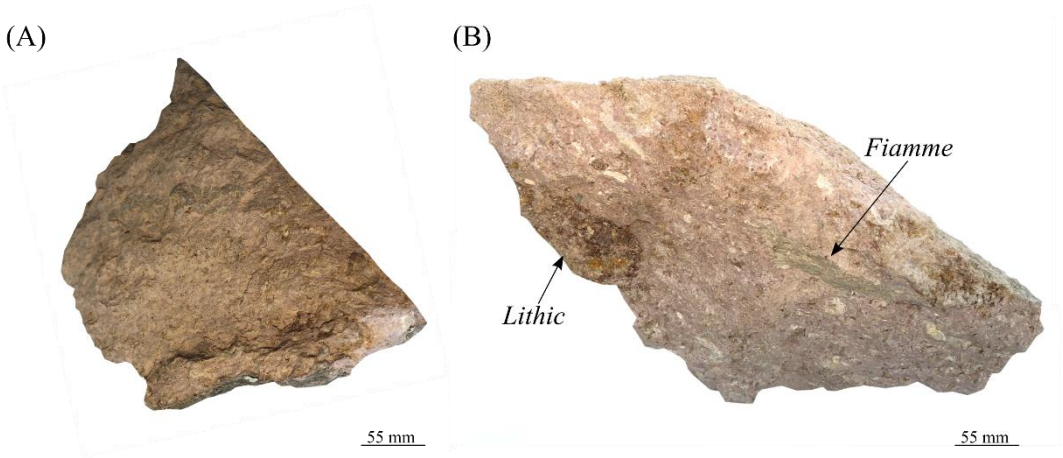


**Figure 2.15:** General appearance of subfacies PiWd; (A) photo showing the overall grey to purple colours; (B) photo showing the occurrence of primary components. Notice the light grey fiamme and the relatively large, weathered lithic**.**

### 2.5.2.2 Lithic-poor ignimbrite facies

The lithic-poor facies represents a non-welded to partially welded, crystal-poor, lithic-poor ignimbrite (Figure 2.16). Outcrops of this ignimbrite are unique for their light colours of pink to purple to grey, extremely chalky, or devitrified appearance, and comparably low concentration of primary components. Pumice throughout this facies, contrary to those observed in the lithic-rich facies, are typically round or sub-round in shape, light grey in colour, and appear extremely fibrous, or devitrified in texture. These clasts are either intact, or have been removed from the rock due to the soft, devitrified texture (Figure 2.16).

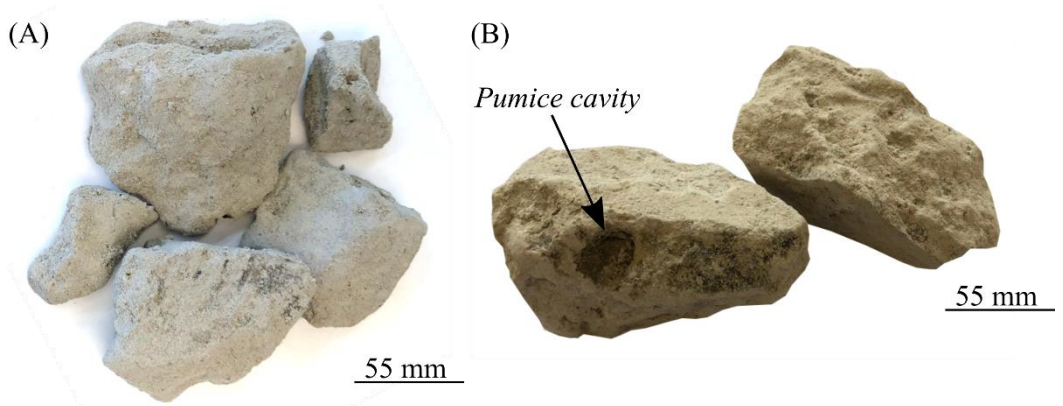


**Figure 2.16:** General lithology and appearance of the lithic-poor facies comprising the Ngaroma Ignimbrite: (A) photograph depicting the extremely chalky texture and light grey colours; (B) hand specimens showing a round to sub-round pumice. Notice the light brown colour and indistinguishable presence of juvenile material.

*Light pink-purple strongly vapour-phase altered subfacies (PiV)*

Subfacies PiV represents a partially to non-welded, strongly vapour-phase altered ignimbrite that is recognised by its indistinguishable concentration of juvenile material, chalky, or devitrified texture, and pastel-like colours of light pink to purple to grey (Figure 2.17). Crystals throughout this subfacies are comprised mostly of small ($\leq$ 1 mm) feldspar that comprise 1-2% of the bulk rock. Opaque minerals here, contrary to those observed in the GrWm and PiWd subfacies, are extremely rare, or absent.

Lithics throughout this deposit are noticeably less abundant, and comprise $\leq$ 1% of the bulk rock. When visible, these clasts occur as sparse fragments of greywacke, rhyolite, and andesite, presumably. They are typically $\leq$ 1 mm in size, angular to sub-angular in shape, and comprise a fine-grained and homogenous groundmass which varies in colour from dark grey to red. Contrary to the GrWm and PiWd subfacies, coarse-grained, crystal-rich lithics of andesite are not recorded within subfacies PiV.

Unique to subfacies PiV, as previously mentioned, is the conspicuous abundance of partially fattened fiamme which form 15-20% of the bulk rock (Figure 2.17). These clasts appear light grey in colour and are somewhat devitrified in texture. They are typically 20 mm in size (with a maximum of 40 mm), and record an average aspect ratio of 2.5 mm.

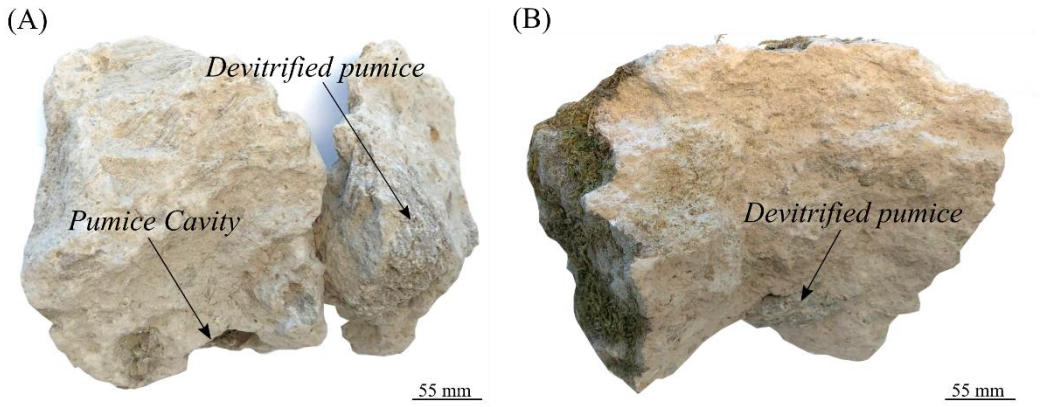


**Figure 2.17:** Photos showing the typical appearance of subfacies PiV. Notice the variation in colour from pale brown to light pink, chalky appearance, and abundance of partially flattened and devitrified pumice. (A) Representative samples of subfacies PiV. Notice the pale brown colour, and light grey, devitrified pumice. Also notice the absence of pumice, represented by the pumice cavity. (B) Subfacies PiV, light pink in colour. Notice the light grey, partially flattened and devitrified pumice.

*Brown to cream vapour-phase altered subfacies (BrV)*

The BrV subfacies is a crystal-poor, lithic-poor ignimbrite that is recognised by its pale cream to brown colours, and extremely devitrified, or chalky texture (Figure 2.18). Crystals throughout this deposit consist almost entirely of feldspar, and comprise 10-15% of the bulk rock. These clasts are typically $\leq$ 1 mm in size, and appear angular to sub-angular in shape. Lithics here account for 1-2% of the bulk rock, and are similar to those observed in subfacies PiV (Figure 2.17), comprising a fine-grained homogenous groundmass (Figure 2.18). These clasts have an average size of 4 mm (with a maximum of 23 mm), appear sub-round to sub-angular in shape, and vary in composition from greywacke and argillite to rhyolite and andesite. Pumice throughout this deposit occurs as thin wispy lenticular forms which vary in colour from white to light grey, and comprise 7-10% of the bulk rock.

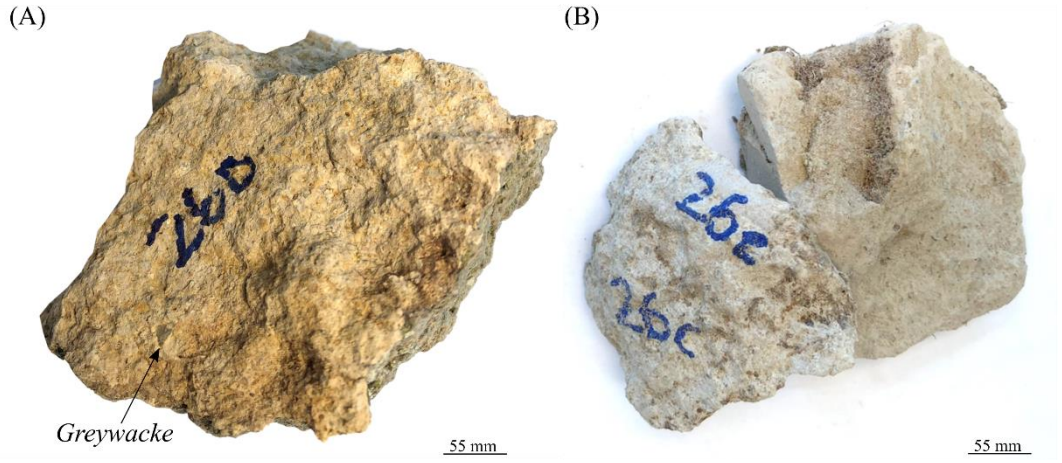


**Figure 2.18:** Samples showing the general appearance of subfacies BrV (A) hand specimen showing a minor abundance of lithics, somewhat chalky texture, and pale cream or brown colours (B) hand specimen showing a near-by absence of lithics, extremely chalky or powdery texture, and light grey colour.

### 2.5.3 Facies architecture throughout the field area

The two primary facies (Figures 2.13 and 2.16), and four subfacies that comprise the Ngaroma Ignimbrite extend both laterally and vertically throughout the field area. Subfacies GrWm and PiWd are the most well preserved and thus frequently exposed subfacies, while exposures of subfacies PiV and BrV are rather sparse.

Overall, the vertical variations recorded throughout the Ngaroma Ignimbrite are extremely subtle, and the ignimbrite is generally a massive, or uniform deposit (Figures 2.9-2.12). These changes in particular, occur both in the percentage abundance and average clast size of primary components, and are most commonly observed between subfacies GrWm and PiWd (Figures 2.14 and 2.15), and subfacies PiV and BrV (Figures 2.17 and 2.18).

Due to the undulating topographic surface and the infrequent distribution, or position in which these boulder fields outcrop, the exact elevation representing the gradual transition recorded between subfacies PiV and BrV (Figure 2.10) is unknown, however based on extensive field observations and the recorded elevations acquired using the GPS, is presumed to occur between 1 and 2 m.

*Mangawhio Road North*

There is an abrupt and rather significant contact change observed between unit B and subfacies PiWd (of the Ngaroma Ignimbrite), which is observed at the northern-end of Mangawhio Road (Figure 2.9). Here, unit B measures a relative thickness of 0.2 m and the PiWd subfacies 2 m, thick.

*Mangawhio Road South*

Vertical variations recorded between subfacies PiV and subfacies BrV are gradual, and occur in areas south, and south-west of Mangawhio Road (Figure 2.10). At this locality, subfacies PiV extends from 0 to 1 m, and again from 3 to 6 m, measuring a maximum thickness of 3 m (Figure 2.10). Likewise, subfacies BrV extends from 1.2 to 3.2 m, and from 6 to 6.2 m, and records a maximum thickness of 2 m.

Variations occurring between these subfacies are, although gradual, most noticeable at 1, 3, and 6 m, where changes in both pumice and lithic clasts are discrete (Figure 2.10). Pumice observed from 0 to 1 m and from 3 to 6 m for example, are comprised mostly of partially flattened fiamme that are light grey in colour, and extremely devitrified in texture (Figure 2.17). However, from 1 to 3 m and from 6 to 6.2 m, pumice occurs as thin, wispy, lenticular forms. Likewise, lithics are relatively abundant from 1 to 3 m and at 6 m, and appear angular to sub angular in shape, and dark grey to dark red in colour. However from 0 to 1 m and from 3 to 6 m, are

generally overprinted by a soft, porous devitrified groundmass, and thus indistinguishable.

*Wairehi Road*

The PiWd subfacies is perhaps the most uniform deposit of the Ngaroma Ignimbrite (Figure 2.11). As shown in Figure 2.11, the subfacies extends from 0 to 36 m, thus measuring a maximum representative thickness of 36 m. Variations in primary components observed here, are subtle, and can be observed at 20 m, where pumice clasts increase in size, shape, and percentage abundance, while lithic clasts decrease in both size and percentage abundance.

The most notable changes recorded throughout the PiWd subfacies however, occur at 10 m and 28 m (Figure 2.11). Here, pumice clasts increase in both percentage abundance and size, while lithics and crystals decrease in both percentage abundance and size. Likewise variations in texture and colour of pumice clasts here are discrete. For example, pumice observed from 0 to 28 m, occur mostly as light grey, partially flattened fiamme (Figure 2.15), whereas pumice occurring from 28 to 36 m, are comprised of both lenticular form (light grey in colour), and round-sub-round clasts which appear porous in texture and light brown, or white in colour. There is a noticeable transition recorded within subfacies PiWd in which colours change from light grey-purple, to dark pink at 10 m, and again at 28 m, from dark pink to light grey-purple.

*Waipari Road*

Perhaps the most frequently distributed, and well exposed succession of subfacies observed throughout the Ngaroma Ignimbrite, are those which occur between subfacies GrWm and PiWd, at Waipairi Road (Figures 2.12 and 2.19). At this exposure, subfacies GrWm occurs from 3 to 9 m, and again from 20 to 21 m, and measures a maximum thickness of 6 m. Likewise, subfacies PiWd occurs from 0 to 2 m, 9 to 10 m, and again from 20 to 40 m, where it measures a maximum thickness of 20 m.

Vertical variations in primary components recorded here, particularly at the upper-most portion of the exposure, which extends from 20 to 40 m, are extremely subtle (Figure 2.12). However, at the lower-most portion, these changes are rather abrupt,

and recorded at 3 m, where pumice and lithic clasts decrease in percentage abundance, as pumice clasts increase in size, while lithic clasts decrease in size (Figure 2.12). Likewise, there is an abrupt transition occurring between subfacies PiWd and GrWm at 9 m, where variations in pumice, texture, and colour are discrete. In particular, the matrix at 9 m becomes increasingly fine-grained while colour changes from light brown to grey. Moreover, the conspicuous abundance of partially flattened fiamme (typically light brown in colour, and porous, or chalky in texture), occurring from 0 m, are replaced by thin, wispy, lenticular pumice (light grey in colour) at 9 m (Figures 2.12 and 2.19).

Similar variations are recorded at 23 m, where colours vary from light brown to light grey, and variations in pumice are distinct. In particular, the occurrence of partially flattened fiamme (light grey in colour, and porous in texture), increase in abundance while thin, wispy, lenticular forms (light grey in colour) decrease in abundance (Figure 2.12).

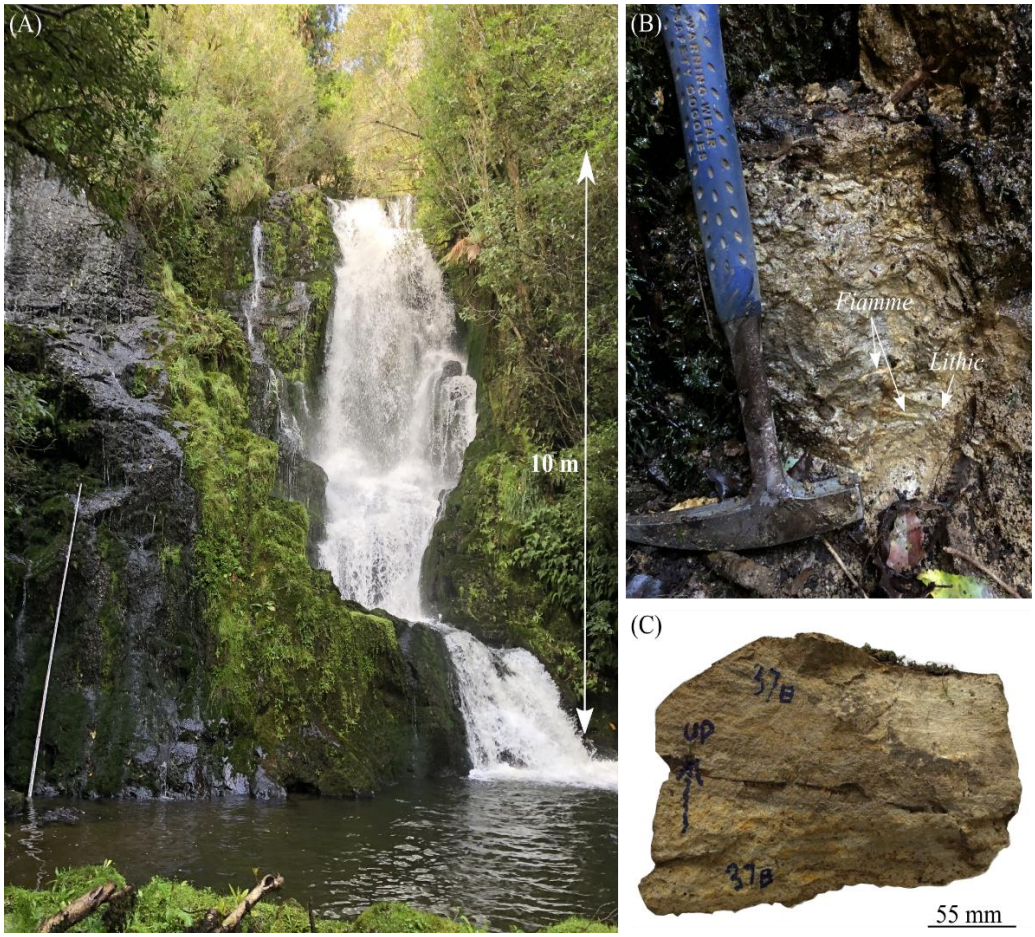


**Figure 2.19:** Outcrop appearance of Ngaroma Ignimbrite observed at Waipari Road (A) Waterfall recording the maximum thickness of Ngaroma Ignimbrite; (B) general lithology of Ngaroma Ignimbrite observed at the lower portion of the waterfall. Notice the frequent occurrence of yellow to white fiamme, and occasional occurrence of lithic fragments; (C) hand specimen showing the transition from subfacies PiWd to GrWm at 9 m.

# Chapter Three

# Petrography

## 3.1 Introduction

This chapter provides detailed descriptions of the mineralogy, and textural variations observed throughout the Ngaroma Ignimbrite. The overall ignimbrite mineralogy and matrix texture, in addition to the various textures observed in both pumice and lithics within the ignimbrite have been described using of the petrographic microscope. The proportions of primary components of the bulk ignimbrite, particularly of crystals, matrix, lithics and pumice were also obtained. Variations in mineral composition and texture, especially of the fine-grained ignimbrite matrix, were examined and documented through scanning electron microscopy (SEM) and associated energy dispersive spectrometry (EDS) analyses. This included detailed descriptions of morphology, or crystal habit, of matrix minerals that could not be resolved by optical microscopy, which were also probed using EDS, and subsequently confirmed by XRD analyses.

## 3.2 Methods

### 3.2.1 Thin Section Preparation

50 thin sections of the Ngaroma Ignimbrite, and pumice and lithics within the ignimbrite (Appendix II) were prepared using standard petrographic techniques. The collected field-samples of whole rock were cut into blocks measuring 4 cm x 2 cm. The cut blocks were then placed on a hot plate at 60 °C, with the freshly cut surface facing up, and subsequently impregnated with resin. This heated surface allowed for increased penetration of resin into the rock to minimize the likelihood of primary components (particularly of crystals) from being plucked out of the soft, porous ignimbrite, which was found to be a particular problem with samples of the Ngaroma Ignimbrite. Once absorbed into the rock, and completely hardened, the resin was ground off on a glass plate using #600 polish powder.

Using Hillquist thin section resin and hardener, with a ratio of 2.3:1., the prepared surface of each sample was mounted onto the frosted sides of a petrographic

microscope glass slide. Once settled, and because of the soft nature of the ignimbrite, the remaining sample was cut into a thickness of approximately 1 mm, and subsequently ground to a thickness of approximately 65 µm rather than a standard thickness of 30 µm using a Struers Discoplan-TS. At this thickness the unfinished thin sections were examined under a petrographic microscope to check for visibility of primary components and to also examine the interference colours in order to establish a suitable thickness. Samples were then further ground by hand using grinding plates, overlain with silicon carbide grinding paper of grit-500 and subsequently by grit-1200 until crystals displayed final interference colours indicating a thickness of 30 µm. The thin sections were then hand polished and left uncovered for SEM and electron microprobe analyses.

Ten unpolished thin sections were needed to properly characterise the texture of the ignimbrite matrix under the petrographic microscope. These blocks were, therefore left at a thickness of 30 µm. Using petropoxy 154, with a ratio of 10:1., cover slips were placed onto the freshly cut surfaces of each sample prior to being cured on a hotplate set at a temperature of 90°C.

### 3.2.2 Transmitted Light Optical Microscopy

The prepared thin sections were examined using the petrographic microscope under both plane polarised light (PPL) and crossed polarised light (XPL) at magnifications of 4x, 10x, 20x, and 40x in order to properly identify and describe the matrix and primary components comprising the Ngaroma Ignimbrite.

Quantitative data of the modal abundance of the different matrix-sized grains and of the pumice comprising the bulk rock was obtained by point counting (Table 3.1). Samples selected for these analyses were chosen to avoid the counting bias towards large lithics and pumice. The stage interval of each sample was set at 3 mm with 200 number counts per slide, which allowed for a precise representation of each sample. Ultimately, point counting data represents the modal abundance of the finer-grained (matrix-sized) components. This data must be considered in context with field/hand sample estimates of large pumice and lithic clasts within the ignimbrite.

### 3.2.3 X-Ray Diffraction (XRD) Analyses

Identification of both primary and secondary minerals comprising the Ngaroma Ignimbrite was conducted by using the Panalytical Empyrean X-ray powder diffraction (XRD) instrument in the Faculty of Science and Engineering at the University of Waikato. The collected samples of Ngaroma Ignimbrite were commonly weathered and showed significant signs of alteration. Samples which appeared to have minimal weathering were selected and analysed by XRD (Appendix VII). These samples were also chosen to avoid large juvenile clasts and lithics.

The selected samples of whole rock were dried in an oven and subsequently crushed into fine powder using a tungsten-carbide ring mill. Approximately 10 grams of crushed powder per sample was carefully placed into a metal holder and subsequently placed into the XRD. A copper Kα source was used and each sample ran from 2-80 °2Θ at 50 seconds per step. Mineral peaks and diffraction patterns were then recorded and analysed using Highscore Plus indexing software.

Using Highscore Plus, peak matching was conducted by comparing the diffraction patterns of the Ngaroma Ignimbrite to the 2019 Powder Diffraction File (PDF-4) database. Peak matching in particular, required the identification of at least two intense peaks, or d-spacing values. This in turn allowed for the presence of any existing, although optically unresolvable minerals within the ignimbrite matrix to be further analysed. The mineral peaks observed here sometimes overlap or are indistinguishable from one another, therefore some mineral phases recorded by XRD were also confirmed by SEM/EDS analyses.

Four clay separates (Appendix VII) were prepared and analysed by XRD using the methods provided by Cunningham (2012; after Whitton and Churchman, 1987 and Lowe and Nelson, 1983). Each sample was run from 2-45 °2θ at 120 seconds per step. Four treatments were undertaken per sample; the first run was untreated, the second run was after treatment with ethylene glycol; the third run was after heating to a temperature of 110°C for one hour, and the fourth run was after heating to 550°C for one hour.

### 3.2.4 Scanning Electron Microscopy (SEM) and Energy Dispersive Spectrometry (EDS) SEM/EDS

SEM/EDS analyses were acquired using the Hitachi S-4700 cold field emission SEM at the University of Waikato. Ten polished thin sections and seven rough chips were examined (Appendix III). These were vacuum-coated in platinum prior to being placed into the SEM. Operating conditions used for analysing the polished thin sections using backscattered electrons required an accelerating voltage of 15-20 kV, while secondary electron imaging of rough chips was acquired at 5.0 kV. Backscattered imaging was used to observe the matrix textures of polished thin sections and set to multiple magnifications ranging from 3.00 µm to 30 µm. The identification and confirmation of mineral phases comprising the ignimbrite was carried out by energy dispersive spectrometry (EDS) analyses. Secondary electron imaging of rough chips (<0.5 mm) were used to illustrate both the surface morphology and crystal habits of both matrix and of pumice.

## 3.3 Observations by Optical Microscopy

The Ngaroma eruption is preserved as a densely welded and strongly vapour-phase altered ignimbrite that records variations in texture and in primary components both macroscopically and petrographically. When examined under the petrographic microscope, very little glass is preserved, and the intensity of alteration in terms of textural overprinting is variable. The ignimbrite matrix in particular varies in texture from (a) eutaxitic, in which glass shards appear well-formed, however extensively devitrified to (b) a fine-grained, homogenous, and optically unresolvable medium; the latter of which has been resolved by SEM/EDS analyses (Figures 3.9-3.11).

Crystals throughout this deposit account for 2-3 % (up to 7 %) of the bulk rock and consist mostly of feldspar and opaque minerals and lesser-scattered fragments of pyroxene, and in rare occurrences of quartz (Table 3.1). Pumice clasts throughout the deposit are comparatively abundant and comprise 10-15 % (up to 40 %) of the bulk rock. These clasts occur either as thin, wispy lenticular forms or as flattened fiamme. Lithics comprise < 1 % of the bulk rock. These clasts vary in composition from greywacke and argillite to andesite and rhyolite.

**Table 3.1:** Point counting data showing the modal abundance of primary components. Pyroxene here includes both clinopyroxne (CPX) and orthopyroxene (OPX). Unknown crystals represent those which have been plucked out of the sample.

| Sample Number | S13 | S14 | S15 | S16 | S26C | S32 | S36 | S50 | S51 | S52 |
|---|---|---|---|---|---|---|---|---|---|---|
| Feldspar | 3 | 5.5 | 9.5 | 14.5 | 8.5 | 8.5 | 5.5 | 7.5 | 4.5 | 9.5 |
| Opaque | 4.5 | 1.5 | 3.5 | 5 | 1.5 | 3 | 5.5 | 5 | 3 | 1.5 |
| Pyroxene | 2 | - | - | - | - | 1.5 | - | 1 | - | 1 |
| Unknown Crystals | 2 | 5.5 | 5.5 | 5.5 | 1 | 3 | 3.5 | 4 | 4.5 | 1 |
| Crystals and Matrix | 77.5 | 71.5 | 68 | 69 | 69 | 69.5 | 70.5 | 71 | 75.5 | 81 |
| Pumice | 11 | 8 | 6.5 | 1 | 1 | 11 | 10 | 9 | 5.5 | 4 |
| Lithics | 1.5 | 8 | 7 | 5 | 5 | 3.5 | 6 | 2.5 | 7 | 2 |

### 3.3.1 Plagioclase

Plagioclase is the most common occurring crystal observed throughout the matrix of the Ngaroma Ignimbrite, and comprises > 95% of crystals. These crystals uphold an average size of 0.97 mm (with a maximum size of 2.92 mm and a minimum of 0.4 mm), appear euhedral to subhedral in shape, or are fragmented (Figure 3.1). Polysynthetic twinning and concentric zoning are amongst the two most commonly observed optical characteristics of the plagioclase (Figure 3.1). These textures however, are typically overprinted by fracture planes, or by small (<0.5 mm) quartz veins (Figure 3.1).

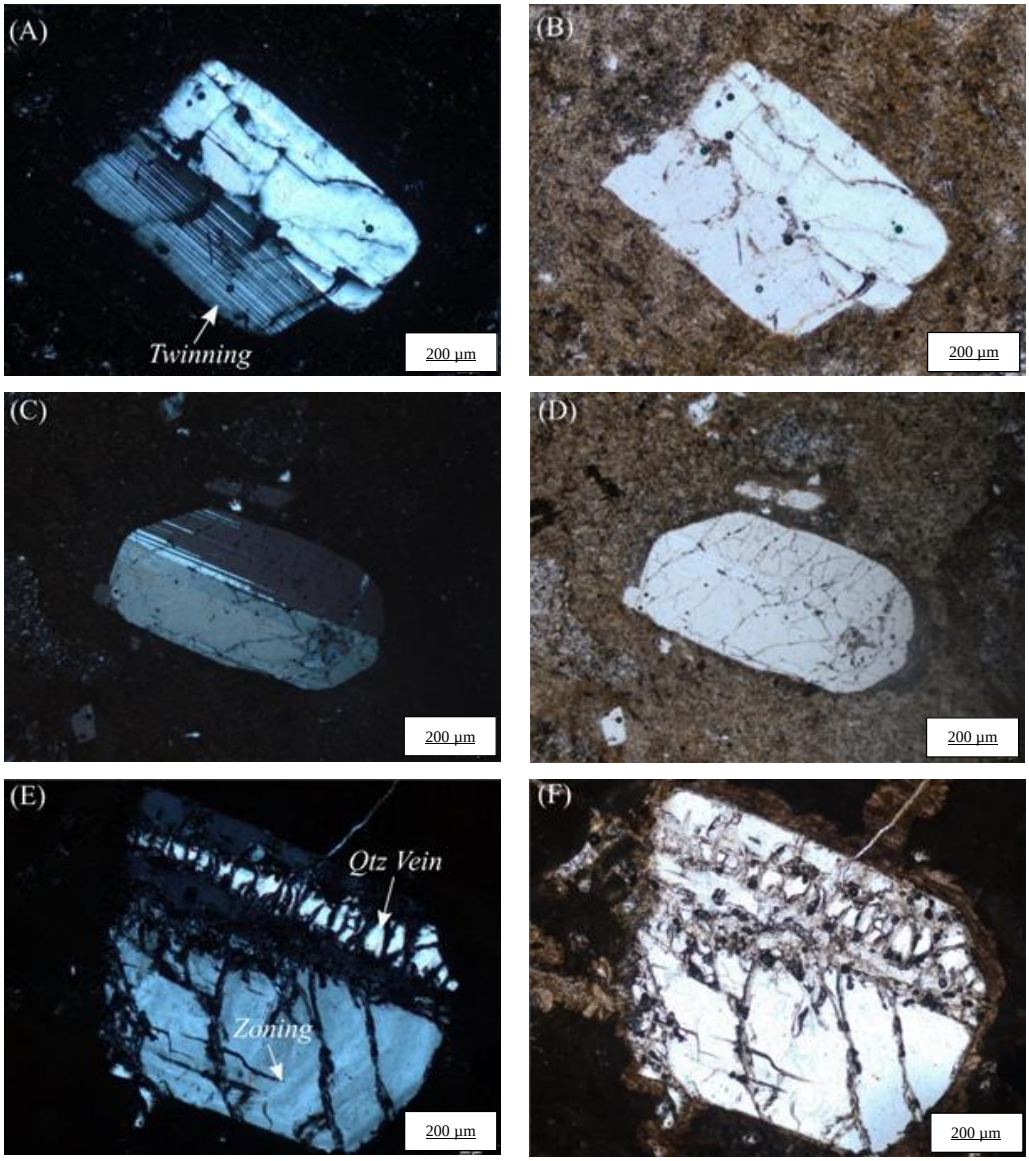


**Figure 3.1:** Plagioclase phenocrysts observed under the petrographic microscope. (A) Euhedral-shaped plagioclase with polysynthetic twinning and opposite extinction observed under XPL, and (B) under PPL. (C) Subhedral-shaped plagioclase with polysynthetic twinning and opposite extinction observed under XPL, and (C) under PPL. (E) Plagioclase with concentric zoning and quartz vein observed under XPL, and (F) under PPL.

#### 3.3.1.1 Opaque Minerals

Small opaque crystals, likely to be Fe-Ti oxides are the second most common ignimbrite crystal phase, following plagioclase. These crystals record an average size of 0.15 mm (with a maximum of 0.48 and a minimum of 0.1 mm), are anhedral to subhedral in shape, and comprise 1-2 % of crystals. They are thought, on the basis of shape and colour, to be of hematite, magnetite, and ilmenite. Opaques or semi-transparent crystals, which appear dark red or maroon in colour and euhedral to subhedral in shape, for example, are presumed to be of hematite. Crystals that are black in colour and round, or isometric in shape are of magnetite, and those

which are hexagonal and somewhat elongated in shape, are presumed to be of ilmenite.

### 3.3.1.2 Pyroxene

Pyroxene crystals observed throughout the ignimbrite occur in traces and consist mostly of orthopyroxene, and rarely of clinopyroxene (Figure 3.2). Orthopyroxenes exhibit pleochroic colours of either pale pink or green (Figure 3.2), and require a straight angle of extinction. Likewise, clinopyroxenes are typically pale grey to brown in colour, and become extinct at inclined angles. These fragmented phenocrysts are typically $\leq$ 1 mm in size, anhedral to euhedral in shape, and comprise <1% of crystals (Figure 3.2).

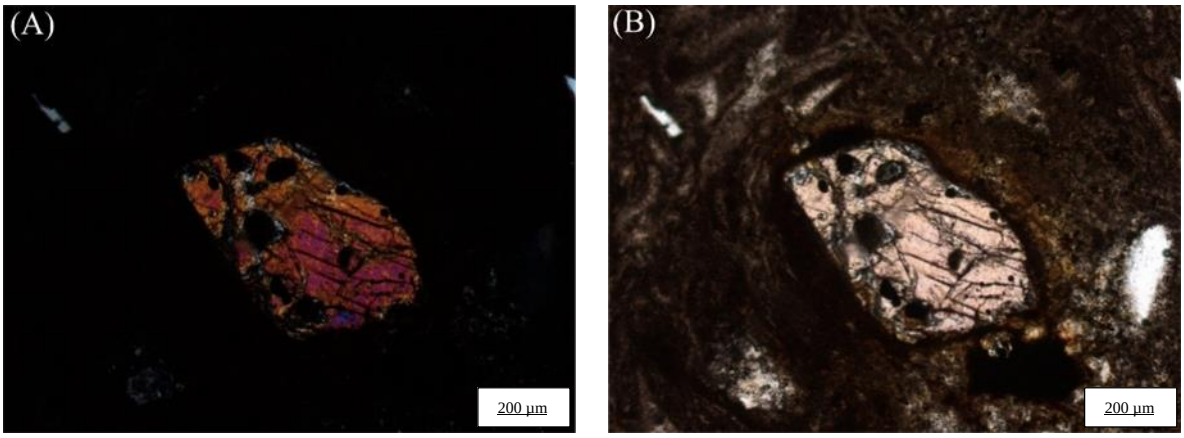


**Figure 3.2:** Orthopyroxene (OPX) crystal observed under the petrographic microscope (A) showing a low birefringence when examined under XPL, and (B) displaying pale colours of light pink, under PPL.

### 3.3.1.3 Pumice

In hand specimen pumice clasts comprise up to 40% of the bulk rock while lithics comprise up to 7%, and the matrix, up to 53 %. When observed in thin section, these clasts are preserved either as thin, wispy lenticular forms, or as highly compact fiamme. These clasts are phenocryst-poor and non-vesicular in texture (therefore they are not by definition of pumice anymore, however are referred to here as pumice to distinguish them from lithics and matrix), and instead exhibit a crypto-to microcrystalline groundmass comprised of aggregates of small (<0.5 mm) quartz crystals (Figure 3.3).

The pumice groundmass observed here varies in texture from (a) spherulitic in which quartz aggregates appear fibrous, or needle-like in form, and radiate away from a single point (Figure 3.3 C,D) to (b) axiolitic where needle-like crystals are observed radiating away from a centre seem, rather than from a single point (figure 3.3 A,B).

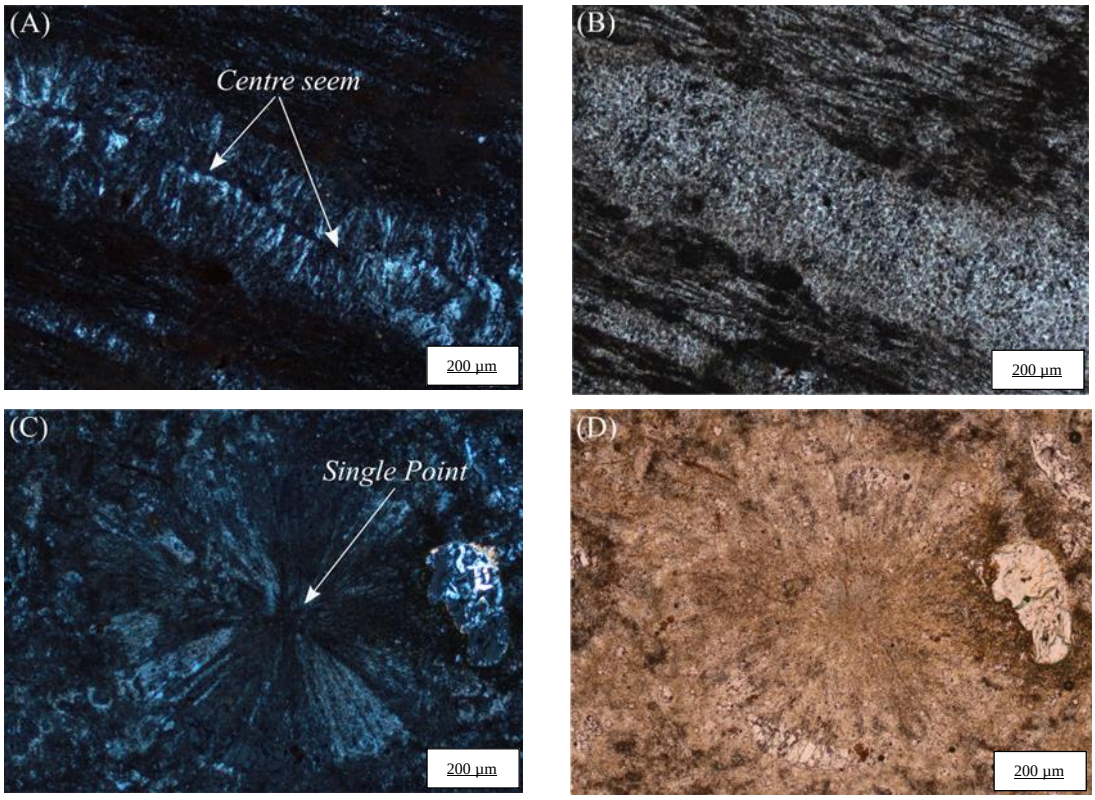


**Figure 3.3:** Pumice groundmass textures observed under the petrographic microscope. (A) Axiollitic pumice texture observed under XPL, and (B) under PPL. Notice the needle-like crystals radiating away from the central plane. (C) Spherulitic pumice showing the needle-like crystals radiating away from a single point under XPL, and (D) under PPL.

#### 3.3.1.4 Lithics

Lithics within the Ngaroma Ignimbrite include, in order of most to least frequent, greywacke and argillite, rhyolite and andesite, and in extremely rare occurrences of gabbro (Figures 3.4-3.6). When observed under the petrographic microscope, these clasts have an average size of 0.9 mm (with a maximum of 6 mm, observed in thin section, and a minimum of 0.2 mm). In hand specimen however, large lithics (up to 25 mm) are observed. They are typically sub-round to sub-angular in shape, and form $\leq$ 2% of the bulk rock.

*Greywacke*

Fragments of greywacke are the most commonly occurring lithic observed throughout the matrix of the Ngaroma Ignimbrite (Figure 3.4). These clasts are typically sub-angular to sub-rounded in shape, and can be recognised by their fine- grained sandstone texture, comprised of quartz, feldspar, and lithic fragments that are poorly sorted and angular to sub-angular in shape (Figure 3.4).

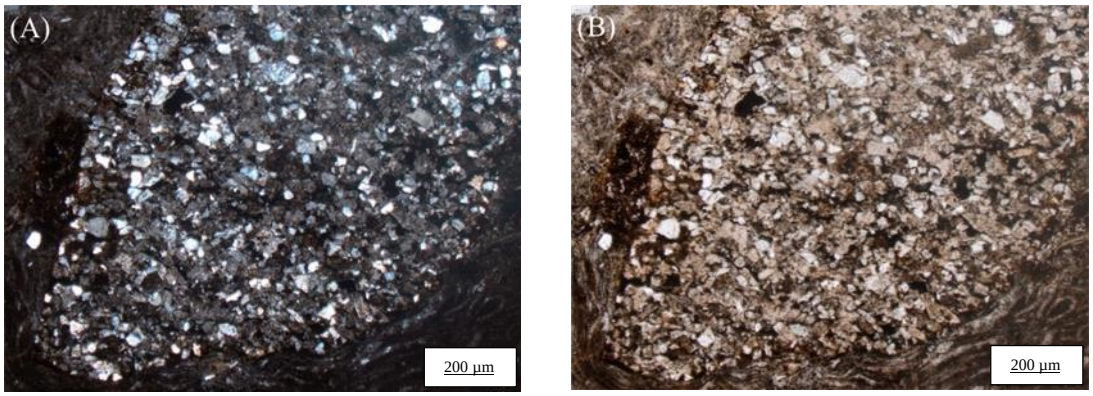


**Figure 3.4:** Greywacke lithic observed under the petrographic microscope (A) under XPL, and (B) under PPL. Notice the fine-grained, poorly sorted matrix.

*Argillite*

Argillite fragments are the second most commonly occurring lithic observed throughout the matrix of this deposit. They are characterised by their extremely fine grained, homogenous texture comprised of quartz and feldspar, followed by relatively large (up to 0.5 mm) lithics, which vary from sub-round to sub-angular in shape (Figure 3.5).

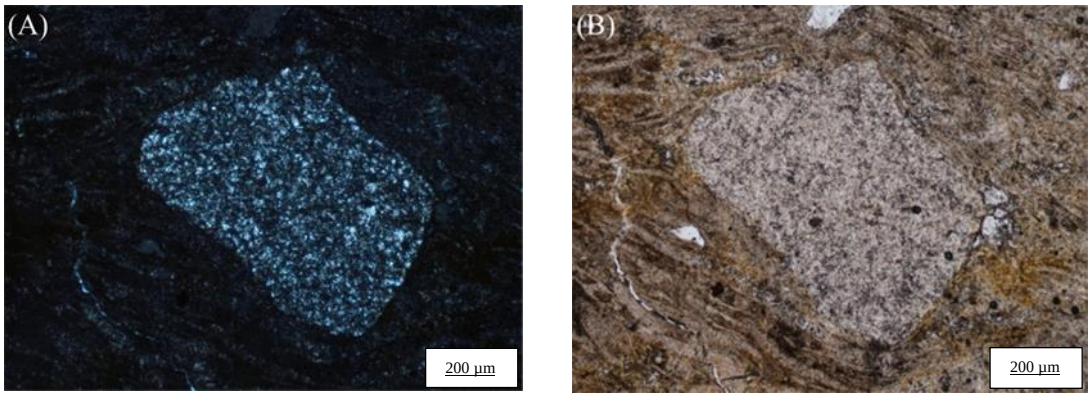


**Figure 3.5:** Argillite lithic observed under the petrographic microscope (A) under XPL, and (B) under PPL. Notice the fine-grained, homogenous texture(s).

*Andesite*

These fragments are rarely observed under the petrographic microscope (c.f. relative abundance in lapilli-sized fraction observed in hand sample/outcrop, see Chapter 2), however when visible, they can be recognised by their porphyritic texture with relatively coarse-grained phenocrysts (Figure 3.6). Crystals comprising the groundmass are discrete, and consist mostly of quartz, feldspar, and pyroxene. They are typically euhedral to subhedral in shape, and are commonly observed set within a fine-grained, cryptocrystalline groundmass (Figure 3.6).

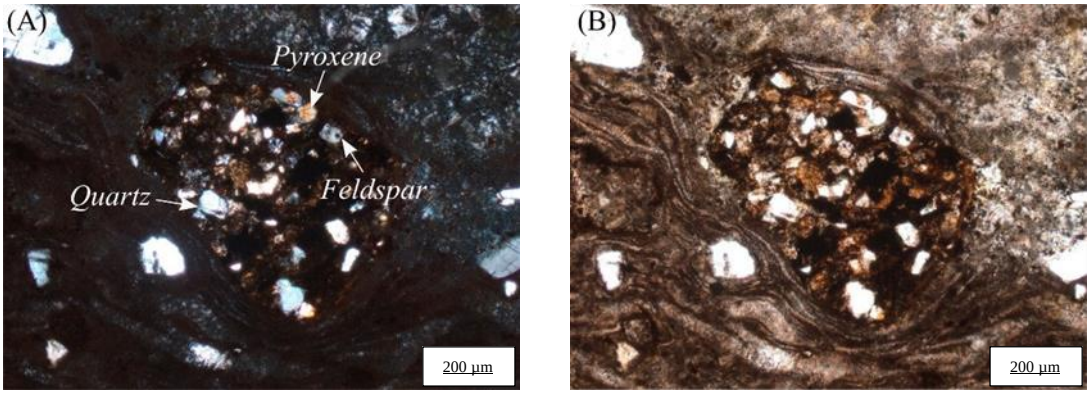


**Figure 3.6:** Andesite lithic observed under the petrographic microscope (A) under XPL, and (B) under PPL. Notice the relatively large crystals of quartz, feldspar (plagioclase), and pyroxene.

*Rhyolite*

Fragments of rhyolite are amongst the least commonly occurring lithic observed within the Ngaroma Ignimbrite. These clasts are recognised by their relatively fine-grained, crystalline groundmass of quartz and feldspar that, in extremely rare occurrences, appear recrystallised or spherulitic in texture.

*Gabbro*

These fragments are the least commonly occurring lithic. When visible however, they are most notable for their coarse-grained groundmass of feldspar, and pyroxene.

#### 3.3.1.5 Matrix

The Ngaroma Ignimbrite comprises a crystal and lithic poor, however comparatively pumice- and glass shard-rich matrix (N.B. crystals, pumice and

lithics are described above) that varies in texture from cryptocrystalline/homogeneous to eutaxitic with visible glass shards, and forms 80- 90% of the bulk rock (Figure 3.7). The fine-grained, cryptocrystalline matrix is optically unresolvable, however glass shards observed in eutaxitic matrices (Figure 3.7) are typically 300-800 µm in size and are thus petrographically described below.

The glass shards comprising the ignimbrite matrix appear well-formed, or cuspate in shape, and are significantly devitrified (Figure 3.7). These fragments exhibit original C and Y shapes, which are somewhat compact or deformed, and are observed wrapping around either feldspar crystals, or juvenile clasts. Under plane polarised light, the glass shards are light brown in colour, and when observed under cross-polarised light, they comprise a cryptocrystalline texture of quartz and feldspar microlites (Figure 3.7).

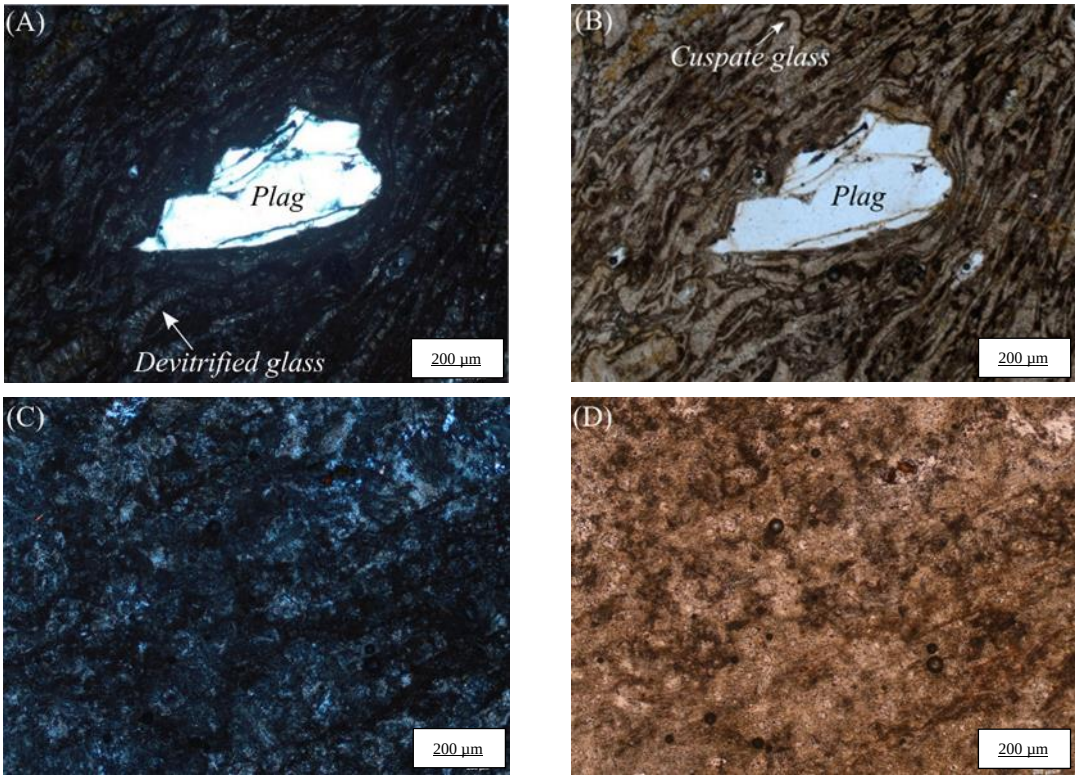


**Figure 3.7:** Primary textures comprising the Ngaroma Ignimbrite matrix observed under the petrographic microscope. (A) Glass shards observed under XPL, and (B) under PPL. Notice the glass is recrystallised, or devitrified in texture. Notice, also the original C and Y shapes which are somewhat deformed and wrapped around plagioclase. (C) Optically unresolvable, fine-grained matrix observed under XPL, and (D) under PPL.

## 3.4 SEM imaging and associated EDS analyses

The polished thin sections examined under the SEM exhibit overall, an ultra-fine-grained, nearly amorphous texture, and near-absence of primary glass shards. The glass shards, when visible, are typically 300-800 µm in size, appear well-formed or cuspate in shape, and comprise a silica-rich crystalline groundmass in which poorly formed crystallites of quartz and cristobalite, form a "feathery-like" (or devitrified) surface (Figure 3.8).

The ultra-fine grained, or otherwise optically unresolvable medium, however, under high magnification, reveals a silicate-rich texture that comprises two forms of crystalline material (Figure 3.8). The two mineral phases of which, were confirmed by EDS analyses (Figure 3.9) and XRD (presented in Section 3.5), to be a mixture of micron-sized crystals of K-feldspar (sanidine), intermixed with intergrown sub-micron-sized crystals of cristobalite (± trydimite) (Figures 3.10 and 3.11).

Crystals of K-feldspar (sanidine) are typically <5 µm in size and somewhat compact, and blocky in form. These crystals are typically associated with the light grey colour observed on polished surfaces under backscattered SEM images (Figure 3.9), while the interstitial cristobalite (± trydimite), which is acicular in form under higher magnifications, corresponds to dark grey surface areas which appear patchy, or devitrified (Figure 3.8).

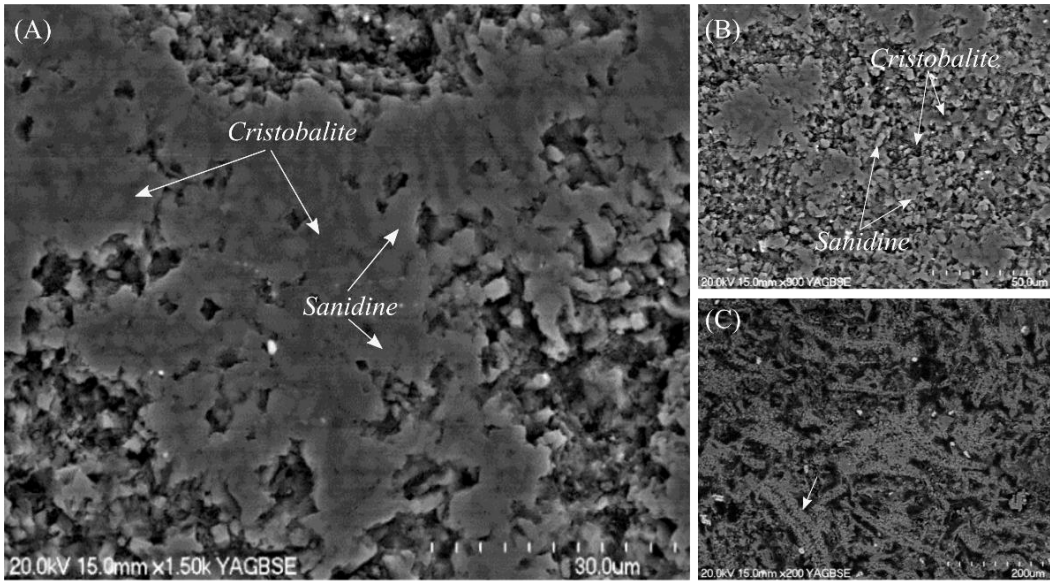


**Figure 3.8:** Polished thin sections observed under the SEM using backscattered electron imaging (BSE). (A) Polished surface showing the two mineral phases, distinguished by light (sanidine) and dark grey (cristobalite) colours. (B) The overall distribution of sanidine and cristobalite crystals. (C) Glass shards showing microcrystals of quartz and feldspar comprising the glass shard groundmass.

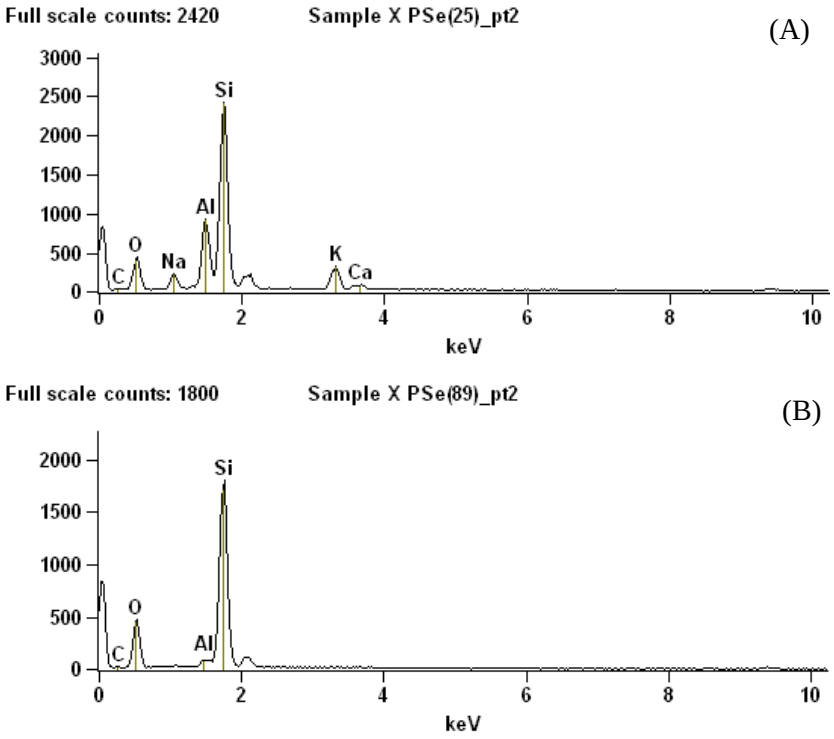


**Figure 3.9:** EDS analysis spectra of ignimbrite matrix showing the two mineral phases: (A) mineralogical composition of K-feldspar (sanidine) and (B) of cristobalite.

SEM imagery of rough chips representative of both matrix and pumice reveal in detail the surface morphology and crystal habit of the two mineral phases identified. Crystals of K-feldspar appear platy in form and euhedral in shape, and show a smooth surface with 'fish-scale' cracking (Horwell et al., 2013) that is occasionally overprinted by finer-grained precipitates of secondary minerals, presumed to be of clay (Figure 3.10). Likewise, crystals of cristobalite are observed growing either within the interconnected pore spaces between K-feldspar, or appear to blanket the smooth surface of these well-formed crystals (Figure 3.10). Patches of cristobalite that blanket the K-feldspar are botryoidal in form (Figure 3.10) and are comprised of sub-micron-sized cristobalite aggregates (Figures 3.10 and 3.11). Cristobalite crystals infilling pore spaces occur as subparallel intergrowths (Figure 3.11) which appear to penetrate away from the vug walls where they join the surrounding crystals of K-feldspar and in part form the ultra-fine-grained, homogenous matrix of the Ngaroma Ignimbrite.

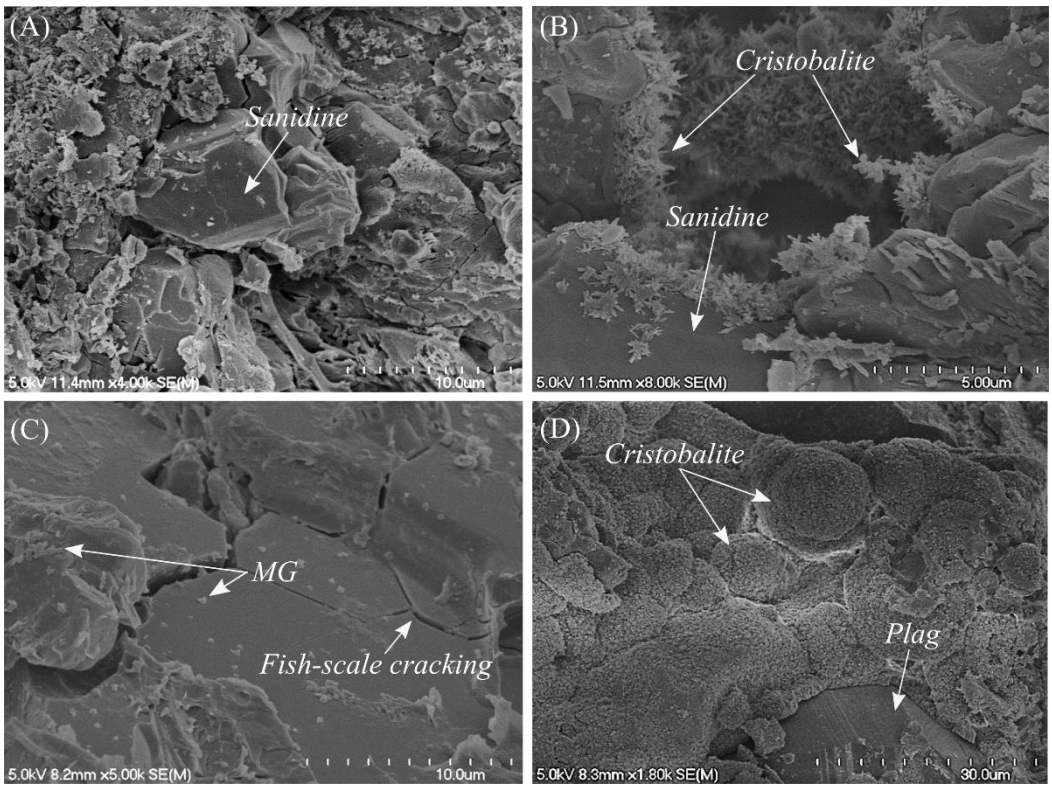


**Figure 3.10:** Morphology of crystal aggregates in rough chips examined under SEM (A) Crystal(s) of sanidine. (B) The occurrence of sanidine and cristobalite crystal aggregates. Notice the cristobalite aggregates growing within and above the smoothed-surface sanidine. (C) Sanidine crystal face showing fish-scale cracking and the occurence of secondary mineral growth (MG). (D) Cristobalite aggregates, botryoidal in form.

Two morphological forms of cristobalite have been recognised within the matrix of the Ngaroma Ignimbrite: platy and prismatic (Figure 3.11).

*Platy Cristobalite*

In polished thin section, platy cristobalite is commonly associated with the open pore spaces between the relatively larger crystals of K-feldspar (sanidine) (Figure 3.9). When examined in rough chips, these crystals are observed growing either alongside, or within the vug walls, and interconnected pore spaces of the surrounding crystals of K-feldspar (Figure 3.10). These plates are typically 40-50 µm in size and hexagonal in form (Figure 3.11).

*Prismatic Cristobalite*

In rough chips, these crystals are typically 0.6 µm in size and appear elongated and prismatic in form (Figure 3.11). They occur as intergrown, subparallel crystals which either protrude away from the smooth surfaces of vug walls and

interconnected pore spaces, or form directly above the surface of K-feldspar crystals (Figures 3.10 and 3.11). In polished thin section, these crystals appear acicular in form, and contrary to the platy cristobalite, are associated with the patchy, or devitrified matrix (Figure 3.8).

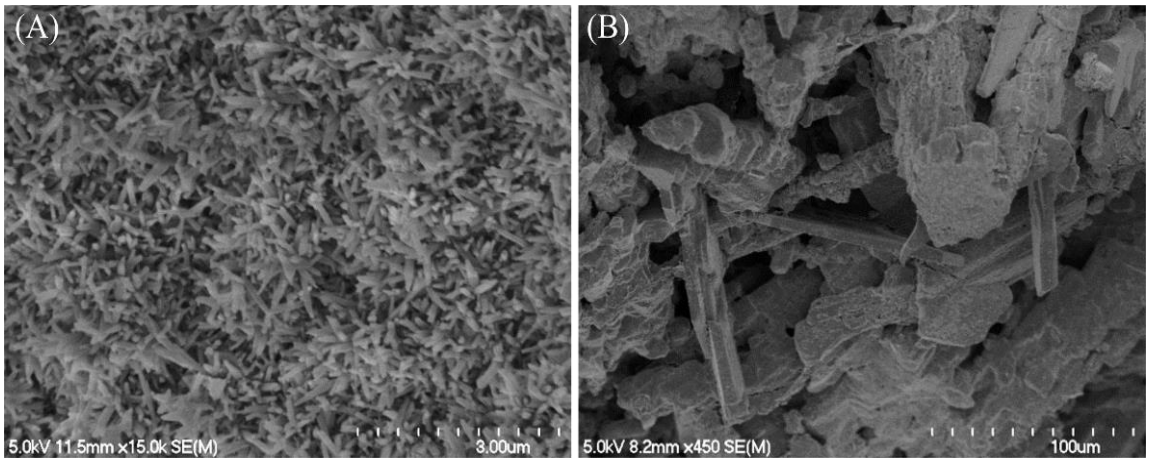


**Figure 3.11:** Morphologies of cristobalite crystals in rough chips examined under the SEM: (A) prismatic cristobalite, and (B) platy cristobalite.

## 3.5 XRD Analyses

The fourteen samples analysed by XRD display diffraction patterns that together suggest a strong presence of cristobalite and sanidine, followed by tridymite and kaolinite (Appendix VII). Additional minerals, including the presence of hematite and ferromagnesian pyroxene, were also recorded, however these diffraction patterns are unique. The XRD analyses were targeted for each of the observed and previously described subfacies types and represent samples from different field localities and heights within the stratigraphic logs (Figures 2.10-2.12).

### 3.5.1 XRD Analyses of Subfacies GrWm

The GrWm subfacies records intense peaks at [Å]: 4.0370, [Å]: 3.1841, and [Å]: 2.8824 (Figure 3.12) which suggest a strong presence of cristobalite. Sanidine was also recorded, and is represented by the intense peaks at [Å]: 3.8637, [Å]: 3.1841, and [Å]: 1.7893. Lastly, the intense peak recorded at [Å]: 7.3693 is characteristic of kaolinite.

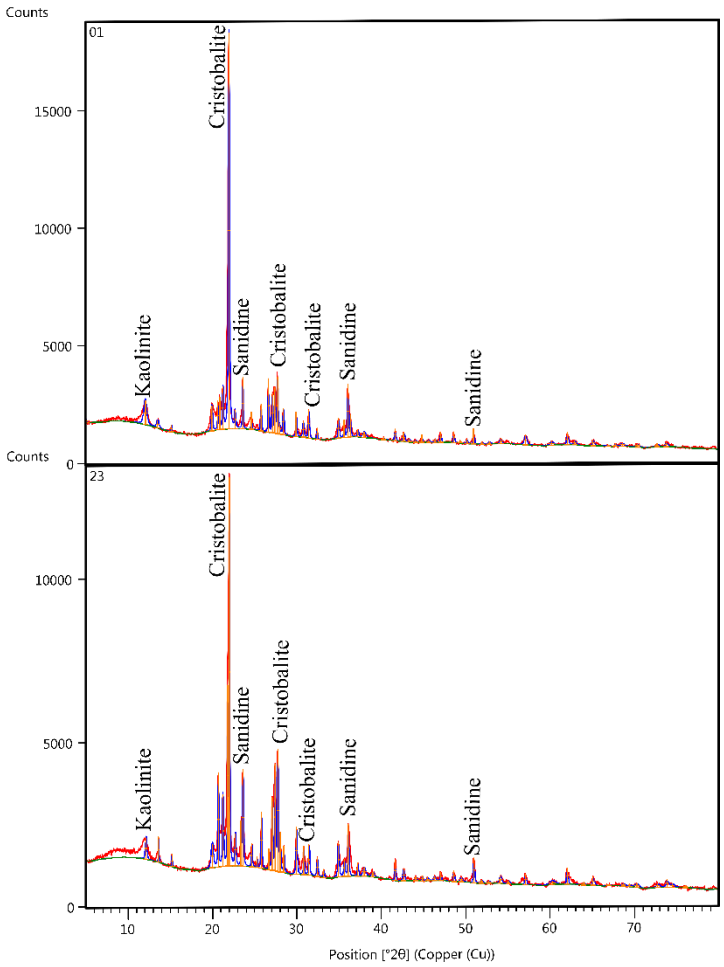


**Figure 3.12:** Diffraction patterns showing the presence of sanidine and cristobalite, and to a lesser extent, of kaolinite recorded in samples 01 and 23 in subfacies GrWm.

### 3.5.2 XRD Analyses of Subfacies PiWd

Similar to subfacies GrWm, subfacies PiWd display intense peaks that also suggest a strong presence of cristobalite and sanidine (Figure 3.13). For example, intense peaks at [Å]: 4.0370, [Å]: 2.8824, and [Å]: 2.4927 (Figure 3.14) are characteristic of cristobalite, while intense peaks occurring at [Å]: 6.3207, [Å]: 3.2997, and [Å]: 1.7893 characterise the presence of sanidine. There is a strong presence of tridymite recorded in the PiWd subfacies. It is characterised by the intense peaks occurring at [Å]: 4.2670, and [Å]:3.7635 (Figure 3.13).

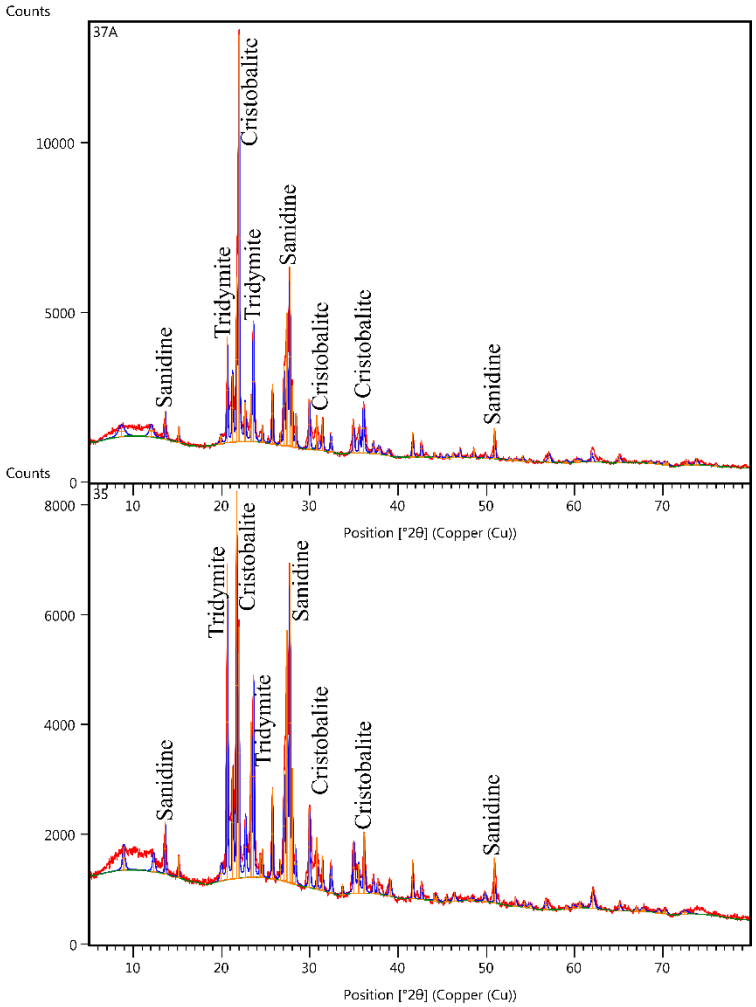


**Figure 3.13:** Diffraction patterns showing the presence of sanidine and cristobalite, followed by tridymite in samples 37A and 35 of subfacies PiWd.

### 3.5.3 XRD Analyses of Subfacies PiV

Subfacies PiV records a strong presence of cristobalite (± tridymite) and sanidine followed by intense peaks of hematite, and ferromagnesian pyroxene (Figure 3.15). In particular, the intense peaks occurring at [Å]: 6.3207, [Å]: 3.2997, and [Å]: 1.7893 (Figure 3.14) suggest a strong presence of sanidine, while the presence of cristobalite (± tridymite) is represented by intense peaks which occur at [Å]:4.0370, [Å]: 2.3039 and [Å]: 2.3076 (Figure 3.14).

The presence of hematite recorded in subfacies PiV can be characterised by the intense peaks recorded at [Å]: 2.4927, and [Å]: 2.7122 (Figure 3.14). Likewise, the presence of ferromagnesian pyroxene may be represented by intense peaks which occur at [Å]: 2.8824, and [Å]: 2.5616 (Figure 3.14).

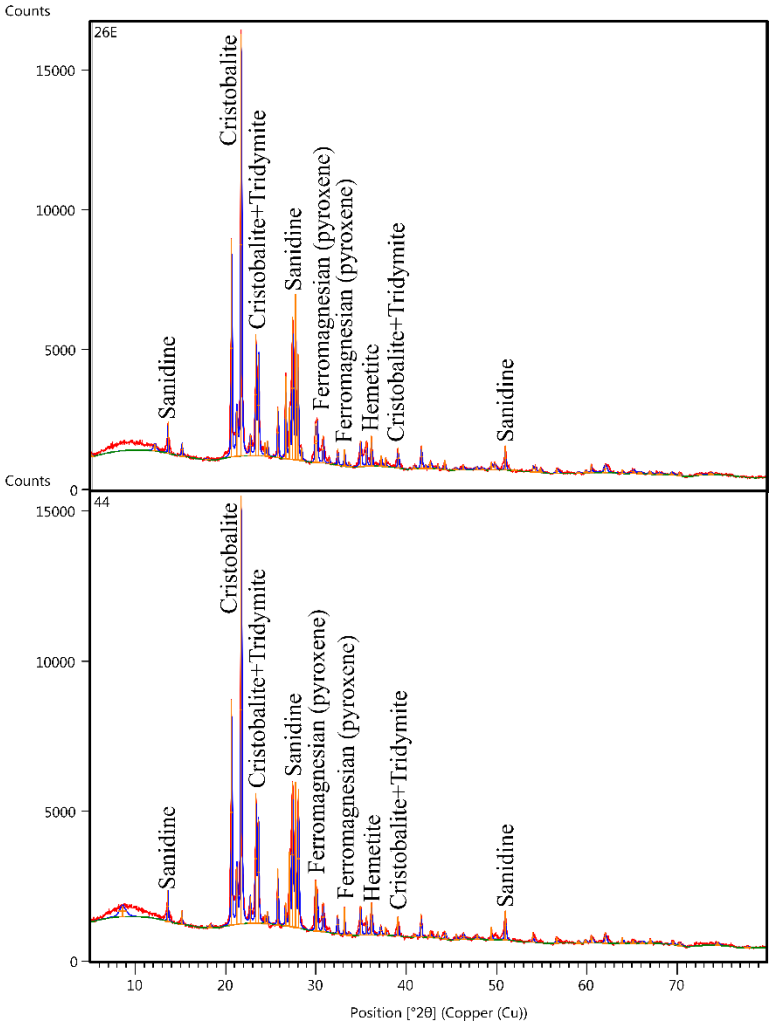


**Figure 3.14:** Diffraction patterns in samples 26E and 44 of subfacies PiV recorded by XRD analyses (A) diffraction patterns showing a strong presence of sanidine and cristobalite (±tridymite) followed by ferromagnesian and hematite (B) diffraction patterns of sanidine, cristobalite (± tridymite), and hematite.

### 3.5.4 XRD Analyses of Subfacies BrV

The BrV subfacies record a strong presence of cristobalite occurring at [Å]: 4.0370, [Å]: 3.1841, and [Å]: 2.492 (Figure 3.15). Sanidine is also present and is associated with intense peaks at [Å]: 6.3207, [Å]: 3.2997, and [Å]: 1.7893 (Figure 3.15). Lastly, the intense peak occurring at [Å]: 7.3693 suggests the presence of kaolinite.

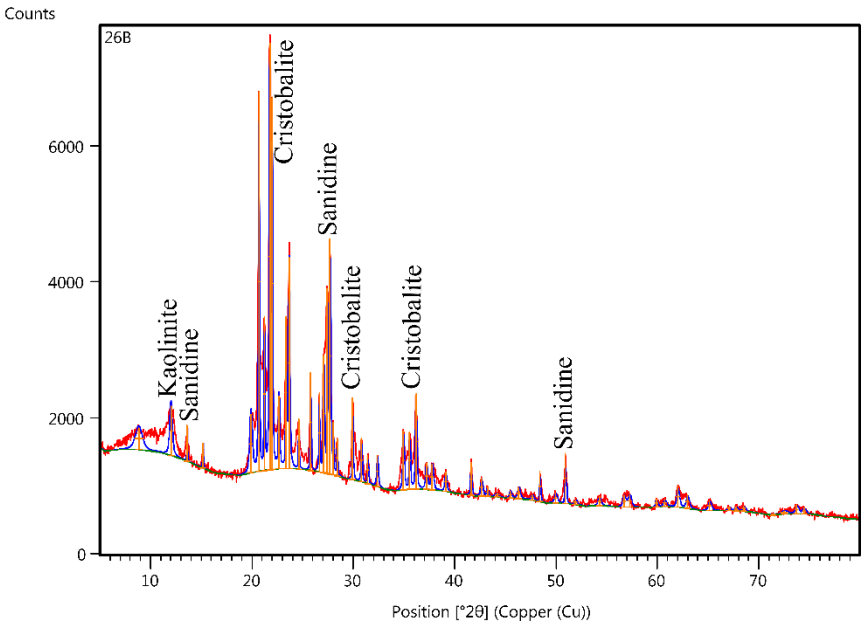


**Figure 3.15:** Diffraction patterns showing the presence of sanidine and cristobalite recorded in sample 26B of subfacies BrV. The presence of kaolinite is also recorded here.

### 3.5.5 XRD Analyses of clay separates

The precipitating minerals observed growing above the smooth surfaces of the K-feldspar crystals (Figure 3.10), could explain the intense peaks occurring at [Å]: 7.3693 (Figures 3.12 and 3.15) which suggests there to be a strong presence of kaolinite. Due to the infrequent occurrence of this mineral however, clay separates were subsequently analysed by XRD which confirmed the suggested clay minerals to be of kaolinite (Figure 3.16).

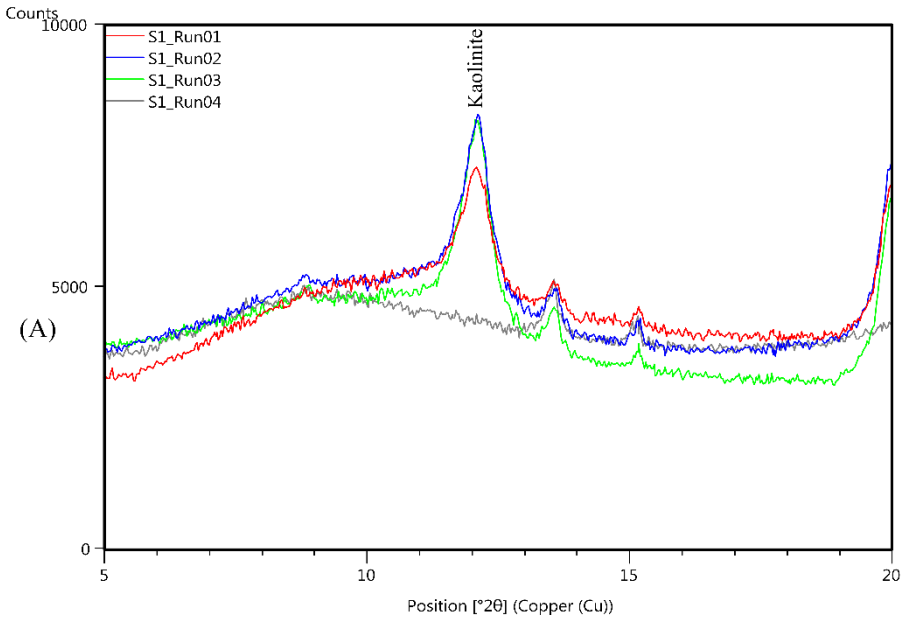


**Figure 3.16:** Diffraction patterns of clay separates confirming the presence of kaolinite. Notice the different colours that correspond to each of the four runs.

### 3.5.6 Summary of XRD Analyses

The selected samples analysed by XRD show similar diffraction patterns which demonstrate a strong presence of K-feldspar and cristobalite (± tridymite), followed by kaolinite, and in extremely rare occasions, of ferromagnesian pyroxene (Figure 3.14).

The two silica polymorphs (cristobalite ± tridymite) recorded here, reflect various intensities of vapour-phase alteration and devitrification processes that, based on texture, colour, and changes in primary componentry, are observed both macroscopically and petrographically. Moreover, the strong XRD peaks for cristobalite (± tridymite) and sanidine (Figures 3.12-3.15) may be associated with the crystals of K-feldspar and nano-scale crystals of cristobalite (± tridymite) observed previously in SEM and EDS analyses, where both minerals comprise the ultra-fine-grained, homogenous matrix of the Ngaroma Ignimbrite (Figure 3.8).

# Chapter Four

# Geochemistry

## 4.1 Introduction

This chapter will discuss the bulk rock and mineral geochemical compositions of the Ngaroma Ignimbrite. Major and trace elements of bulk rock and pumice were acquired by x-ray fluorescence (XRF) spectrometry while additional trace element analyses of selective pumice were obtained using laser ablation inductively coupled plasma mass spectrometry (LA-ICPMS). Both bulk rock ignimbrite samples and pumice however, have been pervasively devitrified and vapour-phase altered, therefore the chemical compositions of these samples will reflect a combination of primary magmatic and secondary compositions. Mineral compositions of major elements for phenocrysts were measured by electron probe microanalysis (EPMA). The minerals analysed include both primary (plagioclase, orthopyroxene and Fe-Ti oxides) and secondary minerals (sanidine and quartz). Findings from the bulk rock analyses are presented in a series of Harker variation diagrams to assess the compositional changes related to post alteration processes while total alkali versus silica (TAS) and Winchester and Floyd (1977) diagrams are used as a rock classification tool. Multielement diagrams are also presented in this chapter to provide insight into magmatic processes and the effects of alteration. Ternary diagrams are used to determine the compositions of crystalline phases.

## 4.2 Methods

### 4.2.1 X-ray fluorescence (XRF) spectrometry

Fourteen samples of Ngaroma Ignimbrite and three samples of Ngaroma pumice were used to analyse the geochemical compositions of both major (bulk ignimbrite and pumice) and trace (bulk ignimbrite only, see Section 4.2.2 for pumice) elements (Appendix IV). Of the fourteen ignimbrite samples analysed however, twelve ignimbrite samples and two pumice samples are presented in this chapter, as the remaining samples showed either low $SiO_2$ concentrations or high totals. The samples selected showed minimal signs of weathering and bulk ignimbrite samples

were chosen to avoid the presence of large lithics which allowed for a better representation of the juvenile rock composition.

The elemental abundances of each selected sample was measured using the Bruker S8 Tiger XRF machine at the School of Science, University of Waikato. Prior to being analysed by XRF, the samples were crushed into a fine powder using a tungsten-carbide ring-mill (following the techniques required for XRD preparation) and once crushed, made into pressed pellets for trace element analysis, and fused glass discs for major element analysis.

The fused glass disks were prepared by mixing approximately 0.8 g of powdered sample with 8.0 g of 12:22 flux (Li-tetraborate 35%, Li-metaborate 64.7%) combined with NH4I. Once mixed properly, individual samples within a Pt/Au crucible were heated in a furnace at a set temperature of 1050° C for 20 minutes. Molten rock produced from this step was subsequently poured onto a mold and fan cooled. The loss of ignition (LOI) was attained by calculating the difference in weight by heating two grams of each sample at 1100°C for one hour.

Pressed powder pellets were also prepared for trace element analyses. Preparation of these pellets required combining approximately 7 to 8 g of powdered rock with 20 drops of PVA binder. Using a hydraulic press, the samples were subsequently pressed into an aluminum cap and once bound, heated at 70°C overnight to allow for the binder to evaporate off.

### 4.2.2 LA-ICP-MS

Trace element analyses of pumice by LA-ICP-MS were acquired using a RESOlution-SE Compact 193 nm excimer laser ablation (LA) system in tandem with an Agilent 8900 inductively coupled plasma – mass spectrometer (ICP-MS) at the School of Science, University of Waikato (Appendix V). Analyses of each sample required pulsing the laser at 10 Hz with a 100 µm spot size and energy density of 5.0 J/cm2 with an ablation time of 45 s. The analyses required ultra-high purity helium to be used as a carrier gas (370 mL/min) which transferred the ablated sample from the LA system into the ICP-MS. The ICP-MS was optimised to maximum sensitivity daily (Table 4.1). Gas background counts were measured with

the laser off and collected between each individual sample for 30 seconds. NIST (National Institute of Standards and Technology) glass standards of 610 and 612 were analysed after every 10 samples to account for any instrument drift. Once the glass standards were analysed, data processing was subsequently performed using Iolite (v3.32; Paton et al. 2011). The obtained background counts were then subtracted from the raw data. All data acquired from these analyses were standardised to NIST 612 glass, while the NIST 610 glass was utilised here as a secondary standard (Jochum et al., 2005).

**Table 4.1:** ICP-MS Operating Conditions

| **ICP-MS Conditions** | |
|---|---|
| Forward (reflected) power (watt) | 1550 |
| Gas flows (L/min): | |
| Plasma | 15 (Ar) |
| Auxiliary | 0.90 |
| Carrier (Nebulizer) | 1.00 |
| Sampling Depth (mm) | 4.0 |
| Detector mode | Pulse counting |
| Sweep mode | Peak hopping |
| Dwell time (s) | 0.01 - 0.1 |
| Points per peak | 1 |

### 4.2.3 Electron probe microanalyses (EPMA)

Mineral compositions of major elements in the Ngaroma Ignimbrite were acquired by electron probe microanalysis (EPMA) using the JEOL JXA-8230 at Victoria University of Wellington (VUW) (Appendix VI). The major elements analysed within phenocrysts and secondary matrix minerals were determined using an accelerating voltage of 15 kV, current of 12 nA, peak/background count times of 30 s/15 s, and a focused beam which was standardised against plagioclase (NMNH 115900), Kakanui augite (USNM 122142), and synthetic oxides (Jarosewich et al. 1980).

## 4.3 Rock Classification

The geochemical composition of the Ngaroma Ignimbrite, both bulk rock and pumice (Table 4.2), has been classified using the total alkali versus silica (TAS) diagram of Le Maitre et al., (2002) which suggests the ignimbrite varies in composition from dacite to rhyolite, with affinity for rhyolite (Figure 4.1). Samples which are dacitic in composition vary from 68-70 wt. % $SiO_2$ while rhyolites range from 70-72 wt. % $SiO_2$ (Figure 4.1).

**Table 4.2:** Bulk rock geochemical compositions of ignimbrite and pumice samples[1] acquired by X-ray fluorescence (XRF) spectrometry and where specified[2] by LA-ICP-MS.

| Sample | 1 | 26B | 26C | 26E | 26E(P) | 30C | 35 | 37A | 37B | 44 | 44(P) | 48 | 51A |
|---|---|---|---|---|---|---|---|---|---|---|---|---|---|
| *Major elements (XRF, wt. %)* | | | | | | | | | | | | | |
| *(normalized to 100%, volatile free; Totals listed are of original values; with Fe expressed as $Fe_2O_3$)* | | | | | | | | | | | | | |
| $SiO_2$ | 69.54 | 69.76 | 70.84 | 70.77 | 72.21 | 70.41 | 71.54 | 72.32 | 71.82 | 69.90 | 72.39 | 68.18 | 72.34 |
| $TiO_2$ | 0.38 | 0.41 | 0.35 | 0.31 | 0.19 | 0.35 | 0.32 | 0.26 | 0.23 | 0.37 | 0.21 | 0.50 | 0.26 |
| $Al_2O_3$ | 20.38 | 18.91 | 16.19 | 16.00 | 15.07 | 16.22 | 15.32 | 15.55 | 14.61 | 17.04 | 15.00 | 19.67 | 14.89 |
| $Fe_2O_3$ | 4.76 | 4.65 | 3.92 | 3.72 | 2.76 | 4.14 | 3.44 | 3.02 | 3.84 | 4.16 | 2.73 | 5.75 | 3.22 |
| MnO | 0.03 | 0.13 | 0.16 | 0.05 | 0.06 | 0.06 | 0.19 | 0.06 | 0.17 | 0.08 | 0.04 | 0.09 | 0.02 |
| MgO | 0.22 | 0.19 | 0.14 | 0.18 | 0.15 | 0.31 | 0.20 | 0.15 | 0.14 | 0.46 | 0.12 | 0.12 | 0.14 |
| CaO | 0.25 | 0.46 | 0.86 | 0.84 | 0.59 | 0.72 | 0.91 | 0.70 | 0.87 | 0.60 | 0.79 | 0.50 | 0.93 |
| $Na_2O$ | 1.33 | 1.89 | 3.22 | 3.49 | 3.40 | 3.09 | 3.42 | 3.09 | 3.51 | 2.62 | 3.77 | 1.91 | 3.47 |
| $K_2O$ | 2.89 | 3.42 | 4.11 | 4.43 | 5.37 | 4.49 | 4.44 | 4.63 | 4.60 | 4.52 | 4.73 | 3.09 | 4.50 |
| $P_2O_5$ | 0.11 | 0.08 | 0.08 | 0.09 | 0.07 | 0.08 | 0.09 | 0.08 | 0.08 | 0.10 | 0.08 | 0.10 | 0.09 |
| LOI | 6.07 | 4.98 | 3.57 | 3.91 | 2.55 | 3.96 | 2.46 | 2.34 | 1.83 | 5.72 | 2.14 | 5.71 | 2.03 |
| Total | 100.622 | 100.966 | 101.041 | 101.055 | 100.34 | 100.837 | 100.939 | 100.779 | 100.776 | 100.99 | 100.59 | 100.8 | 101.071 |
| | | | | | | | | | | | | | |
| *Trace elements (XRF, ppm)* | | | | | | | | | | | | | |
| Sample | 1 | 26B | 26C | 26E | 26E(P) | 30C | 35 | 37A | 37B | 44 | 44(P) | 48 | 51A |
| F | 296 | 400 | 148 | 59 | - | 52 | 483 | 194 | 179 | 252 | - | 180 | 359 |
| S | 18 | 10 | 70 | 168 | - | 146 | - | - | - | 190 | - | 76 | - |
| Cl | 167 | 171 | 394 | 353 | - | 110 | 365 | 332 | 255 | 154 | - | 166 | 471 |
| Sc | 10 | 14 | 12 | 9 | 8.45 | 9 | 9 | 9 | 9 | 11 | 7.72 | 15 | 10 |
| V | 28 | 22 | 22 | 19 | 21.71 | 16 | 22 | 14 | 17 | 14 | 25.42 | 26 | 17 |
| Co | 9 | 11 | 11 | 8 | 19.16 | 10 | 15 | 21 | 12 | 9 | 12.21 | 13 | 12 |
| Ni | - | - | - | - | 11.74 | - | - | - | - | - | 18.8 | - | - |
| Cu | 21 | 8 | 12 | 12 | 12.49 | 11 | 8 | 8 | 5 | 12 | 10.83 | 7 | 8 |
| Zn | 68 | 60 | 61 | 57 | - | 46 | 77 | 61 | 85 | 43 | - | 85 | 68 |
| Ga | 20 | 22 | 19 | 18 | 15.54 | 20 | 19 | 18 | 18 | 19 | 15.32 | 22 | 17 |
| As | 18 | 8 | 10 | 9 | - | 8 | 8 | 8 | 12 | 10 | - | 8 | 8 |
| Rb | 113 | 128 | 152 | 164 | 186.9 | 168 | 165 | 173 | 171 | 168 | 159.6 | 117 | 166 |
| Sr | 44 | 66 | 101 | 95 | 74.7 | 88 | 98 | 86 | 90 | 81 | 84.9 | 67 | 96 |
| Y | 61 | 10 | 17 | 10 | 12.68 | 12 | 20 | 15 | 15 | 11 | 12.44 | 9 | 34 |
| Zr | 332 | 295 | 301 | 308 | 270.4 | 337 | 296 | 309 | 289 | 332 | 270.5 | 289 | 284 |
| Nb | 12 | 10 | 10 | 10 | 12.37 | 11 | 11 | 11 | 11 | 11 | 9.79 | 10 | 11 |
| Sn | - | - | - | - | - | - | - | - | - | - | - | - | - |
| Ba | 940 | 672 | 868 | 815 | 928 | 800 | 1001 | 996 | 928 | 844 | 899 | 599 | 842 |
| La | 69 | - | 9 | 9 | 18.95 | 7 | 16 | 12 | 7 | 13 | 28.7 | - | 34 |
| Ce | 40 | 25 | 59 | 37 | 56.2 | 29 | 56 | 40 | 50 | 46 | 55.3 | 164 | 88 |
| Nd | 52 | 5 | 16 | 14 | 8.28 | 10 | 27 | 19 | 14 | 19 | 13.39 | 5 | 38 |
| Pb | 17 | 18 | 15 | 16 | 13.91 | 16 | 18 | 19 | 24 | 16 | 14.8 | 26 | 17 |
| Th | 25 | 21 | 18 | 18 | 15 | 24 | 22 | 23 | 22 | 21 | 16.02 | 19 | 22 |
| U | - | - | - | - | 3.85 | - | - | - | - | - | 3.8 | - | - |

[1] Samples 26E (P) and 44 (P) are analyses of pumice; or other samples of bulk ignimbrite.
[2] Trace element data for samples 26E (P) and 44 (P) were acquired by LA-ICP-MS on the same glass disks used for major elements by XRF; all other major and trace element data in table was acquired by XRF.

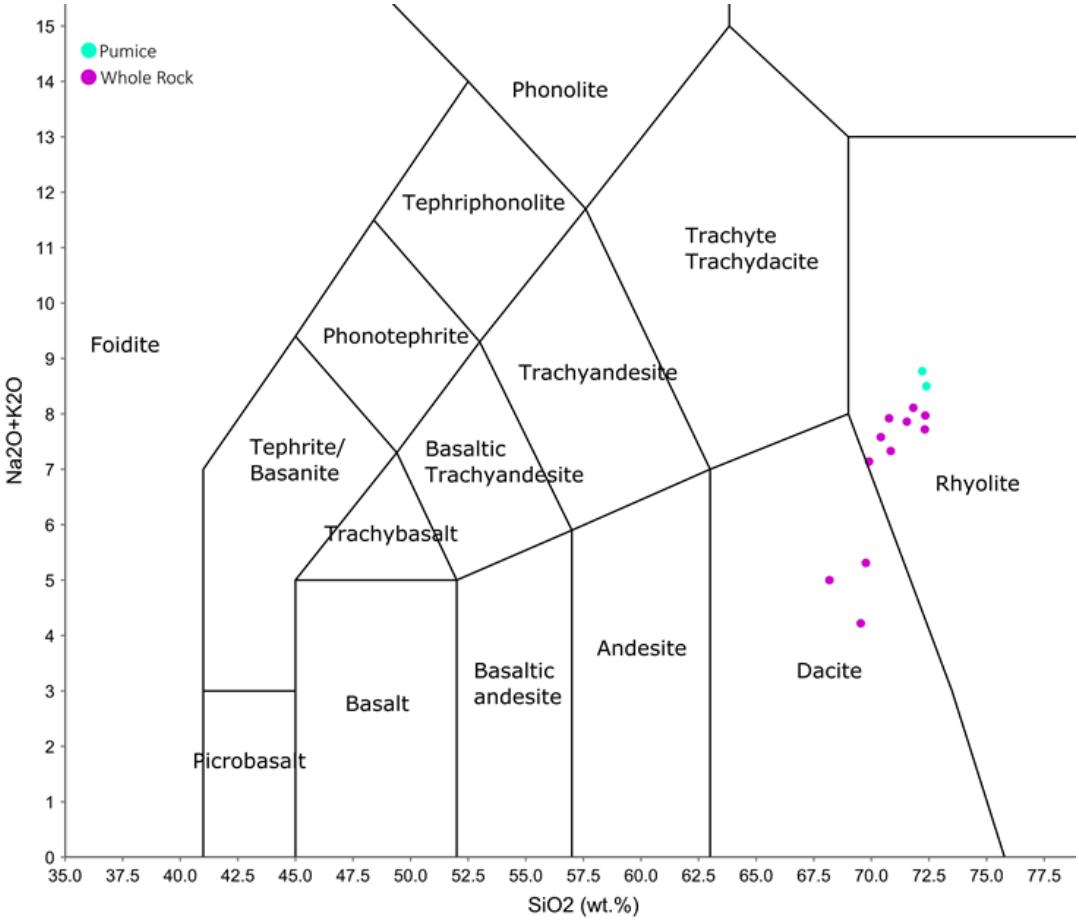


**Figure 4.1:** Total alkalis versus silica (TAS) diagram showing the geochemical classification of volcanic rocks. Provided by Le Maitre et al., (1989; currently recognised as Le Maitre et al., 2002).

As previously stated, the Ngaroma Ignimbrite is significantly devitrified and vapour- phase altered and the TAS classification diagram (Figure 4.1), which uses mobile elements $Na_2O$, $K_2O$, and $SiO_2$, is vulnerable to the effects of these post alteration processes and somewhat deceptive. The ignimbrite was thus further analysed using the volcanic rock classification diagram of Winchester and Floyd (1977) (Figure 4.2). This diagram uses selected immobile minor and trace elements (including $TiO_2$, Zr, Y, and Nb) to minimise the effects of post alteration processes, or secondary mineral compositions.

When examined using selective trace element ratios of $Zr/TiO_2$ and Nb/Y the Ngaroma Ignimbrite varies in composition from rhyodacite/dacite and rhyolite to comendite/pantellerite and trachyandesite (Figure 4.2). The samples however are concentrated within the trachyandesite and rhyolite fields, as only two samples plot

within the rhyodacite/dacite and one sample within the comendite/pantellerite fields (Figure 4.2).

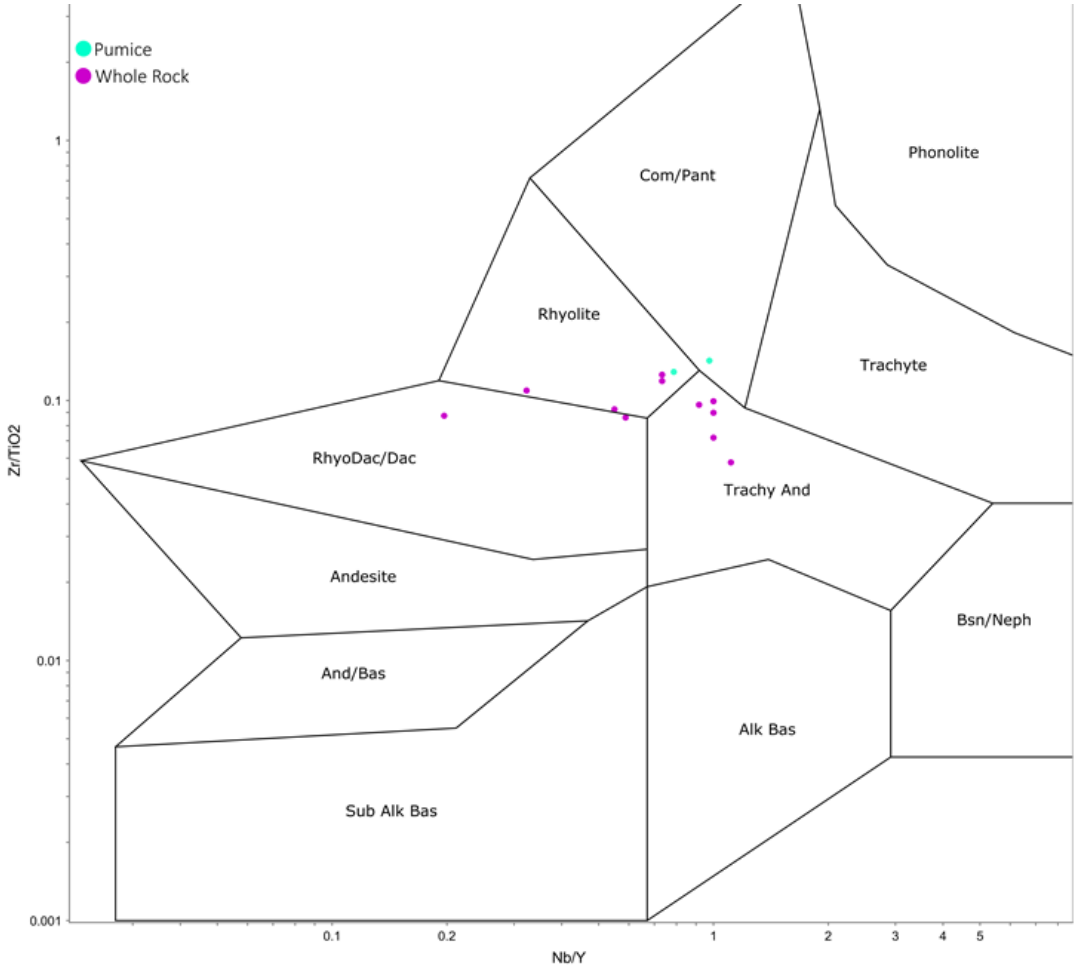


**Figure 4.2:** Volcanic rock classification diagram showing the geochemical composition of the Ngaroma Ignimbrite using selected trace elements (after Winchester and Floyd, 1977).

## 4.4 Major Element Trends associated with Pumice and Bulk Ignimbrite

Major element concentrations for both pumice and bulk rock concentrations are listed in Table 4.2. Harker variation diagrams are presented in Figure 4.3. The major elements presented here that show well-defined trends when plotted against $SiO_2$ include: $TiO_2$, $Al_2O_3$, $Fe_2O_3$, MgO, CaO, $Na_2O$, and $K_2O$ (Figure 4.3). The abundances of all major elements have been normalised to 100 % volatile free and range from 68 to 72 wt. %. Also plotted against $SiO_2$ are the original LOI values.

The abundances of CaO range between 0.24 and 0.93 wt. % while $Na_2O$ varies from 1.33 to 3.77 wt. % and $K_2O$ from 2.89 to 5.37 wt. % (Figure 4.3). The abundances

of $TiO_2$ varies from 0.19 to 0.5 wt. % while $Al_2O_3$ ranges between 14.61 and 20.38 wt. % (Figure 4.3). Similarly, the wt. % abundances of $Fe_2O_3$ and MgO are exceptionally low, as $Fe_2O_3$ varies between 2.73 and 5.75 wt. % while MgO ranges from 0.12 to 0.46 wt. %. Lastly, the LOI ranges between 1.83 and 6.07 wt. % (Figure 4.3).

There is a positive correlation between $SiO_2$ and CaO, $Na_2O$ and $K_2O$. Negative correlations are observed between $SiO_2$ and $Al_2O_3$, $TiO_2$, FeO, and LOI (Figure 4.3). Pumice from the Ngaroma Ignimbrite record high concentrations of $SiO_2$ (up to 72 wt. %) and are associated with relatively low concentrations of $TiO_2$, $Al_2O_3$, $Fe_2O_3$, MgO, and LOI, and relatively high concentrations of CaO, $Na_2O$, and $K_2O$ (Figure 4.3). Likewise, subfacies GrWm records high concentrations of $SiO_2$ (ranging between 71 and 72 wt. %), in association with low concentrations of $TiO_2$, $Al_2O_3$, $Fe_2O_3$, MgO, and LOI, and increasing concentrations of CaO, $Na_2O$, and $K_2O$. The PiV subfacies, similar to subfacies GrWm, is associated with decreasing, although comparably high concentrations of $TiO_2$, $Al_2O_3$, $Fe_2O_3$, MgO, and LOI, and increasing concentrations of CaO, $Na_2O$, and $K_2O$ (Figure 4.3).

In contrast, subfacies PiWd and BrV record relatively low concentrations of $SiO_2$ (ranging from 68 - 70 wt. %), in association with relatively high concentrations of $TiO_2$, $Al_2O_3$, $Fe_2O_3$, MgO, and LOI, and lower concentrations of CaO, $Na_2O$, and $K_2O$ (Figure 4.3).

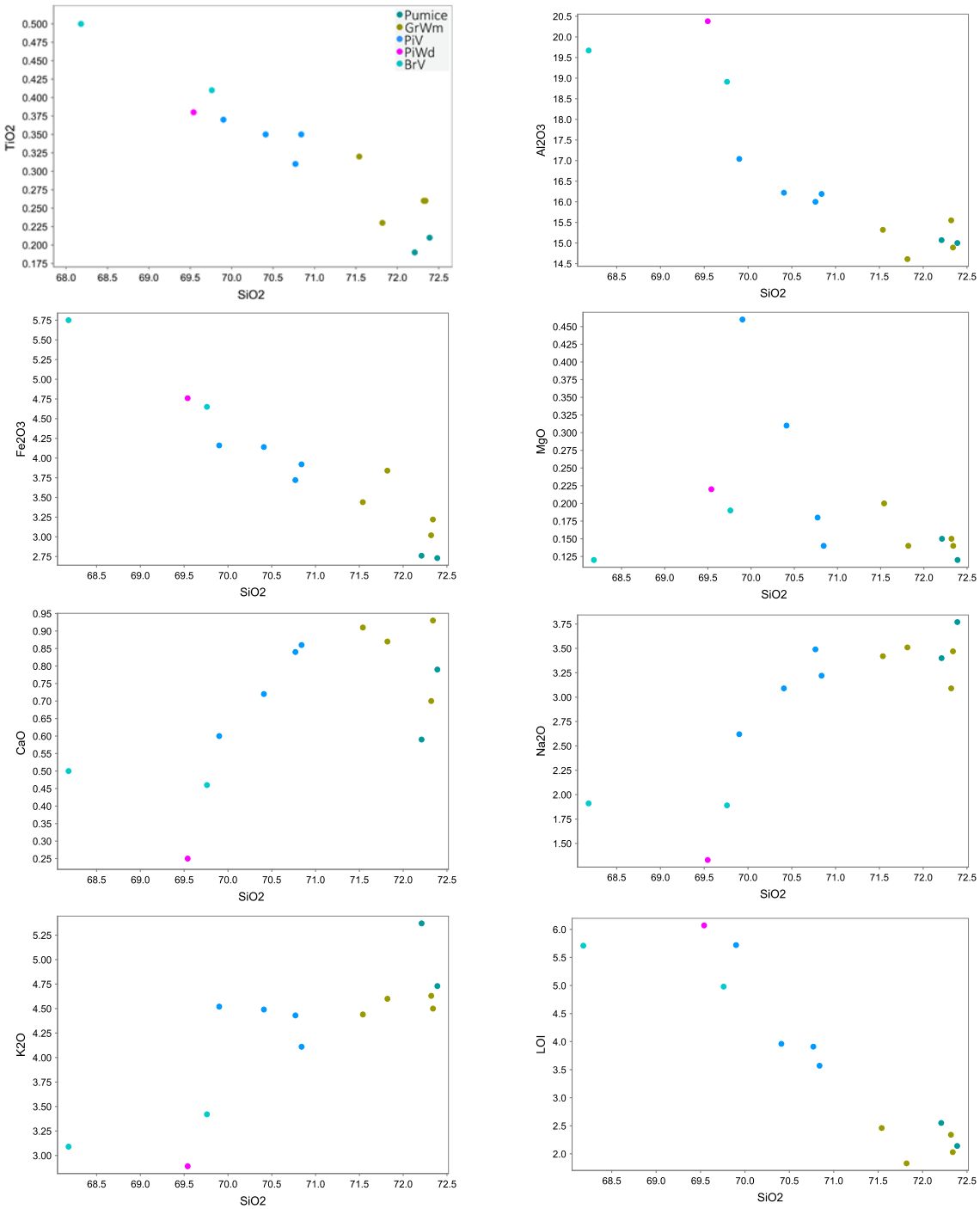


**Figure 4.3:** Harker variation diagrams showing trends of major element data against $SiO_2$ from XRF analyses of pumice and bulk rock. All Fe is expressed here as $Fe_2O_3$.

## 4.5 Trace Element Trends associated with Pumice and Bulk Ignimbrite

The trace element compositions for pumice and bulk rock are listed in Table 4.2. Trends in the concentrations of strontium (Sr), Neodymium (Nd), gallium (Ga), rubidium (Rb), yttrium (Y), zirconium (Zr), barium (Ba), and cerium (Ce) with respect to increasing $SiO_2$ are presented in Figure 4.4.

The variations in trace element abundances observed here are similar to those shown within the major elements, and display a mixture of various, well-defined trends (Figures 4.3 and 4.4). Elements that exhibit decreasing trends in concentration as $SiO_2$ concentrations increase include Ga, and Zr (Figure 4.4), whereas, Ba, Rb, Sr, Y, Ce, and Nd increase in concentration with increasing $SiO_2$ (Figure 4.4).

Relatively high Ba, Sr, Rb, Ce, and Nd with respect to high $SiO_2$, are typical of pumice from the ignimbrite which are also associated with relatively low concentrations of Ga, Y, and Zr (Figure 4.4). Likewise, subfacies GrWm has relatively high concentrations of Ba, Sr, Rb, Y, Ce, and Nd and low concentrations of Ga, and Zr. The PiV subfacies however, has comparably low, but increasing, concentrations of Ba, Sr, Rb, Y, Ce, and Nd, and conversely comparably high, but decreasing, concentrations of Ga, and Y (Figure 4.4).

The PiWd and BrV subfacies record high Ba, Ga, Y, and Zr concentrations, and low Rb, Sr, Ce, and Nd concentrations that coincide with low concentrations of $SiO_2$ (Figure 4.4). Similar to subfacies PiV (Figure 4.3), the comparably high concentrations of Ga, and Y observed in subfacies PiWd (Figure 4.4) show a decreasing trend.

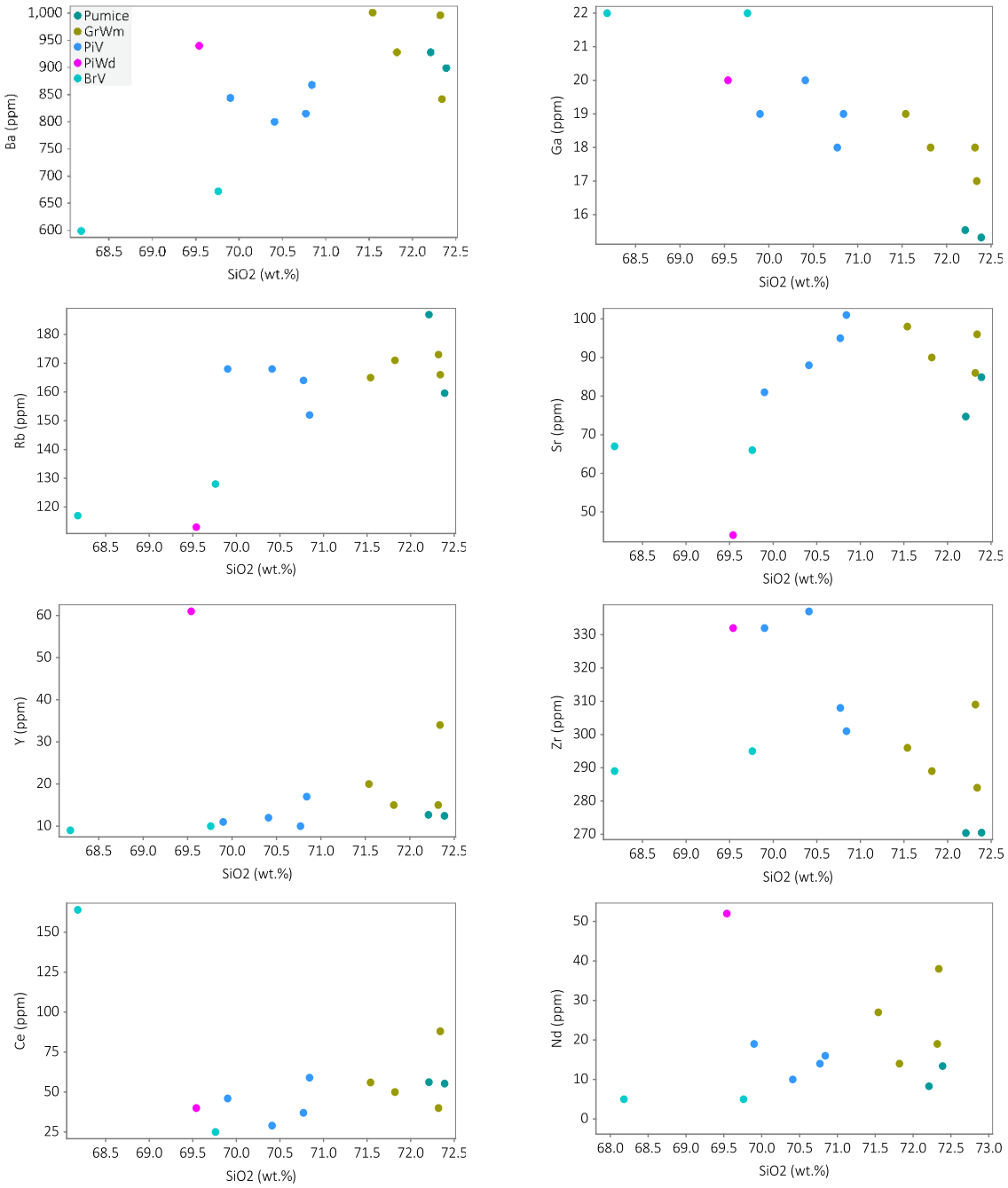


**Figure 4.4:** Harker variation diagrams showing trends of selected trace elements versus $SiO_2$.

Rare earth element (REE) abundances of selected pumice were plotted on the primitive mantle-normalised multielement diagram of Sun and McDonough (1989) (Figure 4.5). All pumice samples show similar trends which are enriched in light rare earth elements (LREE) and depleted in heavy rare earth elements (HREE) (Figure 4.5). There is a positive anomaly of Ce and Eu and a negative Sm anomaly recorded within each selected pumice (Figure 4.5). Trace elements Er, Yb, and Lu are also slightly enriched.

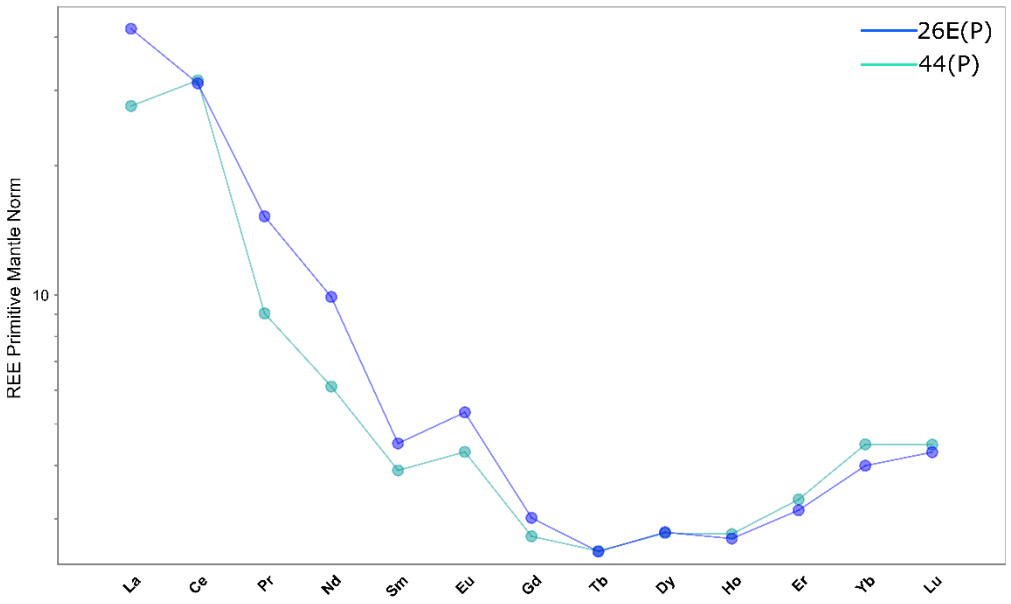


**Figure 4.5:** Primitive mantle-normalised multielement diagram showing the distribution of rare earth elements from the three pumice samples (Sun and McDonough, 1989).

Trace elements of the selected pumice were also analysed using the primordial mantle-normalised multielement diagram of Taylor and McLennan (1985). Similar to the patterns observed in Figure 4.5, the distribution of trace elements across the three pumice samples displayed in Figure 4.6 are nearly indistinguishable from one another and show trends which are generally enriched in large ion lithophile (LIL) elements Cs, Rb, Ba, Th, U, and K and depleted in high field strength (HFS) elements Ta, Nb, and Zr (Figure 4.6). There is a strong negative anomaly of Sr followed by a strong positive anomaly of Zr (Figure 4.6). Less pronounced negative anomalies of Ba, Nb and Ti are also observed (Figure 4.6).

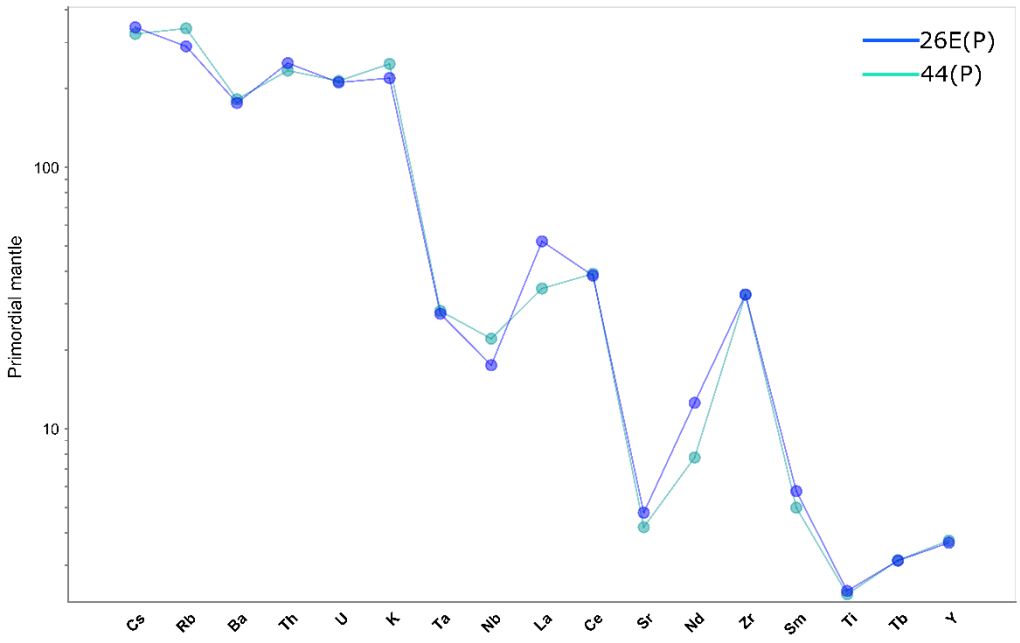


**Figure 4.6:** Multielement diagram showing the distribution of trace elements which have been normalised to primordial mantle compositions (after Taylor and McLennan, 1985).

## 4.6 Mineral Chemistry

Major element concentrations of plagioclase and pyroxene crystals are presented in Figures 4.7-4.9 while the compositions of major elements in Fe-Ti oxides are listed in Table 4.3. Secondary matrix sanidine crystals are presented in Figure 4.10. The major element compositions of feldspars (plagioclase and sanidine) and pyroxene have been plotted using the K-Na-Ca and Ca-Mg-Fe ternary diagrams following the methods of Merrill and McElhinny (1988). The ternary diagrams presented here have been used to clarify the composition of feldspar within the Ngaroma magma and also to understand the chemical changes associated with alteration processes. The origin of the Ngaroma magma and the crystallisation history of phenocrysts are shown in Figures 4.7-4.9. The chemical composition of sanidine shown in Figure 4.10, not only confirms the matrix minerals to be of sanidine and quartz (Figures 3.8-3.10), but provides additional understanding related to devitrification and vapour-phase alteration.

### 4.6.1 Feldspar

The compositions of plagioclase feldspar from the Ngaroma Ignimbrite have been determined using the K-Na-Ca ternary diagram following the method of Merrill and

McElhinny (1988). The samples examined display a strong affinity for oligoclase and range in composition from $An_{15}$-$An_{28}$ and $Or_5$-$Or_{12}$ (Figure 4.7).

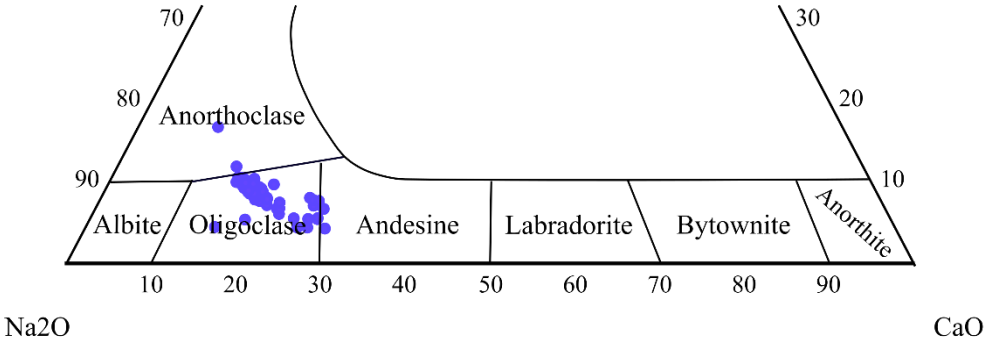


**Figure 4.7:** Feldspar (K-Na-Ca) ternary diagram showing the distribution of geochemical compositions of feldspar crystals (after Merrill and McElhinny, 1988).

### 4.6.1.1 Core and Rim Analyses of Feldspar

Core and rim analyses of feldspars were also analysed on the K-Na-Ca ternary diagram to illustrate evidence for magma differentiation processes (Figure 4.8). The distribution of feldspars observed in Figure 4.8 are nearly indistinguishable to those observed in Figure 4.7 and are concentrated between $An_{14}$-$An_{26}$ and $Or_7$-$Or_{10}$. While these feldspar show little to no changes in chemical composition, the feldspar rims of individual crystals, in contrast to feldspar cores, are generally enriched in $Na_2O$ by 1-2% (up to 6%) (Appendix VI).

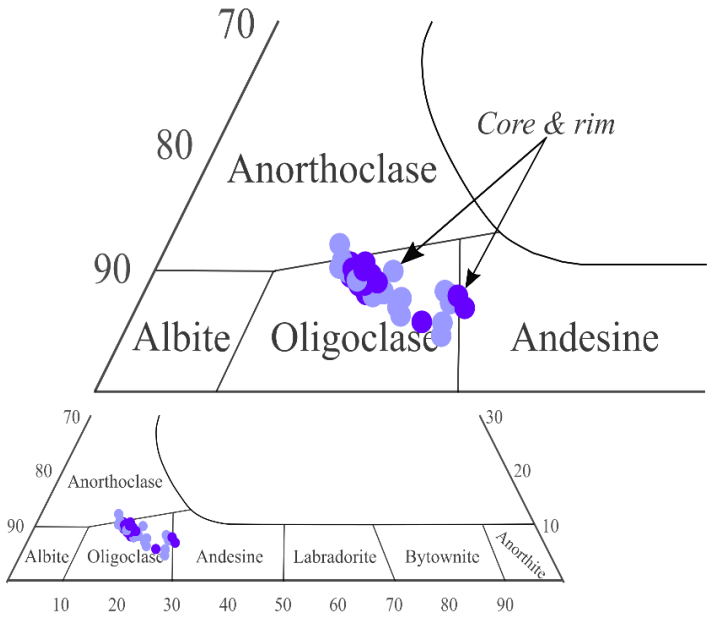


**Figure 4.8:** Feldspar (K-Na-Ca) ternary diagram showing the distribution of geochemical compositions for core versus rim analyses of feldspar crystals. Light purple circles represent feldspar cores while dark purple circles represent feldspar rims. Provided by Merrill and McElhinny (1988).

### 4.6.2 Orthopyroxene

The compositions of pyroxenes comprising the Ngaroma Ignimbrite have been determined using the Ca-Mg-Fe ternary diagram of Merrill and McElhinny (1988). Core and rim data was not attained during EPMA analyses, however the crystals examined here are enstatite in composition and vary between $En_{33}$ and $En_{41}$ (Figure 4.9).

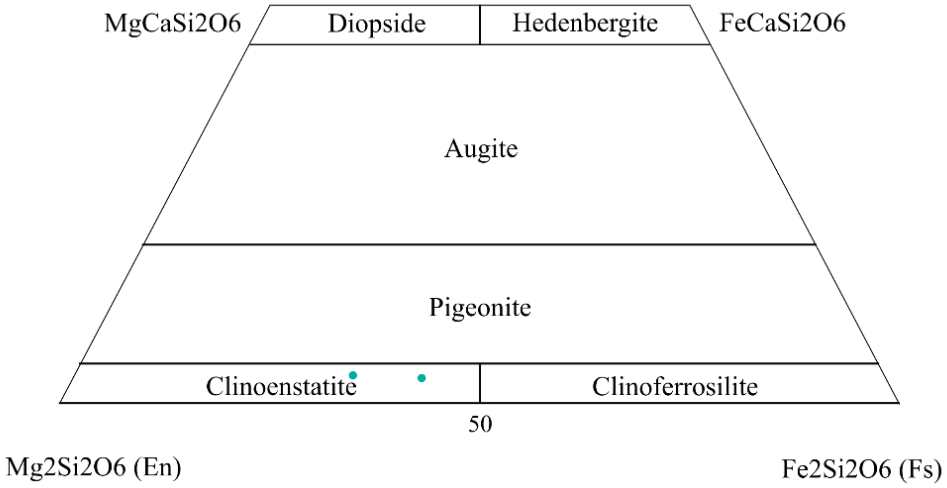


**Figure 4.9:** Ca-Mg-Fe ternary diagram showing the geochemical composition of pyroxene crystals (after Merrill and McElhinny, 1988).

### 4.6.3 Fe-Ti Oxides

Primary minerals of Fe-Ti oxides were also targeted during EPMA analyses (Table 4.3). Analytical totals are low (87-98%), reflecting the variable valence states of iron. Concentrations of key elements are: $Al_2O_3$ (0.8-2.6 wt. %), FeO (45-83 wt. %), $TiO_2$ (15-51 wt. %), MnO (0-0.8 wt. %) and $Cr_2O_3$ (0-.2 wt. %).

**Table 4.3:** Geochemical compositions of Fe-Ti oxides acquired by electron probe microanalyses (EPMA).

| Sample | TiO2 | CaO | MgO | MnO | $Al_2O_3$ | $SiO_2$ | FeO | $Cr_2O_3$ | Total |
|---|---|---|---|---|---|---|---|---|---|
| 1 | 22.04 | 0 | 0.31 | 0.31 | 1.53 | 0.67 | 75.44 | 0.01 | 89.854 |
| 13 | 52.16 | 0 | 0.61 | 0.00 | 0.07 | 0.04 | 47.12 | 0.00 | 89.88 |
| 37A | 14.99 | 0 | 0.42 | 0.00 | 1.53 | 0.10 | 82.90 | 0.06 | 92.147 |
| 37A | 49.56 | 0 | 0.66 | 0.00 | 0.04 | 0.02 | 49.70 | 0.02 | 96.088 |
| 37A | 52.10 | 0 | 0.49 | 0.00 | 0.01 | 0.05 | 47.33 | 0.02 | 98.842 |
| 37A | 28.92 | 0 | 0.39 | 0.00 | 0.86 | 0.15 | 69.66 | 0.01 | 92.259 |
| 44 | 35.02 | 0 | 2.26 | 0.00 | 2.58 | 0.11 | 59.83 | 0.20 | 87.507 |
| 44 | 51.68 | 0 | 2.64 | 0.00 | 0.23 | 0.02 | 45.43 | 0.00 | 89.93 |
| 44 | 16.72 | 0 | 1.10 | 0.00 | 2.00 | 0.13 | 80.05 | 0.00 | 87.472 |
| 44 | 44.92 | 0 | 3.59 | 0.00 | 0.37 | 0.03 | 51.09 | 0.00 | 87.762 |
| 44 | 21.93 | 0 | 0.41 | 0.00 | 1.96 | 0.10 | 75.60 | 0.01 | 89.595 |
| 44 | 25.43 | 0 | 0.49 | 0.21 | 1.64 | 0.11 | 72.08 | 0.03 | 90.66 |
| 44 | 20.57 | 0 | 1.72 | 0.82 | 1.84 | 0.13 | 74.88 | 0.04 | 87.877 |
| 44 | 49.12 | 0 | 5.46 | 0.00 | 0.39 | 0.03 | 45.00 | 0.00 | 90.288 |

### 4.6.4 Sanidine

During electron probe microanalyses (EPMA) analyses, both matrix compositions (the dark and light grey areas observed by BSE/SEM; see Figure 3.8) which were previously indicated by SEM and EDS to be of quartz and sanidine, were targeted on pure single crystals. The crystals presented here were selected based on reliable totals (98-100%) and in which the molar proportions of Na, Ca, K, Al and Si were in the correct range to be of feldspars, or had extremely high Si (>95%) to be consistent with quartz.

Geochemical compositions of micro to submicron-sized crystals comprising the ignimbrite matrix were confirmed by SEM and EDS analyses to be of sanidine and silica (quartz) (Figure 3.9). These crystals were further examined by EPMA analyses, and when observed on the K-Na-Ca feldspar ternary diagram they show affinity for sanidine, varying in composition from $Or_{59}$-$Or_{73}$ (Figure 4.10).

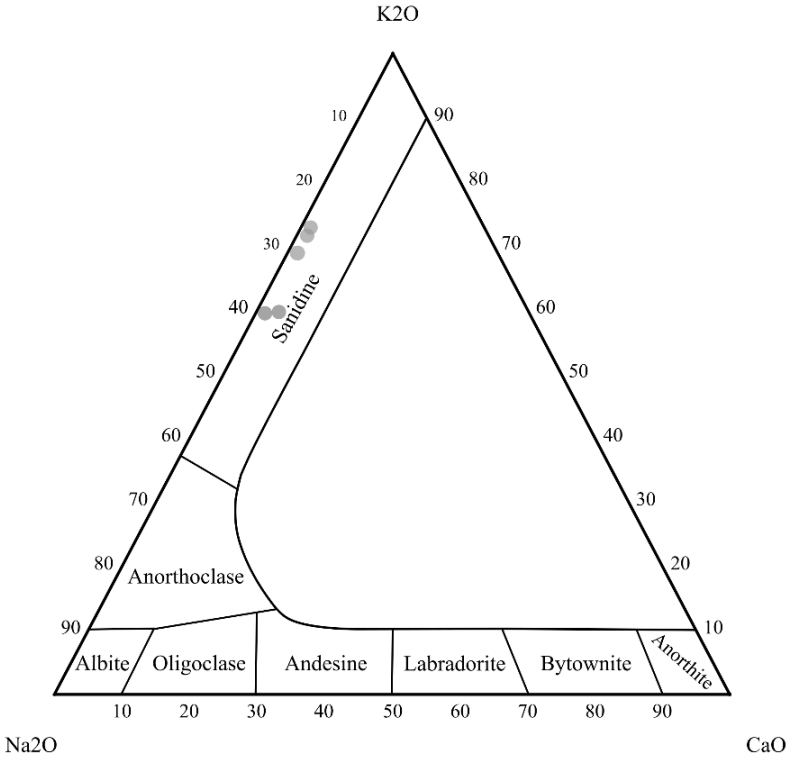


**Figure 4.10:** Feldspar (K-Na-Ca) ternary diagram showing the geochemical composition(s) of sanidine crystals that comprise part of the ignimbrite matrix (after Merrill and McElhinny, 1988).

### *Matrix Quartz*

A total of seventeen points were probed while targeting the fine-grained matrix of the Ngaroma Ignimbrite. Of these points targeted, nine are of quartz and five are of sanidine (Figure 4.10). Due to relatively low totals (<95%), the three remaining analyses are unreliable and thus, are not presented. The nine points which recorded high ($\geq$ 95 %) concentrations of $SiO_2$ however, re-confirms the fine-grained, cryptocrystalline matrix of the Ngaroma Ignimbrite to consist, at least in part, of pure quartz (particularly of cristobalite).

# Chapter Five

# Discussion

## 5.1 Introduction

This chapter discusses the physical transport and emplacement mechanisms associated with both primary facies and subfacies produced during the 1.6 Ma Ngaroma eruption. Post-emplacement processes, including the geochemical alteration processes observed in this study, will also be addressed here. These interpretations are then followed by a discussion regarding the origin and primary influences responsible for generating the 1.6 Ma Ngaroma eruption sourced from the MVC.

## 5.2 Physical distribution and emplacement processes of the Ngaroma Ignimbrite

Ignimbrites are the products of pumiceous pyroclastic density currents (PDC), or pyroclastic flows that comprise hot particles of magma and country rock, mixed with magmatic volatiles, water vapour, and entrained air which cool and solidify together during deposition (Keating, 2005; Sohn et al., 2009). These deposits typically display lateral and vertical variations in primary componentry that provide critical information regarding the physical properties and emplacement mechanisms occurring during and after emplacement (Sohn et al., 2009). Recognizing the presence of primary and secondary sedimentary structures and textures, and characterising the presence of any existing primary facies and subfacies within these deposits, is therefore essential for interpreting the mode of transportation and emplacement mechanisms.

Studies conducted by Luchetti et al., (2018) further suggest that the varying textures preserved throughout these deposits provide diagnostic insights as to whether the ignimbrite succession was emplaced by dense and laminar or dilute and turbulent pyroclastic flows. Moreover, clarification of these emplacement processes may provide additional understandings regarding the magnitude of the eruption responsible for producing the ignimbrite (Luchetti et al., 2018).

*Emplacement mechanisms and implications of Ngaroma Ignimbrite*

The extremely subtle, or gradational variations in primary components, particularly of clast size and percentage abundance (of pumice, lithic, and crystals) observed both laterally and vertically throughout the Ngaroma Ignimbrite within the field area are characteristic of a massive or uniform deposit (Sohn et al., 2009). These are generally emplaced either by en masse freezing or by progressive aggradation of a highly concentrated pyroclastic flow (Sohn et al., 2009). Primary facies and subfacies comprising the Ngaroma Ignimbrite preserve ubiquitous moderate to well-developed eutaxitic pumice textures which vary from partially and extremely flattened fiamme to thin wispy lenticulates (Figures 2.13-2.15). The varying intensities of welding observed throughout the Ngaroma Ignimbrite, particularly between subfacies PiV and BrV (Figure 2.10) and subfacies PiWd and GrWm (Figure 2.12) are presumed to result from aggradation of continuous, subtle depositional pulses occurring during emplacement of a hot, dense, pyroclastic flow (Willcock and Cas, 2014).

When analysing welded ignimbrites, Willcock and Cas (2014) suggest that these products can be characterised and classified as either 'simple' or 'compound' cooling units. Simple cooling units are presumed to represent an ignimbrite succession emplaced by single or successive pyroclastic flows that cool rapidly to produce a single thermal unit. Due to the overall uniform appearance and gradational contact changes observed within subfacies PiWd (Figure 2.11) in addition to those which occur between the PiWd and GrWm subfacies (Figure 2.12) and subfacies PiV and BrV (Figure 2.10), it may be presumed that the Ngaroma Ignimbrite as a whole, represents a simple cooling unit.

The internal variations in welding intensity observed throughout the deposit however, suggest that cooling and compaction processes were not uniform and likely did not occur synchronously during emplacement of the pyroclastic flow (Willcock and Cas, 2014). This may be illustrated by changes in the aspect ratios of pumice observed between the lithic-rich facies (subfacies PiWd and GrWm) and the lithic-poor facies (subfacies PiV and BrV), wherein pumice shape changes from sub-equant and partially flattened fiamme in the lithic-poor facies (Figures 2.16 and 2.17) to extremely flattened and highly compact lenticular pumice in the lithic-rich facies (Figure 2.13). These variations do not occur vertically, but rather, are

observed at individual outcrops within the field area. Thus, it is suggested that deposits of the lithic-rich and lithic-poor facies cannot be correlated laterally.

The lithic population found in general from ignimbrites derived from the MVC typically comprise 1-10% of the overall rock and vary in composition from rhyolite, dacite, andesite, and basaltic andesite lava, welded ignimbrite tuff, volcanic breccia, biotite granite, granodiorite porphyry, siltstone, sandstone, greywacke, metagreywacke, metaconglomerate, biotite, and hornblende-biotite schist (Krippner et al., 1998). As previously mentioned, the MVC eruptions occurred in two distinct time periods (period I and II) and based on previous studies, it is understood that period I ignimbrites (i.e., the Ngaroma Ignimbrite) are dominated by andesite lava fragments which are geochemically distinct from the nearby contemporaneous andesite volcanoes, Titiruapenga and Pureora.

Lithics comprising the Ngaroma Ignimbrite, when observed in the field, account for 5 to 7 % of the bulk rock and can be recognised by their conspicuous abundance of coarse-grained, crystal-rich andesites followed by relatively small ($\leq$ 6 mm) fragments of greywacke, argillite, andesite, and rhyolite (Figure 2.13). Vent-derived lithics are presumed to be those which are typically $\leq$ 6 mm in size, which are mainly andesitic to rhyolitic in composition. Relatively, larger lithics (up to 19 mm in size) vary from greywacke to argillitic to andesitic in composition and are presumed to be accidental; that is they were locally entrained into the pyroclastic flow from the ground surface (Figure 5.1).

The lithic-rich facies, and thus subfacies GrWm and PiWd, are comprised mostly of andesite and rhyolite lithics followed by fragments of greywacke and argillite and are ubiquitous (Figure 2.13). Lithics observed throughout the lithic poor facies (and thus subfacies PiV and BrV) however, are rare ($\leq$ 1% of the bulk rock) and comprised mostly of fine-grained fragments of andesite and rhyolite (Figure 2.17).

Recent studies conducted by Sohn et al., (2009) and Willcock and Cas (2014) suggest that these cold, locally-derived fragments, were most likely incorporated into the pyroclastic system at the base of the flow, where they promote a decrease in temperature of the pyroclastic flow, and in turn cause welding of the parental (lithic-rich) pyroclastic flow to also decrease. Similar processes could have

occurred during emplacement of the Ngaroma Ignimbrite, particularly during deposition of the lithic-rich facies, wherein relatively large lithics of andesite and greywacke are thought to have been incorporated into the system at the base of the parent pyroclastic flow (Figure 5.1). However, the increase in welding observed throughout the lithic-rich facies, and thus in the PiWd and GrWm subfacies is unique, and suggest that the lithics incorporated into this deposit did not have a significant effect on temperature. Moreover, it may be presumed that the parent pyroclastic flow which entrained these large lithics (Figure 5.1) was comparably more dense, and thus capable of retaining its high temperatures for a substantial duration of time, which in turn allowed for welding to increase.

Further evidence, which suggest that these clasts were introduced locally, may also be inferred by the vertical changes in lithic concentration recorded particularly throughout subfacies GrWm and PiWd, where lithic fragments decrease in concentration with increasing height, while their size and shape are retained (Figure 2.12). These vertical lithic gradations have also been observed by Smith and Cole (1997), and are typically associated with a decreasing supply in lithics rather than in eruption intensity. Such implications would most likely result from a decrease in wall-rock erosion of the conduit-wall which further suggests that the majority of lithic fragments comprising the lithic-rich facies were incorporated locally into the system rather than derived from the eruption conduit-walls (Smith and Cole, 1997).

It is well known that tuff layers associated with ignimbrite successions result from co-ignimbrite processes (Smith and Cole, 1997). The absence of tuff layers within the Ngaroma Ignimbrite strongly suggest that the parent pyroclastic flow of the Ngaroma Ignimbrite was not accompanied by a co-ignimbrite ash deposit. However, it is possible that the PDC was emplaced as simple classic flow-units which required each flow-unit to follow the next almost simultaneously such that co-ignimbrite ash deposits did not have time to form (Smith and Cole, 1997). Another mechanism which could be responsible for the absence of co-ignimbrite deposits may be that any co- ignimbrite ash layers was completely homogenised during deposition as a result of post-emplacement welding (Smith and Cole, 1997). Lastly, pyroclastic flows which experience ‘progressive aggradation’ could also result in the absence of co-ignimbrite ash layers (Smith and Cole, 1997). These processes would imply that, within-flow agglutination, and during the passage of a single, or massive sheet-

forming pyroclastic flow, the aggradation of successive non-particulate flow components were likely to have been transported by momentum and shear stress of the overlying particulate flow (Smith and Cole, 1997). Due to the absence of tuff layers, extremely subtle vertical and lateral variations in primary componentry, and highly compact, or intense degree of welding, it is plausible that the absence of co-ignimbrite ash deposits in the Ngaroma Ignimbrite are the result of late stage welding and progressive aggradation of a parent pyroclastic flow.

These implications may also be represented by the thin (mm) laminae and relatively fine-grained matrix observed along Waipari Road at the waterfall, at 9 m between subfacies GrWm and PiWd (Figures 2.12 and 2.19). This parallel bedding in particular is characteristic of flow-laminated structures and may represent a flow boundary zone from the passage of two distinct pyroclastic flow pulses.

*Eruption processes and volcanic implications*

Studies conducted by Sparks and Wilson (1976) suggest that variations in the amount of cooling that takes place during the collapse of vertical eruption columns, which occur particularly during highly explosive (often plinian style) eruptions, influence the variations in emplacement temperature and thus, in the intensity of welding observed in ignimbrite deposits. This study also described that high emplacement temperatures, which typically coincide with increased welding intensities (Luchetti et al., 2018), are favoured by eruption columns that retain high gas contents and low gas velocities which are commonly associated with vertical eruption columns that experience immediate gravitational collapse to an ash fountain (Sparks et al., 1978). Such mechanisms are presumed to have played a significant role during the 1.6 Ma Ngaroma eruption and prior to emplacement of the Ngaroma Ignimbrite (Figure 5.1).

These implications may not only be represented by the intense degree of welding observed throughout the Ngaroma Ignimbrite as a whole, but could also account for the increase in welding observed throughout the lithic-rich facies (Figures 2.13- 2.15). Likewise, the lack, or absence of a pyroclastic ash-fall deposit observed beneath the ignimbrite, may also suggest that the eruption column of the 1.6 Ma Ngaroma eruption was short-lived.

The limited proportion of vent-derived lithic fragments recorded throughout the Ngaroma Ignimbrite suggest that the parent pyroclastic flow resulted from, on the basis of highly explosive eruptions, relatively low conduit wall-rock fragmentation (Figure 5.1; Luchetti et al., 2018). These processes would further suggest that during the eruption, there was little vent erosion, thus the ability to incorporate lithics into the magma was restricted. Moreover, the vertical variations in primary componentry, particularly the decreasing supply of lithic content with increasing height observed between subfacies GrWm and PiWd (Figure 2.12) may result from a further decrease in conduit wall-rock erosion over time, as well as from lithics derived from the local substrate which are more abundant (Figure 5.1; Smith and Cole, 1997).

In previous studies conducted by Krippner et al., (1998), it is described that rhyolite lithics are abundant in all Mangakino-derived ignimbrites, however they are especially conspicuous in the younger period II ignimbrites (i.e., Ongatiti, Unit 'D', Ahuroa, Rocky Hill, Kaahu, Marshall 'B', Marshall 'A', and Waioraka). From these observations, it is understood that rhyolitic lava domes and flows were likely interspersed with Mangakino caldera-forming eruptions however, they were subsequently buried by later eruptives (Briggs et al., 1993). Rhyolite lithics observed throughout the Ngaroma Ignimbrite occur as sparse fragments which may further imply that rhyolite dome building was not significant prior to, or during the 1.6 Ma Ngaroma eruption.

Moreover, Krippner et al., (1998) have also described, based on the abundance of andesite lithics in MVC ignimbrites, the possible presence of a buried andesite volcano in the volcanic pile beneath MVC (Figure 1.5) that is geochemically discrete from Titiraupenga or Pureora and older than the period I ignimbrites (i.e., Ngaroma, Ignimbrite 'B', and Ignimbrite 'C'). Such implications may coincide with the conspicuous abundance of andesite lithics observed throughout the Ngaroma Ignimbrite, particularly the frequently occurring coarse-grained, crystal-rich andesite fragments observed throughout the lithic-rich facies (and thus subfacies PiWd and GrWm) (Figure 2.13). Thus, the underlying unit of andesite (unit B) which rests stratigraphically beneath subfacies PiWd (Figures 2.4 and 2.9) may

result from, and further support the presence of a buried andesite volcano beneath the MVC (Figure 1.5; Krippner et al., 1998).

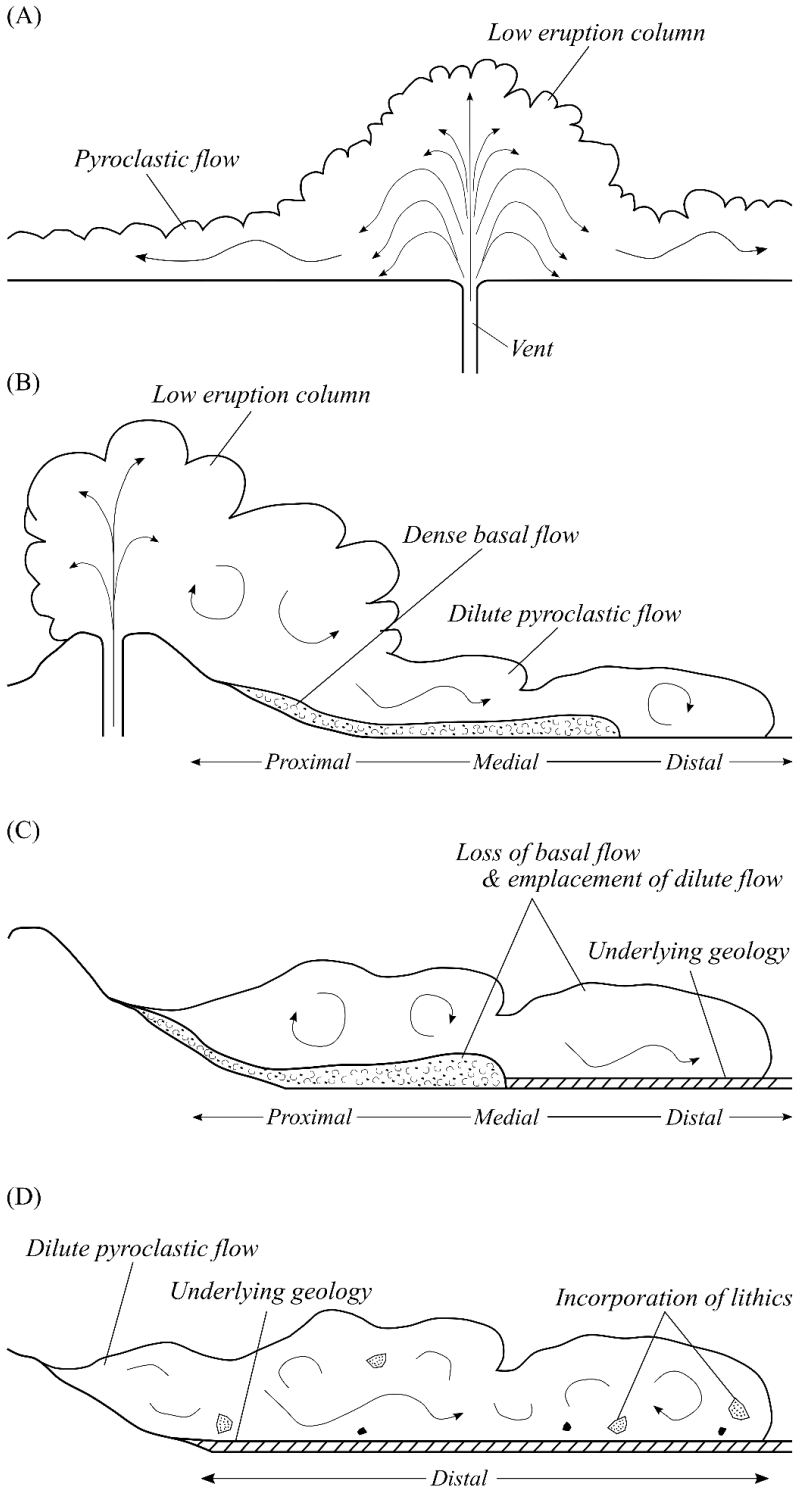


**Figure 5.1:** Schematic diagram showing the transport and emplacement mechanisms of the Ngaroma Ignimbrite after Doyle et al., (2010) and Luchetti et al., (2018) showing: (A) collapsed eruption column and formation of the parent pyroclastic flow; (B) transport and emplacement of the dilute parent pyroclastic flow; (C) incorporation of the underlying basement greywacke and/or andesite (unit B), and; (D) incorporation of locally derived lithics into the system, at the base of the pyroclastic flow.

## 5.3 Post-emplacement Processes of the Ngaroma Ignimbrite

The depositional structures and primary textures of ignimbrite deposits are commonly obscured by numerous processes including compactional welding, devitrification, and vapour phase mineralisation which take place both during and after deposition of a cooling pyroclastic flow (Grunder and Russell, 2005; Keating, 2005). Many recent studies suggest that, as cooling and solidification of a pyroclastic flow takes place, compactional welding occurs, promoting viscous deformation and adhesion of hot, molten glass shards and pumice clasts throughout the interior of the ignimbrite and in turn modify the overall structure, texture, and thus physical properties of the volcanic deposit.

*Interpretations and implications of welding*

The juvenile glass shards and flattened pumice comprising the Ngaroma Ignimbrite, when observed in petrographic analyses, show horizontal, subparallel alignment, or otherwise eutaxitic texture which are characteristic of densely welded, high grade ignimbrites (Figure 3.8; Fülöp and Kovacs, 2003).

Compactional welding observed within these volcanic deposits commonly result from post-emplacement load compaction that takes place beneath an overburden pressure at extremely high temperatures (Fülöp and Kovacs, 2003; Willcock and Cas, 2014). The high intensity of welding observed throughout the Ngaroma Ignimbrite, both macroscopically and petrographically may therefore result from a pyroclastic flow that, upon emplacement, retained an extremely high temperature and thus relatively low cooling rates which subsequently allowed for dense welding to occur. This implication would further support that the parent pyroclastic flow of the Ngaroma Ignimbrite was formed from a short-lived eruption column (Figure 5.1).

*Interpretations and implications of devitrification*

Recent studies conducted by Grunder and Russell (2005) and Keating (2005) further state that the volatiles released during the devitrification of volcanic glass shards migrate in an upward direction, where they precipitate into pore spaces as vapour phase minerals. Such processes (both devitrification and vapour-phase

mineralisation) are diagnostic textures preserved and recognised throughout the Ngaroma Ignimbrite, and strongly imply that secondary, post-emplacement processes played a significant role during and after emplacement of the parent pyroclastic flow.

The well-formed, eutaxitic glass shards observed throughout the Ngaroma Ignimbrite, as previously mentioned, comprise a fine-grained, cryptocrystalline groundmass (Figures 3.8 and 3.9). The groundmass in particular displays replacement, or relict devitrified shard textures, where the original glass composition has been replaced with microcrystalline quartz and feldspar (Figure 3.8; Willcock and Cas, 2014). Axiolitic and spherulitic intergrowths are common (Figure 3.3). These well-preserved, secondary replacement textures represent weak to moderately altered volcanic deposits and are typically associated with increased feldspar replacement, groundmass and matrix crystallisation, and subsequent loss of primary textures which imply that primary vitriclastic textures comprising the Ngaroma Ignimbrite were destroyed by post-emplacement crystallisation and/or devitrification (Willcock and Cas, 2014).

The previously described spherulitic intergrowths are also observed comprising the groundmass of highly flattened and compact pumice throughout the Ngaroma Ignimbrite (Figure 3.3). Fülöp and Kovacs (2003) and Rowe et al., (2012) suggest that conditions which allow for the preservation of spherulitic intergrowths in pumice are exceptionally high, or close to liquidus temperatures. These studies in particular, suggest that these textures form during the spherulitic stage of acid, rhyolitic glass shard devitrification, during which, a very low cooling rate is required, while high temperatures are likely to remain; therefore, it can be assumed that these textures were preserved during emplacement of a hot pyroclastic flow, while pumice clasts were extremely hot and plastically deformed.

The secondary crystallisation textures preserved in both glass shards and in pumice comprising the Ngaroma Ignimbrite are presumed to have formed during cooling of a densely welded, however still viscous, pyroclastic deposit (Willcock and Cas, 2014). Furthermore, it is presumed that, due to the extent of crystallisation and mineral replacement, crystallisation was likely to have continued after cooling and

through the glass transition, therefore causing extreme devitrification of both glass shards and pumice (Willcock and Cas, 2014).

## 5.4 Post-emplacement geochemical alteration processes

Rapidly cooled silicic volcanic deposits, or ignimbrites that undergo syn- and post-emplacement alteration processes such as vapour phase mineralisation and devitrification are susceptible to significant compositional changes (Kochhar, 1977; Scott, 1971). These processes of which, typically involve the extensive loss of magmatic volatiles, and usually take place between the time of eruption and during emplacement of the pyroclastic flow, particularly as the ignimbrite cools and glass shards devitrify (Scott, 1971).

Modifications that result from these post-alteration processes may be represented by geochemical changes associated with major and trace element concentrations, and have been recognised in both pumice and subfacies PiWd, GrWm, PiV, and BrV of the Ngaroma Ignimbrite (Figures 4.3 and 4.4).

*Interpretations and implications for vapour phase alteration*

Silicic ignimbrite deposits that show decreased concentrations of $Na_2O$, $P_2O_5$ and $K_2O$, with increased concentrations of $SiO_2$, $Al_2O_3$, MgO, and LOI are associated with, and result from exchanges of magmatic volatiles and leaching of major elements which occur during vapour phase mineralisation (Chigira et al., 2002).

The increased concentrations of $SiO_2$ recorded within pumice and in subfacies GrWm and PiV, in addition to the increased concentrations of $Al_2O_3$ and LOI and decreased concentrations of CaO and $Na_2O$ associated with subfacies PiWd and BrV (Figure 4.3), strongly suggest that the Ngaroma Ignimbrite endured significant vapour phase mineralisation (Chigira et al., 2002). Likewise, the low concentrations of $P_2O_5$, $N_2O$, and $K_2O$, which are typical of subfacies PiWd and BrV (Figure 4.3) are characteristic of, and coincide with hydration and softening of a volcanic deposit which is presumed to take place subsequent to emplacement of the ignimbrite and during vapour phase mineralisation (Chigira et al., 2002).

Studies conducted by Chigira et al., (2002) suggest that these changes in major and trace element concentrations are often associated with the disappearance of tridymite and the formation of cristobalite. Such implications may in part be represented by SEM/EDS analyses (Figures 3.8 and 3.10) which confirmed the cryptocrystalline groundmass to be comprised mostly of cristobalite (Figures 3.8 and 3.11). This could also account for the intense peaks of cristobalite recognised by XRD analyses (Figures 3.12-3.15).

*Interpretations and implications for devitrification*

Volcanic products, which undergo devitrification of glass shards, can be geochemically recognised by their decreased concentrations of $Na_2O$ and of major elements $SiO_2$, $Al_2O_3$, and CaO and increased concentrations of $Fe_2O_3$, MgO, $K_2O$ and LOI, as the result of excess hydration that takes place during groundwater leaching (Kochhar, 1977).

The devitrification of glass shards comprising the Ngaroma Ignimbrite is therefore represented by the decreased concentrations of $Al_2O_3$ and increased concentrations of $K_2O$ which are characteristic of pumice comprising the Ngaroma Ignimbrite and of subfacies GrWm and PiV (Figure 4.3). Likewise, increased concentrations of $Fe_2O_3$, MgO, and LOI, with decreased concentrations of CaO and $Na_2O$ are typical of subfacies PiWd and BrV, and thus diagnostic implications of devitrification (Figure 4.3).

It is commonly understood that pyroclastic deposits that are porous in nature generally comprise a vitric groundmass which can be equally susceptible to the leaching of $Na_2O$ (Kochhar, 1977). Thus, the low concentration of $Na_2O$ associated with subfacies PiWd and BrV, in conjunction with the well preserved and previously described fine-grained, cryptocrystalline matrix comprising the Ngaroma Ignimbrite, may imply that the deposit cooled as a porous ash bed. This, in addition to the significant devitrification observed both macroscopically, petrographically, and now geochemically would further imply that, upon emplacement of the porous ash bed (i.e., Ngaroma Ignimbrite), cooling occurred rapidly and allowed for groundwater to be incorporated into the deposit which consequently allowed for enhanced devitrification (Kochhar, 1977). Such

mechanisms may be especially recognised in the lithic-poor facies, and thus subfacies PiV and BrV which are extremely soft, porous, and chalky in texture (Figures 2.16-2.18).

## 5.5 Magmatic Processes of the Ngaroma Ignimbrite

As previously mentioned, the Ngaroma Ignimbrite has endured significant vapour phase mineralisation and devitrification, and the selected samples of bulk rock ignimbrite and pumice are pervasively altered. Therefore, due to the lack of primary material, particularly of fresh glass shards and pumice, the following interpretations of magmatic processes are limited. Moreover, the patterns observed on the classification diagrams (Figures 4.1 and 4.2) relating to trace elements provide insight from bulk rock analyses. It is recognised that some of the observed patterns relating to primary magmatic processes reflect modifications from secondary alteration processes. The EPMA analyses of plagioclase and orthopyroxene crystals provide better insight into magmatic differentiation.

Major element geochemistry of pumice and bulk rock has determined the rhyolitic composition of the Ngaroma Ignimbrite using a TAS classification diagram (Figure 4. 1) provided by Le Maitre et al., (2002) and a volcanic rock classification diagram following the methods of Winchester and Floyd (1977; Figure 4.2). When illustrated on the TAS diagram (Figure 4.1), the data plot both within the dacite and rhyolite fields however are more concentrated within the rhyolite field. Likewise, when plotted on the Winchester and Floyd (1977) diagram, the data is concentrated within the rhyolite to trachyandesite fields, which further implies that the ignimbrite is rhyolitic in composition (Figure 4.2). The data plotted within the dacite and trachyandesite fields (Figures 4.1 and 4.2) however, are inferred to reflect the contamination of lithic clasts and the secondary alteration.

*Geochemical signatures and magmatic implications*

The pumice comprising the Ngaroma Ignimbrite (Figures 4.5 and 4.6) show REE concentrations that are enriched in LREE elements and depleted in HREE elements, which are typical of calk-alkaline suite ignimbrites, or subduction related magmas (Fülöp and Kovacs, 2003). Trace element geochemical signatures show enrichments of LILE and depletions of HFSE (Figures 4.5 and 4.6). The

corresponding enrichments of LILE and LREE together suggest that the mantle source was enriched in these elements and most likely result from subducted slab contributions that experienced involvement of silica-rich fluids.

It is well known that trace elements Zr, Nb, Th, and LREE are weakly soluble in hydrous fluids, therefore any enrichment, or depletion of these elements, would require a liquids phase (Ayalew et al., 2002; Dupay and Dostal, 1978; Gamble et al., 1994; Kürkçüoglu et al., 1998; Pérez-Torrado et al., 1995; Portnyagin et al., 2007). Thus, the overall enrichment of LREE and the coexisting anomalies of Th, Nb, Sr, Zr and Ti, and Zr recorded in pumice comprising the Ngaroma Ignimbrite (Figure 4.6) are presumed to result from a subducting slab which experienced partial melting of a mantle enriched with LREE elements. Likewise, it is commonly understood that strong negative anomalies of Nb, Ba, Sr, and Ti are characteristics of either arc-volcanics, or crustal rocks (Ayalew et al., 2002).

Studies conducted by Temel et al., (1998) and Portnyagin et al., (2007), suggest that enrichments in K, Rb, and Ba are typical of magmas that have experienced crustal contamination. The overall enrichment of LREE elements with discrete negative anomalies of Nb and Ti, in addition to positive anomalies of K and Rb recognised in Ngaroma Ignimbrite pumice (Figure 4.6) therefore suggest that fractional crystallisation was involved during the genesis of these magmas and most likely involved contamination or assimilation of a crustal source. Moreover, studies conducted by Kürkçüoglu et al., (1998) indicate that trace elements Ce and Nb are more incompatible in comparison to Y and Zr. Thus, the negative anomaly of Nb and positive anomalies of Ce and Zr (Figures 4.5 and 4.6) may represent partial melting of a subducting slab that was contaminated with a lower crustal source enriched in LILE elements.

Overall, the geochemical signatures of pumice comprising the Ngaroma Ignimbrite are presumed to represent involvement of hydrous, slab-derived fluids which were likely derived from the partial melting of a subducting slab (Ayalew et al., 2002; Dupay and Dostal, 1978; Gamble et al., 1994; Kürkçüoglu et al., 1998; Pérez-Torrado et al., 1995; Portnyagin et al., 2007). This understanding may be especially represented by the strong negative anomaly of Ce and its corresponding REE trends which has also been observed by Graham et al., (1995), who suggest that such

compositional trends would result from post-eruptive hydration (rather than to hornblende fractionation).

Based on the overall enrichments of LILE elements, and the discrete negative anomalies of Sr and Nb (Figure 4.6), it is also presumed that the subducting slab likely induced convection in the mantle wedge which subsequently generated advection within either the lower crust or upper mantle (Fülöp and Kovacs, 2003). Furthermore, it is likely that as the subduction fluids generated from these melts ascended through the magma chamber, trace elements Ba and Nb were removed. Likewise, enrichments of Rb, Zr, and LREE were most likely incorporated into the system by partial melting of lower crustal rocks which synchronously removed trace elements Sr and Ti (Ayalew et al., 2002; Dupay and Dostal, 1978; Fülöp and Kovacs, 2003).

Finally, it is well-known that enrichments in LREE elements are usually accompanied with negative anomalies of Eu as a result of plagioclase fractionating out of the system (Fülöp and Kovacs, 2003). Pumice comprising the Ngaroma Ignimbrite however, show a discrete positive anomaly of Eu (Figure 4.5). This is unique in silicic volcanic deposits and suggests that plagioclase was incorporated into the system rather than fractionated out (Dupuy and Dostal, 1978; Fülöp and Kovacs, 2003). Such implications may imply that, in addition to fractional crystallisation, crustal contamination of a lower crustal component was effective during the genesis of the Ngaroma eruption. Moreover, studies conducted by Cole (1979) and Graham et al., (1995) suggest that this anomaly, in assimilation with the overall geochemical signatures recorded here, may reflect the presence of residual melt. However, this would imply that cumulative phases, or fractional crystallisation did not play a significant role in the petrogenesis of the Ngaroma Ignimbrite. Similar geochemical signatures have also been accounted for by Cole (1979) and Graham et al., (1995) who suggest that these trends may result from the presence of a once basaltic or mafic crystal-rich ‘mush’. These implications may not only account for the positive anomaly of Eu, but may also be responsible for producing crystal poor rhyolitic ignimbrites such as that of the Ngaroma Ignimbrite.

*Magma composition and crystallisation history*

When observed petrographically, plagioclase crystals are poorly concentrically zoned (Figure 3.1), and when plotted on the ternary diagrams (Figures 4.7 and 4.8), are concentrated between $An_{14}$-$An_{26}$ and $Or_{7}$-$Or_{10}$, showing little to no variations in composition between core and rim concentration (Figure 4.8). The simplicity of these individual crystals suggest that the crystallisation history was short-lived, (Ewart, 1971; Gansecki et al., 1996). The core and rim analyses of individual orthopyroxenes were not attained in EPMA analyses. However, when observed petrographically these crystals appeared to be unzoned (Figure 3.2). Moreover, when plotted on the ternary diagrams, the orthopyroxene vary from $En_{32}$-$En_{41}$ in composition which is typical in the mineral assemblage of rhyolitic magmas (Figure 4.9; Deering et al., 2011).

# Chapter Six

# Conclusions and Further Research

The Mangakino Volcanic Centre (MVC) occupies the western-most boundary of the TVZ (Wilson, 1986). Products produced from this volcanic centre, including the major welded and non-welded ignimbrite successions are divided into two distinct time periods (period I and II) that coincide precisely with highly explosive caldera-forming eruptions (Cooper et al., 2014; Wilson, 1986). Of these volcanic eruptions, the 1.6 Ma Ngaroma eruption is the first-known rhyolitic eruption sourced from the MVC and of TVZ origin.

Findings and interpretations from this study have provided intriguing insight into the physical emplacement and post-emplacement processes of the 1.6 Ma Ngaroma Ignimbrite. Further interpretations of the magmatic composition and crystallisation history of the 1.6 Ma Ngaroma eruption have also been described. The significant findings from this study are listed below:

- two primary facies and four subfacies have been recognised within the Ngaroma Ignimbrite which reflect syn- and post-deposition and alteration processes including compactional welding, devitrification, and vapour phase mineralisation;
- variations in the degree of welding observed between the lithic-rich and lithic-poor facies are presumed to result from progressive aggradation of continuous, however subtle depositional pulses of a hot, dense, parent pyroclastic flow;
- the ubiquitous abundance of locally derived andesite lithics observed throughout the Ngaroma Ignimbrite, in conjunction with the underlying unit of andesite (unit B) coincide with studies conducted by Krippner et al., (1998) and further support the presence of a buried andesite volcano beneath the MVC ; and
- the intense degree of welding, absence of pumice or ash fall deposits, and the limited proportion of vent-derived lithic fragments observed throughout the Ngaroma Ignimbrite within this field area suggest that the parent

pyroclastic flow of this deposit formed from a short-lived plinian eruption column.

Petrographic observations further imply that the 1.6 Ma Ngaroma Ignimbrite endured, or has been modified by syn- and post-emplacement alteration processes, in particular, the fine-grained, optically unresolvable medium comprising the matrix of the Ngaroma Ignimbrite was confirmed to be a mixture of K-feldsar (sanidine) and cristobalite (± tridymite).

Due to the lack of primary material (fresh glass shards and pumice) preserved within the Ngaroma Ignimbrite, detailed understanding of magmatic processes associated with the 1.6 Ma Ngaroma eruption were limited. The geochemical composition of the Ngaroma Ignimbrite was determined to be of rhyolite, and calc-alkaline in character. The various well-defined trends of major and trace element concentrations have been affected by vapour-phase alteration and devitrification processes which are presumed to have occurred both during and after emplacement of the parent pyroclastic flow. Geochemical trends of LREE and HREE observed in pumice, are associated with subduction-related magmas and may imply that the parent magma of the 1.6 Ma Ngaroma eruption experienced crustal contamination prior to, or during magma ascent.

The composition of plagioclase (ranging from $An_{15}$-$An_{28}$ and $Or_5$-$Or_{12}$) and pyroxene ($En_{32}$-$En_{41}$) crystals are typical of rhyolitic magmas, and the nearly indistinguishable variation in compositions observed between core and rim concentrations of plagioclase crystals indicate that the crystallisation history was short-lived (Ewart, 1971; Gansecki et al., 1996).

- Detailed mapping of the Ngaroma Ignimbrite across the whole extent of its preserved distribution could be conducted to re-evaluate, or clarify the lateral distribution and vertical contact changes of the Ngaroma Ignimbrite and the subsequently recognised ignimbrites, or units within the field area. In doing so, additional field localities from areas far-east of the current field area (Figure 2.1), particularly along Wairehi Road, could be included. Should the presence of additional (whether it be ‘new’ or pre-existing) formations or geological units be recognised, they could be incorporated into the field map, and described in more detail.

- In this study, the origin of underlying andesite (unit B) observed at the northern-end of Mangawhio Road is unknown, and it is presumed to pre-date the Ngaroma Ignimbrite based only on its stratigraphic position (Figures 2.4 and 2.9). Detailed radiometric age dating of this unit B, in addition to geochemical analyses could therefore be performed to determine the age of this deposit, and geochemical relationship to other nearby volcanoes.
- Finally, this study was conducted within the area of Ngaroma due its close proximity to the MVC. Moreover, the collected samples of Ngaroma Ignimbrite analysed here, were pervasively altered by vapour-phase mineralisation and devitrification and thus, geochemical and petrological analyses of fresh, unaltered material was not attained. Further research could therefore involve sample collecting from more distal sources to the MVC. This is assuming that in distal outcrops, the likelihood of finding unaltered glass shards and pumice would increase. Should fresh glass and pumice be recognised and analysed in future studies, the deposit could be re-evaluated, and in turn provide increased understanding into the geochemistry and petrogenesis of the 1.6 Ma Ngaroma eruption.

# References


Ayalew, D., Barbey, P., Marty, B., Reisberg, L., Yirgu, G., and Pik, R., 2002, Source, genesis, and timing of giant ignimbrite deposits associated with Ethiopian continental flood basalts: Geochimica et Cosmochimica Acta, v. 66, p. 1429–1448, doi: 10.1016/s0016-7037(01)00834-1.

Barker, S.J., Wilson, C.J.N., Smith, E.G.C., Charlier, B.L.A., Wooden, J.L., Hiess, J., and Ireland, T.R., 2014, Post-supereruption Magmatic Reconstruction of Taupo Volcano (New Zealand), as Reflected in Zircon Ages and Trace Elements: Journal of Petrology, v.55, p. 1511–1533, doi: 10.1093/petrology/egu032.

Blank, H.R., 1965, Ash-flow deposits of the central king country, New Zealand: New Zealand Journal of Geology and Geophysics, v. 8, p. 588–610, doi: 10.1080/00288306.1965.10423193.

Briggs, R., Gifford, M., Moyle, A., Taylor, S., Norman, M., Houghton, B., and Wilson, C., 1993, Geochemical zoning and eruptive mixing in ignimbrites from Mangakino volcano, Taupo Volcanic Zone, New Zealand: Journal of Volcanology and Geothermal Research, v. 56, p.175–203, doi: 10.1016/0377-0273(93)90016-k.

Briggs, J., 2005, The use of indigenous knowledge in development: problems and challenges: Progress in Development Studies, v. 5, p. 99–114, doi: 10.1191/1464993405ps105oa.

Brink, M., 2012, Emplacement processes of ignimbrites in the Ongatiti Valley, southeast Te Kuiti (MSc Thesis): The University of Waikato, p. 27-44.

Brown, S.J., and Smith, R.T., 2004, Crystallisation history and crustal inheritance in a large silicic magma system: 206Pb/238U ion probe dating of zircons from the 1.2 Ma Ongatiti ignimbrite, Taupo Volcanic Zone: Journal of Volcanology and Geothermal Research, v.135, p. 247–257, doi: 10.1016/j.jvolgeores.2004.03.004.

Chigira, M., Nakamoto, M., and Nakata, E., 2002, Weathering mechanisms and their effects on the landsliding of ignimbrite subject to vapor-phase crystallization in the Shirakawa pyroclastic flow, northern Japan: Engineering Geology, v. 66, p. 111–125, doi: 10.1016/s0013-7952(02)00035-2.

Cooper, G.F., Morgan, D.J., and Wilson, C.J., 2017, Rapid assembly and rejuvenation of a large silicic magmatic system: Insights from mineral diffusive profiles in the Kidnappers and Rocky Hill deposits, New Zealand: Earth and Planetary Science Letters, v. 473, p. 1–13, doi: 10.1016/j.epsl.2017.05.036.

Cooper, G.F., Wilson, C.J.N., Charlier, B.L.A., Wooden, J.L., and Ireland, T.R., 2014, Temporal evolution and compositional signatures of two supervolcanic systems recorded in zircons from Mangakino volcanic centre, New Zealand: Contributions to Mineralogy and Petrology, v. 167, doi: 10.1007/s00410-014-1018-2.

Cooper, G.F., and Wilson, C.J., 2014, Development, mobilisation and eruption of a large crystal- rich rhyolite: The Ongatiti ignimbrite, New Zealand: Lithos, v. 198-199, p. 38–57, doi: 10.1016/j.lithos.2014.03.014.

Cooper, G.F., Wilson, C.J., Millet, M.-A., Baker, J.A., and Smith, E.G., 2012, Systematic tapping ofindependent magma chambers during the 1Ma Kidnappers supereruption: Earth and Planetary Science Letters, v. 313-314, p. 23–33, doi: 10.1016/j.epsl.2011.11.006.

Cole, J.W., 1979, Structure, petrology, and genesis of Cenozoic volcanism, Taupo Volcanic Zone, New Zealand—a review: New Zealand Journal of Geology and Geophysics, v. 22, p. 631–657, doi: 10.1080/00288306.1979.10424173.

Cunningham, MJ 2012. Sensitive rhyolitic pyroclastic deposits in the Tauranga Region: Mineralogy, geomechanics and microstructure of peak and remoulded states. Unpublished MSc thesis, University of Waikato, Hamilton, New Zealand.

Deering, C.D., Bachmann, O., Dufek, J., and Gravley, D.M., 2011, Rift-Related Transition from Andesite to Rhyolite Volcanism in the Taupo Volcanic Zone (New Zealand) Controlled by Crystal–melt Dynamics in Mush Zones with Variable Mineral Assemblages: Journal of Petrology, v. 52, p. 2243– 2263, doi: 10.1093/petrology/egr046.

Doyle, E.E., Hogg, A.J., and Mader, H.M., 2010, A two-layer approach to modelling the transformation of dilute pyroclastic currents into dense pyroclastic flows: Proceedings of the Royal Society A: Mathematical, Physical and Engineering Sciences, v. 467, p. 1348–1371, doi: 10.1098/rspa.2010.0402.

Dupuy, C., and Dostal, J., 1978, Geochemistry of calc-alkaline volcanic rocks from southeastern Iran (kouh-e-shahsavaran): Journal of Volcanology and Geothermal Research, v. 4, p. 363–373, doi: 10.1016/0377-0273(78)90022-7.

Evans, Thomas P.H., 2003, Stratigraphy and Sedimentology of Early to Middle Miocene Strata, Western Taumarunui Region, King Country Basin (MSc Thesis): The University of Waikato, p. 2-6.

Ewart, A., 1971, Chemical changes accompanying spherulitic crystallization in rhyolitic lavas, Central Volcanic Region, New Zealand: Mineralogical Magazine, v. 38, p. 424–434, doi: 10.1180/minmag.1971.038.296.04.

Fülöp Alexandrina, and Kovacs, M., 2003, Petrology of Badenian ignimbrites, Gutai Mts. (Eastern Carpathians): Studia Universitatis Babes-Bolyai, Geologia, v. 48, p. 17–28, doi: 10.5038/1937-8602.48.1.2.

Gamble, J.A., Wright, I.C., Woodhead, J.D., and Mcculloch, M.T., 1994, Arc and back-arc geochemistry in the southern Kermadec arc-Ngatoro Basin and offshore Taupo Volcanic Zone, SW Pacific: Geological Society, London, Special Publications, v. 81, p. 193–212, doi: 10.1144/gsl.sp.1994.081.01.11.

Gansecki, C., Mahood, G., and Mcwilliams, M., 1996, 40Ar39Ar geochronology of rhyolites erupted following collapse of the Yellowstone caldera, Yellowstone Plateau volcanic field: implications for crustal contamination: Earth and Planetary Science Letters, v. 142, p. 91–107, doi: 10.1016/0012-821x(96)00088-x.

Graham, I., Cole, J., Briggs, R., Gamble, J., and Smith, I., 1995, Petrology and petrogenesis of volcanic rocks from the Taupo Volcanic Zone: a review: Journal of Volcanology and Geothermal Research, v. 68, p. 59–87, doi: 10.1016/0377-0273(95)00008-i.

Grunder, A., and Russell, J., 2005, Welding processes in volcanology: insights from field, experimental, and modeling studies: Journal of Volcanology and Geothermal Research, v. 142, p. 1–9, doi: 10.1016/j.jvolgeores.2004.10.010.

Horwell, C.J., Williamson, B.J., Llewellin, E.W., Damby, D.E., and Blond, J.S.L., 2013, The nature and formation of cristobalite at the Soufrière Hills volcano, Montserrat: implications for the petrology and stability of silicic lava domes: Bulletin of Volcanology, v. 75, doi: 10.1007/s00445-013-0696-3.

Houghton, B.F., Wilson, C.J.N., Mcwilliams, M.O., Lanphere, M.A., Weaver, S.D., Briggs, R.M., and Pringle, M.S., 1995, Chronology and dynamics of a large silicic magmatic system: Central Taupo Volcanic Zone, New Zealand: Geology, v. 23, p. 13, doi: 10.1130/0091 7613(1995)023<0013:cadoal>2.3.co;2.

Jarosewich, E., J. Nelen, and J. A. Norberg (1980). “Reference Samples for Electron Microprobe Analysis”. Geostandards and Geoanalytical Research 4.1, pp. 43– 47. doi:10.1111/j.1751-908x.1980.tb00273.x.

Jochum, K.P., Nohl, U., Herwig, K., Lammel, E., Stoll, B., and Hofmann, A.W., 2005, GeoReM: A New Geochemical Database for Reference Materials and Isotopic Standards: Geostandards and Geoanalytical Research, v. 29, p. 333–338, doi: 10.1111/j.1751-908x.2005.tb00904.x.

Kamp, Peter JJ, Adam J. Vonk, Kyle J. Bland, Angela Griffin, Shaun Hayton, Austin JW Hendy, Avon P. McIntyre, Campbell S. Nelson, and Timothy R. Naish., 2002 Megasequence architecture of Taranaki, Wanganui, and King Country basins and Neogene progradation of two continental margin wedges across western New Zealand, p. 464-480.

Kamp, P.J.J., Vonk, A.J., Bland, K.J., Hansen, R.J., Hendy, A.J.W., Mcintyre, A.P., Ngatai, M., Cartwright, S.J., Hayton, S., and Nelson, C.S., 2004, Neogene stratigraphic architecture and tectonic evolution of Wanganui, King Country, and eastern Taranaki Basins, New Zealand: New Zealand Journal of Geology and Geophysics, v. 47, p. 625–644, doi:10.1080/00288306.2004.9515080.

Keating, G.N., 2005, The role of water in cooling ignimbrites: Journal of Volcanology and Geothermal Research, v. 142, p. 145–171, doi: 10.1016/j.jvolgeores.2004.10.019.

Kochhar, N.A.R.E.S.H., 1977, Post-emplacement alkali modifications in rapidly cooled acid volcanic rocks. American Mineralogist, v. 62 (3-4), p. 333-335.

Krippner, S.J.P., Briggs, R.M., Wilson, C.J.N., and Cole, J.W., 1998, Petrography and geochemistry of lithic fragments in ignimbrites from the Mangakino Volcanic Centre: Implications for the composition of the subvolcanic crust in western Taupo Volcanic Zone, New Zealand: New Zealand Journal of Geology and Geophysics, v. 41, p. 187–199, doi: 10.1080/00288306.1998.9514803.

Kürkçüoglu, B., Sen, E., Aydar, E., Gourgaud, A., and Gündogdu, N., 1998, Geochemical approach to magmatic evolution of Mt. Erciyes stratovolcano Central Anatolia, Turkey: Journal of Volcanology and Geothermal Research, v. 85, p. 473–494, doi: 10.1016/s0377-0273(98)00067-5.

Le Maitre, R. W., Streckeisen, A., Zanettin, B., Le Bas, M., Bonin, B., & Bateman, P. (2002). Igneous rocks: a classification and glossary of terms: recommendations of the International Union of Geological Sciences Subcommission on the Systematics of Igneous Rocks. Cambridge University Press.

Leonard, G. S., Begg, J. G., Wilson, C. J. N., & Leonard, G. S., 2010, Geology of the Rotorua area.GNS Science.

Lowe, DJ, Nelson, CS 1983. Guide to the nature and methods of analysis of the clay fraction of tephras from the South Auckland Region, New Zealand. Occasional Report No. 11, University of Waikato, Department of Earth Sciences. 69 p.

Luchetti, A.C.F., Gravley, D.M., Gualda, G.A., and Nardy, A.J., 2018, Textural evidence for high-grade ignimbrites formed by low-explosivity eruptions, Paraná Magmatic Province, southern Brazil: Journal of Volcanology and Geothermal Research, v. 355, p. 87–97, doi: 10.1016/j.jvolgeores.2017.04.012.

Luchetti, A.C.F., Nardy, A.J., and Madeira, J., 2018, Silicic, high- to extremely high-grade ignimbrites and associated deposits from the Paraná Magmatic Province, southern Brazil: Journal of Volcanology and Geothermal Research, v. 355, p. 270–286, doi: 10.1016/j.jvolgeores.2017.11.010.

Martin, R.C., 1961, Stratigraphy and structural outline of the Taupo Volcanic Zone: New Zealand Journal of Geology and Geophysics, v. 4, p. 449–478, doi: 10.1080/00288306.1961.10420134.

McCormack, K.D., Gee, M.M., Mcnaughton, N.J., Smith, R., and Fletcher, I.R., 2009, U–Pb dating of magmatic and xenocryst zircons from Mangakino ignimbrites and their correlation with detrital zircons from the Torlesse metasediments, Taupo Volcanic Zone, New Zealand: Journal of Volcanology and Geothermal Research, v. 183, p. 97–111, doi: 10.1016/j.jvolgeores.2009.03.005.

Merrill, R.T., and McElhinny, M.W., 1988, The earths magnetic field: its history, origin and planetary perspective: London, Academic Press.

Paton, C., Hellstrom, J., Paul, B., Woodhead, J., and Hergt, J., 2011, Iolite: Freeware for the visualisation and processing of mass spectrometric data: Journal of Analytical Atomic Spectrometry, v. 26, p. 2508, doi: 10.1039/c1ja10172b.

Pérez-Torrado, F., Martí, J., Queralt, I., and Mangas, J., 1995, Alteration processes of the Roque Nublo ignimbrites (Gran Canaria, Canary Islands): Journal of Volcanology and Geothermal Research, v. 65, p. 191–204, doi: 10.1016/0377-0273(94)00115-w.

Portnyagin, M., Bindeman, I., Hoernle, K., and Hauff, F., 2007, Geochemistry of primitive lavas of the Central Kamchatka Depression: Magma generation at the edge of the Pacific Plate: Volcanism and Subduction: The Kamchatka Region Geophysical Monograph Series, p. 199–239, doi: 10.1029/172gm16.

Price, R.C., Gamble, J.A., Smith, I.E., Stewart, R.B., Eggins, S., and Wright, I.C., 2005, An integrated model for the temporal evolution of andesites and rhyolites and crustal development in New Zealands North Island: Journal of Volcanology and Geothermal Research, v. 140, p. 1–24, doi: 10.1016/j.jvolgeores.2004.07.013.

Rogan, A. M., 1982, A geophysical study of the Taupo Volcanic Zone, New Zealand: Journal of Geophysical Research, v. 87, p. 4073– 4088.

Rowe, M.C., Ellis, B.S., and Lindeberg, A., 2012, Quantifying crystallization and devitrification of rhyolites by means of X-ray diffraction and electron microprobe analysis: American Mineralogist, v. 97, p. 1685–1699, doi: 10.2138/am.2012.4006.

Scott, R.B., 1971, Alkali Exchange during Devitrification and Hydration of Glasses in Ignimbrite Cooling Units: The Journal of Geology, v. 79, p. 100–110, doi: 10.1086/627591.

Smith, T., and Cole, J., 1997, Somers Ignimbrite Formation: Cretaceous high-grade ignimbrites from South Island, New Zealand: Journal of Volcanology and Geothermal Research, v. 75, p. 39–57, doi: 10.1016/s0377-0273(96)00040-6.

Soengkono, S., Hochstein, M.P., Smith, I.E.M., and Itaya, T., 1992, Geophysical evidence for widespread reversely magnetised pyroclastics in the western Taupo Volcanic Zone (New Zealand): New Zealand Journal of Geology and Geophysics, v. 35, p. 47–55, doi: 10.1080/00288306.1992.9514499.

Sohn, Y., Son, M., Jeong, J., and Jeon, Y., 2009, Eruption and emplacement of a laterally extensive, crystal-rich, and pumice-free ignimbrite (the Cretaceous Kusandong Tuff, Korea): Sedimentary Geology, v. 220, p. 190–203, doi: 10.1016/j.sedgeo.2009.04.020.

Sparks, R.S.J., and Wilson, L., 1976, A model for the formation of ignimbrite by gravitational column collapse: Journal of the Geological Society, v. 132, p. 441–451, doi: 10.1144/gsjgs.132.4.0441.

Sparks, R.S.J., Wilson, L., and Hulme, G., 1978, Theoretical modeling of the generation, movement, and emplacement of pyroclastic flows by column collapse: Journal of Geophysical Research: Solid Earth, v. 83, p. 1727–1739, doi: 10.1029/jb083ib04p01727.

Stern, T.A., 1979, Regional and residual gravity fields, central North Island, New Zealand: New Zealand Journal of Geology and Geophysics, v. 22, p. 479–485, doi:10.1080/00288306.1979.10424156.

Stern, T.A., Stratford, W.R., and Salmon, M.L., 2006, Subduction evolution and mantle dynamics at a continental margin: Central North Island, New Zealand: Reviews of Geophysics, v. 44, doi: 10.1029/2005rg000171.

Sun, S.-S., and Mcdonough, W.F., 1989, Chemical and isotopic systematics of oceanic basalts: implications for mantle composition and processes: Geological Society, London, Special Publications, v. 42, p. 313–345, doi: 10.1144/gsl.sp.1989.042.01.19.

Taylor, S.R. and McLennan, S.M. (1985), The Continental Crust; Its composition and evolution; an examination of the geochemical record preserved in sedimentary rocks. Blackwell, Oxford. 312.

Temel, A., Gündoğdu, M., Gourgaud, A., and Pennec, J.-L.L., 1998, Ignimbrites of Cappadocia (Central Anatolia, Turkey): petrology and geochemistry: Journal of Volcanology and Geothermal Research, v. 85, p. 447–471, doi: 10.1016/s0377-0273(98)00066-3.

Wallace, L.M., 2004, Subduction zone coupling and tectonic block rotations in the North Island, New Zealand: Journal of Geophysical Research, v. 109, doi: 10.1029/2004jb003241. Wilson, C. J. N., 1986, Reconnaissance stratigraphy and volcanology of ignimbrites from Mangakino volcano. Late Cenozoic volcanism in New Zealand. Royal Society of New Zealand Bulletin, 23, 179-193 p.

Whitton, JS, Churchman, GJ 1987. Standard methods for mineral analysis of soil survey samples for characterisation and classification in NZ Soil Bureau. NZ Soil Bureau Scientific Report 79. 27 p.

Willcock, M.A.W., and Cas, R.A.F., 2014, Primary welding and crystallization textures preserved in the intra-caldera ignimbrites of the Permian Ora Formation, northern Italy: implications for deposit thermal state and cooling history: Bulletin of Volcanology, v. 76, doi: 10.1007/s00445-014-0819-5.

Wilson, C. J. N. 1986: Reconnaissance stratigraphy and volcanology of ignimbrites from Mangakino volcano. In: Smith, I. E. M. ed. Late Cenozoic volcanism in New Zealand. Royal Society of New Zealand Bulletin 23: 179- 193.12.

Wilson, C.J.N., Houghton, B.F., Kampt, P.J.J., and Mcwilliamst, M.O., 1995, An exceptionally widespread ignimbrite with implications for pyroclastic flow emplacement: Nature, v. 378, p. 605–607, doi: 10.1038/378605a0.

Wilson, C., Houghton, B., Mcwilliams, M., Lanphere, M., Weaver, S., and Briggs, R., 1995, Volcanic and structural evolution of Taupo Volcanic Zone, New Zealand: a review: Journal of Volcanology and Geothermal Research, v. 68, p. 1–28, doi: 10.1016/0377-0273(95)00006-g.

Wilson, C.J.N., Rogan, A.M., Smith, I.E.M., Northey, D.J., Nairn, I.A., and Houghton, B.F., 1984, Caldera volcanoes of the Taupo Volcanic Zone, New Zealand: Journal of Geophysical Research, v. 89, p. 8463, doi: 10.1029/jb089ib10p08463.

Winchester, J., and Floyd, P., 1977, Geochemical discrimination of different magma series and their differentiation products using immobile elements: Chemical Geology, v. 20, p. 325–343, doi: 10.1016/0009-2541(77)90057-2.

# Appendices

**Appendix I:** Field Localities

| Locality Number | Latitude | Longitude | Sample Number | Description |
|---|---|---|---|---|
| 1 | N/A | N/A | 1 | Roadcutting to the east of Mangawhio road |
| 2 | N/A | N/A | 2 | Quarry at north end of Waipari road |
| 3 | N/A | N/A | 3 | Roadcutting to the east of Mangawhio road |
| 4 | N/A | N/A | 4 | Boulder at bend of Waipari road |
| 5 | N/A | N/A | 5 | Stream along Waipari road |
| 5 | N/A | N/A | 6 | Stream along Waipari road |
| 5 | N/A | N/A | 7 | Stream along Waipari road |
| 6 | 38 18 03.65595 S | 175 34 01.32492 E | 8 | Roadcutting to the east of Mangawhio Road |
| 6 | 38 18 03.65595 S | 175 34 01.32492 E | 9 | Roadcutting to the east of Mangawhio Road |
| 7 | 38 18 04.13675 S | 175 33 58.62513 E | 10 | Ignimbrite plateau to the west of Mangawhio Road |
| 8 | 38 18 05.19734 S | 175 33 57.59228 E | 11 | Ignimbrite plateau to the west of Mangawhio Road |
| 9 | 38 18 05.11631 S | 175 33 56.84849 E | 12 | Ignimbrite plateau to the west of Mangawhio Road |
| 10 | 38 18 05.11631 S | 175 33 56.84849 E | 12 | Ignimbrite plateau to the west of Mangawhio Road |
| 11 | 38 19 06.08089 S | 175 35 07.01508 E | 13 | Roadcutting to the east of Mangawhio Road |
| 12 | 38 19 06.10604 S | 175 35 07.34536 E | 14 | Roadcutting to the east of Mangawhio Road |
| 13 | 38 19 07.78960 S | 175 36 28.02113 E | 15 | Roadcutting to the east of Mangawhio Road |
| 14 | 38 19 00.66414 S | 175 36 29.00087 E | 16 | Roadcutting to the east of Mangawhio Road |
| 15 | 38 19 01.98958 S | 175 36 04.38658 E | 17 | Roadcutting to the east of Mangawhio Road |
| 16 | 38 18 21.90000 S | 175 37 48.24000 E | 18 | Roadcutting along Mangawhio Road |
| 16 | 38 18 21.90000 S | 175 37 48.24000 E | 19 | Roadcutting along Mangawhio Road |
| 17 | 38 18 45.24000 S | 175 37 41.94000 E | 20 | Hillside boulders on west side of Mangawhio Road |
| 18 | 38 18 51.18000 S | 175 37 31.44000 E | 21 | Hillside boulders on west side of Mangawhio Road |
| 18 | 38 18 51.18000 S | 175 37 31.44000 E | 22 | Hillside boulders on west side of Mangawhio Road |
| 19 | 38 19 05.22000 S | 175 35 14.40000 E | 23 | Roadcutting along Mangawhio Road |
| 19 | 38 19 05.22000 S | 175 35 14.40000 E | 24 | Roadcutting along Mangawhio Road |
| 20 | 38 18 49 S | 175 34 29 E | 25 | Hillside boulders on east side of Mangawhio Road |

| Locality Number | Latitude | Longitude | Sample Number | Description |
|---|---|---|---|---|
| 21 | 38 19.178 S | 175 34 188 E | 26A | Weathered through ignimbrite on the west side of Mangawhio Road |
| 21 | 38 19.178 S | 175 34 188 E | 26B | Weathered through ignimbrite on the west side of Mangawhio Road |
| 21 | 38 19.178 S | 175 34 188 E | 26C | Weathered through ignimbrite on the west side of Mangawhio Road |
| 21 | 38 19.178 S | 175 34 188 E | 26D | Weathered through ignimbrite on the west side of Mangawhio Road |
| 21 | 38 19.178 S | 175 34 188 E | 26E | Weathered through ignimbrite on the west side of Mangawhio Road |
| 22 | 38 19 06.24000 S | 175 34 31.38000 E | 27 | Paddocks on the east side of Mangawhio Road |
| 23 | 38 19 04.98000 S | 175 35 39.24000 E | N/A | Hillside boulders along Mangawhio Road |
| 24 | 38 19 08.70000 S | 175 36 03.66000 E | N/A | Hillside boulders along Mangawhio Road |
| 25 | 38 19 13.50000 S | 175 36 25.92000 E | N/A | Roadcutting along Mangawhio Road |
| 25B | 38 18 52.50000 S | 175 37 37.74000 E | 28 | Hillside boulders along Mangawhio Road |
| 26 | 38 19 10.20000 S | 175 34 29.10000 E | N/A | Paddocks on the east side of Mangawhio Road |
| 27 | 38 19 18.48000 S | 175 34 31.38000 E | 29 | Hillside boulders along Mangawhio Road |
| 27 | 38 19 18.48000 S | 175 34 31.38000 E | 29A | Hillside boulders along Mangawhio Road |
| 27 | 38 19 18.48000 S | 175 34 31.38000 E | 30A | Hillside boulders along Mangawhio Road |
| 27 | 38 19 18.48000 S | 175 34 31.38000 E | 30B | Hillside boulders along Mangawhio Road |
| 27 | 38 19 18.48000 S | 175 34 31.38000 E | 30C | Hillside boulders along Mangawhio Road |
| 29 | 38 17 47 S | 175 34 25 E | 31 | Ignimbrite forming plateau north of Wairehi Road |
| 29 | 38 17 47 S | 175 34 25 E | 32 | Ignimbrite forming plateau north of Wairehi Road |
| 30 | 38 17 49 S | 175 34 29 E | 33 | Ignimbrite forming plateau north of Wairehi Road |
| 31 | 38 19 03.76693 S | 175 33 58.13424 E | 34D | Dome-like feature to the west side of Mangawhio Road |
| 31 | 38 19 03.76693 S | 175 33 58.13424 E | 35D | Dome-like feature to the west side of Mangawhio Road |
| 31 | 38 19 03.76693 S | 175 33 58.13424 E | 36D | Dome-like feature to the west side of Mangawhio Road |
| 31 | 38 19 03.76693 S | 175 33 58.13424 E | 37D | Dome-like feature to the west side of Mangawhio Road |

| Locality Number | Latitude | Longitude | Sample Number | Description |
|---|---|---|---|---|
| 32 | 38 19 5 S | 175 32 34 E | 38 | Roadcutting along Tolley Road |
| 33 | 38 19 52 S | 175 32 34 E | N/A | Roadcutting along Tolley Road |
| 34 | 38 19 41 S | 175 32 31 E | 39 | Roadcutting along Tolley Road |
| 35 | 38 19 11 S | 175 32 36 E | 40 | Roadcutting along Tolley Road |
| 36 | 38 19 4 S | 175 32 37 E | 41 | Roadcutting along Tolley Road |
| 36 | 38 19 4 S | 175 32 37 E | 42 | Roadcutting along Tolley Road |
| 37 | 38 19 5 S | 175 32 37 E | 43 | Roadcutting along Tolley Road |
| 38 | 38 17 53.50688 S | 175 34 42.53977 E | 44 | Hillside boulders/Roadcutting along Wairehi Road |
| 39 | 38 17 48.86957 S | 175 35 31.02697 E | 45 | Hillside boulders/Roadcutting along Wairehi Road |
| 39 | 38 17 48.86957 S | 175 35 31.02697 E | 46 | Hillside boulders/Roadcutting along Wairehi Road |
| 39 | 38 17 48.86957 S | 175 35 31.02697 E | 47 | Hillside boulders/Roadcutting along Wairehi Road |
| 40 | 38 17 52.64972 S | 175 35 03.78959 E | 48 | Hillside boulders/Roadcutting along Wairehi Road |
| 42 | 38 17 657 S | 175 34 126 E | 31 | North end of Waipari Road at waterfall |
| 42 | 38 17 657 S | 175 34 126 E | 34 | North end of Waipari Road at waterfall |
| 42 | 38 17 657 S | 175 34 126 E | 35 | North end of Waipari Road at waterfall |
| 42 | 38 17 657 S | 175 34 126 E | 36 | North end of Waipari Road at waterfall |
| 42 | 38 17 657 S | 175 34 126 E | 37A | North end of Waipari Road at waterfall |
| 42 | 38 17 657 S | 175 34 126 E | 37B | North end of Waipari Road at waterfall |
| 42 | 38 17 657 S | 175 34 126 E | 37C | North end of Waipari Road at waterfall |
| 42 | 38 17 657 S | 175 34 126 E | 50 | North end of Waipari Road at waterfall |
| 42 | 38 17 657 S | 175 34 126 E | 51 | North end of Waipari Road at waterfall |
| 42 | 38 17 657 S | 175 34 126 E | 51A | North end of Waipari Road at waterfall |
| 42 | 38 17 657 S | 175 34 126 E | 52 | North end of Waipari Road at waterfall |

**Appendix II:** Sample List

| Locality Number | Sample Number | Thin Sections | XRF | XRD | SEM Thin Section | SEM Chips | LA-ICP-MS | EPMA |
|---|---|---|---|---|---|---|---|---|
| 1 | 1 | X | √ | √ | √ | √ | X | √ |
| 2 | 2 | √ | X | X | X | X | X | X |
| 3 | 3 | X | X | X | X | X | X | X |
| 4 | 4 | X | X | X | X | X | X | X |
| 5 | 5 | √ | X | X | X | X | X | X |
| 5 | 6 | √ | X | X | X | √ | X | X |
| 6 | 7 | √ | X | X | X | X | X | X |
| 6 | 8 | √ | X | X | X | X | X | X |
| 6 | 9 | X | X | X | X | X | X | X |
| 7 | 10 | X | X | X | X | X | X | X |
| 8 | 11 | √ | √ | √ | X | X | X | X |
| 9 | 12 | X | X | X | X | X | X | X |
| 10 | 12 | √ | X | X | X | X | X | X |
| 11 | 13 | √ | X | X | √ | X | X | √ |
| 12 | 14 | √ | X | X | X | X | X | X |
| 13 | 15 | √ | X | X | X | X | X | √ |
| 14 | 16 | √ | X | X | X | X | X | X |
| 15 | 17 | X | X | X | X | X | X | X |
| 16 | 18 | X | X | X | X | X | X | X |
| 16 | 19 | X | X | X | X | X | X | X |
| 17 | 20 | X | X | X | X | X | X | X |
| 18 | 21 | X | X | X | X | X | X | X |
| 18 | 22 | X | X | X | X | X | X | X |
| 19 | 23 | √ | √ | √ | X | √ | X | X |
| 19 | 24 | X | X | X | X | X | X | X |
| 20 | 25 | √ | X | X | X | X | X | X |

| Locality Number | Sample Number | Thin Sections | XRF | XRD | SEM Thin Section | SEM Chips | LA-ICP-MS | EPMA |
|---|---|---|---|---|---|---|---|---|
| 21 | 26A | √ | X | X | X | √ | X | X |
| 21 | 26B | √ | X | X | X | √ | X | X |
| 21 | 26C | √ | X | X | X | √ | X | X |
| 21 | 26D | √ | X | X | X | X | X | √ |
| 21 | 26E | √ | X | X | X | √ | √ | X |
| 22 | 27 | √ | √ | √ | X | √ | X | X |
| 23 | N/A | X | X | X | X | X | X | X |
| 24 | N/A | X | X | X | X | X | X | X |
| 25 | N/A | X | X | X | X | X | X | X |
| 25B | 28 | X | X | X | X | X | X | X |
| 26 | N/A | X | X | X | X | X | X | X |
| 27 | 29 | X | X | X | X | X | X | X |
| 27 | 29A | X | X | X | X | X | X | X |
| 27 | 30A | X | X | X | X | X | X | X |
| 27 | 30B | X | X | X | X | X | X | X |
| 27 | 30C | X | √ | √ | √ | √ | X | √ |
| 28 | 31 | √ | X | X | X | √ | X | X |
| 29 | 32 | √ | X | X | X | X | X | X |
| 30 | 33 | X | X | X | X | X | X | X |
| 31 | 34D | √ | X | X | X | X | X | X |
| 31 | 35D | X | X | X | X | X | X | X |
| 31 | 36D | X | X | X | X | X | X | X |
| 31 | 37D | X | X | X | X | X | X | X |
| 32 | 38 | X | X | X | X | X | X | X |
| 33 | N/A | X | X | X | X | X | X | X |
| 34 | 39 | X | X | X | X | X | X | X |
| 35 | 40 | X | X | X | X | X | X | X |

| Locality Number | Sample Number | Thin Sections | XRF | XRD | SEM Thin Section | SEM Chips | LA-ICP-MS | EPMA |
|---|---|---|---|---|---|---|---|---|
| 36 | 41 | X | X | X | X | X | X | X |
| 36 | 42 | X | X | X | X | X | X | X |
| 37 | 43 | √ | X | X | X | X | X | X |
| 38 | 44 | X | √ | √ | √ | √ | √ | √ |
| 39 | 45 | X | X | X | X | X | X | X |
| 39 | 46 | X | X | X | X | X | X | X |
| 39 | 47 | X | X | X | X | X | X | X |
| 40 | 48 | √ | √ | √ | √ | √ | X | X |
| 41 | 37A | √ | √ | √ | √ | √ | X | √ |
| 41 | 37B | √ | √ | √ | √ | √ | X | √ |
| 41 | 37C | X | X | X | X | X | X | X |
| 42 | 31 | X | X | X | X | X | X | X |
| 42 | 34 | X | X | X | X | X | X | X |
| 42 | 35 | √ | √ | √ | √ | √ | X | X |
| 42 | 36 | √ | X | X | X | X | X | X |
| 42 | 37 | X | X | X | X | X | X | X |
| 42 | 50 | √ | X | X | X | X | X | X |
| 42 | 51 | √ | X | X | X | √ | X | X |
| 42 | 51A | √ | √ | √ | √ | √ | X | X |
| 42 | 52 | √ | X | X | X | X | X | X |

**Appendix III**: Scanning Electron Microscopy (SEM) and Energy Dispersive Spectrometry (EDS) Analyses of selected areas observed and analysed in polished thin section and in rough chips.

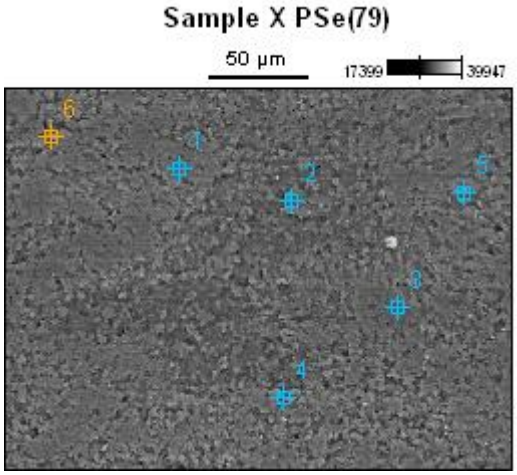


Image Name: Sample 13 PSe(79)

Accelerating Voltage: 20.0 kV

Magnification: 500

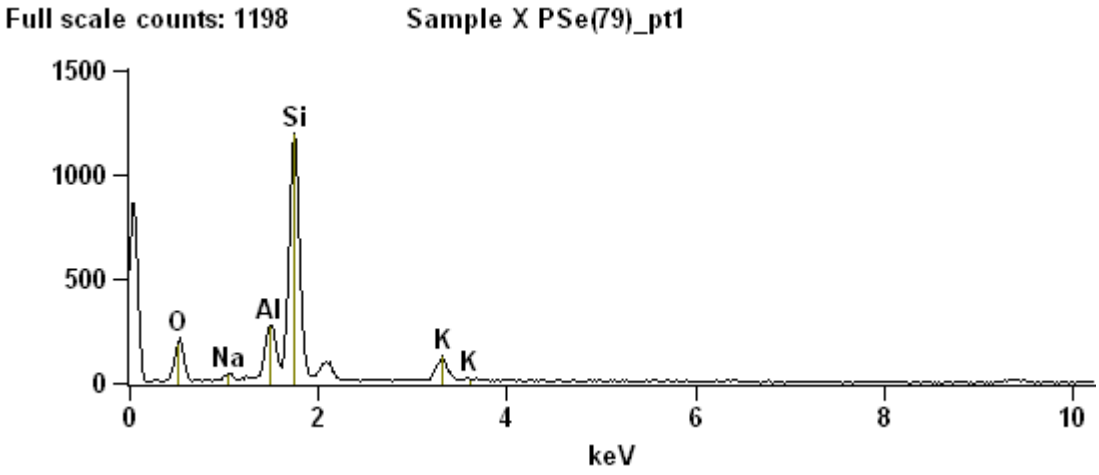


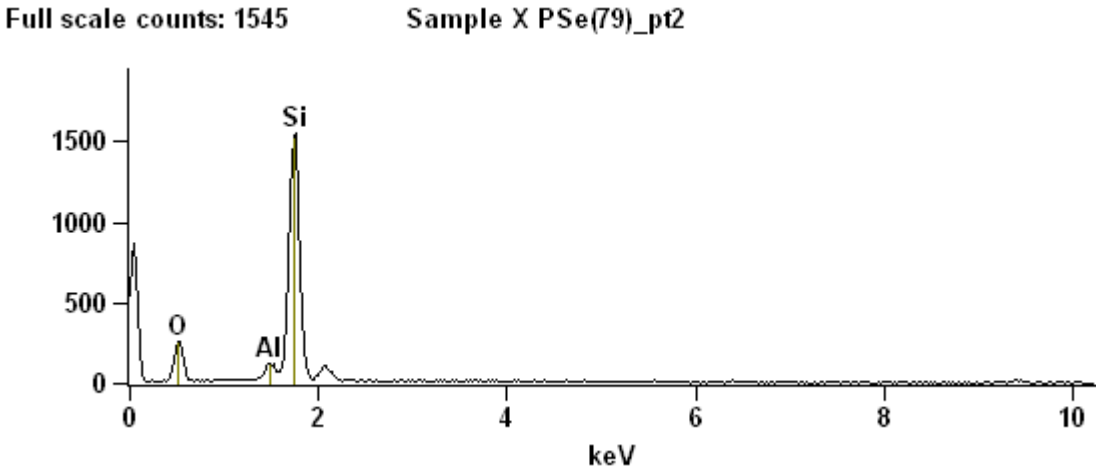

Full scale counts: 1263 Sample X PSe(79)_pt3

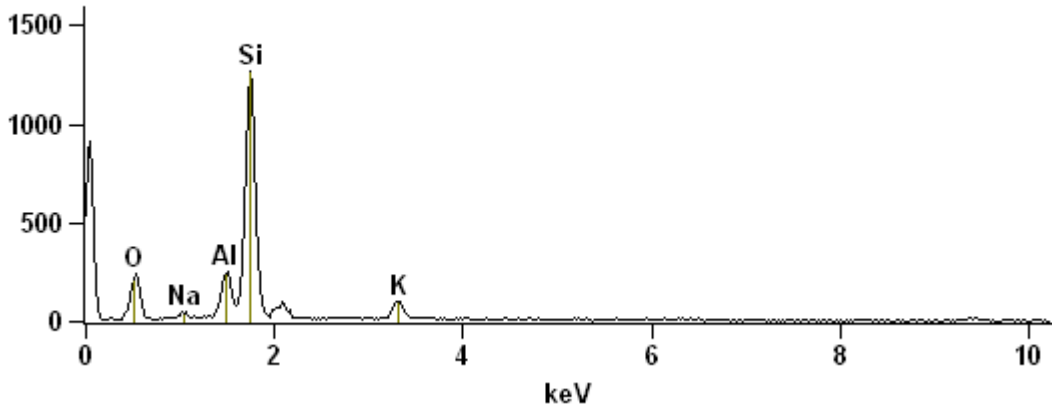


Full scale counts: 1084 Sample X PSe(79)_pt4

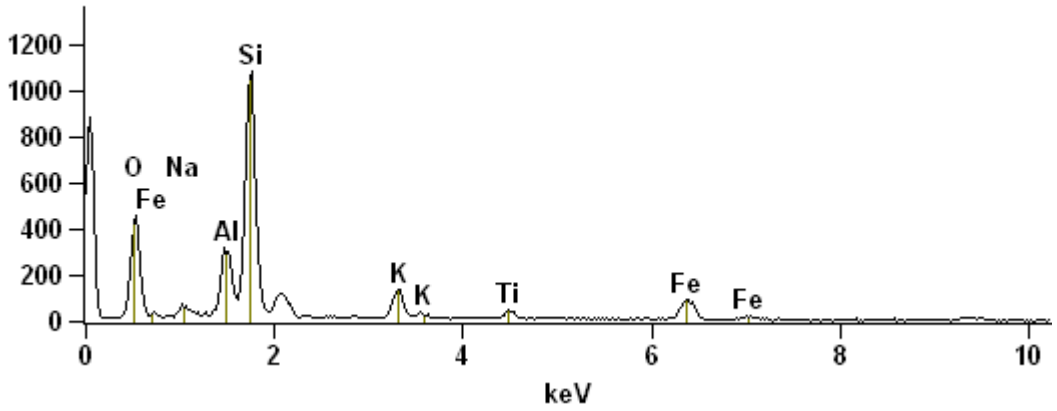


Full scale counts: 972 Sample X PSe(79)_pt5

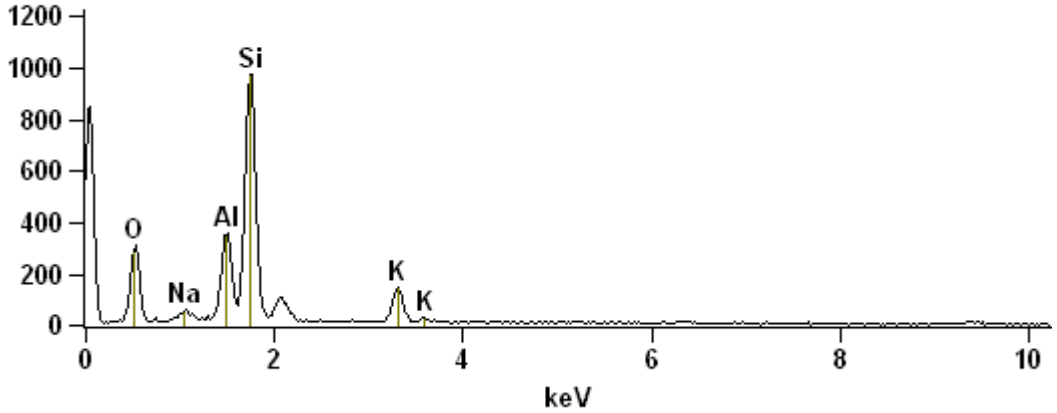

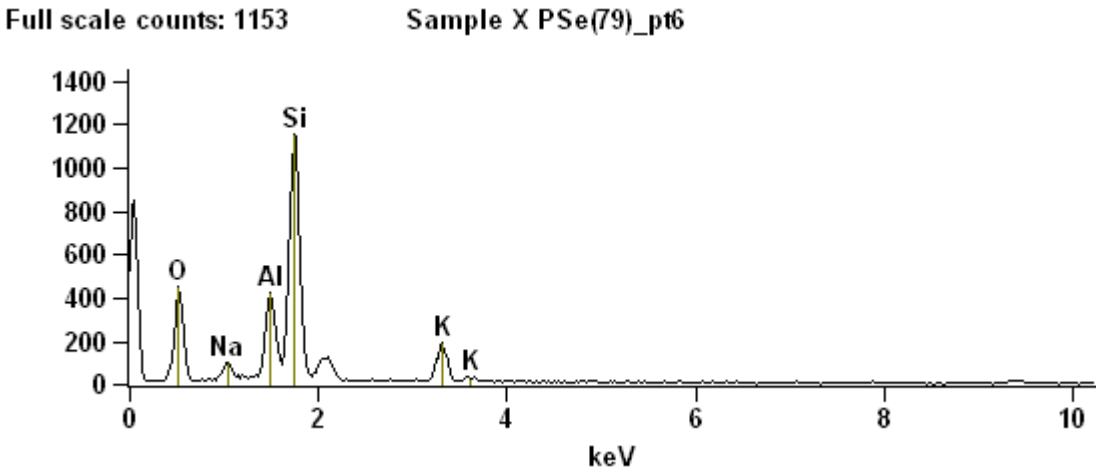


Weight %

| | O-K | Na-K | Al-K | Si-K | K-K | Ti-K | Fe-K |
|---|---|---|---|---|---|---|---|
| ***Sample X PSe(79)_pt1*** | 27.42 | 1.64 | 9.49 | 52.63 | 8.83 | | |
| ***Sample X PSe(79)_pt2*** | 31.38 | | 2.91 | 65.71 | | | |
| ***Sample X PSe(79)_pt3*** | 30.26 | 1.39 | 8.02 | 53.06 | 7.27 | | |
| ***Sample X PSe(79)_pt4*** | 32.03 | 2.20 | 8.20 | 34.01 | 5.82 | 2.69 | 15.05 |
| ***Sample X PSe(79)_pt5*** | 34.01 | 2.39 | 11.72 | 41.99 | 9.89 | | |
| ***Sample X PSe(79)_pt6*** | 36.94 | 3.22 | 10.75 | 39.12 | 9.97 | | |

Weight % Error (+/- 1 Sigma)

| | O-K | Na-K | Al-K | Si-K | K-K | Ti-K | Fe-K |
|---|---|---|---|---|---|---|---|
| ***Sample X PSe(79)_pt1*** | +/-0.68 | +/-0.23 | +/-0.38 | +/-0.69 | +/-0.47 | | |
| ***Sample X PSe(79)_pt2*** | +/-0.67 | | +/-0.30 | +/-0.68 | | | |
| ***Sample X PSe(79)_pt3*** | +/-0.69 | +/-0.23 | +/-0.36 | +/-0.67 | +/-0.43 | | |
| ***Sample X PSe(79)_pt4*** | +/-0.62 | +/-0.25 | +/-0.31 | +/-0.50 | +/-0.32 | +/-0.34 | +/-0.78 |
| ***Sample X PSe(79)_pt5*** | +/-0.70 | +/-0.25 | +/-0.38 | +/-0.63 | +/-0.44 | | |
| ***Sample X PSe(79)_pt6*** | +/-0.64 | +/-0.24 | +/-0.34 | +/-0.55 | +/-0.38 | | |

Atom %

| | O-K | Na-K | Al-K | Si-K | K-K | Ti-K | Fe-K |
|---|---|---|---|---|---|---|---|
| ***Sample X PSe(79)_pt1*** | 40.45 | 1.68 | 8.30 | 44.23 | 5.33 | | |
| ***Sample X PSe(79)_pt2*** | 44.49 | | 2.44 | 53.07 | | | |
| ***Sample X PSe(79)_pt3*** | 43.74 | 1.40 | 6.87 | 43.69 | 4.30 | | |
| ***Sample X PSe(79)_pt4*** | 48.98 | 2.34 | 7.43 | 29.63 | 3.64 | 1.37 | 6.59 |
| ***Sample X PSe(79)_pt5*** | 48.18 | 2.35 | 9.84 | 33.89 | 5.74 | | |
| ***Sample X PSe(79)_pt6*** | 51.36 | 3.11 | 8.87 | 30.99 | 5.67 | | |

Atom % Error (+/- 1 Sigma)

| | O-K | Na-K | Al-K | Si-K | K-K | Ti-K | Fe-K |
|---|---|---|---|---|---|---|---|
| ***Sample X PSe(79)_pt1*** | +/-1.01 | +/-0.24 | +/-0.33 | +/-0.58 | +/-0.28 | | |
| ***Sample X PSe(79)_pt2*** | +/-0.95 | | +/-0.25 | +/-0.55 | | | |
| ***Sample X PSe(79)_pt3*** | +/-0.99 | +/-0.23 | +/-0.31 | +/-0.56 | +/-0.26 | | |
| ***Sample X PSe(79)_pt4*** | +/-0.95 | +/-0.27 | +/-0.29 | +/-0.43 | +/-0.20 | +/-0.18 | +/-0.34 |
| ***Sample X PSe(79)_pt5*** | +/-1.00 | +/-0.25 | +/-0.32 | +/-0.51 | +/-0.25 | | |
| ***Sample X PSe(79)_pt6*** | +/-0.89 | +/-0.23 | +/-0.28 | +/-0.44 | +/-0.22 | | |

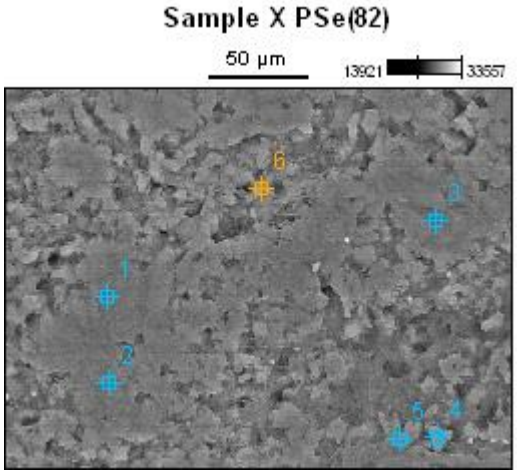


Image Name: Sample 13 PSe(82)

Accelerating Voltage: 20.0 kV

Magnification: 500

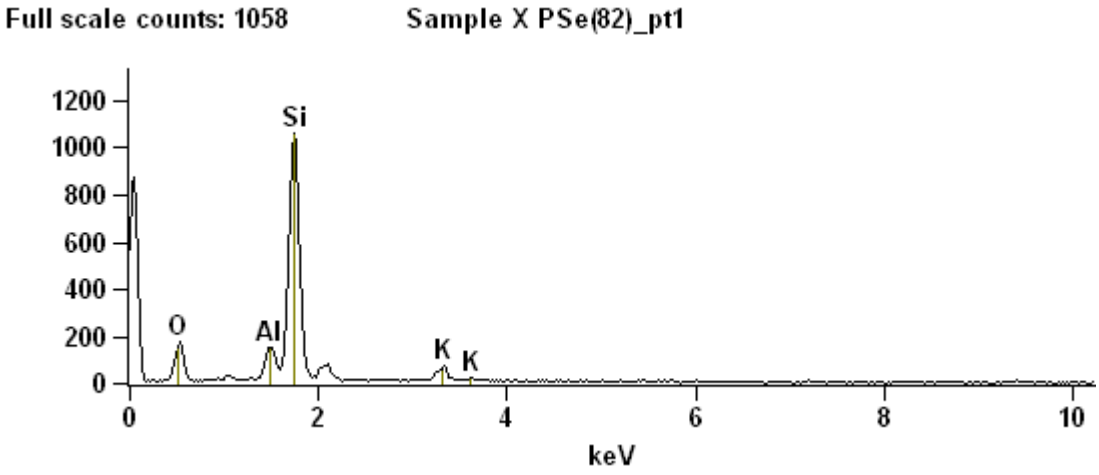


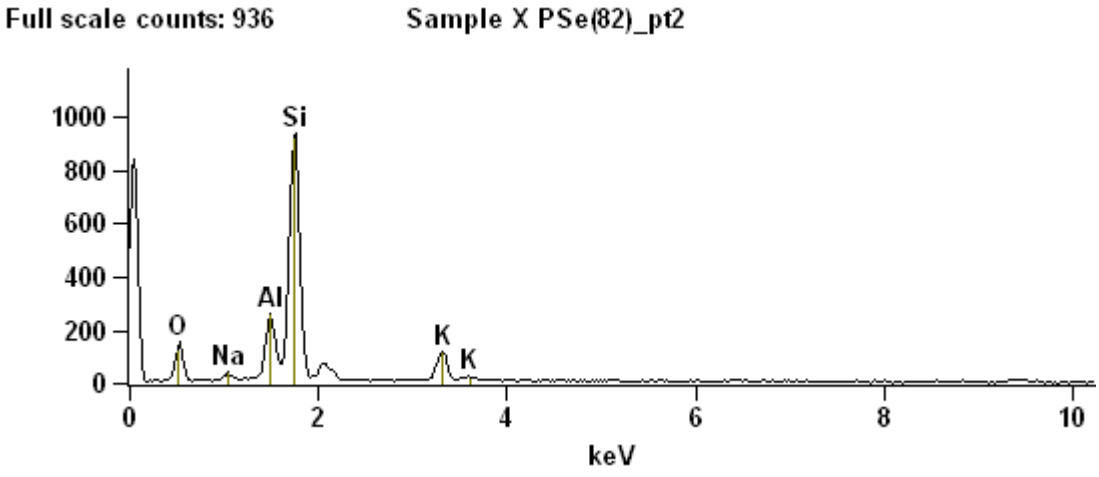

Full scale counts: 976 Sample X PSe(82)_pt3

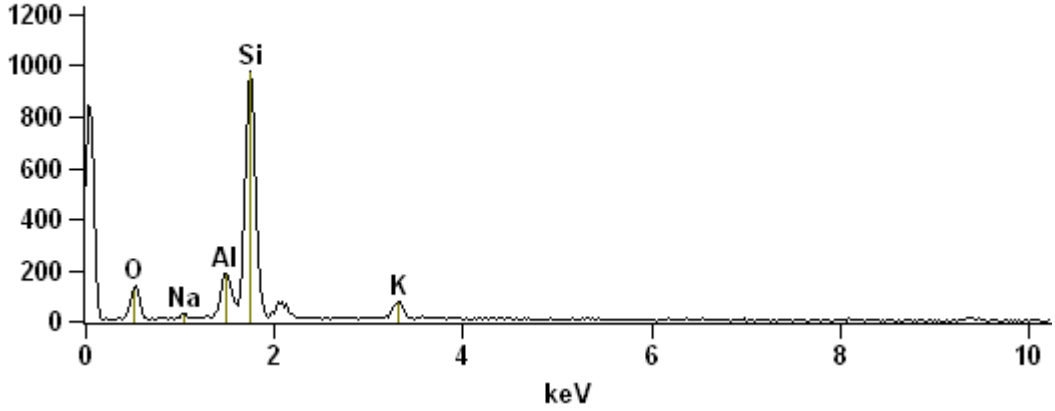


Full scale counts: 1019 Sample X PSe(82)_pt4

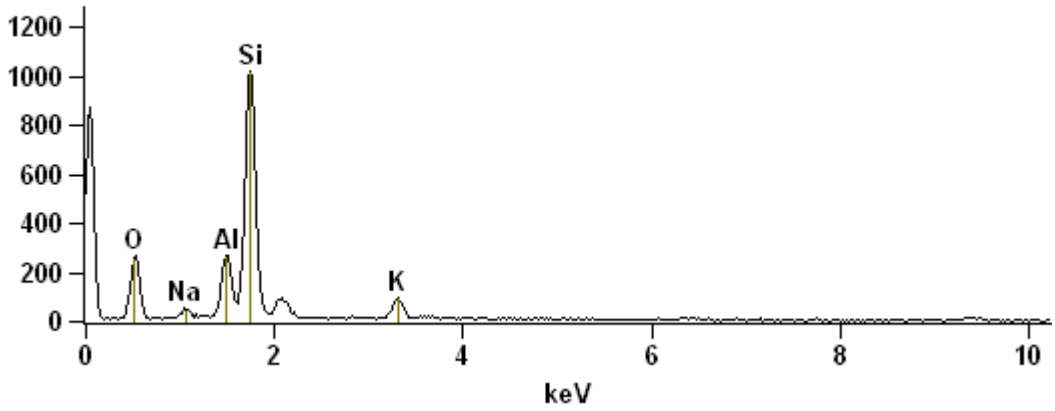


Full scale counts: 1020 Sample X PSe(82)_pt5

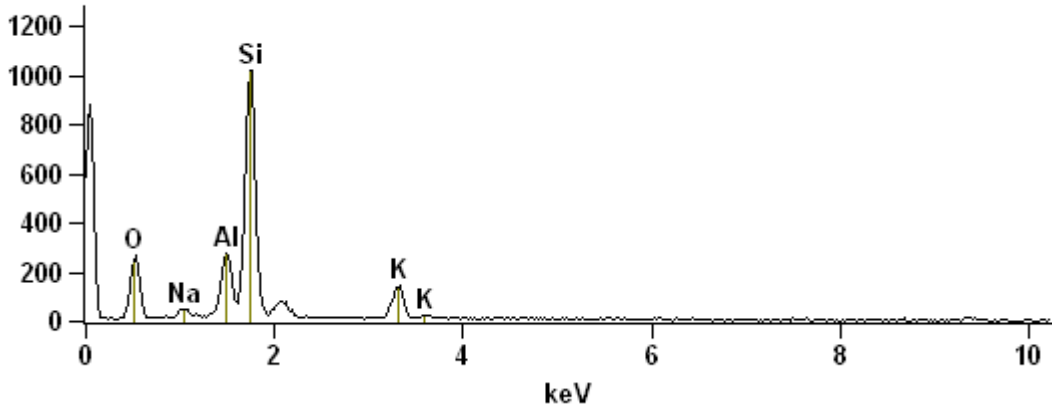

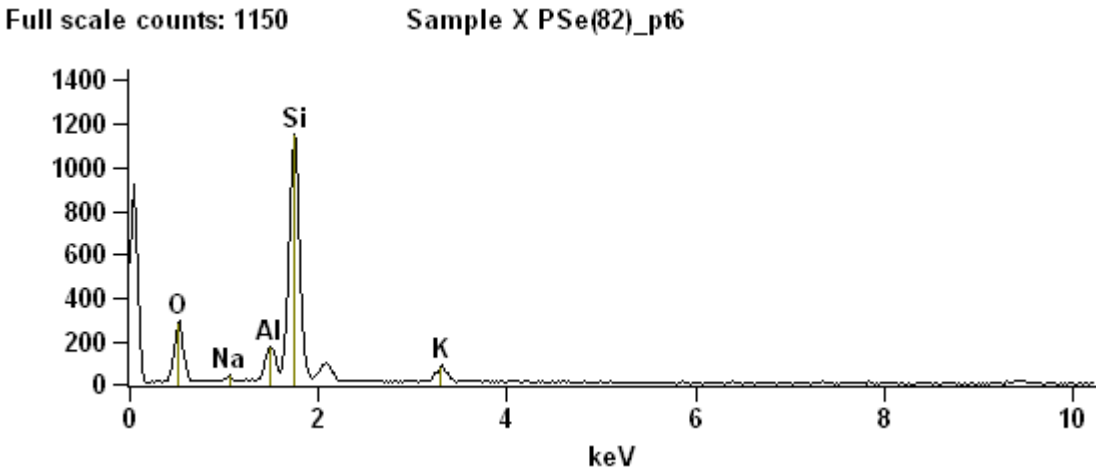


Weight %

| | O-K | Na-K | Al-K | Si-K | K-K |
|---|---|---|---|---|---|
| ***Sample X PSe(82)_pt1*** | 27.38 | | 6.38 | 59.71 | 6.53 |
| ***Sample X PSe(82)_pt2*** | 23.28 | 1.52 | 10.23 | 53.87 | 11.10 |
| ***Sample X PSe(82)_pt3*** | 24.39 | 1.12 | 8.50 | 58.32 | 7.67 |
| ***Sample X PSe(82)_pt4*** | 33.20 | 2.18 | 9.63 | 48.04 | 6.95 |
| ***Sample X PSe(82)_pt5*** | 32.99 | 2.16 | 9.69 | 45.15 | 10.00 |
| ***Sample X PSe(82)_pt6*** | 35.08 | 1.18 | 5.78 | 52.62 | 5.34 |

Weight % Error (+/- 1 Sigma)

| | O-K | Na-K | Al-K | Si-K | K-K |
|---|---|---|---|---|---|
| ***Sample X PSe(82)_pt1*** | +/-0.79 | | +/-0.39 | +/-0.79 | +/-0.51 |
| ***Sample X PSe(82)_pt2*** | +/-0.76 | +/-0.25 | +/-0.44 | +/-0.80 | +/-0.58 |
| ***Sample X PSe(82)_pt3*** | +/-0.78 | +/-0.14 | +/-0.43 | +/-0.82 | +/-0.53 |
| ***Sample X PSe(82)_pt4*** | +/-0.73 | +/-0.25 | +/-0.38 | +/-0.69 | +/-0.44 |
| ***Sample X PSe(82)_pt5*** | +/-0.70 | +/-0.24 | +/-0.37 | +/-0.64 | +/-0.45 |
| ***Sample X PSe(82)_pt6*** | +/-0.74 | +/-0.23 | +/-0.34 | +/-0.67 | +/-0.41 |

Atom %

| | O-K | Na-K | Al-K | Si-K | K-K |
|---|---|---|---|---|---|
| ***Sample X PSe(82)_pt1*** | 40.36 | | 5.57 | 50.13 | 3.94 |
| ***Sample X PSe(82)_pt2*** | 35.47 | 1.61 | 9.25 | 46.76 | 6.92 |
| ***Sample X PSe(82)_pt3*** | 36.64 | 1.17 | 7.57 | 49.90 | 4.71 |
| ***Sample X PSe(82)_pt4*** | 47.00 | 2.15 | 8.09 | 38.74 | 4.02 |
| ***Sample X PSe(82)_pt5*** | 47.09 | 2.15 | 8.20 | 36.71 | 5.84 |
| ***Sample X PSe(82)_pt6*** | 49.08 | 1.15 | 4.79 | 41.93 | 3.06 |

Atom % Error (+/- 1 Sigma)

| | O-K | Na-K | Al-K | Si-K | K-K |
|---|---|---|---|---|---|
| ***Sample X PSe(82)_pt1*** | +/-1.17 | | +/-0.34 | +/-0.66 | +/-0.31 |
| ***Sample X PSe(82)_pt2*** | +/-1.16 | +/-0.27 | +/-0.39 | +/-0.69 | +/-0.36 |
| ***Sample X PSe(82)_pt3*** | +/-1.18 | +/-0.15 | +/-0.38 | +/-0.70 | +/-0.33 |
| ***Sample X PSe(82)_pt4*** | +/-1.03 | +/-0.25 | +/-0.32 | +/-0.55 | +/-0.25 |
| ***Sample X PSe(82)_pt5*** | +/-1.00 | +/-0.24 | +/-0.31 | +/-0.52 | +/-0.26 |
| ***Sample X PSe(82)_pt6*** | +/-1.03 | +/-0.22 | +/-0.28 | +/-0.53 | +/-0.23 |

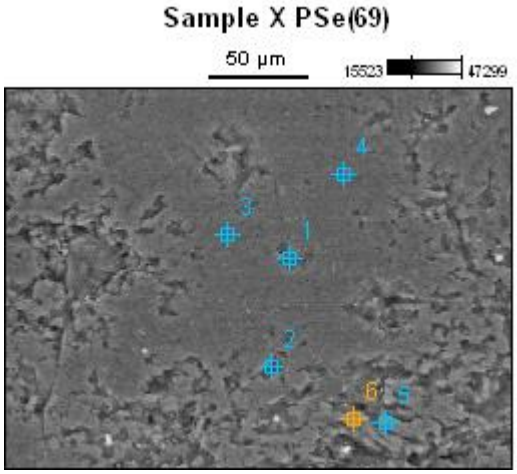


Image Name: Sample 13 PSe(69)

Accelerating Voltage: 20.0 kV

Magnification: 500

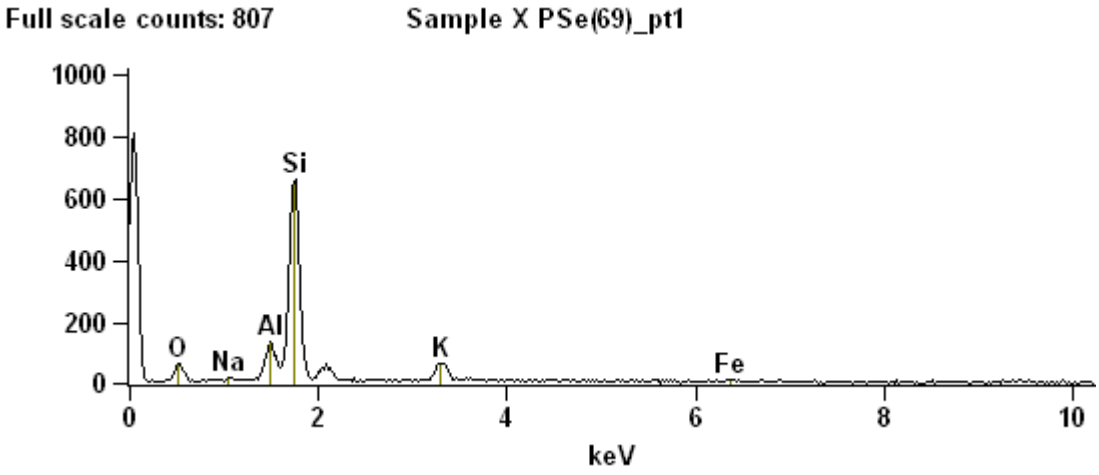


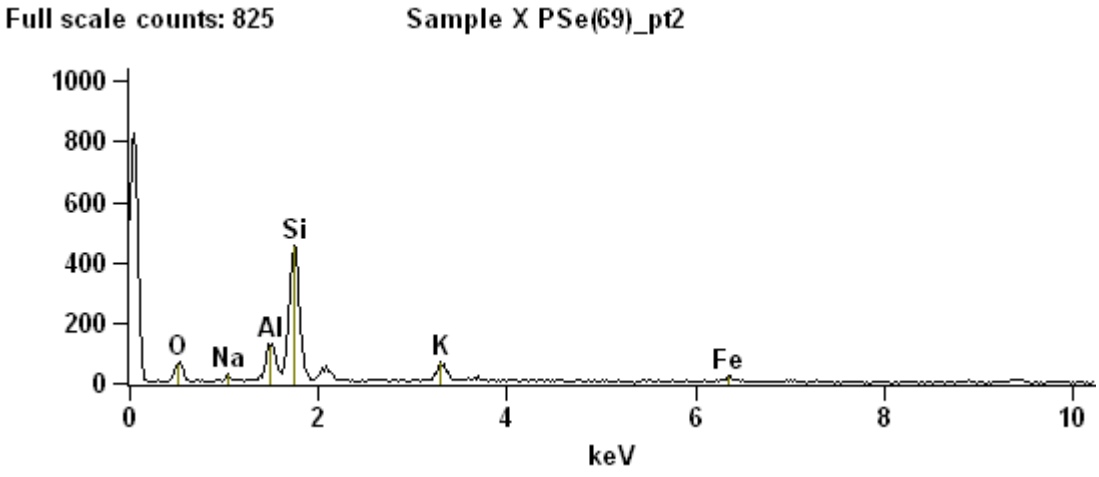

Full scale counts: 896 Sample X PSe(69)_pt3

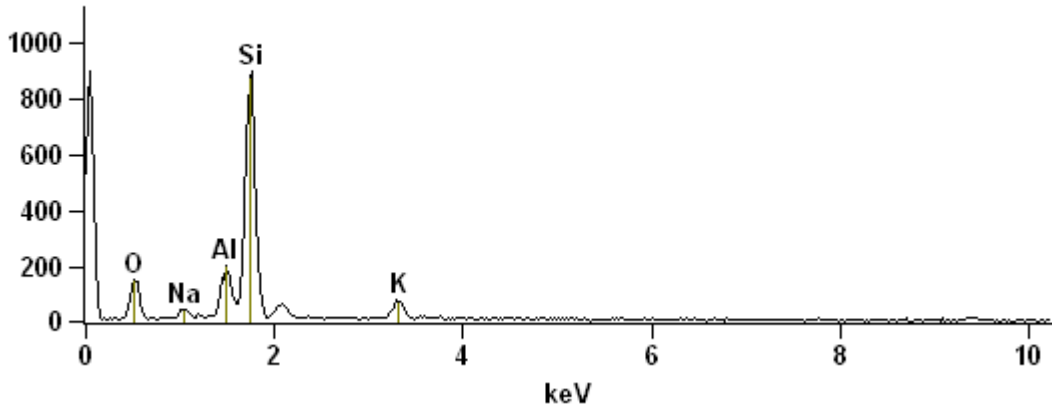


Full scale counts: 856 Sample X PSe(69)_pt4

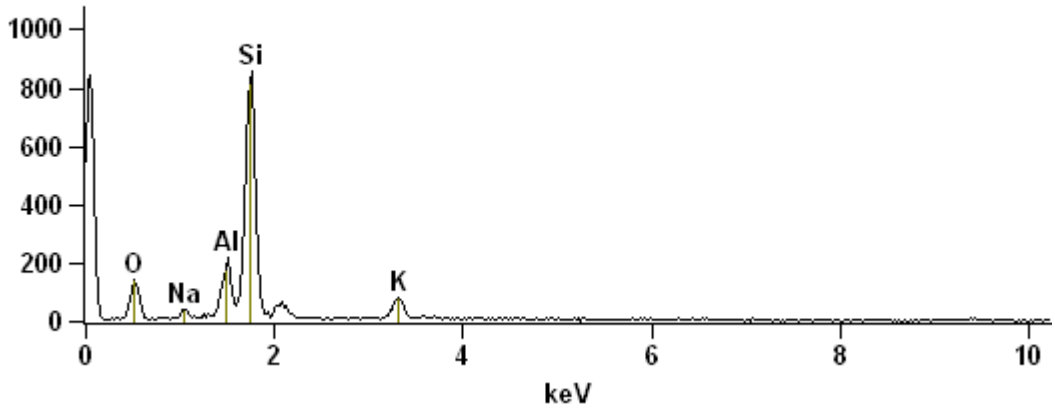


Full scale counts: 922 Sample X PSe(69)_pt5

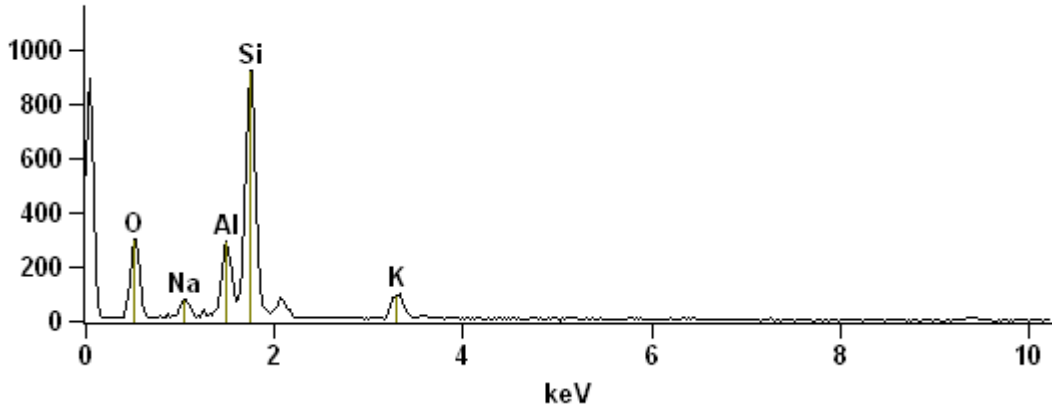

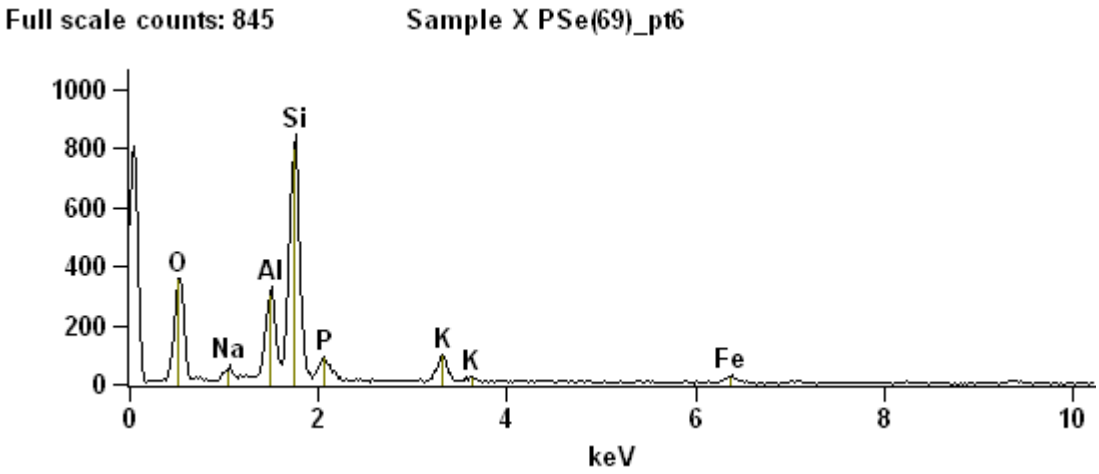


Weight %

| | O-K | Na-K | Al-K | Si-K | P-K | K-K | Fe-K |
|---|---|---|---|---|---|---|---|
| ***Sample X PSe(69)_pt1*** | 17.71 | 1.02 | 8.10 | 58.46 | | 11.78 | 2.93 |
| ***Sample X PSe(69)_pt2*** | 21.09 | 2.17 | 10.64 | 50.63 | | 9.74 | 5.73 |
| ***Sample X PSe(69)_pt3*** | 27.07 | 2.59 | 9.21 | 54.05 | | 7.08 | |
| ***Sample X PSe(69)_pt4*** | 26.07 | 2.36 | 8.85 | 53.37 | | 9.34 | |
| ***Sample X PSe(69)_pt5*** | 36.41 | 3.85 | 9.93 | 41.77 | | 8.04 | |
| ***Sample X PSe(69)_pt6*** | 37.90 | 2.28 | 10.58 | 34.43 | 3.12 | 6.67 | 5.02 |

Weight % Error (+/- 1 Sigma)

| | O-K | Na-K | Al-K | Si-K | P-K | K-K | Fe-K |
|---|---|---|---|---|---|---|---|
| ***Sample X PSe(69)_pt1*** | +/-0.90 | +/-0.19 | +/-0.50 | +/-0.99 | | +/-0.79 | +/-0.66 |
| ***Sample X PSe(69)_pt2*** | +/-1.08 | +/-0.21 | +/-0.60 | +/-1.07 | | +/-0.78 | +/-0.90 |
| ***Sample X PSe(69)_pt3*** | +/-0.79 | +/-0.28 | +/-0.45 | +/-0.82 | | +/-0.53 | |
| ***Sample X PSe(69)_pt4*** | +/-0.80 | +/-0.27 | +/-0.44 | +/-0.81 | | +/-0.55 | |
| ***Sample X PSe(69)_pt5*** | +/-0.73 | +/-0.28 | +/-0.39 | +/-0.64 | | +/-0.42 | |
| ***Sample X PSe(69)_pt6*** | +/-0.78 | +/-0.26 | +/-0.38 | +/-0.68 | +/-0.53 | +/-0.37 | +/-0.69 |

Atom %

| | O-K | Na-K | Al-K | Si-K | P-K | K-K | Fe-K |
|---|---|---|---|---|---|---|---|
| ***Sample X PSe(69)_pt1*** | 28.47 | 1.14 | 7.72 | 53.56 | | 7.75 | 1.35 |
| ***Sample X PSe(69)_pt2*** | 33.27 | 2.38 | 9.95 | 45.51 | | 6.29 | 2.59 |
| ***Sample X PSe(69)_pt3*** | 39.79 | 2.65 | 8.03 | 45.27 | | 4.26 | |
| ***Sample X PSe(69)_pt4*** | 38.81 | 2.44 | 7.81 | 45.25 | | 5.69 | |
| ***Sample X PSe(69)_pt5*** | 50.52 | 3.72 | 8.17 | 33.02 | | 4.57 | |
| ***Sample X PSe(69)_pt6*** | 53.27 | 2.23 | 8.82 | 27.56 | 2.27 | 3.83 | 2.02 |

Atom % Error (+/- 1 Sigma)

| | O-K | Na-K | Al-K | Si-K | P-K | K-K | Fe-K |
|---|---|---|---|---|---|---|---|
| ***Sample X PSe(69)_pt1*** | +/-1.45 | +/-0.21 | +/-0.48 | +/-0.90 | | +/-0.52 | +/-0.31 |
| ***Sample X PSe(69)_pt2*** | +/-1.70 | +/-0.23 | +/-0.56 | +/-0.96 | | +/-0.51 | +/-0.41 |
| ***Sample X PSe(69)_pt3*** | +/-1.17 | +/-0.29 | +/-0.39 | +/-0.68 | | +/-0.32 | |
| ***Sample X PSe(69)_pt4*** | +/-1.19 | +/-0.28 | +/-0.39 | +/-0.69 | | +/-0.34 | |
| ***Sample X PSe(69)_pt5*** | +/-1.01 | +/-0.27 | +/-0.32 | +/-0.51 | | +/-0.24 | |
| ***Sample X PSe(69)_pt6*** | +/-1.09 | +/-0.26 | +/-0.31 | +/-0.54 | +/-0.38 | +/-0.21 | +/-0.28 |

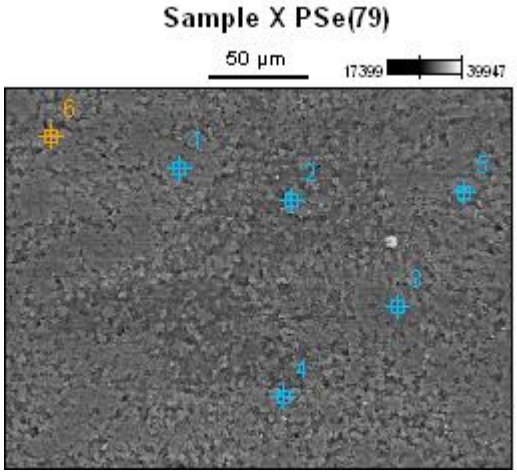


Image Name: Sample 13 PSe(79)

Accelerating Voltage: 20.0 kV

Magnification: 500

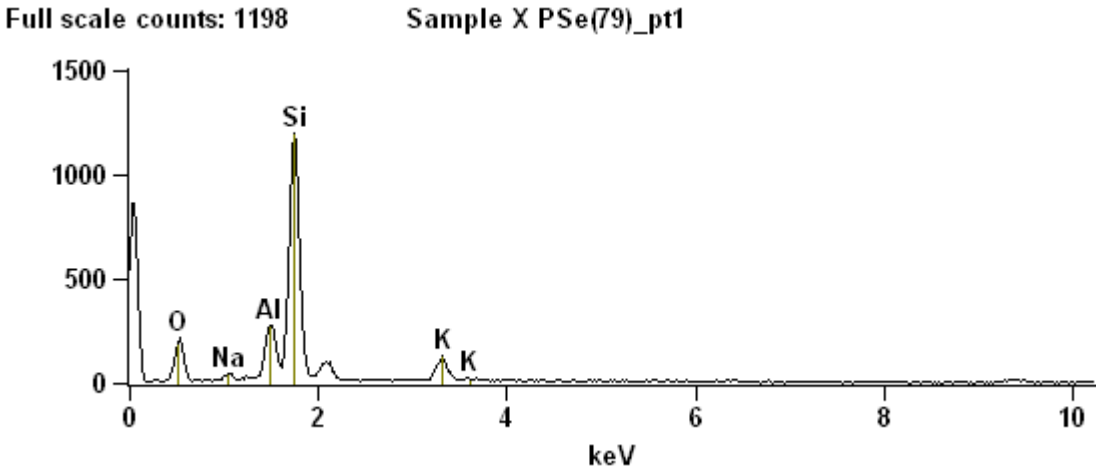


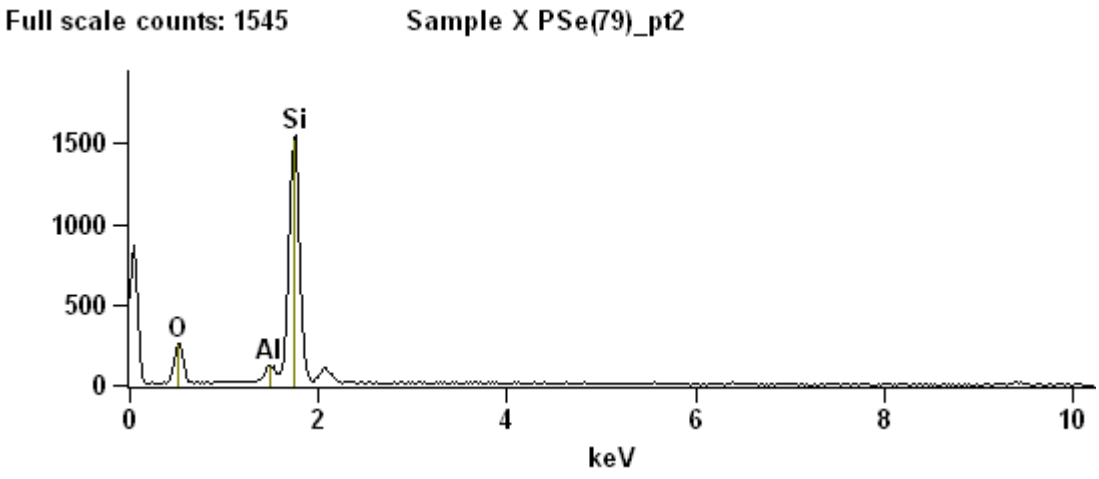

Full scale counts: 1263 Sample X PSe(79)_pt3

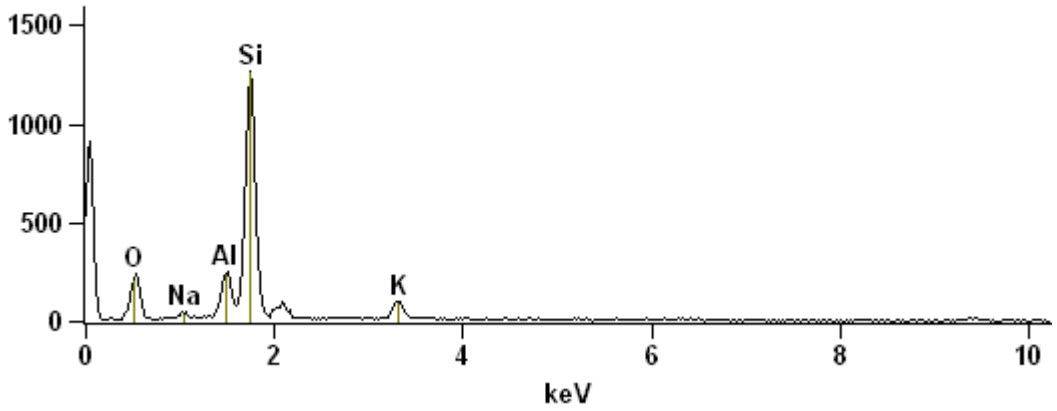


Full scale counts: 1084 Sample X PSe(79)_pt4

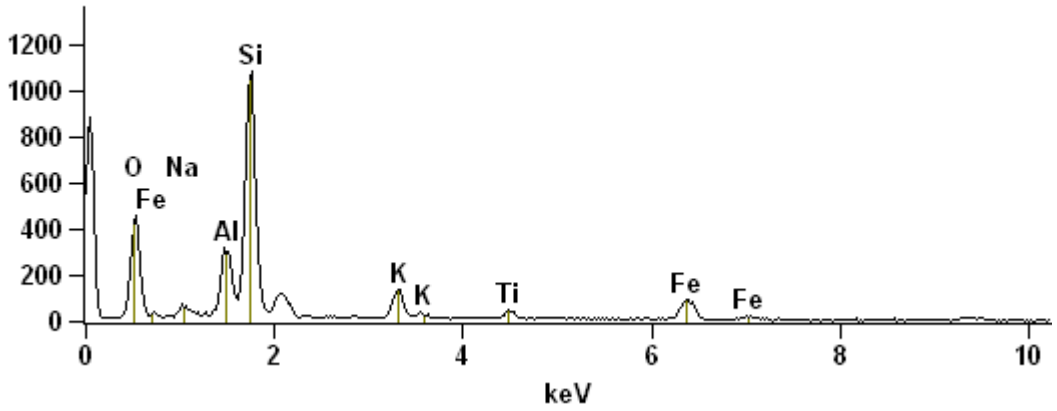


Full scale counts: 972 Sample X PSe(79)_pt5

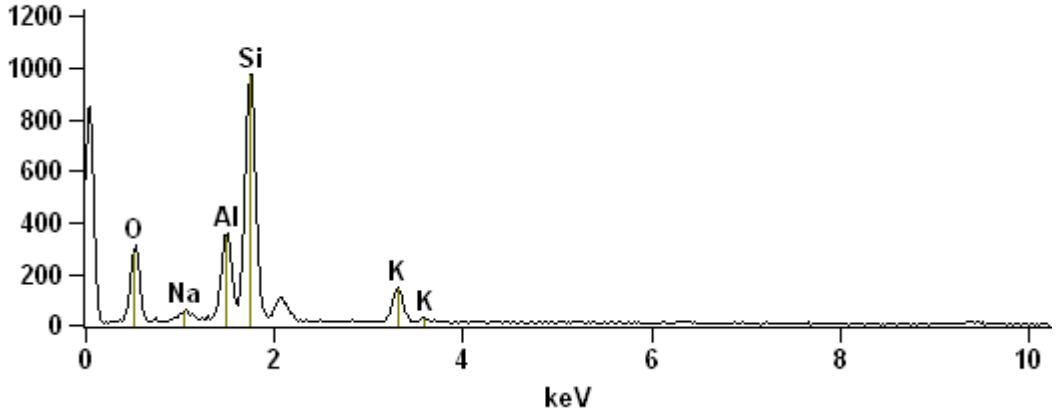

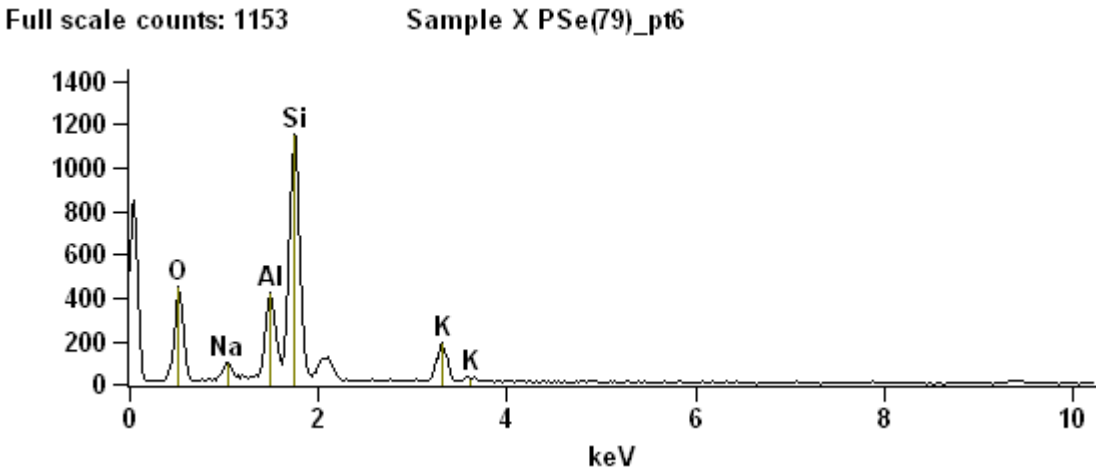


Weight %

| | O-K | Na-K | Al-K | Si-K | K-K | Ti-K | Fe-K |
|---|---|---|---|---|---|---|---|
| ***Sample X PSe(79)_pt1*** | 27.42 | 1.64 | 9.49 | 52.63 | 8.83 | | |
| ***Sample X PSe(79)_pt2*** | 31.38 | | 2.91 | 65.71 | | | |
| ***Sample X PSe(79)_pt3*** | 30.26 | 1.39 | 8.02 | 53.06 | 7.27 | | |
| ***Sample X PSe(79)_pt4*** | 32.03 | 2.20 | 8.20 | 34.01 | 5.82 | 2.69 | 15.05 |
| ***Sample X PSe(79)_pt5*** | 34.01 | 2.39 | 11.72 | 41.99 | 9.89 | | |
| ***Sample X PSe(79)_pt6*** | 36.94 | 3.22 | 10.75 | 39.12 | 9.97 | | |

Weight % Error (+/- 1 Sigma)

| | O-K | Na-K | Al-K | Si-K | K-K | Ti-K | Fe-K |
|---|---|---|---|---|---|---|---|
| ***Sample X PSe(79)_pt1*** | +/-0.68 | +/-0.23 | +/-0.38 | +/-0.69 | +/-0.47 | | |
| ***Sample X PSe(79)_pt2*** | +/-0.67 | | +/-0.30 | +/-0.68 | | | |
| ***Sample X PSe(79)_pt3*** | +/-0.69 | +/-0.23 | +/-0.36 | +/-0.67 | +/-0.43 | | |
| ***Sample X PSe(79)_pt4*** | +/-0.62 | +/-0.25 | +/-0.31 | +/-0.50 | +/-0.32 | +/-0.34 | +/-0.78 |
| ***Sample X PSe(79)_pt5*** | +/-0.70 | +/-0.25 | +/-0.38 | +/-0.63 | +/-0.44 | | |
| ***Sample X PSe(79)_pt6*** | +/-0.64 | +/-0.24 | +/-0.34 | +/-0.55 | +/-0.38 | | |

Atom %

| | O-K | Na-K | Al-K | Si-K | K-K | Ti-K | Fe-K |
|---|---|---|---|---|---|---|---|
| ***Sample X PSe(79)_pt1*** | 40.45 | 1.68 | 8.30 | 44.23 | 5.33 | | |
| ***Sample X PSe(79)_pt2*** | 44.49 | | 2.44 | 53.07 | | | |
| ***Sample X PSe(79)_pt3*** | 43.74 | 1.40 | 6.87 | 43.69 | 4.30 | | |
| ***Sample X PSe(79)_pt4*** | 48.98 | 2.34 | 7.43 | 29.63 | 3.64 | 1.37 | 6.59 |
| ***Sample X PSe(79)_pt5*** | 48.18 | 2.35 | 9.84 | 33.89 | 5.74 | | |
| ***Sample X PSe(79)_pt6*** | 51.36 | 3.11 | 8.87 | 30.99 | 5.67 | | |

Atom % Error (+/- 1 Sigma)

| | O-K | Na-K | Al-K | Si-K | K-K | Ti-K | Fe-K |
|---|---|---|---|---|---|---|---|
| ***Sample X PSe(79)_pt1*** | +/-1.01 | +/-0.24 | +/-0.33 | +/-0.58 | +/-0.28 | | |
| ***Sample X PSe(79)_pt2*** | +/-0.95 | | +/-0.25 | +/-0.55 | | | |
| ***Sample X PSe(79)_pt3*** | +/-0.99 | +/-0.23 | +/-0.31 | +/-0.56 | +/-0.26 | | |
| ***Sample X PSe(79)_pt4*** | +/-0.95 | +/-0.27 | +/-0.29 | +/-0.43 | +/-0.20 | +/-0.18 | +/-0.34 |
| ***Sample X PSe(79)_pt5*** | +/-1.00 | +/-0.25 | +/-0.32 | +/-0.51 | +/-0.25 | | |
| ***Sample X PSe(79)_pt6*** | +/-0.89 | +/-0.23 | +/-0.28 | +/-0.44 | +/-0.22 | | |

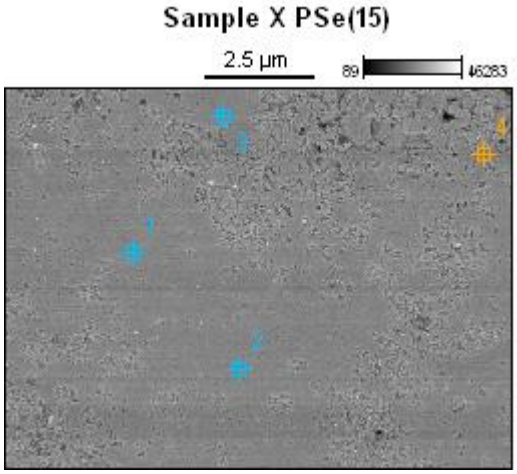


Image Name: Sample 13 PSe(15)

Accelerating Voltage: 20.0 kV

Magnification: 11000

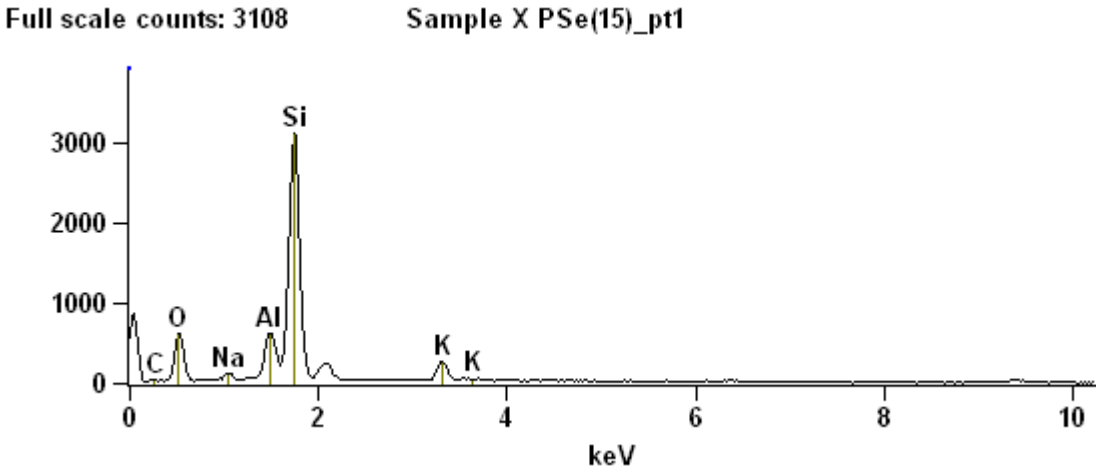


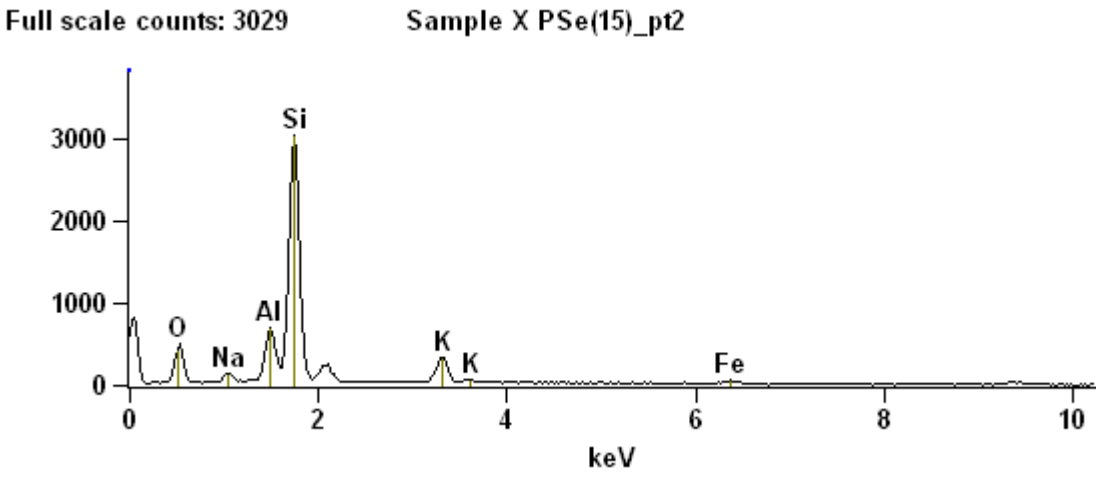

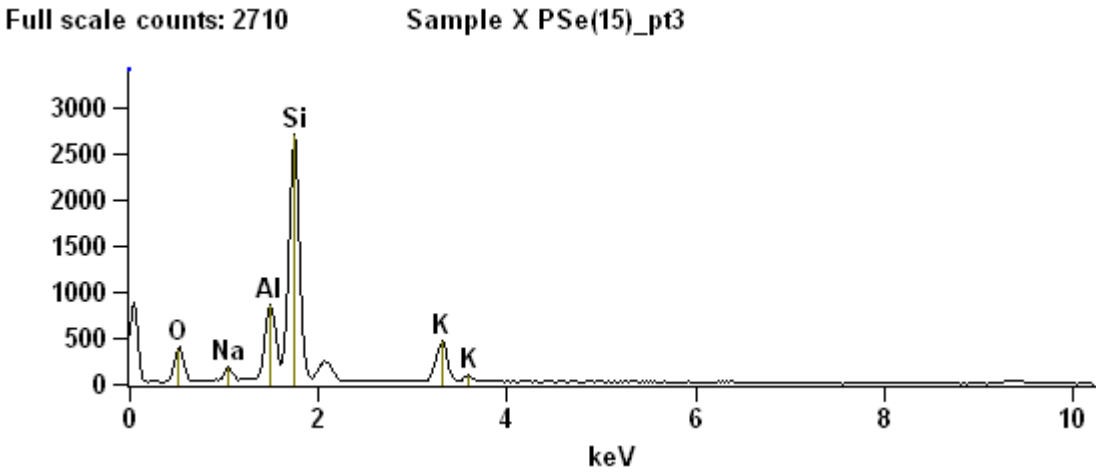


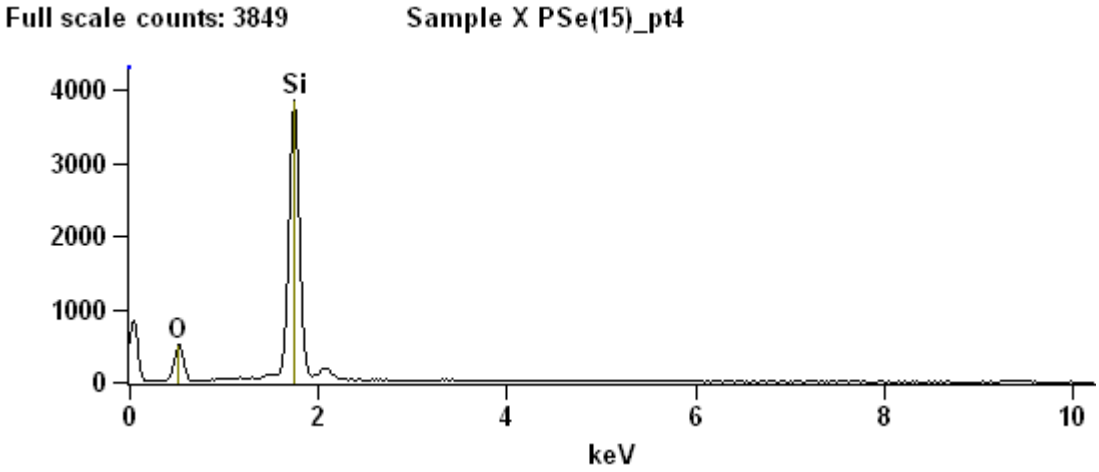


Weight %

| | C-K | O-K | Na-K | Al-K | Si-K | K-K | Fe-K |
|---|---|---|---|---|---|---|---|
| ***Sample X PSe(15)_pt1*** | 5.11 | 29.04 | 1.89 | 7.47 | 50.16 | 6.34 | |
| ***Sample X PSe(15)_pt2*** | | 23.98 | 2.24 | 8.87 | 52.05 | 10.03 | 2.82 |
| ***Sample X PSe(15)_pt3*** | | 22.98 | 2.75 | 11.79 | 48.51 | 13.97 | |
| ***Sample X PSe(15)_pt4*** | | 28.79 | | | 71.21 | | |

Weight % Error (+/- 1 Sigma)

| | C-K | O-K | Na-K | Al-K | Si-K | K-K | Fe-K |
|---|---|---|---|---|---|---|---|
| ***Sample X PSe(15)_pt1*** | +/-0.60 | +/-0.43 | +/-0.14 | +/-0.22 | +/-0.41 | +/-0.26 | |
| ***Sample X PSe(15)_pt2*** | | +/-0.42 | +/-0.15 | +/-0.24 | +/-0.43 | +/-0.30 | +/-0.27 |
| ***Sample X PSe(15)_pt3*** | | +/-0.44 | +/-0.16 | +/-0.26 | +/-0.44 | +/-0.35 | |
| ***Sample X PSe(15)_pt4*** | | +/-0.46 | | | +/-0.43 | | |

Atom %

| | C-K | O-K | Na-K | Al-K | Si-K | K-K | Fe-K |
|---|---|---|---|---|---|---|---|
| ***Sample X PSe(15)_pt1*** | 9.35 | 39.91 | 1.80 | 6.09 | 39.28 | 3.57 | |
| ***Sample X PSe(15)_pt2*** | | 36.69 | 2.39 | 8.05 | 45.36 | 6.28 | 1.24 |
| ***Sample X PSe(15)_pt3*** | | 35.22 | 2.94 | 10.72 | 42.36 | 8.76 | |
| ***Sample X PSe(15)_pt4*** | | 41.51 | | | 58.49 | | |

Atom % Error (+/- 1 Sigma)

| | C-K | O-K | Na-K | Al-K | Si-K | K-K | Fe-K |
|---|---|---|---|---|---|---|---|
| ***Sample X PSe(15)_pt1*** | +/-1.10 | +/-0.59 | +/-0.13 | +/-0.18 | +/-0.32 | +/-0.15 | |
| ***Sample X PSe(15)_pt2*** | | +/-0.64 | +/-0.16 | +/-0.21 | +/-0.38 | +/-0.19 | +/-0.12 |
| ***Sample X PSe(15)_pt3*** | | +/-0.68 | +/-0.17 | +/-0.23 | +/-0.39 | +/-0.22 | |
| ***Sample X PSe(15)_pt4*** | | +/-0.66 | | | +/-0.35 | | |

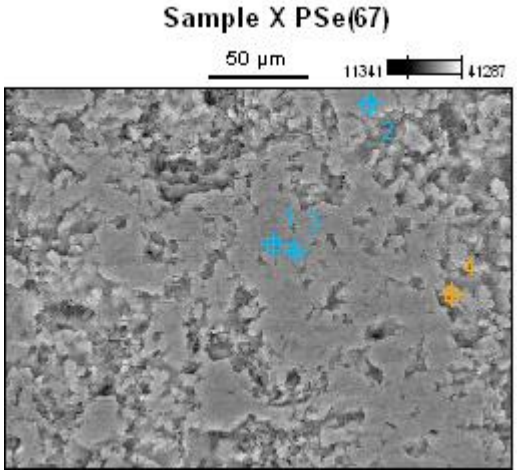


Image Name: Sample 13 PSe(67)

Accelerating Voltage: 20.0 kV

Magnification: 500

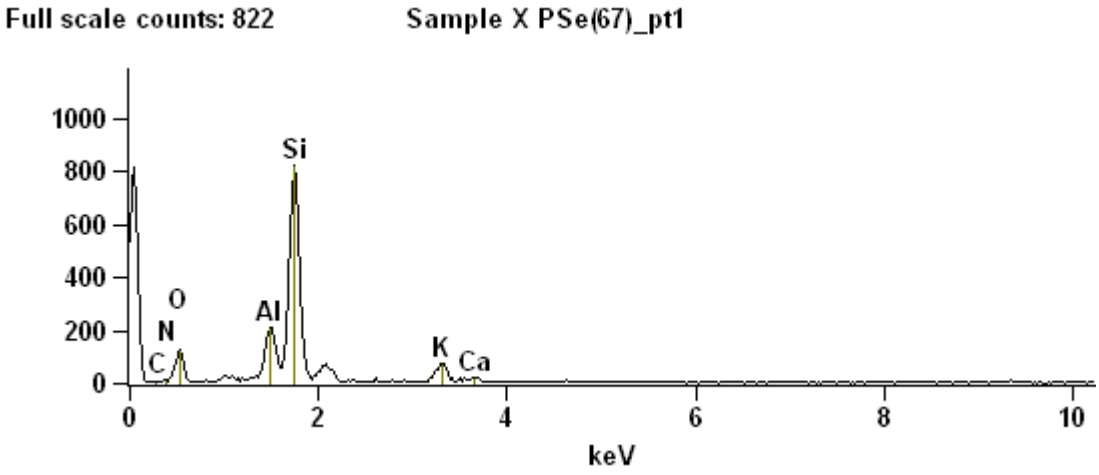

Full scale counts: 873 Sample X PSe(67)_pt2

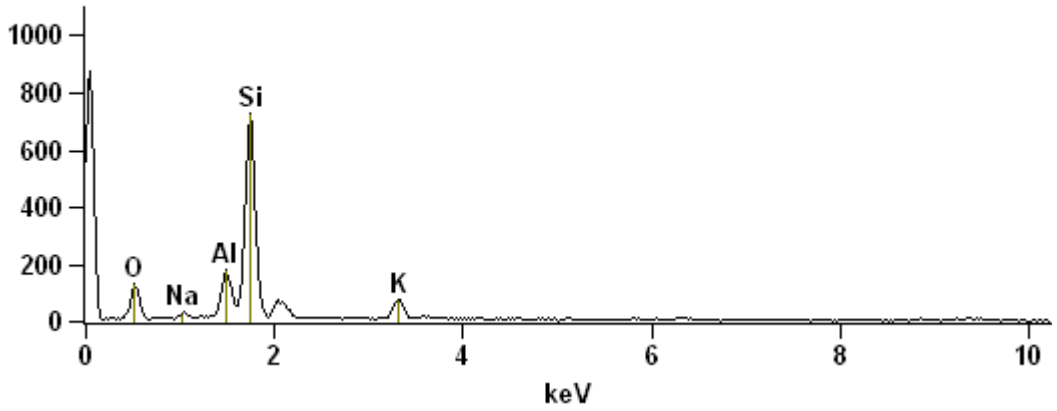


Full scale counts: 815 Sample X PSe(67)_pt3

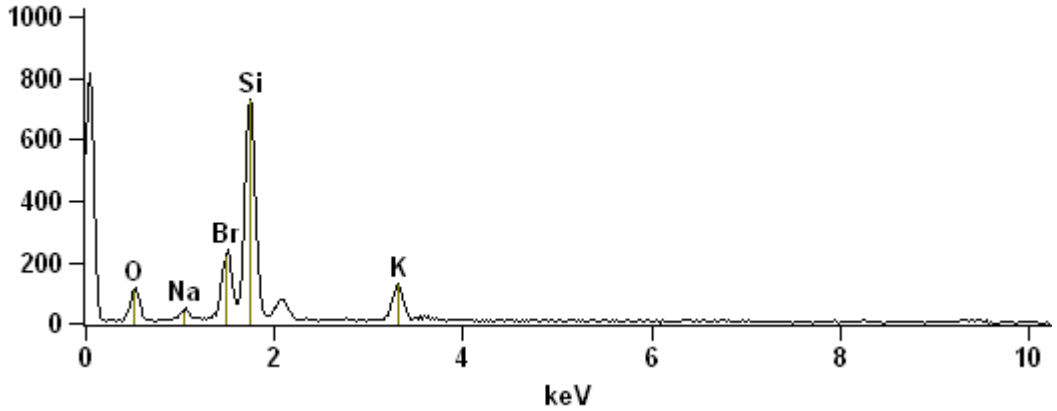


Full scale counts: 870 Sample X PSe(67)_pt4

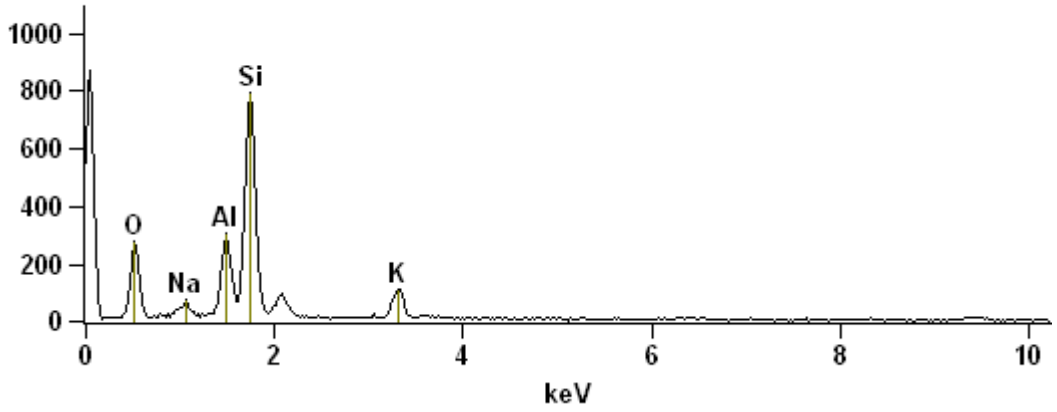

Weight %

| | C-K | N-K | O-K | Na-K | Al-K | Si-K | K-K | Ca-K | Br-K |
|---|---|---|---|---|---|---|---|---|---|
| ***Sample X PSe(67)_pt1*** | 5.06 | 2.82 | 24.07 | | 9.97 | 50.19 | 7.38 | 0.51 | |
| ***Sample X PSe(67)_pt2*** | | | 27.40 | 1.57 | 8.96 | 52.65 | 9.42 | | |
| ***Sample X PSe(67)_pt3*** | | | 27.37 | 3.36 | | 53.65 | 15.63 | | 0.00 |
| ***Sample X PSe(67)_pt4*** | | | 34.47 | 3.25 | 11.57 | 41.39 | 9.31 | | |

Weight % Error (+/- 1 Sigma)

| | C-K | N-K | O-K | Na-K | Al-K | Si-K | K-K | Ca-K | Br-K |
|---|---|---|---|---|---|---|---|---|---|
| ***Sample X PSe(67)_pt1*** | +/- 1.69 | +/- 1.90 | +/- 0.99 | | +/- 0.44 | +/- 0.80 | +/- 0.52 | +/- 0.21 | |
| ***Sample X PSe(67)_pt2*** | | | +/- 0.92 | +/- 0.31 | +/- 0.49 | +/- 0.90 | +/- 0.63 | | |
| ***Sample X PSe(67)_pt3*** | | | +/- 0.98 | +/- 0.37 | | +/- 0.96 | +/- 0.75 | | +/- 0.00 |
| ***Sample X PSe(67)_pt4*** | | | +/- 0.78 | +/- 0.30 | +/- 0.42 | +/- 0.69 | +/- 0.48 | | |

Atom %

| | C-K | N-K | O-K | Na-K | Al-K | Si-K | K-K | Ca-K | Br-K |
|---|---|---|---|---|---|---|---|---|---|
| ***Sample X PSe(67)_pt1*** | 9.40 | 4.49 | 33.54 | | 8.24 | 39.84 | 4.21 | 0.28 | |
| ***Sample X PSe(67)_pt2*** | | | 40.51 | 1.61 | 7.85 | 44.33 | 5.70 | | |
| ***Sample X PSe(67)_pt3*** | | | 41.05 | 3.50 | | 45.85 | 9.60 | | 0.00 |
| ***Sample X PSe(67)_pt4*** | | | 48.56 | 3.19 | 9.67 | 33.21 | 5.37 | | |

Atom % Error (+/- 1 Sigma)

| | C-K | N-K | O-K | Na-K | Al-K | Si-K | K-K | Ca-K | Br-K |
|---|---|---|---|---|---|---|---|---|---|
| ***Sample X PSe(67)_pt1*** | +/- 3.13 | +/- 3.03 | +/- 1.38 | | +/- 0.36 | +/- 0.63 | +/- 0.29 | +/- 0.12 | |
| ***Sample X PSe(67)_pt2*** | | | +/- 1.36 | +/- 0.32 | +/- 0.43 | +/- 0.76 | +/- 0.38 | | |
| ***Sample X PSe(67)_pt3*** | | | +/- 1.47 | +/- 0.39 | | +/- 0.82 | +/- 0.46 | | +/- 0.00 |
| ***Sample X PSe(67)_pt4*** | | | +/- 1.10 | +/- 0.29 | +/- 0.35 | +/- 0.55 | +/- 0.28 | | |

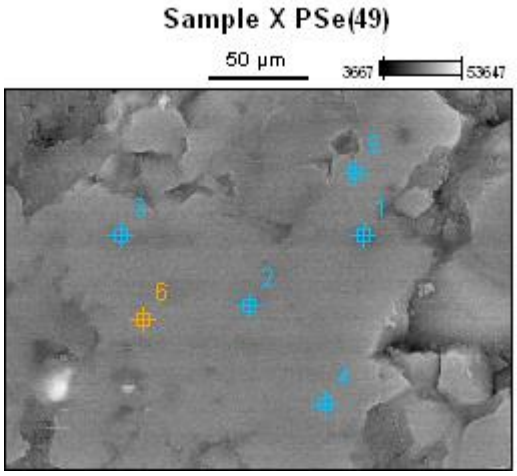


Image Name: Sample 13 PSe(49)

Accelerating Voltage: 20.0 kV

Magnification: 500

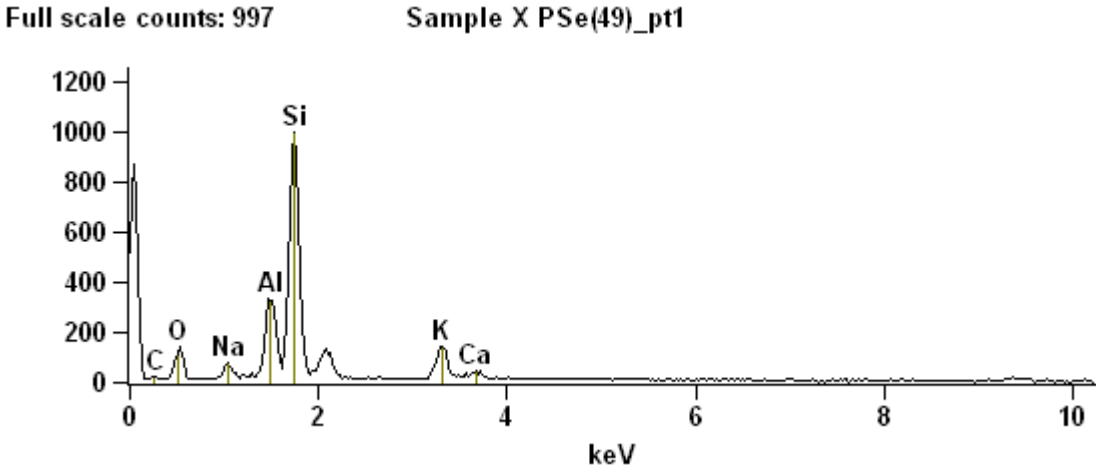


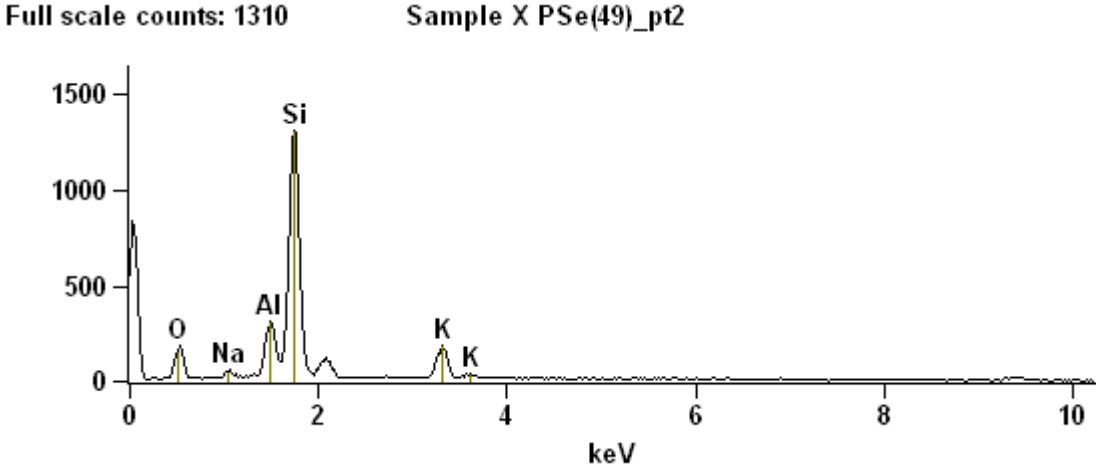

Full scale counts: 1362 Sample X PSe(49)_pt3

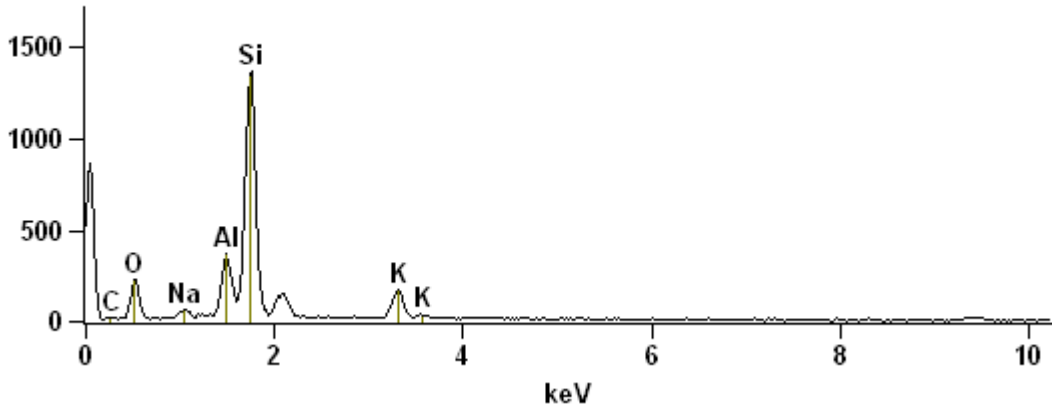


Full scale counts: 1248 Sample X PSe(49)_pt4

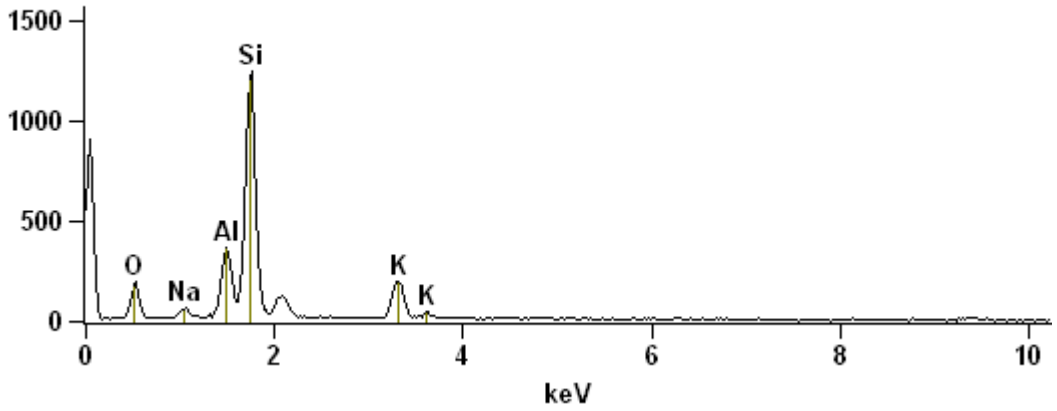


Full scale counts: 1263 Sample X PSe(49)_pt5

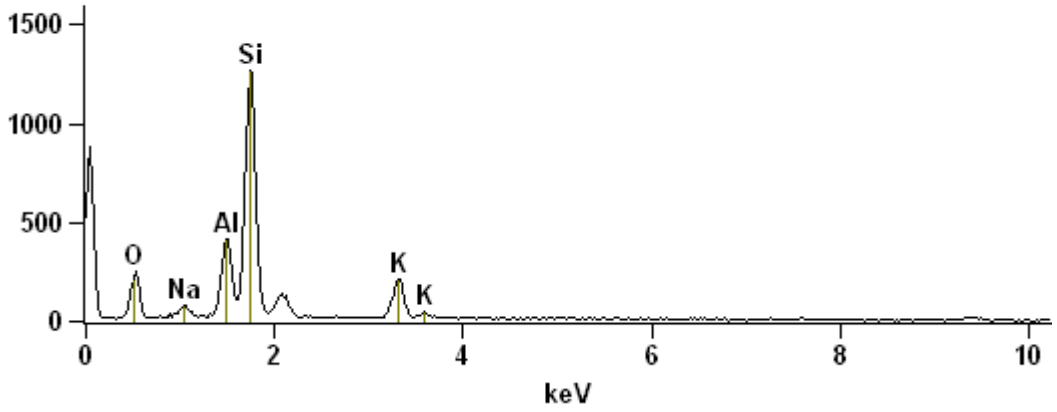

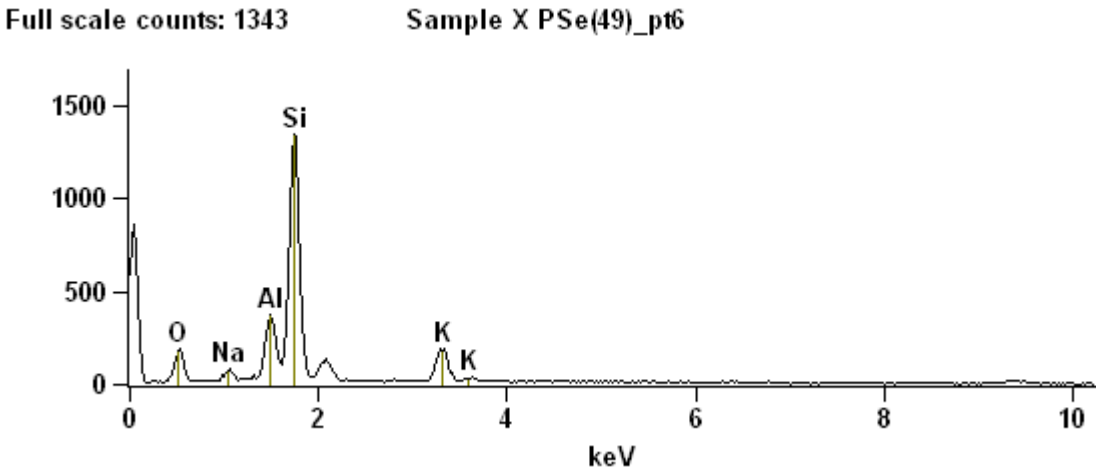


Weight %

| | C-K | O-K | Na-K | Al-K | Si-K | K-K | Ca-K |
|---|---|---|---|---|---|---|---|
| ***Sample X PSe(49)_pt1*** | 6.51 | 19.39 | 3.19 | 12.96 | 45.62 | 10.40 | 1.93 |
| ***Sample X PSe(49)_pt2*** | | 22.63 | 1.68 | 9.40 | 53.73 | 12.56 | |
| ***Sample X PSe(49)_pt3*** | 4.97 | 23.84 | 1.80 | 9.88 | 49.91 | 9.60 | |
| ***Sample X PSe(49)_pt4*** | | 22.12 | 2.57 | 11.48 | 48.96 | 14.87 | |
| ***Sample X PSe(49)_pt5*** | | 26.26 | 2.59 | 11.80 | 46.53 | 12.82 | |
| ***Sample X PSe(49)_pt6*** | | 22.15 | 2.60 | 10.96 | 51.30 | 13.00 | |

Weight % Error (+/- 1 Sigma)

| | C-K | O-K | Na-K | Al-K | Si-K | K-K | Ca-K |
|---|---|---|---|---|---|---|---|
| ***Sample X PSe(49)_pt1*** | +/-1.25 | +/-0.68 | +/-0.25 | +/-0.37 | +/-0.66 | +/-0.51 | +/-0.23 |
| ***Sample X PSe(49)_pt2*** | | +/-0.63 | +/-0.22 | +/-0.37 | +/-0.67 | +/-0.50 | |
| ***Sample X PSe(49)_pt3*** | +/-1.04 | +/-0.62 | +/-0.21 | +/-0.34 | +/-0.62 | +/-0.44 | |
| ***Sample X PSe(49)_pt4*** | | +/-0.65 | +/-0.23 | +/-0.37 | +/-0.65 | +/-0.52 | |
| ***Sample X PSe(49)_pt5*** | | +/-0.63 | +/-0.23 | +/-0.35 | +/-0.61 | +/-0.47 | |
| ***Sample X PSe(49)_pt6*** | | +/-0.65 | +/-0.23 | +/-0.37 | +/-0.65 | +/-0.50 | |

Atom %

| | C-K | O-K | Na-K | Al-K | Si-K | K-K | Ca-K |
|---|---|---|---|---|---|---|---|
| ***Sample X PSe(49)_pt1*** | 12.57 | 28.11 | 3.22 | 11.14 | 37.67 | 6.17 | 1.12 |
| ***Sample X PSe(49)_pt2*** | | 34.74 | 1.80 | 8.56 | 47.01 | 7.89 | |
| ***Sample X PSe(49)_pt3*** | 9.46 | 34.09 | 1.79 | 8.38 | 40.66 | 5.62 | |
| ***Sample X PSe(49)_pt4*** | | 34.19 | 2.77 | 10.52 | 43.11 | 9.41 | |
| ***Sample X PSe(49)_pt5*** | | 39.31 | 2.70 | 10.47 | 39.67 | 7.85 | |
| ***Sample X PSe(49)_pt6*** | | 34.07 | 2.78 | 10.00 | 44.97 | 8.18 | |

Atom % Error (+/- 1 Sigma)

| | C-K | O-K | Na-K | Al-K | Si-K | K-K | Ca-K |
|---|---|---|---|---|---|---|---|
| ***Sample X PSe(49)_pt1*** | +/-2.41 | +/-0.99 | +/-0.25 | +/-0.32 | +/-0.54 | +/-0.31 | +/-0.13 |
| ***Sample X PSe(49)_pt2*** | | +/-0.97 | +/-0.23 | +/-0.33 | +/-0.59 | +/-0.32 | |
| ***Sample X PSe(49)_pt3*** | +/-1.98 | +/-0.89 | +/-0.21 | +/-0.29 | +/-0.50 | +/-0.26 | |
| ***Sample X PSe(49)_pt4*** | | +/-1.01 | +/-0.25 | +/-0.34 | +/-0.57 | +/-0.33 | |
| ***Sample X PSe(49)_pt5*** | | +/-0.95 | +/-0.24 | +/-0.31 | +/-0.52 | +/-0.29 | |
| ***Sample X PSe(49)_pt6*** | | +/-0.99 | +/-0.25 | +/-0.33 | +/-0.57 | +/-0.31 | |

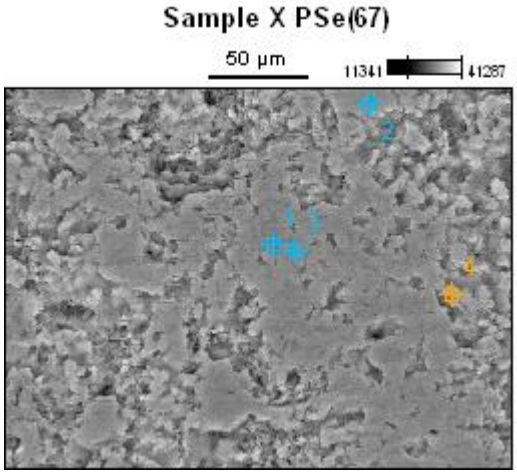


Image Name: Sample 13 PSe(67)

Accelerating Voltage: 20.0 kV

Magnification: 500

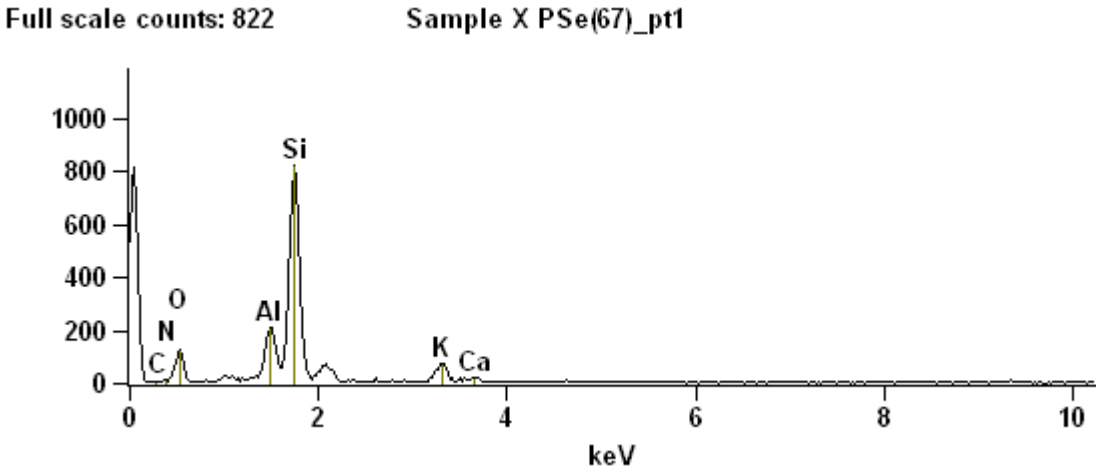


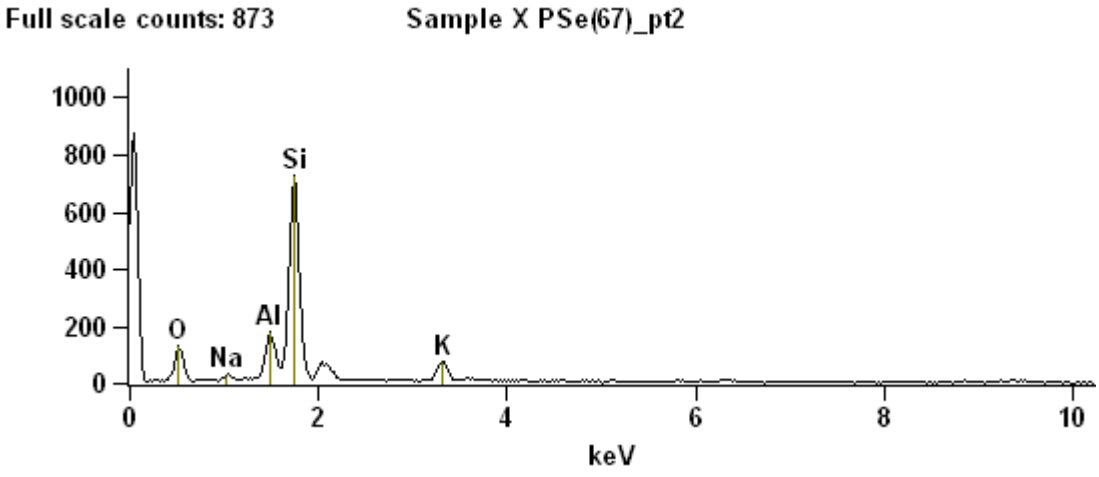

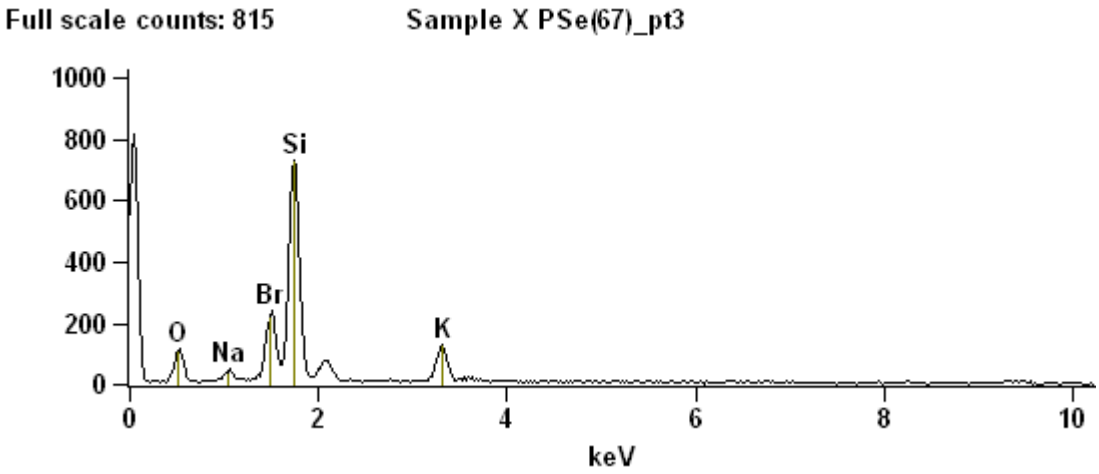


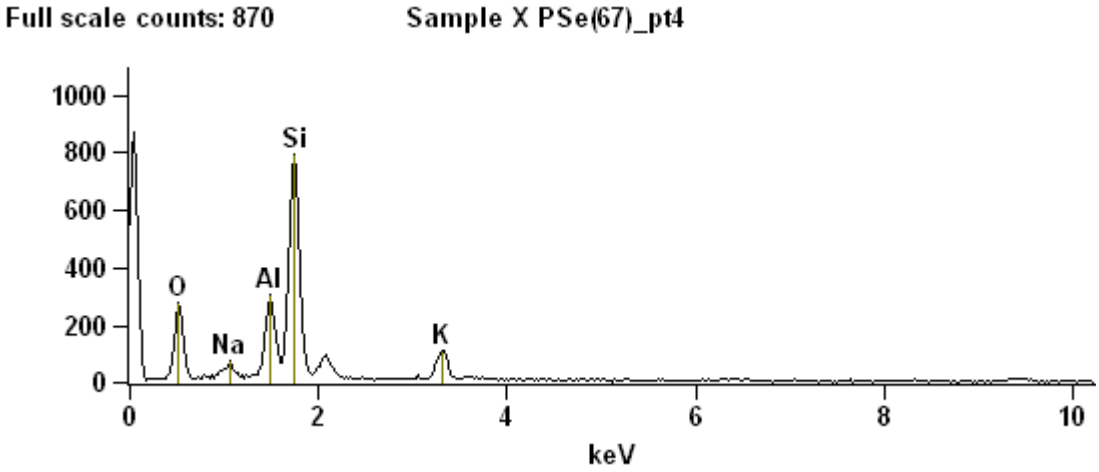


Weight %

| | *C-K* | *N-K* | *O-K* | *Na-K* | *Al-K* | *Si-K* | *K-K* | *Ca-K* | *Br-K* |
|---|---|---|---|---|---|---|---|---|---|
| ***Sample X PSe(67)_pt1*** | 5.06 | 2.82 | 24.07 | | 9.97 | 50.19 | 7.38 | 0.51 | |
| ***Sample X PSe(67)_pt2*** | | | 27.40 | 1.57 | 8.96 | 52.65 | 9.42 | | |
| ***Sample X PSe(67)_pt3*** | | | 27.37 | 3.36 | | 53.65 | 15.63 | | 0.00 |
| ***Sample X PSe(67)_pt4*** | | | 34.47 | 3.25 | 11.57 | 41.39 | 9.31 | | |

Weight % Error (+/- 1 Sigma)

| | C-K | N-K | O-K | Na-K | Al-K | Si-K | K-K | Ca-K | Br-K |
|---|---|---|---|---|---|---|---|---|---|
| Sample X PSe(67)_pt1 | +/- 1.69 | +/- 1.90 | +/- 0.99 | | +/- 0.44 | +/- 0.80 | +/- 0.52 | +/- 0.21 | |
| Sample X PSe(67)_pt2 | | | +/- 0.92 | +/- 0.31 | +/- 0.49 | +/- 0.90 | +/- 0.63 | | |
| Sample X PSe(67)_pt3 | | | +/- 0.98 | +/- 0.37 | | +/- 0.96 | +/- 0.75 | | +/- 0.00 |
| Sample X PSe(67)_pt4 | | | +/- 0.78 | +/- 0.30 | +/- 0.42 | +/- 0.69 | +/- 0.48 | | |

Atom %

| | C-K | N-K | O-K | Na-K | Al-K | Si-K | K-K | Ca-K | Br-K |
|---|---|---|---|---|---|---|---|---|---|
| Sample X PSe(67)_pt1 | 9.40 | 4.49 | 33.54 | | 8.24 | 39.84 | 4.21 | 0.28 | |
| Sample X PSe(67)_pt2 | | | 40.51 | 1.61 | 7.85 | 44.33 | 5.70 | | |
| Sample X PSe(67)_pt3 | | | 41.05 | 3.50 | | 45.85 | 9.60 | | 0.00 |
| Sample X PSe(67)_pt4 | | | 48.56 | 3.19 | 9.67 | 33.21 | 5.37 | | |

Atom % Error (+/- 1 Sigma)

| | C-K | N-K | O-K | Na-K | Al-K | Si-K | K-K | Ca-K | Br-K |
|---|---|---|---|---|---|---|---|---|---|
| Sample X PSe(67)_pt1 | +/- 3.13 | +/- 3.03 | +/- 1.38 | | +/- 0.36 | +/- 0.63 | +/- 0.29 | +/- 0.12 | |
| Sample X PSe(67)_pt2 | | | +/- 1.36 | +/- 0.32 | +/- 0.43 | +/- 0.76 | +/- 0.38 | | |
| Sample X PSe(67)_pt3 | | | +/- 1.47 | +/- 0.39 | | +/- 0.82 | +/- 0.46 | | +/- 0.00 |
| Sample X PSe(67)_pt4 | | | +/- 1.10 | +/- 0.29 | +/- 0.35 | +/- 0.55 | +/- 0.28 | | |

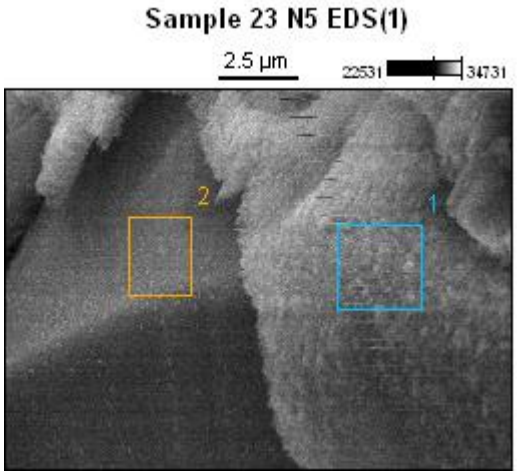


Image Name: Sample 23 N5 EDS(1)

Accelerating Voltage: 20.0 kV

Magnification: 8000

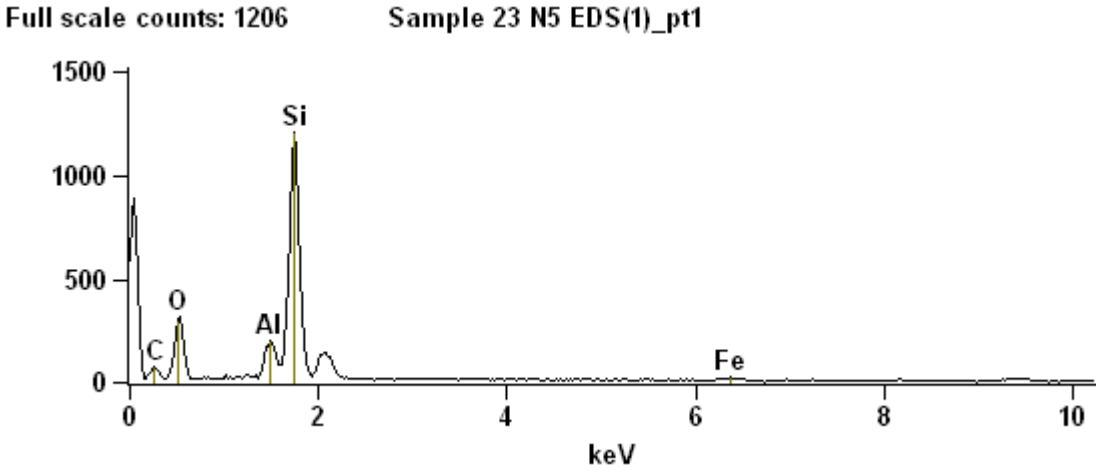


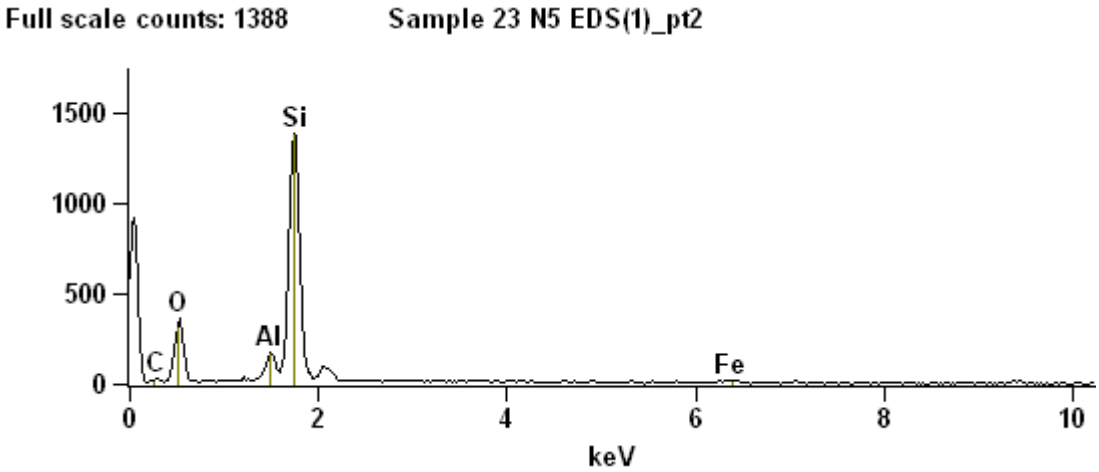


Weight %

| | *C-K* | *O-K* | *Al-K* | *Si-K* | *Fe-K* |
|---|---|---|---|---|---|
| ***Sample 23 N5 EDS(1)_pt1*** | 21.88 | 31.70 | 5.09 | 39.11 | 2.22 |
| ***Sample 23 N5 EDS(1)_pt2*** | 8.24 | 33.73 | 3.84 | 50.58 | 3.60 |

Weight % Error (+/- 1 Sigma)

| | C-K | O-K | Al-K | Si-K | Fe-K |
|---|---|---|---|---|---|
| ***Sample 23 N5 EDS(1)_pt1*** | +/-1.17 | +/-0.72 | +/-0.28 | +/-0.52 | +/-0.36 |
| ***Sample 23 N5 EDS(1)_pt2*** | +/-1.10 | +/-0.69 | +/-0.26 | +/-0.55 | +/-0.66 |

Atom %

| | C-K | O-K | Al-K | Si-K | Fe-K |
|---|---|---|---|---|---|
| ***Sample 23 N5 EDS(1)_pt1*** | 33.59 | 36.53 | 3.48 | 25.68 | 0.73 |
| ***Sample 23 N5 EDS(1)_pt2*** | 14.28 | 43.90 | 2.97 | 37.50 | 1.34 |

Atom % Error (+/- 1 Sigma)

| | C-K | O-K | Al-K | Si-K | Fe-K |
|---|---|---|---|---|---|
| ***Sample 23 N5 EDS(1)_pt1*** | +/-1.80 | +/-0.83 | +/-0.19 | +/-0.34 | +/-0.12 |
| ***Sample 23 N5 EDS(1)_pt2*** | +/-1.90 | +/-0.90 | +/-0.20 | +/-0.41 | +/-0.25 |

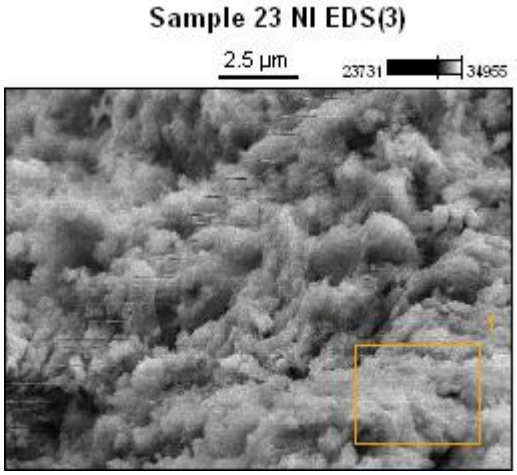


Image Name: Sample 23 NI EDS(3)

Accelerating Voltage: 20.0 kV

Magnification: 8000

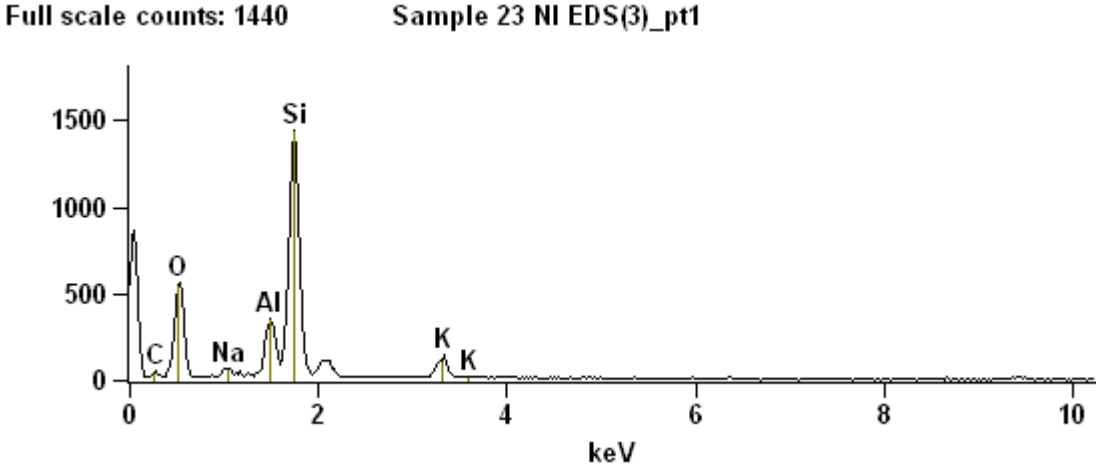

Weight %

| | C-K | O-K | Na-K | Al-K | Si-K | K-K |
|---|---|---|---|---|---|---|
| ***Sample 23 NI EDS(3)_pt1*** | 6.69 | 40.60 | 1.37 | 7.66 | 38.21 | 5.47 |

Weight % Error (+/- 1 Sigma)

| | C-K | O-K | Na-K | Al-K | Si-K | K-K |
|---|---|---|---|---|---|---|
| ***Sample 23 NI EDS(3)_pt1*** | +/-0.90 | +/-0.61 | +/-0.11 | +/-0.25 | +/-0.44 | +/-0.28 |

Atom %

| | C-K | O-K | Na-K | Al-K | Si-K | K-K |
|---|---|---|---|---|---|---|
| ***Sample 23 NI EDS(3)_pt1*** | 11.27 | 51.39 | 1.20 | 5.75 | 27.55 | 2.83 |

Atom % Error (+/- 1 Sigma)

| | C-K | O-K | Na-K | Al-K | Si-K | K-K |
|---|---|---|---|---|---|---|
| ***Sample 23 NI EDS(3)_pt1*** | +/-1.52 | +/-0.78 | +/-0.10 | +/-0.19 | +/-0.32 | +/-0.15 |

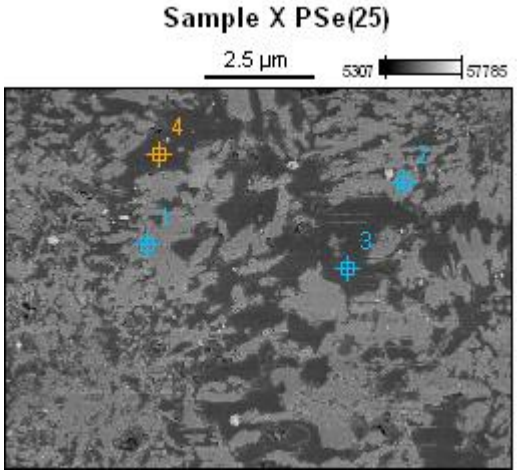


Image Name: Sample 30C PSe(25)

Accelerating Voltage: 20.0 kV

Magnification: 11000

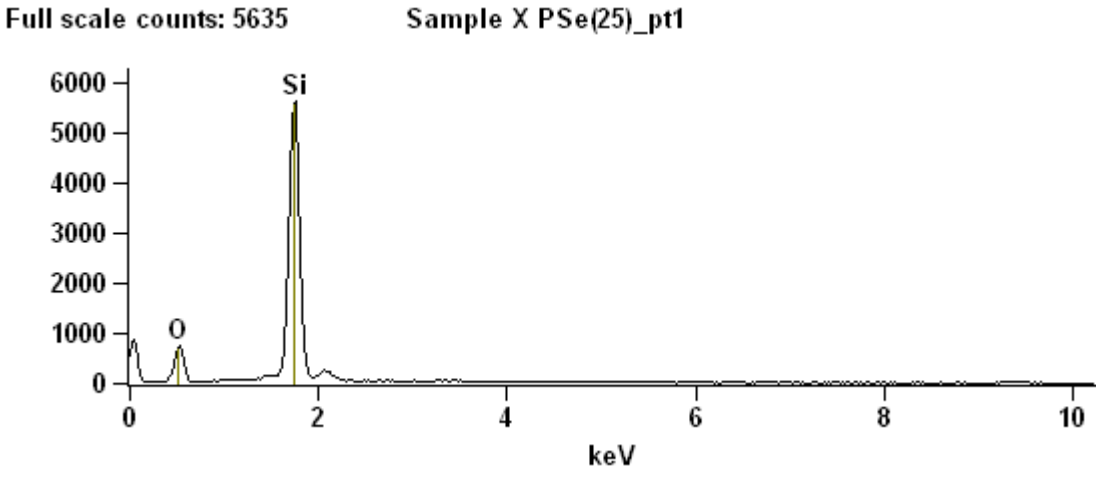

Full scale counts: 2420 Sample X PSe(25)_pt2

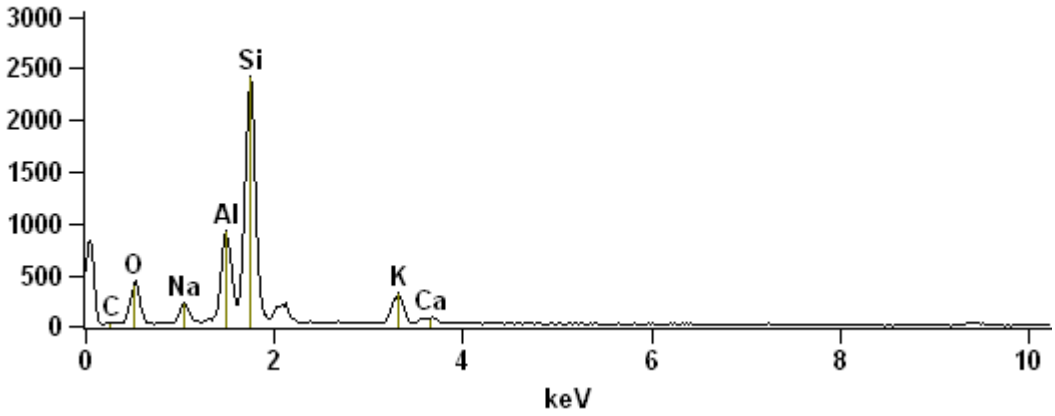


Full scale counts: 805 Sample X PSe(25)_pt3

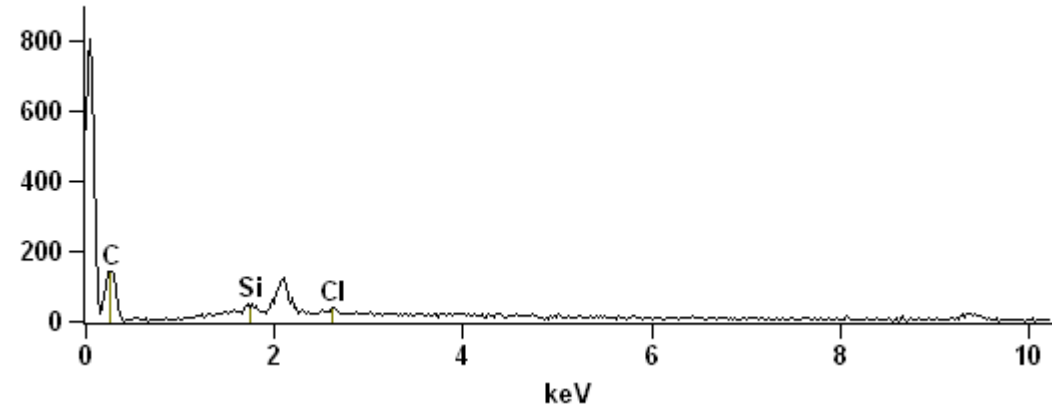


Full scale counts: 834 Sample X PSe(25)_pt4

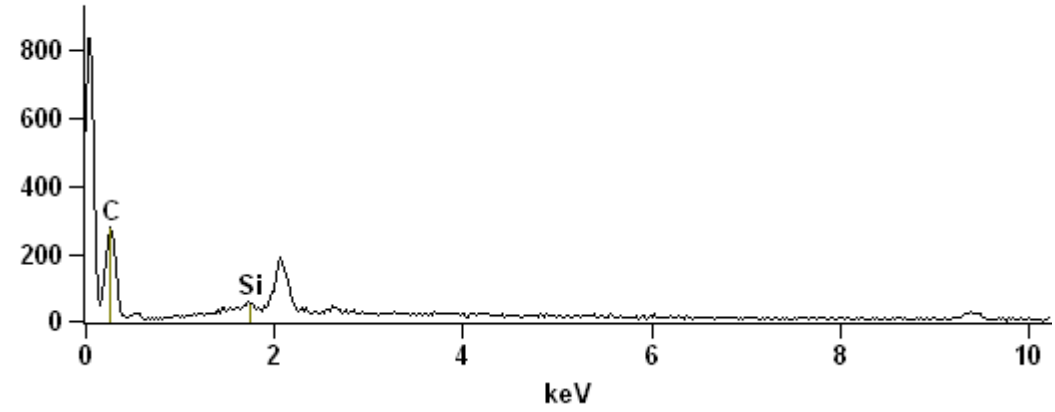

Weight %

| | C-K | O-K | Na-K | Al-K | Si-K | Cl-K | K-K | Ca-K |
|---|---|---|---|---|---|---|---|---|
| ***Sample X PSe(25)_pt 1*** | | 28.32 | | | 71.68 | | | |
| ***Sample X PSe(25)_pt 2*** | 6.59 | 23.78 | 4.22 | 12.28 | 43.28 | | 8.51 | 1.35 |
| ***Sample X PSe(25)_pt 3*** | 91.74 | | | | 5.37 | 2.89 | | |
| ***Sample X PSe(25)_pt 4*** | 95.58 | | | | 4.42 | | | |

Weight % Error (+/- 1 Sigma)

| | C-K | O-K | Na-K | Al-K | Si-K | Cl-K | K-K | Ca-K |
|---|---|---|---|---|---|---|---|---|
| ***Sample X PSe(25)_ pt1*** | | +/- 0.38 | | | +/- 0.36 | | | |
| ***Sample X PSe(25)_ pt2*** | +/- 0.63 | +/- 0.45 | +/- 0.16 | +/- 0.25 | +/- 0.42 | | +/- 0.29 | +/- 0.13 |
| ***Sample X PSe(25)_ pt3*** | +/- 2.61 | | | | +/- 0.74 | +/- 0.56 | | |
| ***Sample X PSe(25)_ pt4*** | +/- 2.28 | | | | +/- 0.71 | | | |

Atom %

| | C-K | O-K | Na-K | Al-K | Si-K | Cl-K | K-K | Ca-K |
|---|---|---|---|---|---|---|---|---|
| ***Sample X PSe(25)_pt 1*** | | 40.95 | | | 59.05 | | | |
| ***Sample X PSe(25)_pt 2*** | 12.28 | 33.29 | 4.11 | 10.19 | 34.51 | | 4.87 | 0.75 |
| ***Sample X PSe(25)_pt 3*** | 96.55 | | | | 2.42 | 1.03 | | |
| ***Sample X PSe(25)_pt 4*** | 98.06 | | | | 1.94 | | | |

Atom % Error (+/- 1 Sigma)

| | C-K | O-K | Na-K | Al-K | Si-K | Cl-K | K-K | Ca-K |
|---|---|---|---|---|---|---|---|---|
| ***Sample X PSe(25)_ pt1*** | | +/- 0.54 | | | +/- 0.30 | | | |
| ***Sample X PSe(25)_ pt2*** | +/- 1.18 | +/- 0.63 | +/- 0.16 | +/- 0.21 | +/- 0.33 | | +/- 0.17 | +/- 0.07 |
| ***Sample X PSe(25)_ pt3*** | +/- 2.75 | | | | +/- 0.33 | +/- 0.20 | | |
| ***Sample X PSe(25)_ pt4*** | +/- 2.34 | | | | +/- 0.31 | | | |

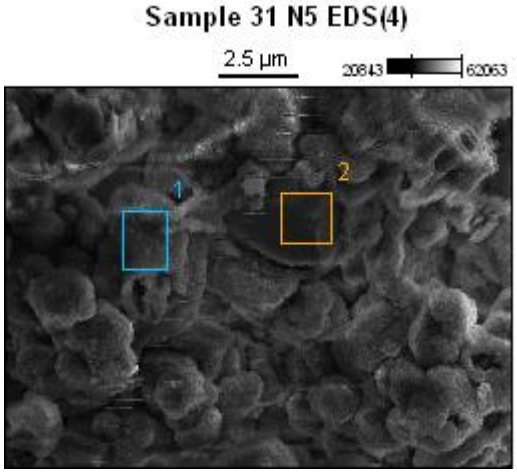


Image Name: Sample 31 N5 EDS(4)

Accelerating Voltage: 20.0 kV

Magnification: 8000

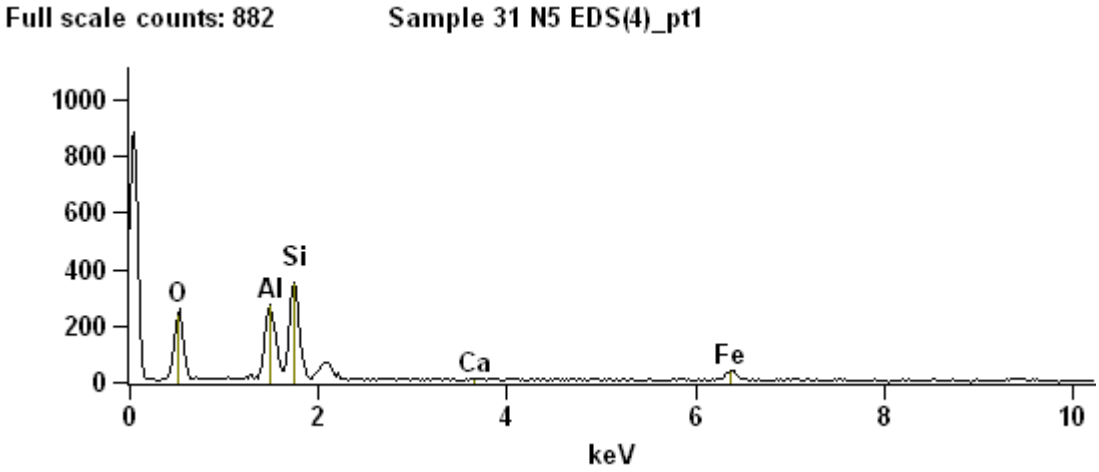


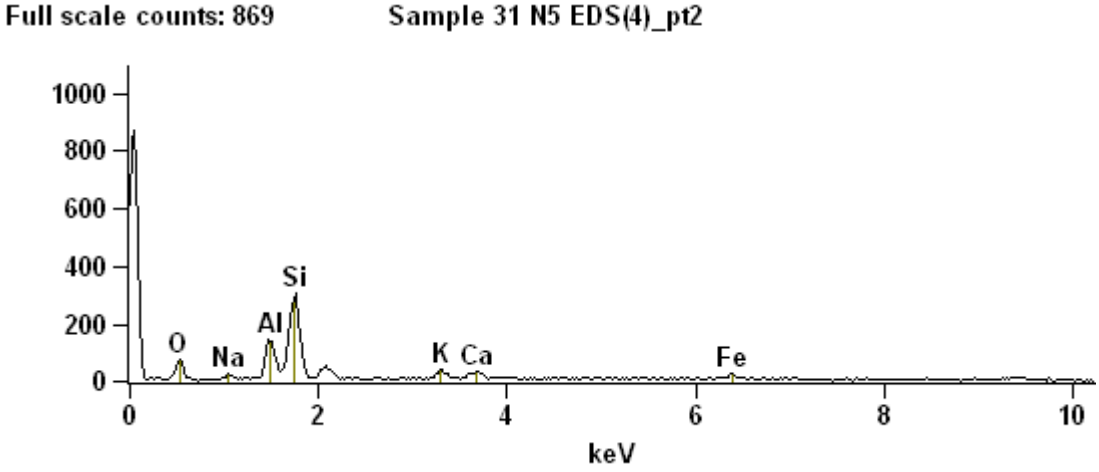


Weight %

| | *O-K* | *Na-K* | *Al-K* | *Si-K* | *K-K* | *Ca-K* | *Fe-K* |
|---|---|---|---|---|---|---|---|
| ***Sample 31 N5 EDS(4)_pt1*** | 38.44 | | 18.97 | 29.90 | | 0.78 | 11.91 |
| ***Sample 31 N5 EDS(4)_pt2*** | 22.51 | 3.02 | 14.91 | 40.72 | 5.94 | 4.32 | 8.57 |

Weight % Error (+/- 1 Sigma)

| | O-K | Na-K | Al-K | Si-K | K-K | Ca-K | Fe-K |
|---|---|---|---|---|---|---|---|
| ***Sample 31 N5 EDS(4)_pt 1*** | +/- 0.95 | | +/- 0.56 | +/- 0.79 | | +/- 0.22 | +/- 0.88 |
| ***Sample 31 N5 EDS(4)_pt 2*** | +/- 1.08 | +/- 0.42 | +/- 0.70 | +/- 1.14 | +/- 0.83 | +/- 0.49 | +/- 1.15 |

Atom %

| | O-K | Na-K | Al-K | Si-K | K-K | Ca-K | Fe-K |
|---|---|---|---|---|---|---|---|
| ***Sample 31 N5 EDS(4)_pt1*** | 54.57 | | 15.97 | 24.18 | | 0.44 | 4.84 |
| ***Sample 31 N5 EDS(4)_pt2*** | 35.58 | 3.32 | 13.98 | 36.67 | 3.84 | 2.72 | 3.88 |

Atom % Error (+/- 1 Sigma)

| | O-K | Na-K | Al-K | Si-K | K-K | Ca-K | Fe-K |
|---|---|---|---|---|---|---|---|
| ***Sample 31 N5 EDS(4)_pt 1*** | +/- 1.35 | | +/- 0.47 | +/- 0.64 | | +/- 0.12 | +/- 0.36 |
| ***Sample 31 N5 EDS(4)_pt 2*** | +/- 1.71 | +/- 0.46 | +/- 0.66 | +/- 1.03 | +/- 0.54 | +/- 0.31 | +/- 0.52 |

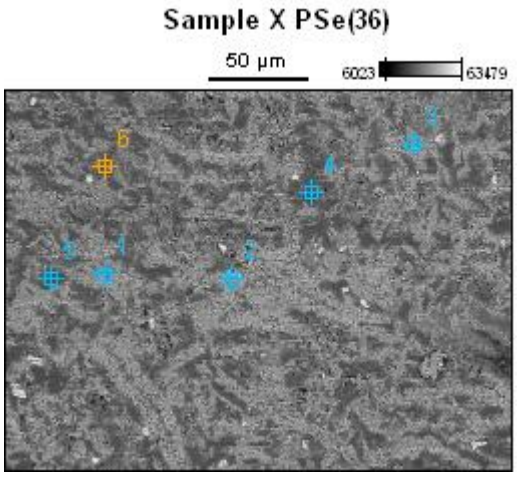


Image Name: Sample 35 PSe(36)

Accelerating Voltage: 20.0 kV

Magnification: 500

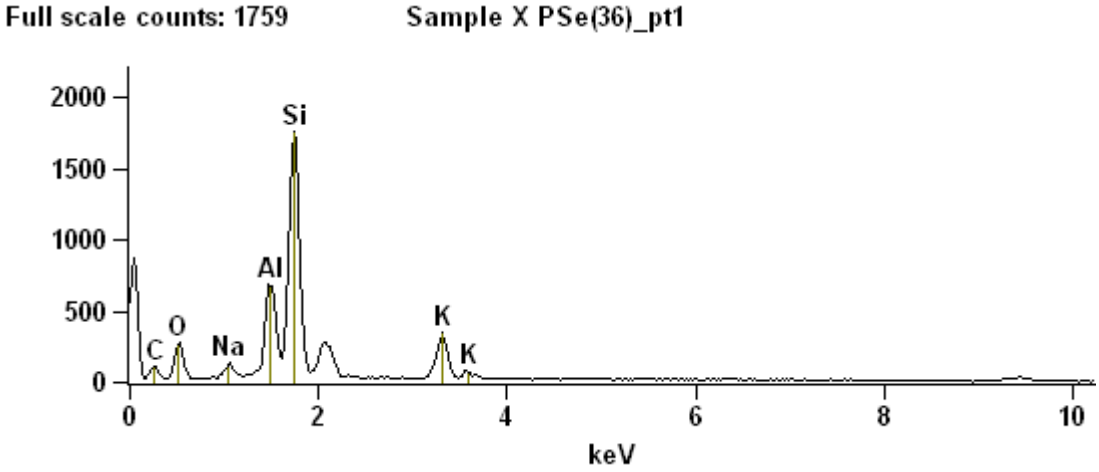

Full scale counts: 2014 Sample X PSe(36)_pt2

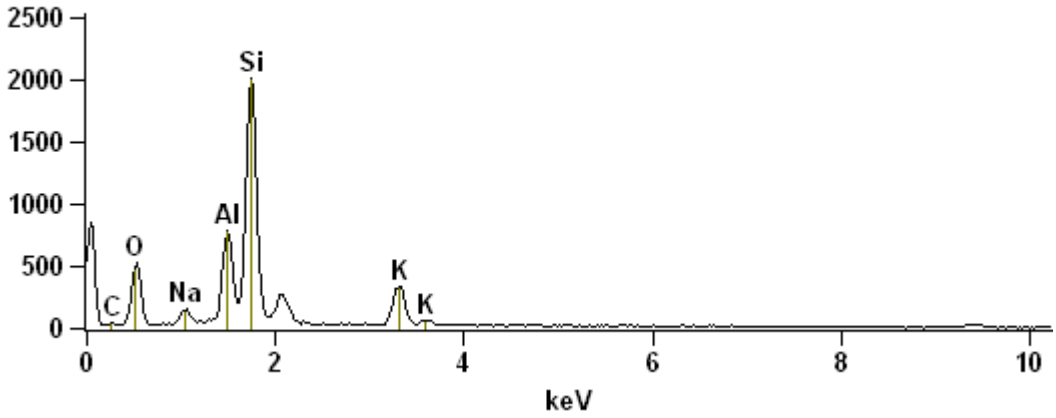


Full scale counts: 1273 Sample X PSe(36)_pt3

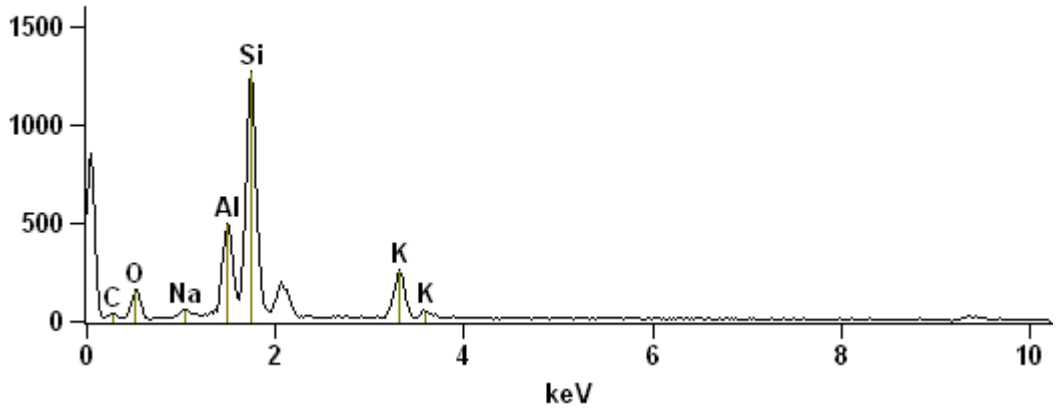


Full scale counts: 859 Sample X PSe(36)_pt4

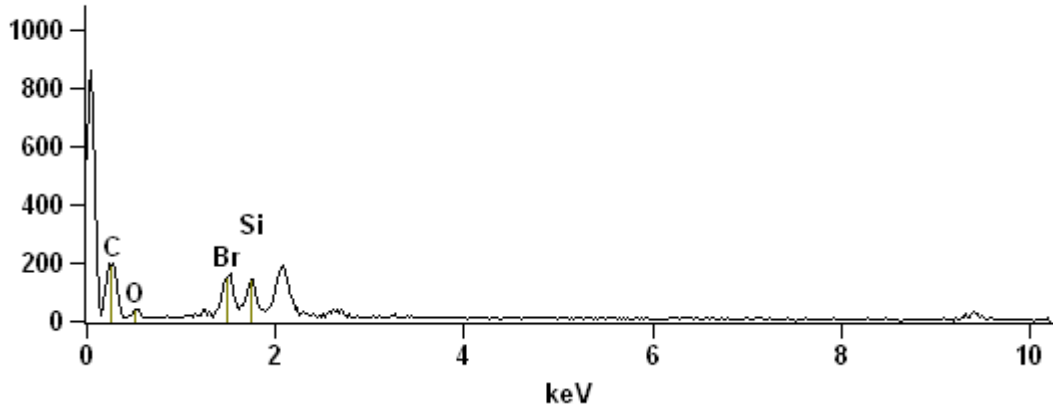

Full scale counts: 846 Sample X PSe(36)_pt5

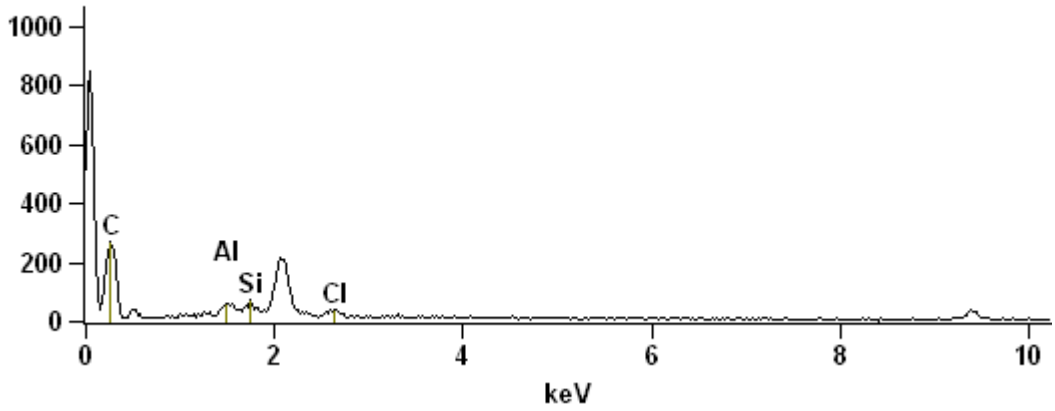


Full scale counts: 1065 Sample X PSe(36)_pt6

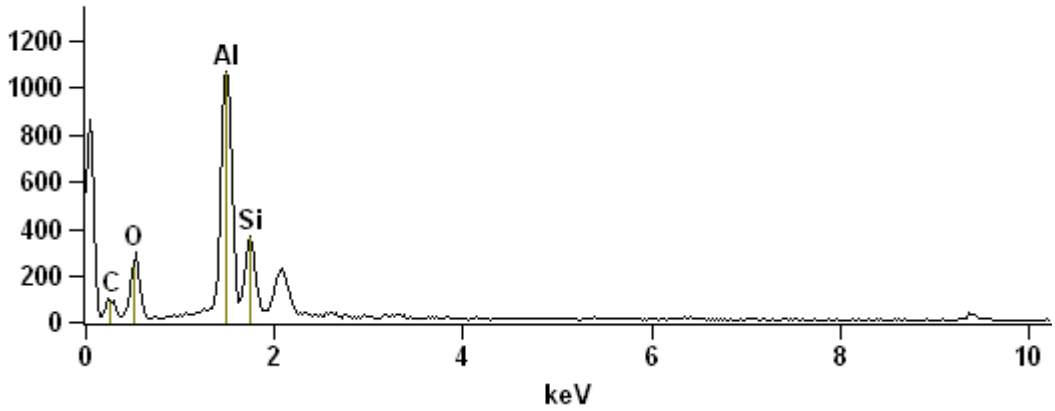


Weight %

| | C-K | O-K | Na-K | Al-K | Si-K | Cl-K | K-K | Br-K |
|---|---|---|---|---|---|---|---|---|
| ***Sample X PSe(36)_pt 1*** | 21.41 | 19.67 | 2.08 | 10.90 | 36.20 | | 9.74 | |
| ***Sample X PSe(36)_pt 2*** | 4.62 | 29.81 | 2.63 | 11.79 | 39.57 | | 11.58 | |
| ***Sample X PSe(36)_pt 3*** | 13.19 | 18.28 | 1.65 | 12.52 | 41.40 | | 12.96 | |
| ***Sample X PSe(36)_pt 4*** | 76.35 | 11.28 | | | 12.37 | | | 0.00 |
| ***Sample X PSe(36)_pt 5*** | 89.21 | | | 2.91 | 4.81 | 3.07 | | |
| ***Sample X PSe(36)_pt 6*** | 28.84 | 26.76 | | 29.53 | 14.87 | | | |

Weight % Error (+/- 1 Sigma)

| | C-K | O-K | Na-K | Al-K | Si-K | Cl-K | K-K | Br-K |
|---|---|---|---|---|---|---|---|---|
| ***Sample X PSe(36)_pt1*** | +/- 1.38 | +/- 0.54 | +/- 0.15 | +/- 0.25 | +/- 0.41 | | +/- 0.31 | |
| ***Sample X PSe(36)_pt2*** | +/- 0.68 | +/- 0.49 | +/- 0.17 | +/- 0.26 | +/- 0.43 | | +/- 0.32 | |
| ***Sample X PSe(36)_pt3*** | +/- 1.79 | +/- 0.65 | +/- 0.19 | +/- 0.34 | +/- 0.57 | | +/- 0.44 | |
| ***Sample X PSe(36)_pt4*** | +/- 2.25 | +/- 1.03 | | | +/- 0.69 | | | +/- 0.00 |
| ***Sample X PSe(36)_pt5*** | +/- 2.07 | | | +/- 0.38 | +/- 0.53 | +/- 0.52 | | |
| ***Sample X PSe(36)_pt6*** | +/- 1.94 | +/- 0.74 | | +/- 0.42 | +/- 0.51 | | | |

Atom %

| | C-K | O-K | Na-K | Al-K | Si-K | Cl-K | K-K | Br-K |
|---|---|---|---|---|---|---|---|---|
| ***Sample X PSe(36)_pt1*** | 35.34 | 24.38 | 1.79 | 8.01 | 25.55 | | 4.94 | |
| ***Sample X PSe(36)_pt2*** | 8.54 | 41.37 | 2.54 | 9.70 | 31.28 | | 6.57 | |
| ***Sample X PSe(36)_pt3*** | 23.97 | 24.94 | 1.56 | 10.13 | 32.17 | | 7.23 | |
| ***Sample X PSe(36)_pt4*** | 84.73 | 9.40 | | | 5.87 | | | 0.00 |
| ***Sample X PSe(36)_pt5*** | 95.31 | | | 1.39 | 2.20 | 1.11 | | |
| ***Sample X PSe(36)_pt6*** | 42.15 | 29.35 | | 19.21 | 9.29 | | | |

Atom % Error (+/- 1 Sigma)

| | C-K | O-K | Na-K | Al-K | Si-K | Cl-K | K-K | Br-K |
|---|---|---|---|---|---|---|---|---|
| ***Sample X PSe(36)_pt1*** | +/- 2.27 | +/- 0.67 | +/- 0.13 | +/- 0.18 | +/- 0.29 | | +/- 0.16 | |
| ***Sample X PSe(36)_pt2*** | +/- 1.25 | +/- 0.68 | +/- 0.16 | +/- 0.21 | +/- 0.34 | | +/- 0.18 | |
| ***Sample X PSe(36)_pt3*** | +/- 3.26 | +/- 0.89 | +/- 0.18 | +/- 0.27 | +/- 0.44 | | +/- 0.25 | |
| ***Sample X PSe(36)_pt4*** | +/- 2.50 | +/- 0.85 | | | +/- 0.33 | | | +/- 0.00 |
| ***Sample X PSe(36)_pt5*** | +/- 2.21 | | | +/- 0.18 | +/- 0.24 | +/- 0.19 | | |
| ***Sample X PSe(36)_pt6*** | +/- 2.83 | +/- 0.81 | | +/- 0.27 | +/- 0.32 | | | |

**Appendix IV:** Raw data of major and trace elements of bulk rock ignimbrite obtained through X-ray fluorescence (XRF) spectrometry.

**Bulk rock Ignimbrite**

| **Sample Name** | **Sc (PPM)** | **V (PPM)** | **Cr (PPM)** | **Co (PPM)** | **Ni (PPM)** | **Cu (PPM)** | **Zn (PPM)** | **Ga (PPM)** | **As (PPM)** | **Rb (PPM)** | **Sr (PPM)** | **Y (PPM)** | **Zr (PPM)** | **Nb (PPM)** |
|---|---|---|---|---|---|---|---|---|---|---|---|---|---|---|
| Sample 1 | 10 | 28 | 0 | 9 | 6 | 21 | 68 | 20 | 18 | 113 | 44 | 61 | 332 | 12 |
| Sample 23 | 11 | 29 | 0 | 12 | 4 | 9 | 49 | 20 | 10 | 163 | 56 | 35 | 308 | 11 |
| Sample 26A | 11 | 31 | 1 | 8 | 4 | 15 | 58 | 21 | 8 | 151 | 58 | 19 | 343 | 11 |
| Sample 26B | 14 | 22 | 0 | 11 | 3 | 8 | 60 | 22 | 8 | 128 | 66 | 10 | 295 | 10 |
| Sample 26C | 12 | 22 | 0 | 11 | 3 | 12 | 61 | 19 | 10 | 152 | 101 | 17 | 301 | 10 |
| Sample 26E | 9 | 19 | 0 | 8 | 3 | 12 | 57 | 18 | 9 | 164 | 95 | 10 | 308 | 10 |
| Sample 27 | 15 | 22 | 2 | 12 | 5 | 16 | 63 | 23 | 9 | 76 | 44 | 49 | 304 | 10 |
| Sample 30C | 9 | 16 | 0 | 10 | 3 | 11 | 46 | 20 | 8 | 168 | 88 | 12 | 337 | 11 |
| Sample 35 | 9 | 22 | 0 | 15 | 5 | 8 | 77 | 19 | 8 | 165 | 98 | 20 | 296 | 11 |
| Sample 37A | 9 | 14 | 0 | 21 | 4 | 8 | 61 | 18 | 8 | 173 | 86 | 15 | 309 | 11 |
| Sample 37B | 9 | 17 | 0 | 12 | 5 | 5 | 85 | 18 | 12 | 171 | 90 | 15 | 289 | 11 |
| Sample 44 | 11 | 14 | 0 | 9 | 7 | 12 | 43 | 19 | 10 | 168 | 81 | 11 | 332 | 11 |
| Sample 48 | 15 | 26 | 0 | 13 | 3 | 7 | 85 | 22 | 8 | 117 | 67 | 9 | 289 | 10 |
| Sample 51A | 10 | 17 | 0 | 12 | 4 | 8 | 68 | 17 | 8 | 166 | 96 | 34 | 284 | 11 |

| Sample Name | Mo (PPM) | Sn (PPM) | Sb (PPM) | Cs (PPM) | Ba (PPM) | La (PPM) | Ce (PPM) | Nd (PPM) | Tl (PPM) | Pb (PPM) | Th (PPM) | U (PPM) | SiO2 (%) | Al2O3 (%) |
|---|---|---|---|---|---|---|---|---|---|---|---|---|---|---|
| Sample 1 | 5 | 5 | 2 | 0 | 940 | 69 | 40 | 52 | 1 | 17 | 25 | 5 | 65.68 | 19.24 |
| Sample 23 | 5 | 3 | 2 | 5 | 808 | 23 | 68 | 24 | 1 | 24 | 24 | 5 | 68.53 | 17.03 |
| Sample 26A | 5 | 4 | 3 | 3 | 735 | 6 | 107 | 19 | 1 | 20 | 26 | 5 | 66.53 | 17.75 |
| Sample 26B | 5 | 4 | 3 | 1 | 672 | 0 | 25 | 5 | 1 | 18 | 21 | 3 | 66.72 | 18.09 |
| Sample 26C | 5 | 2 | 1 | 1 | 868 | 9 | 59 | 16 | 1 | 15 | 18 | 4 | 68.76 | 15.71 |
| Sample 26E | 5 | 2 | 2 | 7 | 815 | 9 | 37 | 14 | 1 | 16 | 18 | 3 | 68.36 | 15.45 |
| Sample 27 | 5 | 5 | 2 | 3 | 340 | 54 | 33 | 53 | 1 | 12 | 21 | 4 | 63.22 | 20.26 |
| Sample 30C | 5 | 2 | 2 | 1 | 800 | 7 | 29 | 10 | 1 | 16 | 24 | 4 | 68.01 | 15.66 |
| Sample 35 | 5 | 3 | 2 | 0 | 1001 | 16 | 56 | 27 | 1 | 18 | 22 | 4 | 70.24 | 15.04 |
| Sample 37A | 5 | 3 | 2 | 2 | 996 | 12 | 40 | 19 | 1 | 19 | 23 | 4 | 70.96 | 15.26 |
| Sample 37B | 5 | 2 | 2 | 3 | 928 | 7 | 50 | 14 | 1 | 24 | 22 | 4 | 70.88 | 14.42 |
| Sample 44 | 5 | 2 | 2 | 5 | 844 | 13 | 46 | 19 | 1 | 16 | 21 | 4 | 66.31 | 16.17 |
| Sample 48 | 5 | 2 | 1 | 4 | 599 | 0 | 164 | 5 | 1 | 26 | 19 | 3 | 64.74 | 18.67 |
| Sample 51A | 5 | 3 | 1 | 2 | 842 | 34 | 88 | 38 | 1 | 17 | 22 | 5 | 71.17 | 14.65 |

| Sample Name | TiO2 (%) | MnO (PPM) | Fe2O3 (%) | Na2O (%) | MgO (%) | K2O (%) | CaO (%) | P2O5 (%) | S (PPM) | F (PPM) | Cl (PPM) | CO2 (%) | Sum (%) | Compton (%) |
|---|---|---|---|---|---|---|---|---|---|---|---|---|---|---|
| Sample 1 | 0.329 | 260 | 4.49769 | 1.253 | 0.208 | 2.722 | 0.232 | 0.102 | 18 | 296 | 167 | 6.07 | 100.59 | 98.549 |
| Sample 23 | 0.306 | 755 | 4.02559 | 1.825 | 0.182 | 4.125 | 0.328 | 0.085 | 0 | 96 | 196 | 3.87 | 100.58 | 99.129 |
| Sample 26A | 0.317 | 752 | 4.16998 | 1.712 | 0.202 | 3.745 | 0.227 | 0.074 | 33 | 175 | 152 | 5.59 | 100.6 | 99.585 |
| Sample 26B | 0.356 | 1201 | 4.44636 | 1.812 | 0.179 | 3.266 | 0.442 | 0.081 | 10 | 400 | 171 | 4.97 | 100.68 | 99.52 |
| Sample 26C | 0.323 | 1582 | 3.80026 | 3.122 | 0.134 | 3.994 | 0.839 | 0.081 | 70 | 148 | 394 | 3.56 | 100.72 | 100.081 |
| Sample 26E | 0.259 | 385 | 3.59277 | 3.375 | 0.172 | 4.271 | 0.812 | 0.085 | 168 | 59 | 353 | 3.88 | 100.52 | 99.134 |
| Sample 27 | 0.336 | 251 | 5.66828 | 1.042 | 0.183 | 1.715 | 0.297 | 0.11 | 65 | 170 | 741 | 7.5 | 100.58 | 98.977 |
| Sample 30C | 0.284 | 516 | 3.99605 | 2.983 | 0.297 | 4.335 | 0.692 | 0.082 | 146 | 52 | 110 | 3.94 | 100.53 | 98.755 |
| Sample 35 | 0.311 | 1935 | 3.37267 | 3.356 | 0.196 | 4.353 | 0.898 | 0.091 | 0 | 483 | 365 | 2.46 | 100.78 | 100.226 |
| Sample 37A | 0.254 | 576 | 2.96499 | 3.031 | 0.143 | 4.545 | 0.69 | 0.079 | 0 | 194 | 332 | 2.33 | 100.55 | 99.642 |
| Sample 37B | 0.224 | 1742 | 3.79341 | 3.46 | 0.141 | 4.54 | 0.857 | 0.084 | 0 | 179 | 255 | 1.82 | 100.62 | 99.55 |
| Sample 44 | 0.298 | 622 | 3.95049 | 2.483 | 0.432 | 4.293 | 0.573 | 0.094 | 190 | 252 | 154 | 5.7 | 100.59 | 99.799 |
| Sample 48 | 0.381 | 753 | 5.45725 | 1.813 | 0.116 | 2.934 | 0.472 | 0.091 | 76 | 180 | 166 | 5.71 | 100.65 | 99.93 |
| Sample 51A | 0.267 | 209 | 3.16922 | 3.415 | 0.141 | 4.425 | 0.92 | 0.088 | 0 | 359 | 471 | 2.02 | 100.55 | 100.233 |



## Pumice

| Sample Name | SiO2 (%) | Al2O3 (%) | TiO2 (%) | MnO (%) | Fe2O3 (%) | MgO (%) | CaO (%) | Na2O (%) | K2O (%) | P2O5 (%) | SO3 (%) | SrO (Sr - PPM) | BaO (Ba - PPM) | CO2 (%) | Sum (%) | Specimen mass | Additive mass |
|---|---|---|---|---|---|---|---|---|---|---|---|---|---|---|---|---|---|
| Sample 11 P | 56.98 | 22.36 | 0.983 | 0.032 | 6.31218 | 0.15 | 1.565 | 2.975 | 1.86 | 0.147 | 0.02 | 227 | 329 | 8.06 | 101.513 | 0.733 | 8.001 |
| Sample 44 P | 71.27 | 14.77 | 0.206 | 0.043 | 2.68891 | 0.115 | 0.773 | 3.707 | 4.66 | 0.08 | 0.03 | 86 | 926 | 2.14 | 100.59 | 0.8007 | 8.0026 |
| Sample 26E P | 70.62 | 14.74 | 0.189 | 0.054 | 2.6969 | 0.144 | 0.579 | 3.327 | 5.25 | 0.07 | 0.02 | 72 | 884 | 2.55 | 100.344 | 0.8033 | 8.0027 |

**Appendix V:** Raw trace element data of the selected pumice clasts acquired using the LA-ICP-MS.

| SelectionLabel | Comments | Si29_CPS | IntStdWv | Na_ppm_m23 | Mg_ppm_m24 | Al_ppm_m27 | K_ppm_m39 | Ca_ppm_m43 | Sc_ppm_m45 | Ti_ppm_m47 | V_ppm_m51 | Cr_ppm_m52 | Mn_ppm_m55 | Fe_ppm_m56 |
|---|---|---|---|---|---|---|---|---|---|---|---|---|---|---|
| G_NIST612_11_0 | NIST_612_spot - 1 | 1.34E+08 | 33.7 | 102200 | 68 | 10770 | 70.4 | 85000 | 40.01 | 44.16 | 38.98 | 36.75 | 38.91 | 51.46 |
| G_NIST612_11_1 | NIST_612_spot - 2 | 1.40E+08 | 33.7 | 101400 | 67.9 | 10730 | 62.9 | 85200 | 39.84 | 44.03 | 38.74 | 36.17 | 38.6 | 50.66 |
| G_NIST612_11_2 | NIST_612_spot - 3 | 1.44E+08 | 33.7 | 101000 | 68.2 | 10740 | 62.01 | 85000 | 39.86 | 43.48 | 38.54 | 35.97 | 38.61 | 50.72 |
| G_NIST612_11_3 | NIST_612_spot - 4 | 1.44E+08 | 33.7 | 101200 | 68 | 10740 | 62.19 | 84900 | 39.81 | 43.99 | 38.79 | 36.38 | 38.52 | 50.64 |
| G_NIST612_11_4 | NIST_612_spot - 5 | 1.43E+08 | 33.7 | 102200 | 67.9 | 10760 | 62.54 | 85170 | 40 | 44.24 | 38.96 | 36.64 | 38.86 | 51.36 |
| | | | | | | | | | | | | | | |
| G_NIST610_11_0 | NIST_610_spot - 1 | 1.41E+08 | 32.6 | 99000 | 434.4 | 10220 | 480.1 | 81800 | 464.4 | 508 | 460.2 | 419.4 | 453.3 | 459 |
| G_NIST610_11_1 | NIST_610_spot - 2 | 1.42E+08 | 32.6 | 99900 | 434.5 | 10290 | 479.9 | 82000 | 465.8 | 505 | 456.6 | 416.7 | 449 | 457 |
| G_NIST610_11_2 | NIST_610_spot - 3 | 1.43E+08 | 32.6 | 99200 | 421 | 10310 | 481.1 | 82000 | 468.1 | 517 | 460.7 | 424 | 453.2 | 459 |
| G_NIST610_11_3 | NIST_610_spot - 4 | 1.45E+08 | 32.6 | 100100 | 419.2 | 10250 | 477.5 | 81600 | 462.1 | 512 | 456.1 | 421.2 | 449 | 454 |
| | | | | | | | | | | | | | | |
| Sample_0 | Chrissanne_26E - 1 | 4.80E+06 | 33 | 22170 | 611.1 | 82900 | 44760 | 5490 | 8.45 | 2232 | 21.71 | 16.72 | 408.9 | 14870 |
| Sample_1 | Chrissanne_44 - 1 | 5.00E+06 | 33.3 | 24040 | 430.9 | 82400 | 39490 | 6860 | 7.72 | 2297 | 25.42 | 19.17 | 328.1 | 14520 |
| Sample_2 | Chrissanne_11 - 1 | 5.40E+06 | 23.6 | 17210 | 457.9 | 112570 | 14010 | 11520 | 14.46 | 6832 | 93.6 | 44.77 | 223.8 | 35290 |
| Sample_3 | Chrissanne_26E - 2 | 5.40E+06 | 33 | 21650 | 594.8 | 81300 | 45240 | 5380 | 8.44 | 2265 | 21.99 | 16.66 | 406.7 | 14990 |

| SelectionLabel | Comments | Si29_CPS | IntStdWv | Co_ppm_m59 | Ni_ppm_m60 | Cu_ppm_m63 | Ga_ppm_m71 | Ge_ppm_m72 | Rb_ppm_m85 | Sr_ppm_m88 | Y_ppm_m89 | Zr_ppm_m90 | Nb_ppm_m93 | Cs_ppm_m133 |
|---|---|---|---|---|---|---|---|---|---|---|---|---|---|---|
| G_NIST612_11_0 | NIST_612_spot - 1 | 1.34E+08 | 33.7 | 35.68 | 39.1 | 38.12 | 37.42 | 36.86 | 32.12 | 79.5 | 38.82 | 38.3 | 39.19 | 43.33 |
| G_NIST612_11_1 | NIST_612_spot - 2 | 1.40E+08 | 33.7 | 35.34 | 38.6 | 37.66 | 36.69 | 35.74 | 31.18 | 78.1 | 38.17 | 37.79 | 38.8 | 42.43 |
| G_NIST612_11_2 | NIST_612_spot - 3 | 1.44E+08 | 33.7 | 35.43 | 38.86 | 37.8 | 36.56 | 35.85 | 31.3 | 78.3 | 38.2 | 37.8 | 38.83 | 42.47 |
| G_NIST612_11_3 | NIST_612_spot - 4 | 1.44E+08 | 33.7 | 35.3 | 38.43 | 37.39 | 36.73 | 35.87 | 31.06 | 77.1 | 37.64 | 37.37 | 38.55 | 42.36 |
| G_NIST612_11_4 | NIST_612_spot - 5 | 1.43E+08 | 33.7 | 35.68 | 38.95 | 37.94 | 37.51 | 36.8 | 31.7 | 79.2 | 38.72 | 38.24 | 39.11 | 42.97 |
| | | | | | | | | | | | | | | |
| G_NIST610_11_0 | NIST_610_spot - 1 | 1.41E+08 | 32.6 | 417.3 | 465 | 420.3 | 441.3 | 413 | 423.2 | 511 | 454 | 448 | 471 | 375 |
| G_NIST610_11_1 | NIST_610_spot - 2 | 1.42E+08 | 32.6 | 419.6 | 469 | 427 | 442.4 | 419 | 429.7 | 520 | 459 | 450 | 472 | 376.2 |
| G_NIST610_11_2 | NIST_610_spot - 3 | 1.43E+08 | 32.6 | 420.7 | 468 | 424.2 | 447.7 | 420.2 | 420.3 | 511 | 455 | 449 | 473 | 378.3 |
| G_NIST610_11_3 | NIST_610_spot - 4 | 1.45E+08 | 32.6 | 413 | 465 | 422 | 444 | 415.5 | 418.8 | 511 | 451 | 446 | 466 | 373.4 |
| | | | | | | | | | | | | | | |
| Sample_0 | Chrissanne_26E - 1 | 4.80E+06 | 33 | 19.16 | 11.74 | 12.49 | 15.54 | 4.29 | 186.9 | 74.7 | 12.68 | 270.4 | 12.37 | 5.83 |
| Sample_1 | Chrissanne_44 - 1 | 5.00E+06 | 33.3 | 12.21 | 18.8 | 10.83 | 15.32 | 1.33 | 159.6 | 84.9 | 12.44 | 270.5 | 9.79 | 6.18 |
| Sample_2 | Chrissanne_11 - 1 | 5.40E+06 | 23.6 | 23.87 | 32.23 | 12.69 | 16.75 | 1.25 | 58.5 | 222.4 | 8.3 | 172.9 | 6.82 | 2.842 |
| Sample_3 | Chrissanne_26E - 2 | 5.40E+06 | 33 | 19.07 | 11.23 | 11.08 | 15.67 | 1.6 | 182.6 | 73.8 | 13.2 | 276 | 12.78 | 5.87 |

| SelectionLabel | Comments | Si29_CPS | IntStdWv | Ba_ppm_m137 | La_ppm_m139 | Ce_ppm_m140 | Pr_ppm_m141 | Nd_ppm_m146 | Sm_ppm_m147 | Eu_ppm_m153 | Gd_ppm_m157 | Tb_ppm_m159 | Dy_ppm_m163 |
|---|---|---|---|---|---|---|---|---|---|---|---|---|---|
| G_NIST612_11_0 | NIST_612_spot - 1 | 1.34E+08 | 33.7 | 39.33 | 36.15 | 38.54 | 38.02 | 35.74 | 37.78 | 35.59 | 37.58 | 37.77 | 35.76 |
| G_NIST612_11_1 | NIST_612_spot - 2 | 1.40E+08 | 33.7 | 39.3 | 35.96 | 38.44 | 37.97 | 35.46 | 37.74 | 35.66 | 37.09 | 37.5 | 35.33 |
| G_NIST612_11_2 | NIST_612_spot - 3 | 1.44E+08 | 33.7 | 39.49 | 36.16 | 38.49 | 37.91 | 35.57 | 37.76 | 35.77 | 37.43 | 37.68 | 35.58 |
| G_NIST612_11_3 | NIST_612_spot - 4 | 1.44E+08 | 33.7 | 38.75 | 35.42 | 37.74 | 37.19 | 34.84 | 37.23 | 35.17 | 36.86 | 37.31 | 35.2 |
| G_NIST612_11_4 | NIST_612_spot - 5 | 1.43E+08 | 33.7 | 39.4 | 36.18 | 38.67 | 38.19 | 35.79 | 37.93 | 35.73 | 37.62 | 37.7 | 35.61 |
| | | | | | | | | | | | | | |
| G_NIST610_11_0 | NIST_610_spot - 1 | 1.41E+08 | 32.6 | 459 | 435 | 451.3 | 445.3 | 442.3 | 463.8 | 446 | 450.6 | 436.6 | 446 |
| G_NIST610_11_1 | NIST_610_spot - 2 | 1.42E+08 | 32.6 | 467 | 444 | 460 | 456 | 452 | 477 | 459 | 461 | 443.8 | 451 |
| G_NIST610_11_2 | NIST_610_spot - 3 | 1.43E+08 | 32.6 | 469.7 | 441.1 | 458.3 | 453.3 | 452.8 | 476.5 | 455.8 | 463.5 | 445 | 457 |
| G_NIST610_11_3 | NIST_610_spot - 4 | 1.45E+08 | 32.6 | 463 | 433 | 455.7 | 445 | 443.8 | 465 | 449 | 460.8 | 443.9 | 455.2 |
| | | | | | | | | | | | | | |
| Sample_0 | Chrissanne_26E - 1 | 4.80E+06 | 33 | 928 | 18.95 | 56.2 | 2.5 | 8.28 | 1.73 | 0.723 | 1.63 | 0.273 | 2.05 |
| Sample_1 | Chrissanne_44 - 1 | 5.00E+06 | 33.3 | 899 | 28.7 | 55.3 | 4.21 | 13.39 | 2 | 0.894 | 1.8 | 0.272 | 2.06 |
| Sample_2 | Chrissanne_11 - 1 | 5.40E+06 | 23.6 | 287.8 | 11.12 | 36.28 | 2.231 | 8.61 | 1.64 | 0.675 | 1.371 | 0.211 | 1.467 |
| Sample_3 | Chrissanne_26E - 2 | 5.40E+06 | 33 | 937 | 19.14 | 56.2 | 2.48 | 8.53 | 1.85 | 0.755 | 1.62 | 0.288 | 2.13 |

| SelectionLabel | Comments | Si29_CPS | IntStdWv | Ho_ppm_m165 | Er_ppm_m166 | Tm_ppm_m169 | Yb_ppm_m172 | Lu_ppm_m175 | Ta_ppm_m181 | Tl_ppm_m205 | Pb_ppm_m206 | Pb_ppm_m207 | Pb_ppm_m208 | Th_ppm_m232 | U_ppm_m238 |
|---|---|---|---|---|---|---|---|---|---|---|---|---|---|---|---|
| G_NIST612_11_0 | NIST_612_spot - 1 | 1.34E+08 | 33.7 | 38.6 | 38.3 | 37.2 | 39.46 | 37.23 | 37.67 | 15.13 | 39.2 | 39.2 | 39.13 | 37.76 | 37.38 |
| G_NIST612_11_1 | NIST_612_spot - 2 | 1.40E+08 | 33.7 | 38.18 | 37.96 | 36.7 | 39.23 | 37 | 37.74 | 14.79 | 38.17 | 38.31 | 38.48 | 38.01 | 37.62 |
| G_NIST612_11_2 | NIST_612_spot - 3 | 1.44E+08 | 33.7 | 38.33 | 38.03 | 36.74 | 39.15 | 36.94 | 37.42 | 14.7 | 38.13 | 37.93 | 38.01 | 37.45 | 37.01 |
| G_NIST612_11_3 | NIST_612_spot - 4 | 1.44E+08 | 33.7 | 37.89 | 37.38 | 36.26 | 38.58 | 36.62 | 37.23 | 14.93 | 38.42 | 38.54 | 38.23 | 37.64 | 37.26 |
| G_NIST612_11_4 | NIST_612_spot - 5 | 1.43E+08 | 33.7 | 38.53 | 38.39 | 37.19 | 39.6 | 37.2 | 37.86 | 15.06 | 39.05 | 39.2 | 39.14 | 38.03 | 37.6 |
| | | | | | | | | | | | | | | | |
| G_NIST610_11_0 | NIST_610_spot - 1 | 1.41E+08 | 32.6 | 446 | 460 | 424 | 478 | 434 | 447 | 65.6 | 442.1 | 444.8 | 439.8 | 448.1 | 454 |
| G_NIST610_11_1 | NIST_610_spot - 2 | 1.42E+08 | 32.6 | 449.6 | 467 | 433 | 487.5 | 447 | 456 | 66.4 | 451.4 | 455.7 | 454.5 | 466 | 470 |
| G_NIST610_11_2 | NIST_610_spot - 3 | 1.43E+08 | 32.6 | 456 | 472 | 432 | 483 | 439 | 450 | 66.2 | 452.4 | 455.7 | 453.6 | 462 | 466.9 |
| G_NIST610_11_3 | NIST_610_spot - 4 | 1.45E+08 | 32.6 | 452.7 | 470 | 429 | 481 | 436 | 447 | 66.7 | 457 | 462 | 459 | 466.3 | 472.7 |
| | | | | | | | | | | | | | | | |
| Sample_0 | Chrissanne_26E - 1 | 4.80E+06 | 33 | 0.454 | 1.6 | 0.26 | 2.21 | 0.331 | 1.128 | 0.15 | 15.15 | 13.91 | 14.48 | 15 | 3.85 |
| Sample_1 | Chrissanne_44 - 1 | 5.00E+06 | 33.3 | 0.443 | 1.51 | 0.25 | 1.97 | 0.318 | 1.101 | 0.262 | 15.5 | 14.8 | 15.2 | 16.02 | 3.8 |
| Sample_2 | Chrissanne_11 - 1 | 5.40E+06 | 23.6 | 0.325 | 1.162 | 0.195 | 1.617 | 0.247 | 0.66 | 0.13 | 17.52 | 15.93 | 16.69 | 7.67 | 1.804 |
| Sample_3 | Chrissanne_26E - 2 | 5.40E+06 | 33 | 0.476 | 1.72 | 0.306 | 2.26 | 0.348 | 1.207 | 0.227 | 15.8 | 14.4 | 14.8 | 14.77 | 3.79 |

**Appendix VI:** Raw data of major and trace element measurements obtained by EPMA analyses

(a) Raw major element measurements of plagioclase crystals. Samples 13 and 37B.

| SiO2 | TiO2 | Al2O3 | FeO | MgO | CaO | Na2O | K2O | Total | Comment |
|---|---|---|---|---|---|---|---|---|---|
| 51.17 | 0.00 | 31.02 | 0.44 | 0.14 | 13.45 | 3.39 | 0.19 | 99.81 | Plag-01 |
| 51.32 | 0.00 | 30.95 | 0.43 | 0.15 | 13.57 | 3.42 | 0.18 | 100.01 | Plag-02 |
| 57.86 | 0.00 | 26.59 | 0.24 | 0.01 | 8.37 | 6.18 | 0.62 | 99.88 | Plagioclase-03 |
| 56.96 | 0.00 | 23.06 | 0.23 | 0.00 | 4.84 | 6.20 | 1.12 | 92.41 | Plagioclase-04 |
| 58.18 | 0.00 | 26.12 | 0.29 | 0.02 | 8.04 | 6.11 | 1.14 | 99.90 | Plagioclase-05 |
| 59.28 | 0.00 | 26.00 | 0.24 | 0.01 | 7.37 | 6.72 | 0.89 | 100.52 | Plagioclase-06 |
| 60.72 | 0.00 | 24.78 | 0.20 | 0.01 | 6.23 | 7.09 | 1.30 | 100.35 | Plagioclase-07 |
| 59.58 | 0.00 | 25.81 | 0.26 | 0.01 | 7.24 | 6.78 | 0.99 | 100.67 | Plagioclase-08 |
| 60.42 | 0.00 | 25.08 | 0.21 | 0.00 | 6.42 | 7.04 | 1.24 | 100.42 | Plagioclase-09 |
| 57.92 | 0.00 | 26.43 | 0.29 | 0.02 | 8.42 | 6.17 | 1.02 | 100.27 | Plagioclase-10 |
| 62.50 | 0.00 | 23.74 | 0.20 | 0.01 | 4.98 | 7.36 | 1.84 | 100.63 | Plagioclase-11 |
| 60.33 | 0.00 | 25.32 | 0.20 | 0.01 | 6.68 | 6.90 | 1.20 | 100.62 | Plagioclase-12 |
| 56.05 | 0.00 | 12.20 | 1.66 | 0.05 | 0.29 | 1.23 | 2.26 | 73.74 | Plagioclase-13 |
| 35.05 | 0.09 | 19.83 | 1.24 | 0.03 | 0.41 | 1.02 | 2.90 | 60.56 | Plagioclase-14 |
| 62.81 | 0.00 | 14.20 | 0.32 | 0.02 | 0.35 | 2.45 | 11.63 | 91.79 | Plagioclase-15 |
| 47.79 | 0.00 | 24.12 | 4.87 | 0.06 | 0.23 | 0.63 | 1.75 | 79.46 | Plagioclase-16 |
| 34.30 | 0.00 | 23.00 | 3.20 | 0.07 | 0.10 | 0.09 | 0.35 | 61.11 | Plagioclase-17 |
| 92.69 | 0.00 | 5.42 | 0.28 | 0.00 | 0.08 | 0.78 | 3.06 | 102.31 | Plagioclase-18 |
| 57.77 | 0.00 | 16.76 | 0.52 | 0.01 | 1.81 | 4.57 | 1.10 | 82.55 | Plagioclase-19 |
| 2.09 | 0.75 | 1.47 | 1.50 | 0.00 | 0.49 | 0.06 | 0.96 | 7.31 | Plagioclase-20 |
| 91.56 | 0.00 | 2.78 | 0.46 | 0.03 | 0.05 | 0.35 | 0.19 | 95.41 | Plagioclase-21 |
| 65.16 | 0.00 | 19.10 | 0.34 | 0.01 | 0.39 | 3.53 | 16.74 | 105.28 | Plagioclase-22 |
| 60.62 | 0.00 | 25.34 | 0.18 | 0.00 | 6.12 | 6.85 | 1.26 | 100.36 | Plagioclase-23 |
| 71.41 | 0.00 | 13.45 | 0.23 | 0.02 | 0.64 | 3.08 | 6.24 | 95.07 | Plagioclase-37b-DM-37 |

| SiO2 | TiO2 | Al2O3 | FeO | MgO | CaO | Na2O | K2O | Total | Comment |
|---|---|---|---|---|---|---|---|---|---|
| 64.67 | 0.00 | 15.86 | 0.32 | 0.01 | 0.32 | 3.76 | 13.43 | 98.37 | Plagioclase-37b-DM-38 |
| 70.28 | 0.32 | 13.57 | 0.26 | 0.00 | 0.88 | 4.10 | 4.69 | 94.09 | Plagioclase-37b-DM-39 |
| 62.95 | 0.15 | 15.98 | 0.82 | 0.00 | 0.54 | 3.15 | 9.27 | 92.87 | Plagioclase-37b-DM-40 |
| 73.81 | 0.00 | 14.80 | 0.26 | 0.00 | 0.27 | 2.73 | 9.06 | 100.93 | Plagioclase-37b-DM-41 |
| 70.73 | 0.62 | 13.26 | 0.30 | 0.00 | 0.14 | 2.68 | 10.66 | 98.40 | Plagioclase-37b-LM-42 |
| 70.70 | 0.00 | 12.38 | 0.20 | 0.00 | 0.77 | 3.27 | 5.69 | 93.02 | Plagioclase-37b-LM-43 |
| 68.40 | 0.00 | 14.88 | 0.53 | 0.01 | 0.21 | 2.88 | 9.60 | 96.51 | Plagioclase-37b-LM-44 |
| 70.32 | 0.00 | 18.93 | 0.76 | 0.00 | 0.59 | 5.19 | 9.73 | 105.51 | Plagioclase-37b-LM-45 |
| 65.38 | 0.09 | 11.04 | 0.26 | 0.00 | 0.65 | 3.67 | 8.83 | 89.90 | Plagioclase-37b-LM-46 |
| 58.51 | 0.00 | 23.64 | 0.19 | 0.01 | 5.16 | 7.18 | 1.37 | 96.05 | Plagioclase-37b-LM-47 |
| 51.20 | 0.00 | 30.64 | 0.47 | 0.11 | 13.42 | 3.56 | 0.19 | 99.58 | Plag-01 |
| 51.06 | 0.00 | 30.89 | 0.46 | 0.14 | 13.46 | 3.46 | 0.17 | 99.64 | Plag-02 |
| 51.06 | 0.09 | 30.91 | 0.45 | 0.14 | 13.84 | 3.41 | 0.20 | 100.10 | Plag-03 |
| 51.33 | 0.00 | 30.91 | 0.44 | 0.15 | 13.92 | 3.45 | 0.17 | 100.36 | Plag-04 |
| 58.43 | 0.00 | 26.22 | 0.22 | 0.00 | 7.75 | 6.34 | 0.78 | 99.74 | Plagioclase-03R |
| 60.11 | 0.00 | 24.41 | 0.25 | 0.02 | 5.93 | 6.92 | 1.32 | 98.96 | Plagioclase-04R |
| 57.06 | 0.00 | 26.50 | 0.40 | 0.01 | 8.56 | 5.86 | 0.92 | 99.32 | Plagioclase-05R |
| 60.49 | 0.00 | 25.14 | 0.23 | 0.00 | 6.38 | 6.94 | 1.22 | 100.41 | Plagioclase-06R |
| 60.79 | 0.00 | 24.85 | 0.29 | 0.01 | 5.94 | 7.07 | 1.35 | 100.30 | Plagioclase-07R |
| 60.58 | 0.00 | 25.27 | 0.28 | 0.00 | 6.45 | 7.28 | 1.20 | 101.06 | Plagioclase-08R |
| 60.84 | 0.00 | 25.02 | 0.28 | 0.00 | 6.05 | 7.24 | 1.30 | 100.73 | Plagioclase-09R |
| 58.74 | 0.00 | 25.84 | 0.41 | 0.01 | 6.65 | 6.71 | 1.43 | 99.79 | Plagioclase-10R |
| 60.93 | 0.00 | 24.95 | 0.27 | 0.00 | 6.16 | 7.05 | 1.33 | 100.69 | Plagioclase-11R |
| 60.92 | 0.00 | 24.81 | 0.29 | 0.01 | 6.06 | 7.15 | 1.34 | 100.57 | Plagioclase-12R |
| 60.45 | 0.00 | 24.89 | 0.22 | 0.00 | 6.19 | 7.08 | 1.26 | 100.09 | Plagioclase-23R |
| 54.92 | 0.00 | 24.72 | 0.15 | 0.00 | 6.83 | 6.40 | 0.70 | 93.72 | Plagioclase-37b-24 |
| 53.92 | 0.00 | 24.98 | 0.18 | 0.01 | 7.35 | 5.89 | 0.69 | 93.02 | Plagioclase-37b-25 |
| 56.43 | 0.00 | 23.79 | 0.19 | 0.00 | 5.71 | 6.63 | 1.00 | 93.75 | Plagioclase-37b-26 |

| SiO2 | TiO2 | Al2O3 | FeO | MgO | CaO | Na2O | K2O | Total | Comment |
|---|---|---|---|---|---|---|---|---|---|
| 57.33 | 0.00 | 23.39 | 0.16 | 0.00 | 5.24 | 6.93 | 1.21 | 94.25 | Plagioclase-37b-27 |
| 58.65 | 0.00 | 23.21 | 0.17 | 0.00 | 4.69 | 7.28 | 1.43 | 95.42 | Plagioclase-37b-28 |
| 56.66 | 0.00 | 24.54 | 0.24 | 0.01 | 6.18 | 6.49 | 0.88 | 95.01 | Plagioclase-37b-29 |
| 57.35 | 0.00 | 24.09 | 0.19 | 0.02 | 5.77 | 6.81 | 1.07 | 95.31 | Plagioclase-37b-30 |
| 57.88 | 0.00 | 23.70 | 0.19 | 0.01 | 5.39 | 7.01 | 1.22 | 95.40 | Plagioclase-37b-31 |
| 58.25 | 0.00 | 23.35 | 0.17 | 0.00 | 4.94 | 6.65 | 1.41 | 94.76 | Plagioclase-37b-32 |
| 56.22 | 0.00 | 24.42 | 0.24 | 0.00 | 6.38 | 6.46 | 0.94 | 94.66 | Plagioclase-37b-33 |
| 68.61 | 0.36 | 15.89 | 1.86 | 0.04 | 0.36 | 3.15 | 10.42 | 100.71 | Plagioclase-37b-34 |
| 58.34 | 0.00 | 23.11 | 0.18 | 0.00 | 4.77 | 7.15 | 1.31 | 94.85 | Plagioclase-37b-35 |
| 59.39 | 0.00 | 24.09 | 0.20 | 0.00 | 5.20 | 7.04 | 1.32 | 97.24 | Plagioclase-37b-36 |
| 58.41 | 0.00 | 24.04 | 0.18 | 0.01 | 5.66 | 6.97 | 1.22 | 96.49 | Plagioclase-13-50 |
| 56.59 | 0.00 | 25.11 | 0.28 | 0.01 | 7.27 | 6.21 | 1.13 | 96.60 | Plagioclase-13-50 |
| 57.88 | 0.00 | 24.68 | 0.18 | 0.00 | 6.11 | 6.75 | 1.06 | 96.66 | Plagioclase-13-50 |
| 0.12 | 576.73 | 1.34 | 56.27 | 0.66 | 0.00 | 0.02 | 0.00 | 635.14 | Plagioclase-13-51 |
| 57.66 | 0.00 | 23.92 | 0.15 | 0.00 | 5.64 | 6.91 | 1.21 | 95.49 | Plagioclase-13-52 |
| 57.26 | 0.00 | 22.69 | 0.16 | 0.01 | 4.57 | 7.18 | 1.34 | 93.21 | Plagioclase-13-53 |
| 48.86 | 0.00 | 20.91 | 0.13 | 0.00 | 4.72 | 6.39 | 0.82 | 81.82 | Plagioclase-13-54 |
| 54.49 | 0.00 | 25.23 | 0.22 | 0.00 | 7.12 | 6.15 | 0.68 | 93.91 | Plagioclase-13-55 |
| 58.82 | 0.00 | 23.16 | 0.19 | 0.00 | 5.16 | 7.19 | 1.41 | 95.91 | Plagioclase-13-56 |
| 59.47 | 0.00 | 23.47 | 0.18 | 0.01 | 5.27 | 7.25 | 1.55 | 97.21 | Plagioclase-13-57 |
| 60.07 | 0.00 | 22.93 | 0.17 | 0.01 | 4.80 | 7.31 | 1.63 | 96.93 | Plagioclase-13-58 |
| 58.55 | 0.00 | 24.39 | 0.20 | 0.02 | 6.05 | 6.96 | 1.14 | 97.30 | Plagioclase-13-59 |
| 66.92 | 0.00 | 19.34 | 0.52 | 0.01 | 1.11 | 3.64 | 8.82 | 100.36 | Plagioclase-13-DM-60 |
| 70.79 | 0.00 | 15.96 | 0.26 | 0.00 | 0.44 | 2.69 | 11.48 | 101.63 | Plagioclase-13-DM-61 |
| 69.26 | 0.00 | 13.76 | 1.10 | 0.05 | 0.47 | 1.68 | 7.29 | 93.61 | Plagioclase-13-DM-62 |
| 74.86 | 0.00 | 13.28 | 0.38 | 0.02 | 0.45 | 2.31 | 9.20 | 100.50 | Plagioclase-13-DM-63 |
| 58.40 | 0.15 | 21.31 | 3.27 | 0.17 | 0.82 | 2.86 | 6.66 | 93.64 | Plagioclase-13-DM-64 |
| 48.84 | 2.70 | 22.76 | 3.64 | 0.11 | 0.80 | 1.74 | 4.51 | 85.11 | Plagioclase-13-DM-65 |

| SiO2 | TiO2 | Al2O3 | FeO | MgO | CaO | Na2O | K2O | Total | Comment |
|---|---|---|---|---|---|---|---|---|---|
| 75.67 | 0.00 | 12.60 | 0.39 | 0.01 | 0.59 | 2.50 | 6.56 | 98.32 | Plagioclase-13-LM-66 |
| 53.39 | 0.26 | 17.04 | 1.86 | 0.11 | 0.17 | 1.71 | 13.22 | 87.76 | Plagioclase-13-LM-67 |
| 20.02 | 0.00 | 22.28 | 2.10 | 0.03 | 0.19 | 0.40 | 0.80 | 45.80 | Plagioclase-13-LM-68 |
| 64.33 | 1.82 | 16.22 | 6.34 | 0.27 | 0.56 | 1.99 | 7.02 | 98.55 | Plagioclase-13-LM-69 |
| 68.27 | 1.54 | 16.23 | 1.06 | 0.02 | 0.48 | 3.06 | 12.22 | 102.88 | Plagioclase-13-LM-70 |
| 51.30 | 0.09 | 30.71 | 0.47 | 0.15 | 13.56 | 3.51 | 0.18 | 99.97 | Plag-01 |
| 51.35 | 0.06 | 31.06 | 0.48 | 0.13 | 13.77 | 3.42 | 0.19 | 100.46 | Plag-02 |
| 51.50 | 0.00 | 30.98 | 0.44 | 0.14 | 13.78 | 3.42 | 0.17 | 100.42 | Plag-03 |
| 51.21 | 0.00 | 30.94 | 0.46 | 0.15 | 13.71 | 3.46 | 0.19 | 100.11 | Plag-04 |
| 56.38 | 0.00 | 23.24 | 0.18 | 0.03 | 5.60 | 6.76 | 1.22 | 93.41 | Plagioclase-37b-24R |
| 57.69 | 0.00 | 22.72 | 0.21 | 0.00 | 4.78 | 7.33 | 1.33 | 94.05 | Plagioclase-37b-25R |
| 58.25 | 0.00 | 23.66 | 0.20 | 0.01 | 5.06 | 7.43 | 1.21 | 95.83 | Plagioclase-37b-26R |
| 57.58 | 0.00 | 23.45 | 0.24 | 0.01 | 5.28 | 6.90 | 1.20 | 94.66 | Plagioclase-37b-27R |
| 58.36 | 0.00 | 23.36 | 0.22 | 0.00 | 5.03 | 7.16 | 1.31 | 95.43 | Plagioclase-37b-28R |
| 57.79 | 0.00 | 23.54 | 0.21 | 0.00 | 5.37 | 7.11 | 1.20 | 95.23 | Plagioclase-37b-29R |
| 58.14 | 0.00 | 23.53 | 0.23 | 0.00 | 5.22 | 7.21 | 1.31 | 95.64 | Plagioclase-37b-30R |
| 57.73 | 0.00 | 23.30 | 0.23 | 0.00 | 5.43 | 7.11 | 1.21 | 95.01 | Plagioclase-37b-31R |
| 58.03 | 0.00 | 24.01 | 0.21 | 0.02 | 5.37 | 6.71 | 1.29 | 95.63 | Plagioclase-37b-32R |
| 57.24 | 0.00 | 23.85 | 0.19 | 0.00 | 5.80 | 6.91 | 1.18 | 95.18 | Plagioclase-37b-33R |
| 59.82 | 0.00 | 15.47 | 8.39 | 0.16 | 0.52 | 2.13 | 7.59 | 94.08 | Plagioclase-37b-34 |
| 58.09 | 0.00 | 23.59 | 0.23 | 0.00 | 5.45 | 6.47 | 1.18 | 95.01 | Plagioclase-37b-35R |
| 57.73 | 0.00 | 23.60 | 0.28 | 0.00 | 5.42 | 7.11 | 1.09 | 95.22 | Plagioclase-37b-36R |
| 58.53 | 0.00 | 23.91 | 0.19 | 0.01 | 5.84 | 7.02 | 1.20 | 96.69 | Plagioclase-37b-LM-47R |
| 69.08 | 0.00 | 14.14 | 0.25 | 0.02 | 1.26 | 3.52 | 2.44 | 90.71 | Plagioclase-13-50R |
| 56.15 | 0.02 | 25.58 | 0.33 | 0.02 | 7.75 | 6.29 | 0.97 | 97.11 | Plagioclase-13-50R |
| 59.04 | 0.00 | 23.80 | 0.22 | 0.00 | 5.71 | 7.05 | 1.23 | 97.05 | Plagioclase-13-50R |
| 0.15 | 323.19 | 2.11 | 69.75 | 0.20 | 0.00 | 0.04 | 0.03 | 395.47 | Plagioclase-13-51R |

| SiO2 | TiO2 | Al2O3 | FeO | MgO | CaO | Na2O | K2O | Total | Comment |
|---|---|---|---|---|---|---|---|---|---|
| 58.90 | 0.15 | 24.69 | 0.23 | 0.02 | 5.81 | 6.32 | 1.24 | 97.35 | Plagioclase-13-52R |
| 56.99 | 0.00 | 23.13 | 0.22 | 0.00 | 5.00 | 7.03 | 1.23 | 93.61 | Plagioclase-13-53R |
| 49.48 | 0.00 | 20.92 | 0.12 | 0.01 | 4.71 | 6.39 | 0.86 | 82.49 | Plagioclase-13-54R |
| 58.51 | 0.00 | 24.18 | 0.21 | 0.00 | 5.82 | 6.89 | 1.20 | 96.82 | Plagioclase-13-55R |
| 59.07 | 0.00 | 23.46 | 0.16 | 0.00 | 5.50 | 7.22 | 1.35 | 96.78 | Plagioclase-13-56R |
| 60.28 | 0.00 | 23.71 | 0.20 | 0.00 | 5.23 | 7.28 | 1.49 | 98.20 | Plagioclase-13-57R |
| 59.35 | 0.00 | 24.10 | 0.21 | 0.00 | 5.73 | 7.13 | 1.39 | 97.92 | Plagioclase-13-58R |
| 59.30 | 0.00 | 24.14 | 0.24 | 0.01 | 5.97 | 7.07 | 1.17 | 97.89 | Plagioclase-13-59R |
| 51.15 | 0.00 | 30.98 | 0.49 | 0.13 | 13.85 | 3.50 | 0.17 | 100.26 | Plag-01 |
| 51.35 | 0.36 | 30.95 | 0.50 | 0.15 | 13.35 | 3.41 | 0.18 | 100.24 | Plag-02 |

(b) Raw major element measurements of plagioclase crystals. Samples 30C and 44

| No. | SiO2 | TiO2 | Al2O3 | FeO | | MgO | CaO | Na2O | K2O | Total | Comment |
|---|---|---|---|---|---|---|---|---|---|---|---|
| 1 | 51.26 | 0.00 | 31.06 | 0.47 | | 0.13 | 13.61 | 3.36 | 0.20 | 100.10 | Plag-01 |
| 2 | 51.01 | 0.00 | 30.76 | 0.44 | | 0.12 | 13.64 | 3.48 | 0.17 | 99.62 | Plag-02 |
| 3 | 58.99 | 0.00 | 25.73 | 0.21 | | 0.00 | 7.39 | 6.79 | 1.00 | 100.12 | Plagioclase-01 |
| 4 | 60.47 | 0.00 | 24.62 | 0.19 | | 0.00 | 5.94 | 7.25 | 1.33 | 99.80 | Plagioclase-S44-01R |
| 5 | 56.84 | 0.00 | 27.08 | 0.25 | | 0.00 | 8.25 | 5.61 | 0.68 | 98.73 | Plagioclase-S44-02 |
| 6 | 61.18 | 0.00 | 24.12 | 0.22 | | 0.00 | 5.28 | 7.40 | 1.53 | 99.72 | Plagioclase-S44-03 |
| 7 | 60.84 | 0.00 | 24.51 | 0.24 | | 0.01 | 5.89 | 7.20 | 1.40 | 100.08 | Plagioclase-S44-03R |
| 8 | 97.58 | 0.00 | 0.66 | 0.02 | | 0.01 | 0.01 | 0.11 | 0.17 | 98.57 | Plagioclase-S44-04 |
| 9 | 95.30 | 0.01 | 1.47 | 0.04 | | 0.00 | 0.01 | 0.14 | 0.20 | 97.16 | Plagioclase-S44-04R |
| 10 | 41.57 | 2.62 | 10.10 | 21.34 | | 7.00 | 10.38 | 2.12 | 1.29 | 96.43 | Plagioclase-S44-05 |
| 11 | 41.99 | 2.47 | 10.00 | 22.23 | | 6.93 | 10.35 | 2.04 | 1.32 | 97.33 | Plagioclase-S44-05 |
| 12 | 40.97 | 1.36 | 10.04 | 22.32 | | 7.92 | 8.74 | 1.20 | 1.11 | 93.64 | Plagioclase-S44-05R |
| 13 | 0.41 | 0.00 | 1.03 | 0.06 | | 0.00 | 0.03 | 0.01 | 0.09 | 1.62 | Plagioclase-S44-06 |
| 14 | 57.00 | 0.00 | 26.77 | 0.23 | | 0.01 | 8.57 | 6.02 | 0.76 | 99.35 | Plagioclase-S44-07 |
| 15 | 52.43 | 0.00 | 22.96 | 0.25 | | 0.01 | 5.34 | 5.83 | 1.38 | 88.20 | Plagioclase-S44-07R |
| 16 | 57.46 | 0.00 | 26.32 | 0.25 | | 0.01 | 8.41 | 6.26 | 0.78 | 99.50 | Plagioclase-S44-08 |
| 17 | 60.63 | 0.00 | 24.54 | 0.34 | | 0.00 | 5.90 | 7.08 | 1.29 | 99.78 | Plagioclase-S44-08R |
| 18 | 57.72 | 0.00 | 25.91 | 0.37 | | 0.02 | 8.13 | 6.02 | 1.09 | 99.27 | Plagioclase-S44-09 |
| 19 | 58.08 | 0.00 | 26.17 | 0.30 | | 0.02 | 8.27 | 5.90 | 1.06 | 99.80 | Plagioclase-S44-09R |
| 20 | 51.40 | 0.00 | 30.98 | 0.38 | | 0.12 | 13.61 | 3.52 | 0.19 | 100.20 | Plag-01 |
| 21 | 51.18 | 0.00 | 30.98 | 0.45 | | 0.12 | 13.73 | 3.47 | 0.20 | 100.13 | Plag-02 |
| 22 | 22.00 | 0.06 | 25.99 | 2.00 | | 0.12 | 0.12 | 0.09 | 0.37 | 50.76 | Plagioclase-S44-10 |
| 23 | 27.32 | 0.00 | 27.91 | 1.12 | | 0.26 | 0.09 | 0.19 | 0.89 | 57.78 | Plagioclase-S44-10R |
| 24 | 61.19 | 0.00 | 24.51 | 0.17 | | 0.01 | 5.76 | 6.51 | 1.31 | 99.46 | Plagioclase-S44-11 |
| 25 | 61.02 | 0.00 | 24.52 | 0.24 | | 0.00 | 5.87 | 7.09 | 1.32 | 100.06 | Plagioclase-S44-11R |
| 26 | 51.25 | 0.00 | 30.74 | 0.45 | | 0.13 | 13.62 | 3.42 | 0.17 | 99.78 | Plag-01 |

| No. | SiO2 | TiO2 | Al2O3 | FeO | | MgO | CaO | Na2O | K2O | Total | Comment |
|---|---|---|---|---|---|---|---|---|---|---|---|
| 27 | 51.40 | 0.00 | 31.12 | 0.45 | | 0.14 | 13.72 | 3.54 | 0.16 | 100.53 | Plag-02 |
| 28 | 12.58 | 0.00 | 10.22 | 0.06 | | 0.01 | 1.21 | 0.38 | 0.31 | 24.78 | Plagioclase-S44-12 |
| 29 | 11.60 | 0.00 | 9.74 | 0.05 | | 0.01 | 1.05 | 0.33 | 0.27 | 23.06 | Plagioclase-S44-12R |
| 30 | 61.05 | 0.00 | 24.47 | 0.24 | | 0.00 | 5.72 | 7.22 | 1.45 | 100.16 | Plagioclase-S44-12R |
| 31 | 59.74 | 0.00 | 25.69 | 0.23 | | 0.00 | 6.92 | 7.03 | 1.08 | 100.69 | Plagioclase-S44-13 |
| 32 | 67.62 | 0.00 | 19.14 | 0.25 | | 0.00 | 0.44 | 4.33 | 13.86 | 105.64 | Plagioclase-S44-13R |
| 33 | 71.18 | 0.00 | 19.72 | 0.27 | | 0.00 | 0.45 | 2.40 | 9.45 | 103.47 | Plagioclase-S44-LM |
| 34 | 53.18 | 0.00 | 21.13 | 0.20 | | 0.03 | 0.48 | 2.23 | 9.57 | 86.82 | Plagioclase-S44-LM |
| 35 | 98.81 | 0.00 | 0.64 | 0.07 | | 0.00 | 0.00 | 0.11 | 0.21 | 99.85 | Plagioclase-S44-LM |
| 36 | 96.71 | 0.00 | 1.97 | 0.10 | | 0.00 | 0.10 | 0.35 | 0.82 | 100.05 | Plagioclase-S44-LM |
| 37 | 10.02 | 4.55 | 8.49 | 1.16 | | 0.06 | 0.17 | 0.08 | 1.44 | 25.96 | Plagioclase-S44-LM |
| 38 | 98.41 | 0.00 | 0.48 | 0.04 | | 0.01 | 0.01 | 0.07 | 0.14 | 99.15 | Plagioclase-S44-LM |
| 39 | 63.19 | 0.00 | 22.06 | 0.22 | | 0.00 | 3.40 | 7.81 | 2.75 | 99.43 | Plagioclase-S44-LM |
| 40 | 66.69 | 0.00 | 19.11 | 0.26 | | 0.00 | 0.28 | 3.67 | 15.43 | 105.43 | Plagioclase-S44-LM |
| 41 | 95.54 | 0.00 | 2.67 | 0.06 | | 0.00 | 0.05 | 0.29 | 1.17 | 99.79 | Plagioclase-S44-LM |
| 42 | 67.75 | 0.00 | 18.39 | 0.22 | | 0.01 | 0.17 | 3.63 | 16.65 | 106.84 | Plagioclase-S44-LM |
| 43 | 61.51 | 0.00 | 24.24 | 0.21 | | 0.00 | 5.71 | 6.95 | 1.39 | 100.01 | Plagioclase-S44-14 |
| 44 | 60.93 | 0.00 | 24.82 | 0.25 | | 0.00 | 6.14 | 7.04 | 1.29 | 100.47 | Plagioclase-S44-15R |
| 45 | 67.30 | 0.00 | 19.96 | 0.27 | | 0.00 | 0.30 | 3.46 | 16.07 | 107.35 | Plagioclase-S44-LM |
| 46 | 90.44 | 0.00 | 3.44 | 0.13 | | 0.00 | 0.11 | 0.68 | 1.36 | 96.16 | Plagioclase-S44-LM |
| 47 | 58.37 | 0.00 | 19.99 | 0.24 | | 0.00 | 0.61 | 3.20 | 11.40 | 93.81 | Plagioclase-S44-LM |
| 48 | 66.12 | 0.00 | 18.00 | 0.22 | | 0.00 | 0.23 | 3.18 | 16.74 | 104.49 | Plagioclase-S44-SLM |
| 49 | 27.15 | 0.17 | 21.74 | 0.87 | | 0.08 | 0.22 | 0.25 | 0.99 | 51.47 | Plagioclase-S44-SLM |
| 50 | 10.91 | 0.19 | 15.48 | 3.92 | | 0.02 | 0.18 | 0.07 | 0.34 | 31.10 | Plagioclase-S44-SLM |
| 51 | 27.81 | 0.00 | 21.04 | 0.51 | | 0.01 | 0.24 | 0.56 | 2.90 | 53.07 | Plagioclase-S44-SLM |
| 52 | 51.36 | 0.00 | 30.99 | 0.43 | | 0.13 | 13.49 | 3.51 | 0.17 | 100.07 | Plag-01 |
| 53 | 51.28 | 0.00 | 30.88 | 0.83 | | 0.32 | 13.39 | 3.42 | 0.18 | 100.29 | Plag-02 |
| 54 | 42.28 | 0.05 | 27.49 | 10.76 | | 0.05 | 0.10 | 0.03 | 0.26 | 81.02 | Plagioclase-S30C-01 |

| No. | SiO2 | TiO2 | Al2O3 | FeO | | MgO | CaO | Na2O | K2O | Total | Comment |
|---|---|---|---|---|---|---|---|---|---|---|---|
| 55 | 52.77 | 0.08 | 0.86 | 26.12 | | 15.17 | 1.34 | 0.02 | 0.02 | 96.39 | Plagioclase-S30C-01R |
| 56 | 60.69 | 0.00 | 24.96 | 0.23 | | 0.00 | 6.07 | 6.70 | 1.26 | 99.90 | Plagioclase-S30C-02 |
| 57 | 61.03 | 0.00 | 24.55 | 0.21 | | 0.00 | 5.71 | 7.32 | 1.42 | 100.24 | Plagioclase-S30C-02R |
| 58 | 53.33 | 0.14 | 1.32 | 18.62 | | 22.15 | 1.50 | 0.02 | 0.02 | 97.10 | Plagioclase-S30C-03 |
| 59 | 53.70 | 0.12 | 1.30 | 18.23 | | 21.81 | 1.43 | 0.02 | 0.03 | 96.64 | Plagioclase-S30C-03R |
| 60 | 57.92 | 0.00 | 26.83 | 0.35 | | 0.02 | 8.46 | 5.93 | 0.76 | 100.27 | Plagioclase-S30C-04 |
| 61 | 60.59 | 0.00 | 24.80 | 0.22 | | 0.00 | 6.27 | 6.94 | 1.28 | 100.11 | Plagioclase-S30C-05 |
| 62 | 60.35 | 0.00 | 25.09 | 0.19 | | 0.00 | 6.50 | 6.89 | 1.20 | 100.22 | Plagioclase-S30C-06 |
| 63 | 60.37 | 0.00 | 24.47 | 0.23 | | 0.02 | 5.91 | 6.72 | 1.35 | 99.08 | Plagioclase-S30C-06R |
| 64 | 60.24 | 0.00 | 25.02 | 0.27 | | 0.00 | 6.57 | 7.08 | 1.26 | 100.44 | Plagioclase-S30C-07 |
| 65 | 60.65 | 0.00 | 24.91 | 0.27 | | 0.01 | 6.17 | 6.82 | 1.35 | 100.19 | Plagioclase-S30C-08 |
| 66 | 61.72 | 0.00 | 23.94 | 0.23 | | 0.00 | 5.42 | 7.33 | 1.61 | 100.26 | Plagioclase-S30C-09 |
| 67 | 61.49 | 0.00 | 24.54 | 0.21 | | 0.00 | 5.69 | 7.19 | 1.44 | 100.56 | Plagioclase-S30C-09R |
| 68 | 61.63 | 0.00 | 24.39 | 0.21 | | 0.01 | 5.53 | 7.29 | 1.47 | 100.53 | Plagioclase-S30C-10 |
| 69 | 60.25 | 0.00 | 24.91 | 0.22 | | 0.00 | 6.36 | 6.97 | 1.16 | 99.87 | Plagioclase-S30C-10R |
| 70 | 42.13 | 0.01 | 31.08 | 7.94 | | 0.07 | 0.07 | 0.01 | 0.22 | 81.53 | Plagioclase-S30C-11 |
| 71 | 49.97 | 0.06 | 0.61 | 28.20 | | 14.21 | 1.51 | 0.00 | 0.02 | 94.58 | Plagioclase-S30C-11R |
| 72 | 60.67 | 0.00 | 24.73 | 0.18 | | 0.01 | 5.93 | 7.07 | 1.30 | 99.89 | Plagioclase-S30C-12 |
| 73 | 61.07 | 0.00 | 24.76 | 0.23 | | 0.00 | 5.79 | 7.24 | 1.41 | 100.52 | Plagioclase-S30C-12R |
| 74 | 60.25 | 0.00 | 25.06 | 0.22 | | 0.01 | 6.45 | 6.91 | 1.19 | 100.09 | Plagioclase-S30C-13 |
| 75 | 61.52 | 0.00 | 24.69 | 0.22 | | 0.02 | 5.87 | 7.12 | 1.40 | 100.83 | Plagioclase-S30C-13R |
| 76 | 60.73 | 0.00 | 25.24 | 0.23 | | 0.00 | 6.36 | 7.02 | 1.25 | 100.83 | Plagioclase-S30C-14 |
| 77 | 60.60 | 0.00 | 24.32 | 0.22 | | 0.00 | 5.90 | 7.14 | 1.31 | 99.49 | Plagioclase-S30C-14R |
| 78 | 43.51 | 0.00 | 30.44 | 10.46 | | 0.05 | 0.08 | 0.03 | 0.19 | 84.76 | Plagioclase-S30C-15 |
| 79 | 52.61 | 0.05 | 0.55 | 28.81 | | 12.51 | 1.61 | 0.02 | 0.04 | 96.19 | Plagioclase-S30C-15R |
| 80 | 60.81 | 0.00 | 24.52 | 0.22 | | 0.01 | 6.06 | 7.07 | 1.33 | 100.01 | Plagioclase-S30C-16 |
| 81 | 60.45 | 0.00 | 24.68 | 0.20 | | 0.00 | 6.08 | 6.91 | 1.33 | 99.65 | Plagioclase-S30C-16R |
| 82 | 60.02 | 0.00 | 25.02 | 0.22 | | 0.01 | 6.50 | 7.05 | 1.15 | 99.96 | Plagioclase-S30C-17 |

| No. | SiO2 | TiO2 | Al2O3 | FeO | | MgO | CaO | Na2O | K2O | Total | Comment |
|---|---|---|---|---|---|---|---|---|---|---|---|
| 83 | 61.11 | 0.00 | 24.95 | 0.25 | | 0.00 | 6.05 | 7.05 | 1.29 | 100.70 | Plagioclase-S30C-17R |
| 84 | 99.43 | 0.00 | 0.60 | 0.05 | | 0.00 | 0.01 | 0.12 | 0.18 | 100.40 | Plagioclase-S30C-18DM |
| 85 | 51.11 | 0.00 | 30.71 | 0.45 | | 0.13 | 13.60 | 3.32 | 0.17 | 99.49 | Plag-01 |
| 86 | 51.44 | 0.00 | 30.97 | 0.43 | | 0.13 | 13.60 | 3.49 | 0.18 | 100.23 | Plag-02 |
| 87 | 98.68 | 0.00 | 0.71 | 0.10 | | 0.00 | 0.01 | 0.21 | 0.17 | 99.88 | Plagioclase-S30C-19DM |
| 88 | 95.51 | 0.00 | 3.37 | 2.36 | | 0.15 | 0.07 | 0.21 | 0.26 | 101.92 | Plagioclase-S30C-20DM |
| 89 | 99.92 | 0.00 | 0.89 | 0.08 | | 0.00 | 0.00 | 0.14 | 0.17 | 101.20 | Plagioclase-S30C-21DM |
| 90 | 98.78 | 0.00 | 0.77 | 0.10 | | 0.00 | 0.01 | 0.20 | 0.21 | 100.06 | Plagioclase-S30C-22DM |
| 91 | 30.40 | 0.00 | 16.22 | 0.19 | | 0.01 | 0.23 | 1.23 | 5.47 | 53.75 | Plagioclase-S30C-23SL |
| 92 | 22.28 | 0.00 | 3.54 | 0.14 | | 0.00 | 0.03 | 0.02 | 0.09 | 26.11 | Plagioclase-S30C-24SL |
| 93 | 64.00 | 0.00 | 20.90 | 0.24 | | 0.02 | 0.45 | 5.05 | 13.50 | 104.17 | Plagioclase-S30C-25SL |
| 94 | 46.64 | 0.00 | 24.11 | 0.26 | | 0.01 | 0.43 | 3.03 | 9.32 | 83.81 | Plagioclase-S30C-26SL |
| 95 | 61.46 | 0.00 | 19.61 | 0.29 | | 0.01 | 0.55 | 5.09 | 11.60 | 98.60 | Plagioclase-S30C-27SL |
| 96 | 38.70 | 0.00 | 18.99 | 0.30 | | 0.01 | 0.49 | 2.58 | 9.31 | 70.39 | Plagioclase-S30C-28SL |
| 97 | 40.20 | 0.00 | 21.47 | 0.36 | | 0.01 | 0.62 | 2.30 | 5.55 | 70.51 | Plagioclase-S30C-29SL |
| 98 | 14.79 | 0.11 | 7.53 | 3.79 | | 0.03 | 0.15 | 0.27 | 2.74 | 29.41 | Plagioclase-S30C-30SL |
| 99 | 51.18 | 0.00 | 30.94 | 0.44 | | 0.14 | 13.76 | 3.31 | 0.19 | 99.95 | Plag-01 |
| 100 | 51.32 | 0.00 | 30.90 | 0.49 | | 0.12 | 13.68 | 3.53 | 0.18 | 100.22 | Plag-02 |
| 101 | 60.60 | 0.00 | 24.49 | 0.21 | | 0.00 | 6.29 | 7.17 | 1.29 | 100.06 | Plagioclase-S1-01 |
| 102 | 61.79 | 0.00 | 24.30 | 0.27 | | 0.01 | 5.49 | 7.21 | 1.57 | 100.63 | Plagioclase-S1-01R |
| 103 | 61.87 | 0.00 | 24.03 | 0.21 | | 0.00 | 5.18 | 7.25 | 1.60 | 100.13 | Plagioclase-S1-02 |
| 104 | 61.71 | 0.00 | 24.44 | 0.20 | | 0.00 | 5.55 | 7.12 | 1.48 | 100.50 | Plagioclase-S1-02R |
| 105 | 60.59 | 0.00 | 24.94 | 0.25 | | 0.01 | 6.33 | 7.03 | 1.23 | 100.38 | Plagioclase-S1-03 |
| 106 | 61.64 | 0.00 | 24.56 | 0.22 | | 0.00 | 5.68 | 6.82 | 1.51 | 100.42 | Plagioclase-S1-03R |
| 107 | 60.69 | 0.00 | 24.85 | 0.20 | | 0.01 | 6.25 | 7.15 | 1.29 | 100.43 | Plagioclase-S1-04 |
| 108 | 59.16 | 0.00 | 25.47 | 0.22 | | 0.00 | 7.13 | 6.62 | 1.08 | 99.67 | Plagioclase-S1-05 |
| 109 | 61.24 | 0.00 | 24.99 | 0.25 | | 0.00 | 6.29 | 7.29 | 1.33 | 101.39 | Plagioclase-S1-05R |
| 110 | 61.28 | 0.00 | 24.59 | 0.21 | | 0.00 | 5.98 | 7.31 | 1.37 | 100.75 | Plagioclase-S1-06 |

| No. | SiO2 | TiO2 | Al2O3 | FeO | | MgO | CaO | Na2O | K2O | Total | Comment |
|---|---|---|---|---|---|---|---|---|---|---|---|
| 111 | 62.05 | 0.00 | 24.65 | 0.26 | | 0.00 | 5.79 | 6.92 | 1.44 | 101.11 | Plagioclase-S1-06R |
| 112 | 60.31 | 0.00 | 25.33 | 0.24 | | 0.01 | 6.73 | 6.92 | 1.18 | 100.72 | Plagioclase-S1-07 |
| 113 | 60.68 | 0.00 | 25.07 | 0.25 | | 0.01 | 6.44 | 6.96 | 1.32 | 100.72 | Plagioclase-S1-07R |
| 114 | 50.93 | 0.00 | 30.80 | 0.44 | | 0.14 | 13.75 | 3.41 | 0.18 | 99.65 | Plag-01 |
| 115 | 51.32 | 0.00 | 30.87 | 0.43 | | 0.12 | 13.60 | 3.54 | 0.18 | 100.06 | Plag-02 |
| 116 | 49.98 | 0.01 | 11.33 | 2.12 | | 0.09 | 0.17 | 0.88 | 3.54 | 68.12 | Plagioclase-S1-LM-01 |
| 117 | 22.69 | 0.00 | 11.91 | 1.96 | | 0.04 | 0.39 | 0.64 | 8.77 | 46.40 | Plagioclase-S1-LM-02 |
| 118 | 39.01 | 0.00 | 19.03 | 0.50 | | 0.01 | 0.61 | 2.23 | 7.40 | 68.79 | Plagioclase-S1-LM-03 |
| 119 | 33.20 | 0.00 | 10.50 | 0.32 | | 0.00 | 0.20 | 0.86 | 15.28 | 60.37 | Plagioclase-S1-LM-04 |
| 120 | 44.49 | 0.00 | 15.92 | 0.36 | | 0.00 | 0.51 | 2.13 | 12.79 | 76.21 | Plagioclase-S1-LM-05 |
| 121 | 89.32 | 0.00 | 1.66 | 0.11 | | 0.00 | 0.02 | 0.26 | 0.47 | 91.84 | Plagioclase-S1-LM-06 |
| 122 | 53.99 | 0.00 | 18.97 | 0.29 | | 0.00 | 0.35 | 2.28 | 13.16 | 89.04 | Plagioclase-S1-LM-07 |
| 123 | 65.99 | 0.00 | 20.15 | 0.41 | | 0.00 | 0.16 | 3.53 | 12.34 | 102.58 | Plagioclase-S1-LM-08 |
| 124 | 58.58 | 0.00 | 18.08 | 0.81 | | 0.05 | 0.26 | 2.10 | 10.70 | 90.58 | Plagioclase-S1-LM-09 |
| 125 | 40.92 | 0.00 | 5.23 | 1.01 | | 0.01 | 0.10 | 0.40 | 2.89 | 50.56 | Plagioclase-S1-LM-10 |
| 126 | 94.64 | 0.00 | 4.91 | 0.24 | | 0.00 | 0.15 | 0.49 | 0.10 | 100.52 | Plagioclase-S1-DM-01 |
| 127 | 61.59 | 0.01 | 27.01 | 3.79 | | 0.14 | 0.07 | 0.17 | 0.80 | 93.59 | Plagioclase-S1-DM-02 |
| 128 | 77.81 | 0.12 | 18.67 | 3.57 | | 0.13 | 0.10 | 0.12 | 0.31 | 100.83 | Plagioclase-S1-DM-03 |
| 129 | 74.94 | 0.00 | 10.95 | 0.30 | | 0.00 | 0.21 | 2.11 | 7.54 | 96.04 | Plagioclase-S1-DM-04 |
| 130 | 59.38 | 0.21 | 13.89 | 2.50 | | 0.04 | 0.22 | 1.69 | 8.71 | 86.64 | Plagioclase-S1-DM-05 |
| 131 | 61.71 | 0.01 | 12.26 | 0.55 | | 0.01 | 0.08 | 1.81 | 11.27 | 87.69 | Plagioclase-S1-LM-11 |
| 132 | 61.24 | 0.00 | 3.75 | 0.63 | | 0.02 | 0.03 | 0.18 | 0.47 | 66.32 | Plagioclase-S1-LM-12 |
| 133 | 50.18 | 0.00 | 16.91 | 0.51 | | 0.00 | 0.27 | 1.20 | 10.39 | 79.46 | Plagioclase-S1-LM-13 |
| 134 | 89.14 | 0.00 | 6.45 | 0.12 | | 0.00 | 0.08 | 0.82 | 2.80 | 99.42 | Plagioclase-S1-LM-14 |
| 135 | 51.46 | 0.01 | 18.80 | 0.55 | | 0.01 | 0.25 | 1.74 | 12.21 | 85.02 | Plagioclase-S1-LM-15 |
| 136 | 51.12 | 0.00 | 30.90 | 0.37 | | 0.11 | 13.66 | 3.35 | 0.17 | 99.68 | Plag-01 |
| 137 | 51.46 | 0.00 | 30.96 | 0.43 | | 0.14 | 13.78 | 3.53 | 0.18 | 100.49 | Plag-02 |

(c) Raw major element measurements of pyroxene crystals. Sample 13.

| No. | SiO2 | TiO2 | Al2O3 | FeO | MnO | MgO | CaO | Na2O | K2O | Cr2O3 | Total | Comment |
|---|---|---|---|---|---|---|---|---|---|---|---|---|
| 1 | 50.63 | 0.77 | 8.78 | 6.27 | 0.11 | 16.56 | 15.61 | 1.31 | 0.00 | 0.17 | 100.21 | Kaknui-01 |
| 2 | 50.76 | 0.73 | 8.62 | 6.41 | 0.11 | 16.58 | 15.90 | 1.24 | 0.00 | 0.15 | 100.50 | Kaknui-02 |
| 3 | 54.11 | 0.00 | 0.96 | 15.16 | 0.42 | 26.99 | 1.22 | 0.01 | 0.00 | 0.62 | 99.48 | Hypersthene-01 |
| 4 | 54.19 | 0.00 | 0.97 | 14.68 | 0.42 | 26.93 | 1.11 | 0.00 | 0.00 | 0.63 | 98.92 | Hypersthene-02 |
| 5 | 60.57 | 0.00 | 25.56 | 0.24 | 0.00 | 0.01 | 6.16 | 7.16 | 0.79 | 0.00 | 100.49 | Pyroxene-01 |
| 6 | 48.98 | 0.47 | 23.21 | 1.49 | 0.02 | 0.06 | 0.93 | 4.17 | 3.56 | 0.00 | 82.89 | Pyroxene-02 |
| 7 | 57.05 | 0.00 | 27.77 | 0.29 | 0.01 | 0.02 | 8.75 | 5.80 | 0.58 | 0.00 | 100.26 | Pyroxene-03 |
| 8 | 0.25 | 13.02 | 1.70 | 79.60 | 0.36 | 0.20 | 0.00 | 0.03 | 0.00 | 0.03 | 95.19 | Pyroxene-04 |
| 9 | 61.50 | 0.00 | 25.19 | 0.10 | 0.00 | 0.01 | 5.21 | 7.70 | 0.68 | 0.00 | 100.38 | Pyroxene-05 |
| 10 | 58.66 | 0.00 | 26.81 | 0.28 | 0.00 | 0.02 | 7.84 | 6.17 | 0.61 | 0.03 | 100.42 | Pyroxene-06 |
| 11 | 56.22 | 0.00 | 25.81 | 0.25 | 0.00 | 0.01 | 6.85 | 6.14 | 0.66 | 0.00 | 95.93 | Pyroxene-13-07 |
| 12 | 59.43 | 0.00 | 24.09 | 0.18 | 0.03 | 0.01 | 4.98 | 7.28 | 0.84 | 0.00 | 96.85 | Pyroxene-13-08 |
| 13 | 50.76 | 0.77 | 8.70 | 6.52 | 0.15 | 16.72 | 15.95 | 1.28 | 0.00 | 0.14 | 101.00 | Kak-01 |
| 14 | 50.76 | 0.68 | 8.82 | 6.16 | 0.15 | 16.73 | 15.83 | 1.26 | 0.01 | 0.14 | 100.54 | Kak-02 |
| 15 | 50.41 | 0.74 | 8.88 | 6.43 | 0.11 | 16.39 | 16.45 | 1.23 | 0.01 | 0.12 | 100.76 | Hyp-03 |
| 16 | 50.40 | 0.83 | 8.95 | 6.33 | 0.10 | 16.43 | 16.12 | 1.24 | 0.00 | 0.17 | 100.56 | Hyp-04 |

(d) Raw major element measurements of pyroxene crystals. Samples 30C and 44.

| No. | SiO2 | TiO2 | Al2O3 | FeO | MnO | MgO | CaO | Na2O | K2O | Cr2O3 | Total | Comment |
|---|---|---|---|---|---|---|---|---|---|---|---|---|
| 1 | 0.00 | 0.00 | 0.00 | 0.04 | 0.01 | 0.00 | 0.02 | 0.03 | 0.01 | 0.00 | 0.12 | Kaknui-01 |
| 2 | 0.03 | 0.00 | 0.01 | 0.03 | 0.00 | 0.01 | 0.03 | 0.01 | 0.00 | 0.00 | 0.12 | Kaknui-02 |
| 3 | 53.83 | 0.08 | 1.02 | 14.82 | 0.48 | 26.73 | 1.20 | 0.00 | 0.00 | 0.79 | 98.96 | Hypersthene-01 |
| 4 | 0.01 | 0.01 | 0.00 | 0.05 | 0.01 | 0.00 | 0.01 | 0.01 | 0.00 | 0.00 | 0.10 | Hypersthene-02 |
| 5 | 14.24 | 0.00 | 17.77 | 0.22 | 0.00 | 0.00 | 0.03 | 0.06 | 0.07 | 0.00 | 32.38 | pyroxene-S44-01 |
| 6 | 54.00 | 0.13 | 3.76 | 24.21 | 0.63 | 20.38 | 1.28 | 0.02 | 0.02 | 0.00 | 104.44 | pyroxene-30C-01 |
| 7 | 34.51 | 0.00 | 0.02 | 58.24 | 1.27 | 1.16 | 0.09 | 0.01 | 0.02 | 0.00 | 95.33 | pyroxene-30C-02 |
| 8 | 30.38 | 0.01 | 18.37 | 0.72 | 0.04 | 0.02 | 0.56 | 1.25 | 3.43 | 0.00 | 54.77 | pyroxene-30C-03 |
| 9 | 0.12 | 41.79 | 2.71 | 63.31 | 0.73 | 1.10 | 0.00 | 0.01 | 0.00 | 0.07 | 109.85 | pyroxene-30C-04 |
| 10 | 51.73 | 0.07 | 0.74 | 25.70 | 0.55 | 19.29 | 1.59 | 0.03 | 0.00 | 0.03 | 99.72 | pyroxene-30C-05 |
| 11 | 39.70 | 0.06 | 25.13 | 14.06 | 0.00 | 0.08 | 0.10 | 0.02 | 0.11 | 0.00 | 79.25 | pyroxene-30C-06 |
| 12 | 52.18 | 0.30 | 1.30 | 20.63 | 0.42 | 22.25 | 1.77 | 0.01 | 0.00 | 0.01 | 98.86 | pyroxene-30C-07 |
| 13 | 50.58 | 0.78 | 8.68 | 6.09 | 0.14 | 16.52 | 15.87 | 1.27 | 0.01 | 0.16 | 100.08 | Kaknui-01 |
| 14 | 50.88 | 0.70 | 8.78 | 6.59 | 0.12 | 16.78 | 15.77 | 1.27 | 0.01 | 0.15 | 101.05 | Kaknui-02 |
| 15 | 53.98 | 0.06 | 1.05 | 15.14 | 0.49 | 26.91 | 1.22 | 0.01 | 0.00 | 0.81 | 99.68 | Hypersthene-01 |
| 16 | 53.80 | 0.00 | 0.97 | 15.28 | 0.46 | 26.65 | 1.22 | 0.01 | 0.00 | 0.77 | 99.16 | Hypersthene-02 |

(e) Raw major element measurements of Fe-Ti oxides. Samples 13 and 37B.

| No. | TiO2 | CaO | MgO | MnO | Al2O3 | SiO2 | FeO | Cr2O3 | Total | Comment |
|---|---|---|---|---|---|---|---|---|---|---|
| 1 | 0.038 | 0 | 0.097 | 0 | 0.027 | 0.014 | 91.74 | 0.194 | 92.11 | Magnetite-01 |
| 2 | 0.075 | 0 | 0.073 | 0 | 0.014 | 0.025 | 91.06 | 0.277 | 91.524 | Magnetite-02 |
| 3 | 47.339 | 0 | 0.282 | 3.571 | 0 | 0.02 | 45.594 | 0 | 96.806 | Ilmenite-01 |
| 4 | 45.704 | 0 | 0.27 | 3.224 | 0.003 | 0 | 48.988 | 0 | 98.189 | Ilmenite-02 |
| 5 | 8.55 | 0 | 0.17 | 0.305 | 1.015 | 0.212 | 77.418 | 0.015 | 87.685 | Opaque-01 |
| 6 | 13.817 | 0 | 0.383 | 0 | 1.413 | 0.094 | 76.387 | 0.053 | 92.147 | Opaque-02 |
| 7 | 47.625 | 0 | 0.634 | 0 | 0.035 | 0.021 | 47.757 | 0.016 | 96.088 | Opaque-03 |
| 8 | 51.501 | 0 | 0.484 | 0 | 0.013 | 0.045 | 46.779 | 0.02 | 98.842 | Opaque-04 |
| 9 | 26.682 | 0 | 0.364 | 0 | 0.798 | 0.138 | 64.269 | 0.008 | 92.259 | Opaque-05 |
| 10 | 0 | 0.026 | 0.013 | 0 | 1.375 | 76.252 | 0.284 | 0 | 77.95 | Opaque-37b-06 |
| 11 | 34.642 | 0 | 0.357 | 0.499 | 0.005 | 0.004 | 38.451 | 0.008 | 73.966 | Opaque-37b-07 |
| 12 | 0 | 0 | 0.006 | 2.2 | 0.02 | 32.741 | 0.095 | 0 | 35.062 | Opaque-37b-08 |
| 13 | 11.486 | 0 | 0.124 | 0 | 0.859 | 0.064 | 68.168 | 0.032 | 80.733 | Opaque-37b-09 |
| 14 | 13.84 | 0 | 0.163 | 0 | 0.758 | 0.111 | 66.606 | 0.039 | 81.517 | Opaque-37b-10 |
| 15 | 41.577 | 0 | 0.477 | 0 | 0.012 | 0.012 | 40.201 | 0.004 | 82.283 | Opaque-37b-11 |
| 16 | 0 | 0.022 | 0.003 | 0 | 0 | 32.684 | 0.055 | 0 | 32.764 | Opaque-37b-12 |
| 17 | 15.114 | 0 | 0.171 | 0 | 0.876 | 0.07 | 65.355 | 0.017 | 81.603 | Opaque-37b-13 |
| 18 | 26.643 | 0 | 0.237 | 0 | 1.662 | 0.145 | 50.322 | 0.031 | 79.04 | Opaque-13-14 |
| 19 | 10.928 | 0 | 0.223 | 1.767 | 1.404 | 0.087 | 69.4 | 0.041 | 83.85 | Opaque-13-15 |
| 20 | 13.512 | 0 | 0.437 | 0 | 2.561 | 0.234 | 66.361 | 0.02 | 83.125 | Opaque-13-16 |
| 21 | 46.881 | 0 | 0.552 | 0 | 0.063 | 0.034 | 42.35 | 0 | 89.88 | Opaque-13-17 |
| 22 | 4.875 | 0 | 0.212 | 0 | 2.592 | 0.064 | 78.626 | 0.052 | 86.421 | Opaque-13-18 |
| 23 | 0.004 | 0.014 | 0 | 0 | 0.058 | 0.086 | 2.879 | 0 | 3.041 | Opaque-13-19 |
| 24 | 27.073 | 0 | 0.604 | 0 | 1.383 | 0.047 | 54.018 | 0.064 | 83.189 | Opaque-13-20 |
| 25 | 0.03 | 0 | 0.057 | 0 | 0.038 | 0.022 | 91.508 | 0.226 | 91.881 | Mag-01 |
| 26 | 0.041 | 0 | 0.083 | 0 | 0.019 | 0.015 | 90.486 | 0.313 | 90.957 | Mag-02 |
| 27 | 45.419 | 0 | 0.282 | 1.279 | 0 | 0.004 | 45.614 | 0.035 | 92.633 | Ill-01 |
| 28 | 46.055 | 0 | 0.305 | 3.807 | 0.041 | 0 | 44.884 | 0.038 | 95.13 | Ill-02 |

(f) Raw major element measurements of Fe-Ti oxides. Samples 30C and 44.

| MnO | Al2O3 | SiO2 | FeO | Cr2O3 | Total | Comment |
|---|---|---|---|---|---|---|
| 0 | 0.026 | 0.025 | 91.447 | 0.294 | 91.889 | Magnetite-01 |
| 0.13 | 0.038 | 0.026 | 91.632 | 0.193 | 92.104 | Magnetite-02 |
| 0 | 0.004 | 0 | 44.943 | 0 | 87.498 | Ilmenite-01 |
| 5.589 | 0.021 | 0.001 | 45.061 | 0.024 | 92.741 | Ilmenite-02 |
| 0 | 2.258 | 0.093 | 52.352 | 0.174 | 87.507 | opaque-S44-01 |
| 0 | 0.208 | 0.021 | 40.852 | 0 | 89.93 | opaque-S44-02 |
| 0 | 3.641 | 0.99 | 70.082 | 0.05 | 82.004 | opaque-S44-03 |
| 0 | 1.746 | 0.114 | 70.025 | 0.003 | 87.472 | opaque-S44-04 |
| 0 | 0.322 | 0.03 | 44.835 | 0 | 87.762 | opaque-S44-05 |
| 0 | 0.392 | 0.094 | 0.115 | 0.014 | 0.626 | opaque-S44-06 |
| 0 | 1.753 | 0.087 | 67.737 | 0.007 | 89.595 | opaque-S44-07 |
| 0.191 | 1.487 | 0.102 | 65.352 | 0.028 | 90.66 | opaque-S44-08 |
| 0.722 | 1.618 | 0.112 | 65.8 | 0.038 | 87.877 | opaque-S44-09 |
| 0 | 0.353 | 0.028 | 40.626 | 0.001 | 90.288 | opaque-S44-10 |
| 0.869 | 26.695 | 22.506 | 22.176 | 0.017 | 73.54 | opaque-S44-10R |
| 0 | 0.03 | 0.012 | 90.192 | 0.314 | 90.608 | Magnetite-01 |
| 0 | 0.019 | 0.024 | 90.784 | 0.192 | 91.1 | Magnetite-02 |
| 0 | 0.01 | 0.021 | 45.585 | 0 | 91.491 | Ilmenite-01 |
| 3.534 | 0.012 | 0.017 | 45.666 | 0.024 | 95.514 | Ilmenite-02 |
| 0 | 0.029 | 35.238 | 56.134 | 0 | 92.629 | Pyroxene-S30C-01 |
| 0 | 6.824 | 3.733 | 77.638 | 0.004 | 88.396 | Pyroxene-S30C-01R |
| 0 | 0.237 | 0 | 41.992 | 0 | 92.588 | Pyroxene-S30C-02 |
| 0 | 2.258 | 0.095 | 64.243 | 0.045 | 88.638 | Pyroxene-S30C-03 |
| 0 | 4.231 | 0.066 | 76.617 | 0.028 | 88.239 | Pyroxene-S30C-04 |
| 3.127 | 0.178 | 0.01 | 37.045 | 0 | 97.767 | Pyroxene-S30C-05 |
| 0 | 1.83 | 0.161 | 50.463 | 0.037 | 88.357 | Pyroxene-S30C-06 |
| 0.552 | 8.768 | 51.699 | 6.256 | 0.138 | 99.941 | Kaknui-01 |
| 6.62 | 8.783 | 51.615 | 6.118 | 0.205 | 105.84 | Kaknui-02 |

| MnO | Al2O3 | SiO2 | FeO | Cr2O3 | Total | Comment |
|---|---|---|---|---|---|---|
| 7.844 | 0.965 | 55.16 | 14.473 | 0.746 | 107.668 | Hypersthene-01 |
| 7.401 | 0.984 | 54.942 | 14.317 | 0.747 | 106.773 | Hypersthene-02 |
| 0 | 1.374 | 0.601 | 67.785 | 0.01 | 89.854 | Opaque-S1-01 |
| 1.371 | 8.77 | 51.664 | 6.318 | 0.128 | 100.718 | Kaknui-01 |
| 4.565 | 8.833 | 51.605 | 6.23 | 0.134 | 104.168 | Kaknui-02 |
| 4.469 | 0.994 | 54.945 | 14.213 | 0.709 | 103.523 | Hypersthene-01 |
| 3.543 | 0.97 | 54.826 | 14.491 | 0.755 | 102.732 | Hypersthene-02 |
| 0 | 0.021 | 0.009 | 90.934 | 0.247 | 91.261 | Magnetite-01 |
| 0 | 0.033 | 0.063 | 90.56 | 0.197 | 90.954 | Magnetite-02 |
| 1.274 | 0.014 | 0.04 | 45.123 | 0.011 | 91.334 | Ilmenite-01 |
| 4.617 | 0.028 | 0.005 | 44.848 | 0.015 | 98.588 | Ilmenite-02 |
| | | | | | | |
| 0 | 0.004 | 0 | 0.115 | 0 | 0.626 | |
| 7.844 | 26.695 | 55.16 | 91.632 | 0.755 | 107.668 | |
| 1.447 | 2.481 | 12.584 | 49.002 | 0.142 | 90.517 | |
| 2.361 | 4.839 | 21.971 | 28.201 | 0.224 | 16.349 | |

**Appendix VII:** X-Ray Diffraction (XRD) Analyses of selected bulk rock ignimbrite with corresponding d-spacing values labelled. Clay separates are also included.

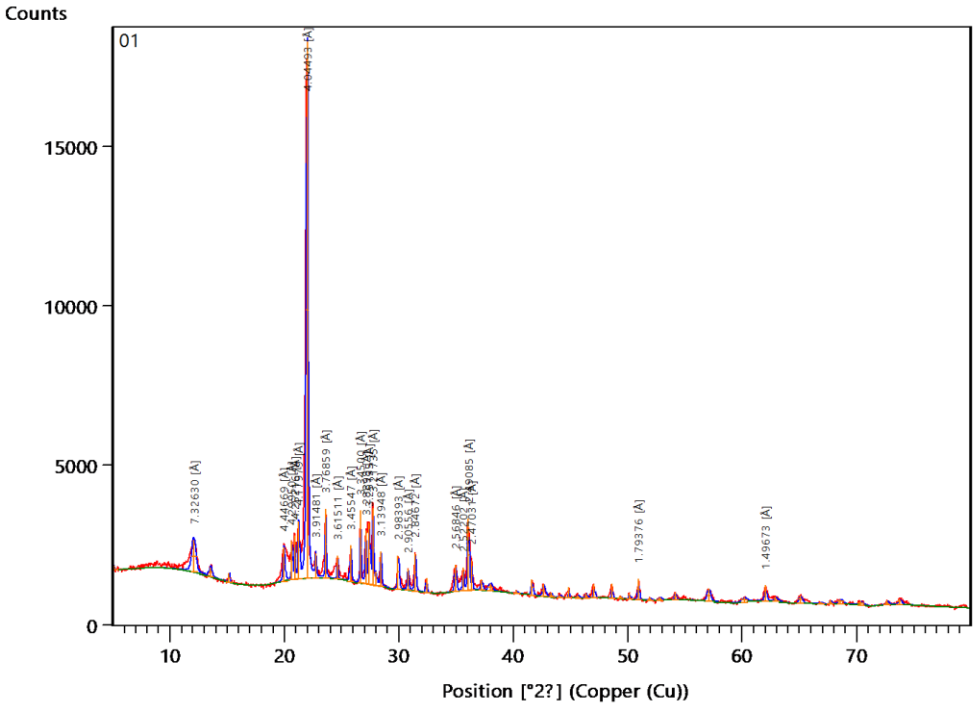


**(a)** Sample Number 01

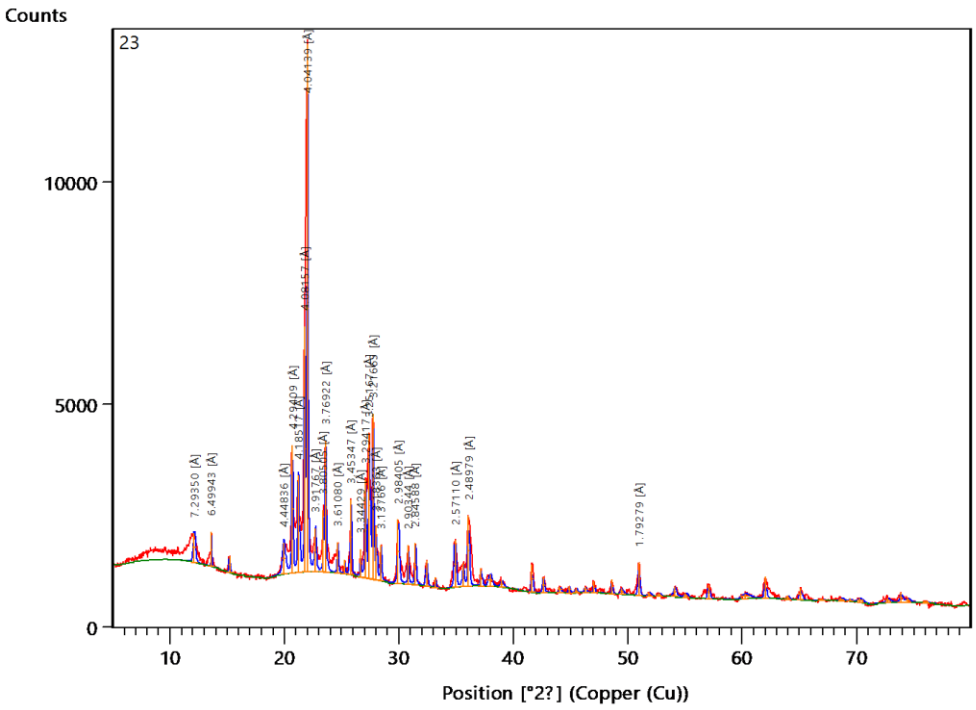


**(b)** Sample Number 23

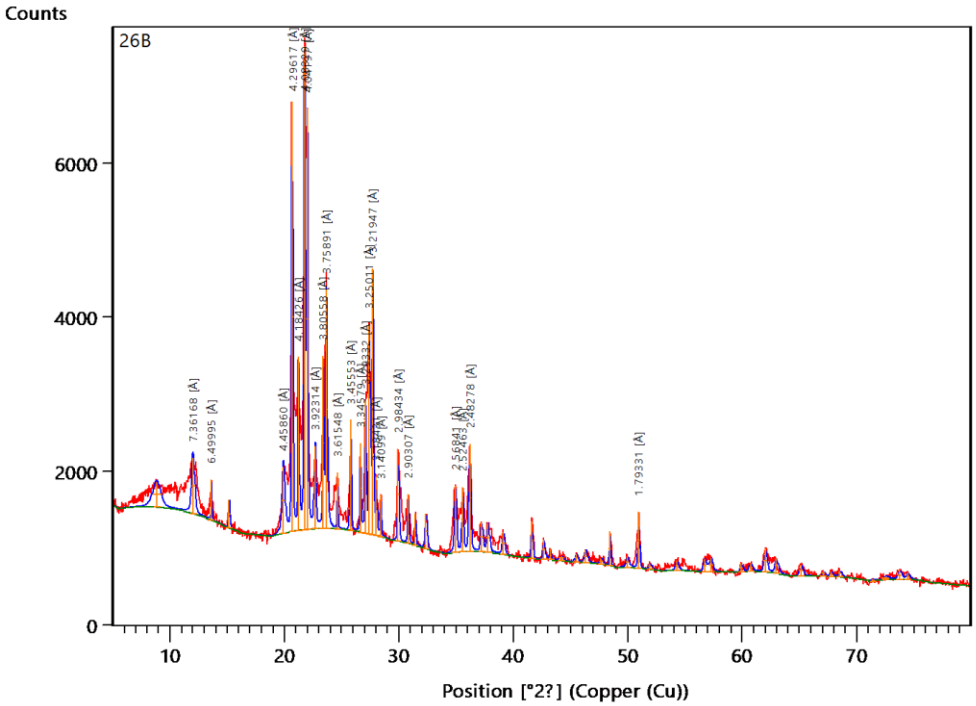


**(c)** Sample Number 26B

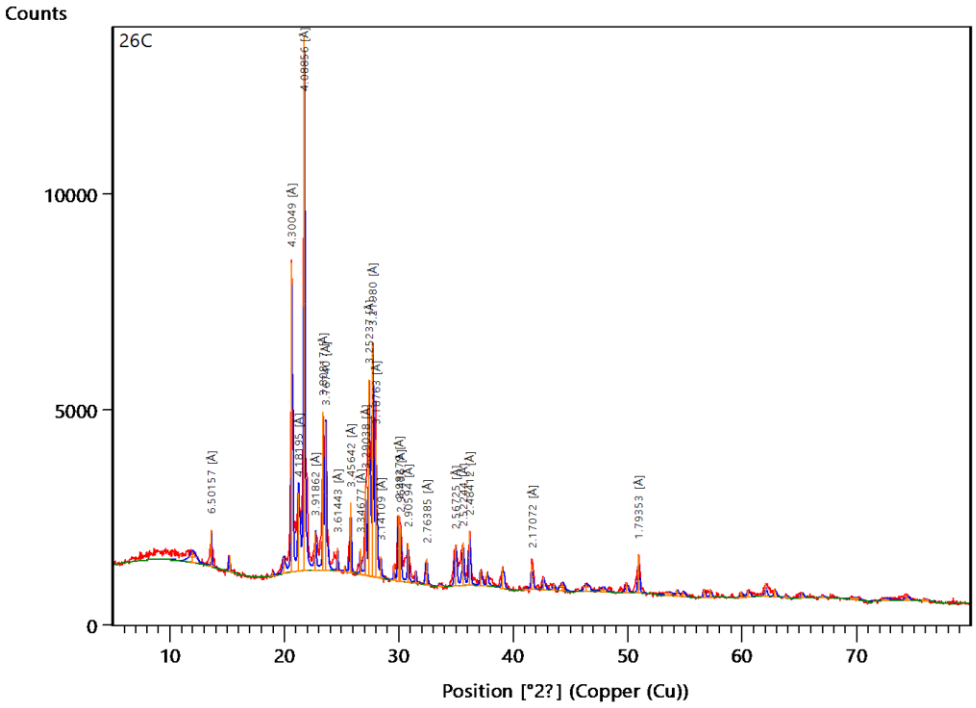


**(d)** Sample Number 26C

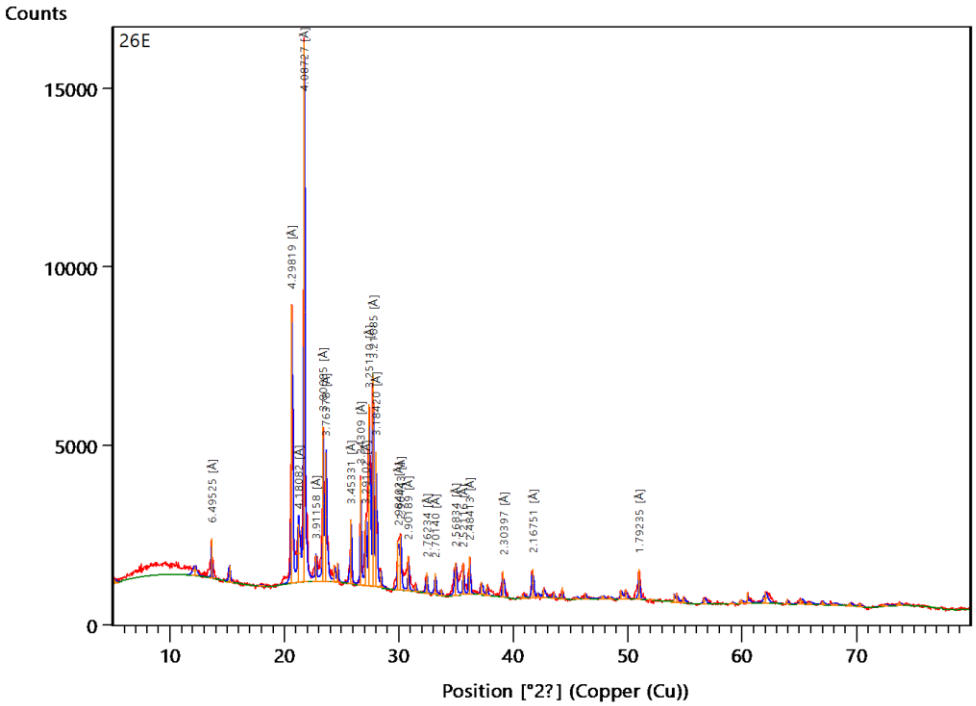


**(e)** Sample Number 26E

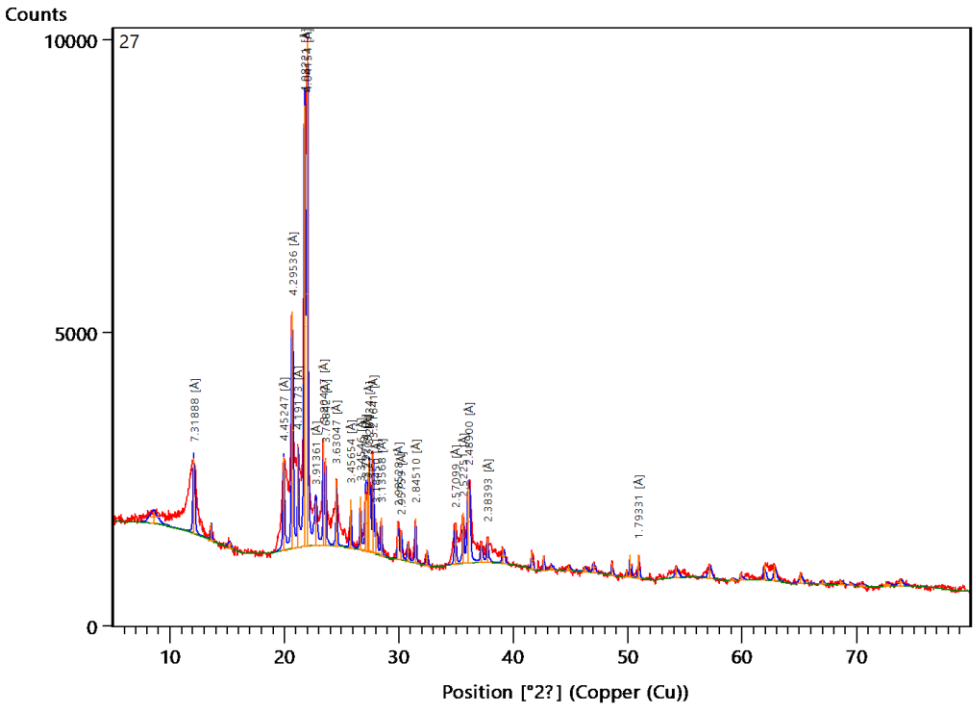


**(f)** Sample Number 27

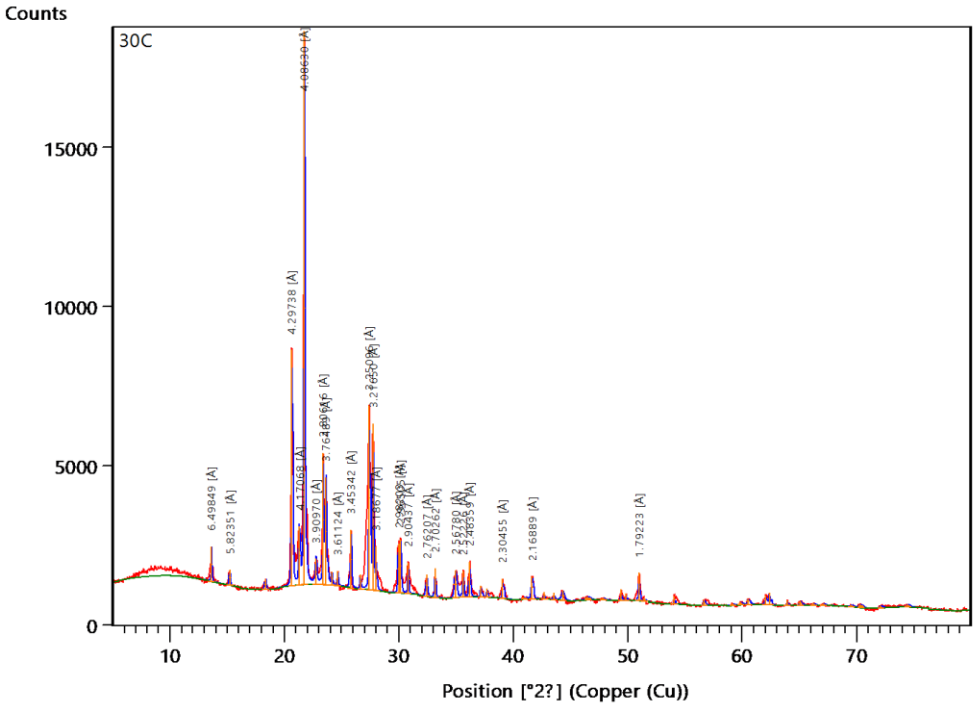


**(g)** Sample Number 30C

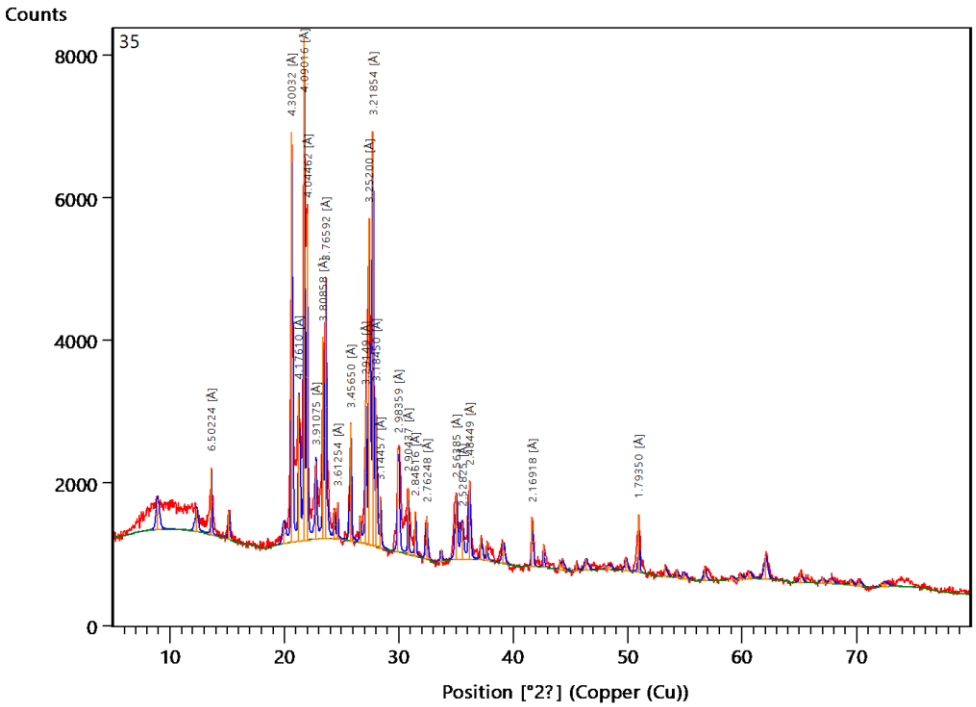


**(h)** Sample Number 35

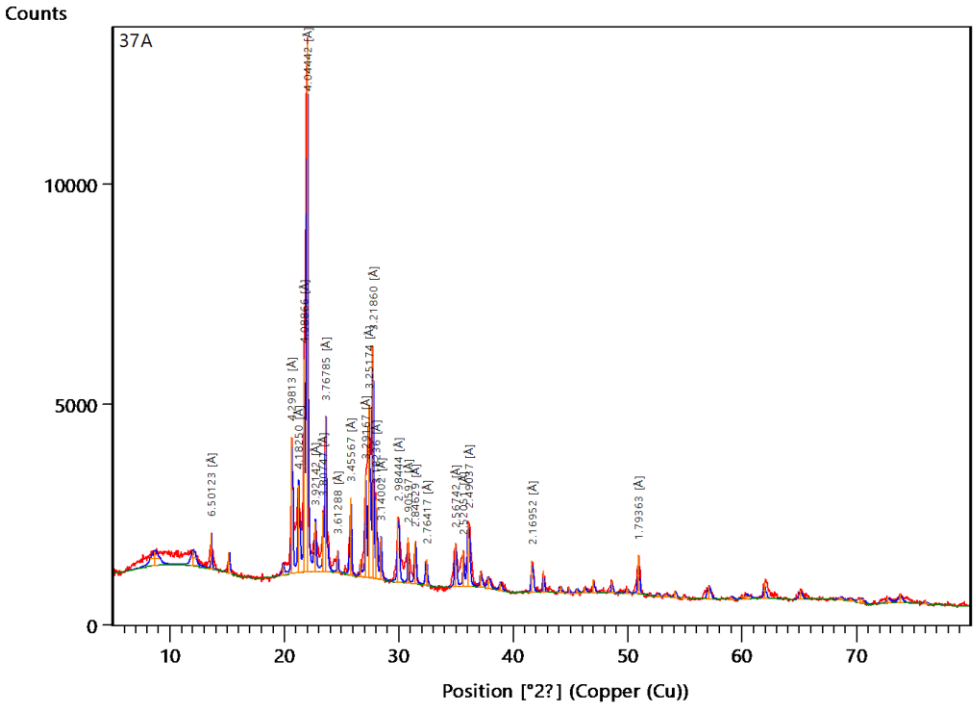


**(i)** Sample Number 37A

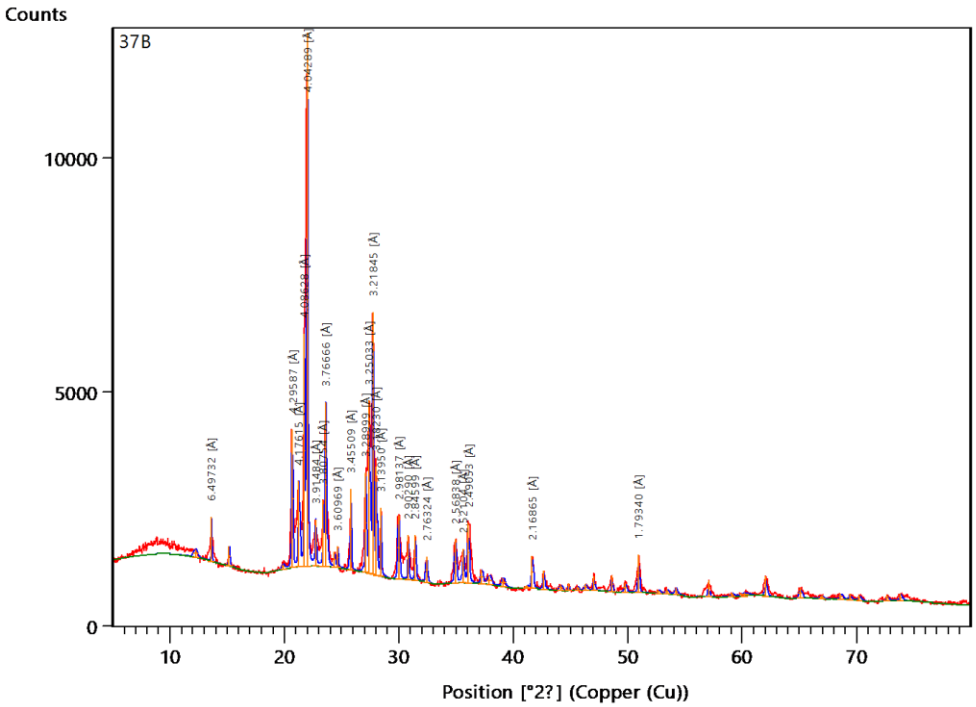


**(j)** Sample Number 37B

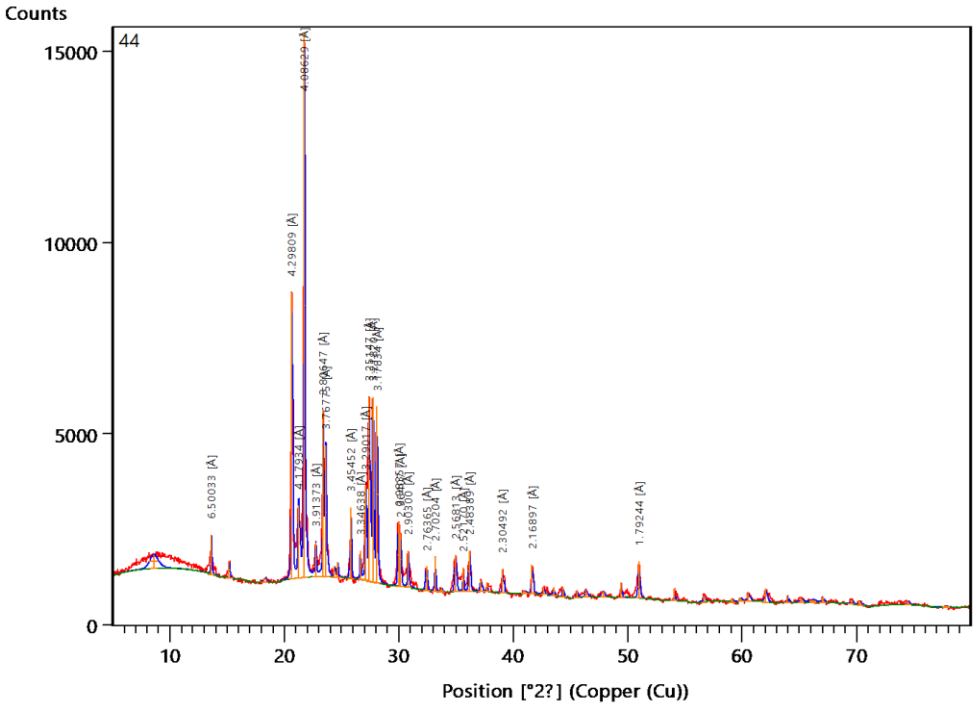


**(k)** Sample Number 44

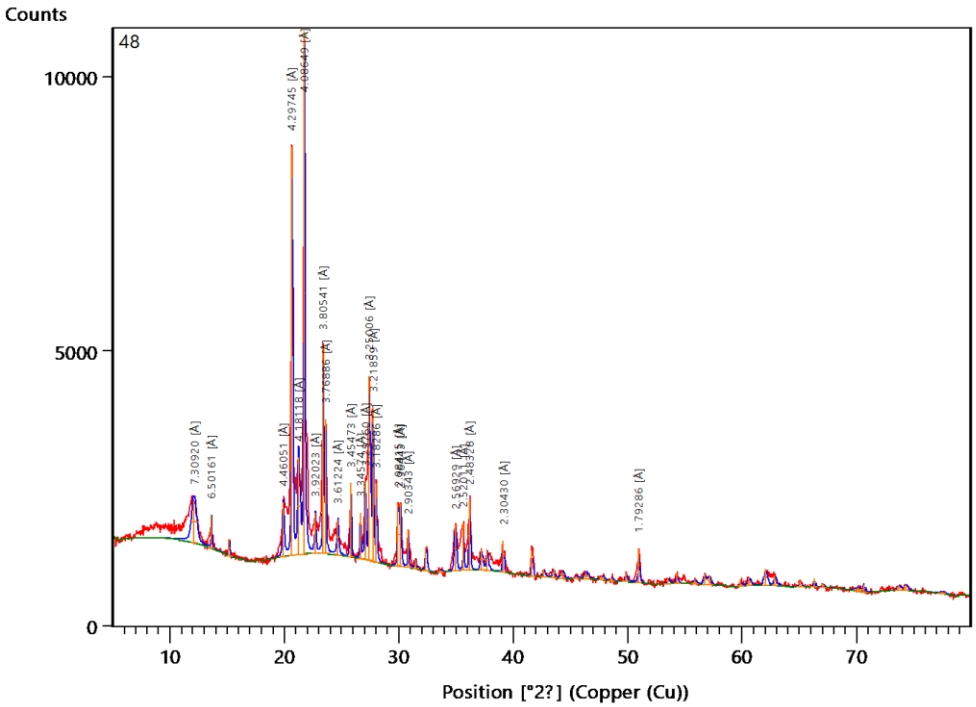


**(l)** Sample Number 48

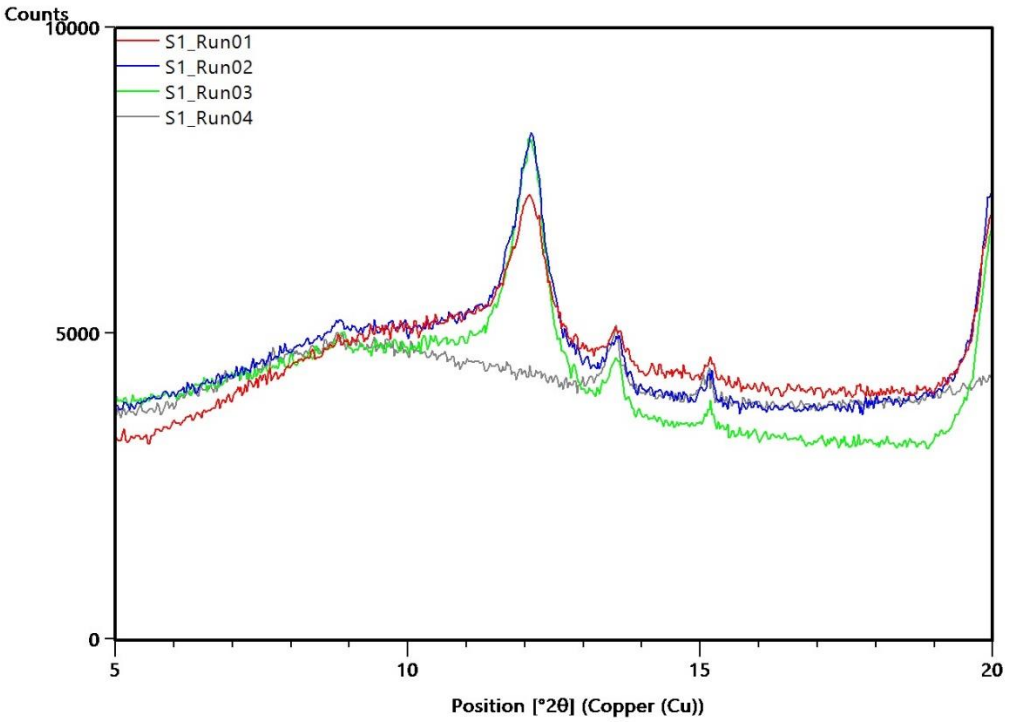


**(m)** Sample Number 01; Clay Separate Analyses confirming the presence of Kaolinite.

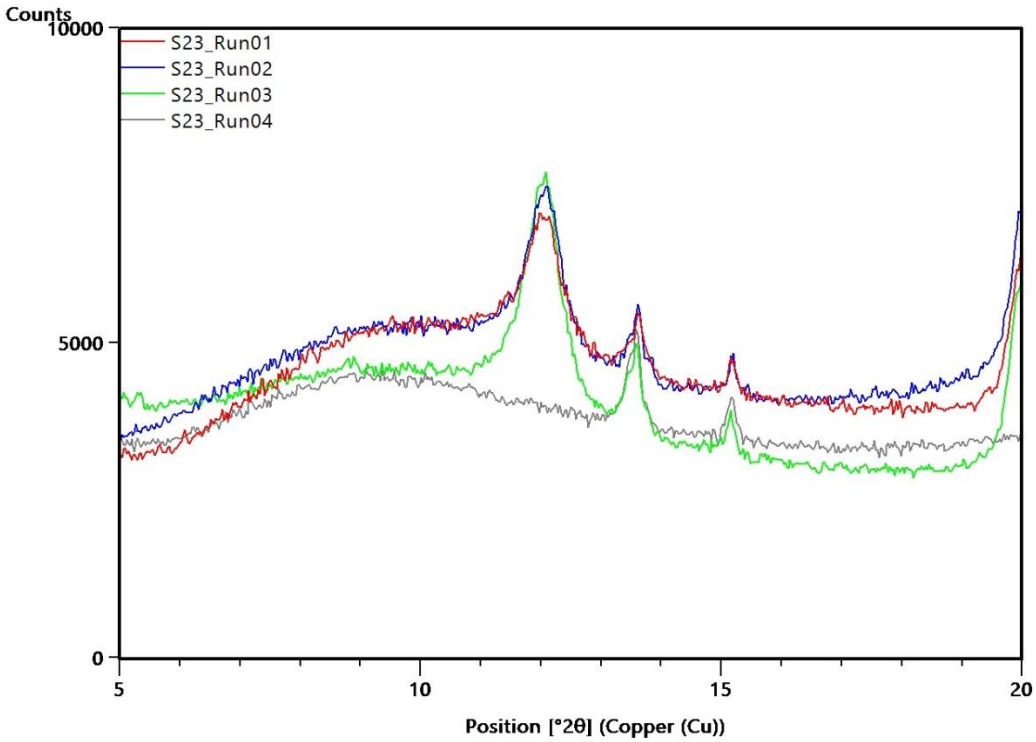


**(n)** Sample Number 23; Clay Separate Analyses confirming the presence of Kaolinite.

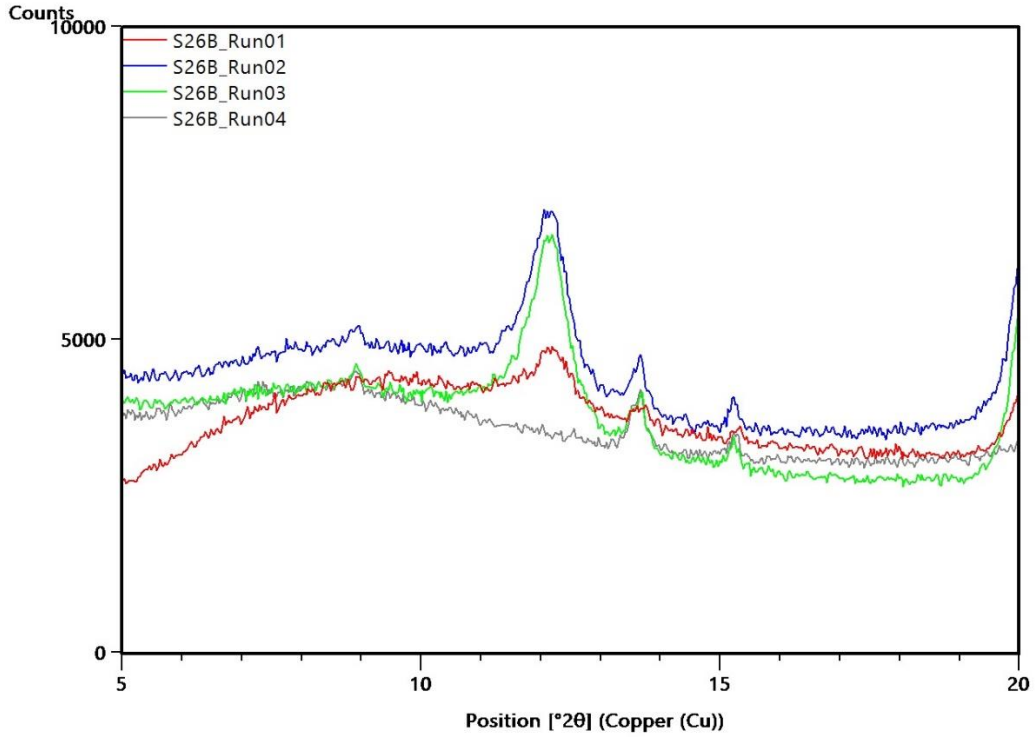


**(o)** Sample Number 26B; Clay Separate Analyses confirming the presence of Kaolinite.

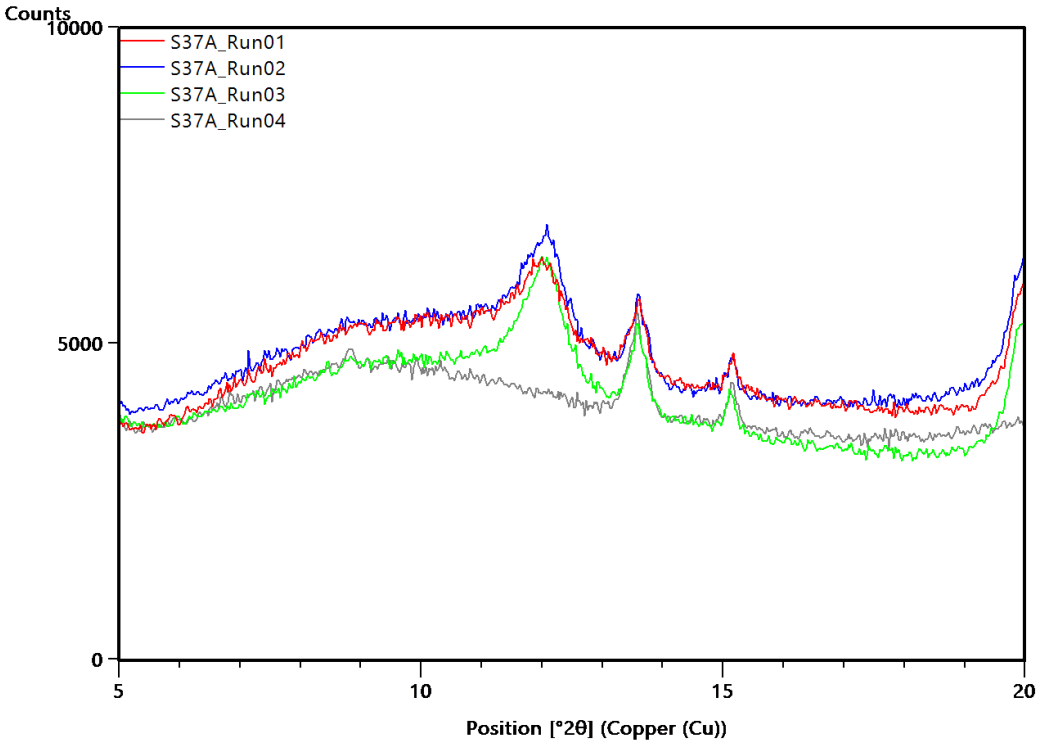


**(p)** Sample Number 37A; Clay Separate Analyses confirming the presence of Kaolinite.